Tethered Coulomb Structure

(Final Report)

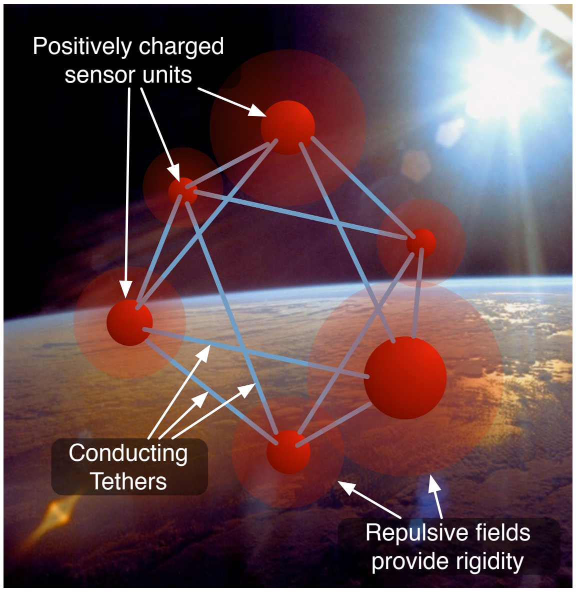

Principal Investigators:

Hanspeter Schaub[1] (PI) and Kurt Maute[2] (Co-PI)
University of Colorado, Boulder, CO 80309-0431

Daniel F. Moorer, Jr.[3] (Co-PI)
Wacari Group, LLC

January 31, 2015

[1]Associate Professor, H. Joseph Smead Fellow, hanspeter.schaub@colorado.edu, (303) 492-2767
[2]Associate Professor, H. Joseph Smead Fellow, maute@colorado.edu, (303) 735-2103
[3]CEO of Wacari Group, dmoorer@wacari.com, (303) 530-5130

Abstract

This research study investigates the feasibility of the Tethered Coulomb Structure (TCS) concept. With the TCS the spacecraft structure is segmented into discrete nodes whose relative positions are controlled through very thin tethers. Tension among all tethers is ensured by employing active charge control on the TCS nodes and raising their potentials to dozens of kilo-Volts. This charging can be done using Watt levels of power and emitting extremely small amounts of fuel. The TCS concept has the benefits that very light weight space structures are feasible that are not only deployable (electrostatic repulsion maintains tension during deployment), but can also change the shape and size to accommodate changing mission requirements. The DII study on the TCS concept focuses on the nonlinear TCS and tether dynamics of a range of deployed TCS configurations to determine how well disturbances can be rejected, and how stiff such a concept would be. Nonlinear 6-degree-of-freedom TCS node simulations are employed to investigate the translational and rotational stiffness as a function of the potentials employed, the tether lengths, as well as the TCS node size and mass properties. The simulations indicate that with voltage ranging up to 30-50kV it is feasible for the TCS node rotational stiffness to accommodate initial rotations of 40-80 degrees per minute.

Further, the TCS shape study has demonstrated that care must be taken when developing the TCS node network. Otherwise, even having all the nodes charged to the same polarity can cause compressive tether elements. Multi-tether connections between the TCS nodes are shown to provide increased resistance to rotations, as well as provide general three-dimensional stiffness. Nonlinear finite element simulations are employed to perform detail studies of the tether dynamics of a TCS system. The results indicate that the tether inertia and bending stiffness play a minor role in the TCS dynamics. Eigenstrains due to fabrication, storage, and environmental effects (partial heating, radiation) may lead to large undesirable TCS motion. However, this study suggests that the electrostatic forces are able to mitigate eigenstrain effects if sufficiently small tether diameters are chosen. Further, electrically conducting, charged tethers aid in mitigating large displacements of the tethers.

The report also outlines the impact of the local space weather on the feasibility of the TCS concept. The nominal geosynchronous plasma environment is very suitable to active spacecraft charging. However, the plasma conditions can vary drastically, and conservative worst case conditions are considered where the Debye length is reduced from 200 meters nominal to about 4 meters in length. Solving the full electrostatic field equations about a charged node in a plasma, the effective Debye lengths are evaluated for TCS configurations. The results indicate that even with short Debye lengths it is feasible to achieve electrostatic repulsion between charged elements up to 2-3 times the Debye length. Further, the power requirements of the TCS concept are studied across the ranges of possible space weather conditions. Nominal Watt-levels of power can increase to 10's of Watt's during solar storms. However, in all space weather configurations electrostatic inflation of the TCS system is found feasible.

Table of Contents

Chapter 1

Introduction

Large space-based platforms on the order of hundreds of meters and more are sought for remote sensing, high resolution surveillance, radiometry, space telescopes, space situational awareness or power collection. Spacecraft formations and large space structures are two methods of achieving a large space-based platform. Advanced spacecraft and formations with shape changing capabilities would allow for long duration missions in that the platform shape can be adjusted to accommodate changing mission requirements.

1.1 Tethered Coulomb Structure Concept

This study investigates a recently introduced large space structure concept called the Tethered Coulomb Structure (TCS).[1,2] The TCS concept offers a number of advantages over the free-flying Coulomb spacecraft cluster concept in that the relative motion is constrained through the tether lengths. The TCS uses discrete spacecraft nodes that are inter-connected with fine, low-mass tethers as illustrated in Figure 1.1. Each node is repelled from the other TCS nodes through the use of electrostatic (Coulomb) forces. The inflationary Coulomb forces provide rigidity and shape control. The TCS size and shape is constrained by the tether lengths which limit how far the nodes can repel from each other. The electrostatic force is applied by manipulating each TCS node's potential with a charge control device. Here active emission of charged particles such as electrons or ions are used to drive the node potential away from its natural space weather dependent equilibrium to a desired potential level.

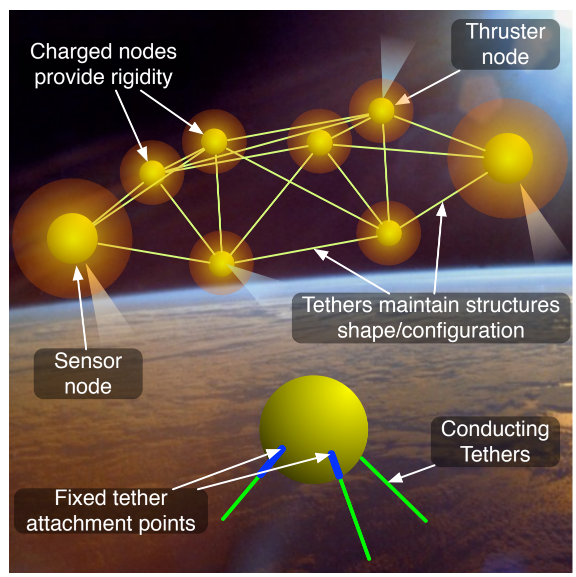

Figure 1.1: *Tethered Coulomb structure concept*

Similar to the Coulomb formation flying benefits, some key advantages of the TCS system is that it only requires Watt-levels of power and very little propellant (low mass ions or electrons). This provides the TCS with long term mission capabilities.[1] The main difference between TCS and Coulomb formation flying scenarios is that the charge control problem is significantly simplified. Instead of requiring precise charge levels to maintain relative positions, as well as complex non-

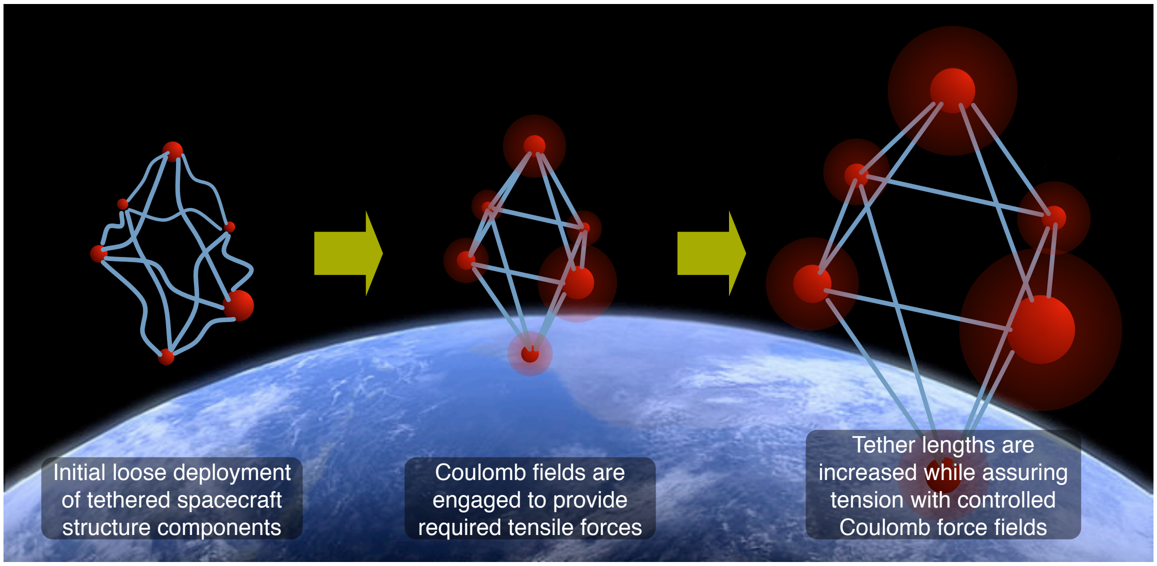

Figure 1.2: *Illustration of TCS being First deployed, and then electrostatically inflated to desired shape and size*

affine control developments, the TCS only requires the charge levels to be maintained above a certain threshold that guarantees robustness to orbital perturbations. For example, to guarantee tether tension in the presence of differential gravity or solar radiation pressure, the electrostatic inflationary force must be larger than these perturbations.

TCS configuration sizes ranging from tens to hundreds of meters are envisioned by connecting strands of charged nodes with tethers. The TCS concept has the advantage of being launched in a compact and stored configuration, that is then inflated or deployed on-orbit as shown in Figure 1.2. A key feature of TCS is that this Coulomb force inflation provides structural rigidity and an ability to resist deformation and disturbances. With length-adjustable tethers it is possible to change the structures shape and size on-orbit providing an adaptable nodal network to meet variable sensing and mission requirements. The concept can also be used to deploy and hold a sensor node in a fixed position from a primary spacecraft providing situational awareness or local sensing (see Figure 1.3). An additional advantage of the TCS concept is that tether tensions can be maintained without requiring a particular orbit, equilibrium configuration or spin, like typical tethered systems.

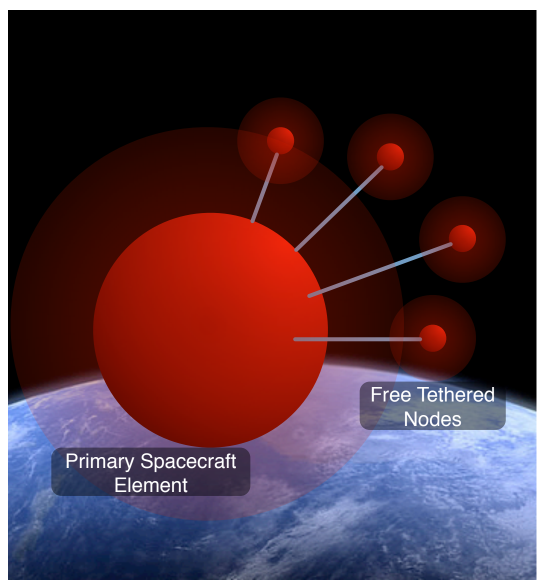

Figure 1.3: *Tether sensor nodes held next to a primary spacecraft component*

The potential benefits and applications of the TCS concept are summarized through:

1. Large light-weight and deployable space structures can be achieved.

2. Provide an adaptable sensor network capable of changing its shape and size to meet changing mission and sensor requirements.

3. Generate 3D tethered structures of sensors without requiring particular equilibrium configurations or spinning to maintain tether tension.

4. Deployment of single sensors about the primary vehicle to monitor the local spacecraft neighborhood, as well as provide external monitoring of the spacecraft health and condition.

1.2 Alternate Concepts

A large platform can be launched as a rigid structure. However, its size and mass is limited by the capabilities of the available launch vehicles. On-orbit construction can increase the overall dimensions of a rigid structure such as has been done with the assembly of the international space station; however, such structures require human construction or advanced autonomous assembly techniques. The design of deployable spacecraft components is an active research area with few having been successfully implemented or tested in space.[3,4,5,6]

Along with the development of large space structure technologies, sophisticated applications and missions are emerging. One such mission is the Eyeglass concept that is intended to be used for Earth surveillance from Geosynchronous Earth Orbit (GEO). A 25-100 m aperture diffractive lens is to be deployed on orbit.[7,8]

Two proposed missions that intend to generate large kilometer size baselines are the NASA Goddard Stellar Imager[9] and the NASA JPL study on the proposed Terrestrial Planet Finder (TPF).[10] Both of these concepts utilize a formation of free-flying spacecraft. Free flying formations offer advantages such as variable baselines, system redundancy and fractionated and responsive architectures.[11] The PRISMA mission is designed specifically to demonstrate advanced autonomous formation flying techniques.[12] A challenge with free-flying craft is the complex relative dynamics, challenging relative motion sensing requirements, and the associated control strategies which can often require high propellant usage to maintain an accurate formation.

Spacecraft formations can be operated with conventional chemical thrusters or electric propulsion where the fuel propellant mass, or electrical power requirements, must be taken into careful consideration. Further, for close proximity operations less than 100 meters, the thruster exhaust plume impingement issues must be taken into account.

Over the last decade, novel, essentially propellant-less relative motion control concepts consider using either Coulomb electrostatic interactions,[13,14,15] magnetic formation flying,[16] Lorentz forces[17,18,19,20] or flux-pinning.[21,22] In particular, the use of inter-spacecraft Coulomb forces offers close formation relative motion control with low power and propellant requirements.[13,23,15] However, the control of a cluster of actively charged spacecraft remains a challenging research area due to the non-affine nature of the electrostatic force actuation.[24,25,26,27] Analytically stable charge feedback control strategies are discussed for a two-spacecraft cluster in References 28, 29, 30, and for a three-vehicle cluster in Reference 24. The control of a larger formation with more than 3 vehicles remains an open research topic. Izzo and Pettazi propose the self-assembly of large space structures with Coulomb spacecraft.[31] However, their N-vehicle charge control law does not have analytical stability guarantees.

Figure 1.4 shows how the concepts shape change attributes and control requirements compare to alternate space platform techniques. A large, monolithic space structure such as the Hubble space telescope is essentially launched and deployed as a single unit (except for the deployed solar arrays). This provides good overall rigidity with very little relative motion or flexing control requirements. Large space structure concepts are considered now. The iSat program for instance, envisions deployable structures that could reach 100 meters in size and larger. This

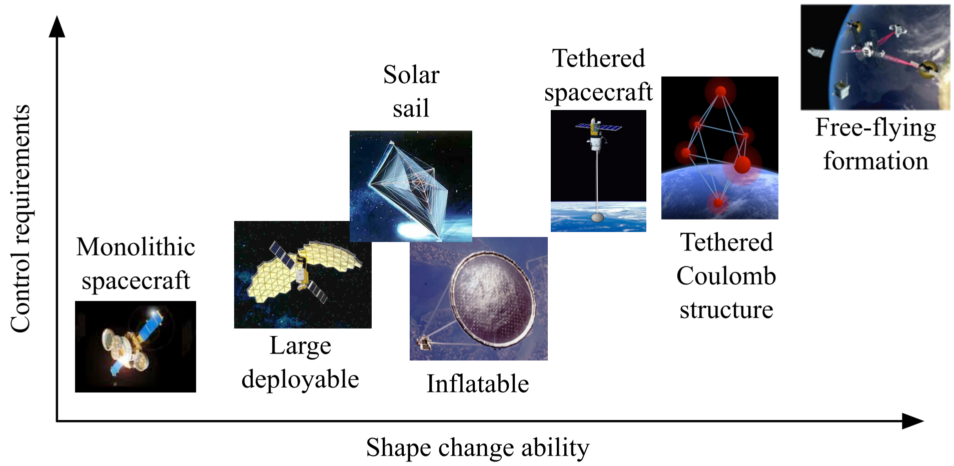

Figure 1.4: *TCS concept shape change attributes and control requirements comparison*

increased shape changing ability results in a very light weight structure that might require active damping and smart materials to dampen out oscillations. Other large spacecraft concepts such as solar sails or gas-inflatable structures achieve even larger shape change capabilities with ever more light-weight structures. On the other end of large space platforms in Figure 1.4 are free-flying formations. Here the space platform shape is free to change subject to thruster propellant and power limitations. However, the relative motion sensing and control requirements are significantly increased in contrast to continuous structures such as iSat or solar sails. The proposed TCS concept falls between the current solar sail and inflatable concepts, and the free-flying spacecraft cluster concepts. While the TCS nodes are interconnected, the milli-Newton tether tensions are small enough such that the orbital motion must be taken into account when studying TCS dynamics.

1.3 TCS Challenges

While the TCS concept has many benefits which enable novel spacecraft missions to be considered, the development of this concept is just beginning. This section outlines the primary challenges that are investigated in this multi-disciplinary study. These are initial studies for prototype TCS to evaluate the feasibility and limitations of the TCS concept. In particular, the study will consider nominally deployed TCS configurations which are holding a constant potential. Deployment studies, or active TCS shape damping methods, are beyond the scope of this 9 month study.

1.3.1 Electrostatic Relative Motion

The charged relative motion of free-flying spacecraft is a highly nonlinear dynamical system. Current research is investigating methods to effectively control a large cluster of charged bodies in space. The TCS concept maintains the desired relative positions through the use of both tethers and Coulomb force fields. Ideally the physical tethers enforce the desired component separation distances. This provides a tremendous control simplification compared to a free-flying sensor cluster, charged or un-charged. While simplified, the resulting TCS dynamical system remains complex and challenging to model and analyze.

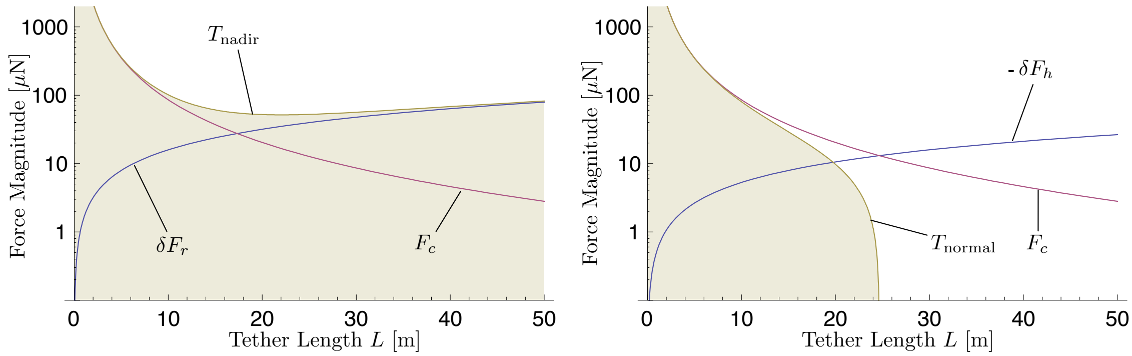

(a) Orbit Radial Deployment (b) Orbit Normal Deployment

Figure 1.5: *Comparison of the Coulomb and differential gravity force magnitude and resulting tether tension for GEO 2-craft TCS with 100 kg nodes and 1μC charge*

The charged relative motion study is challenging in that it involves both the nodal orbital motion, as well as the finite body rotations of each nodal element. Regarding the coupled orbital motion, the Coulomb forces must compensate for the differential gravity forces and produce repulsive Coulomb forces which guarantee that tether tension is maintained. In contrast to the free-flying Coulomb spacecraft concept, TCS only requires the charge levels to exceed a lower bound, and does not have to track specific values. This greatly simplified the implementation of the TCS charge control. Further, as illustrated in Figure: 1.5, the differential gravitational influence can have a distinctly different impact on the TCS charge requirement. Consider a simple charged two-node system interconnected with a tether. If the nodes are aligned in the orbit radial direction, then the differential gravity will always assist in maintaining tether tension. In this scenario the Coulomb force will maintain a strong tether tension at short separation distances where the differential gravity is the weakest, while differential gravity maintains tension for larger separation distances where Coulomb repulsion is the weakest. Both force complement each other. However, if the nodes are aligned with the orbit normal direction as considered in Figure 1.5(b), then the differential gravity will try to compress the TCS structure, and fixed Coulomb charges will only be able to maintain tether tension for a finite range of separation distances. Thus, a particular astrodynamics challenge is how to construct a network of charged nodes such that tension can be maintained for general three-dimensional configurations.

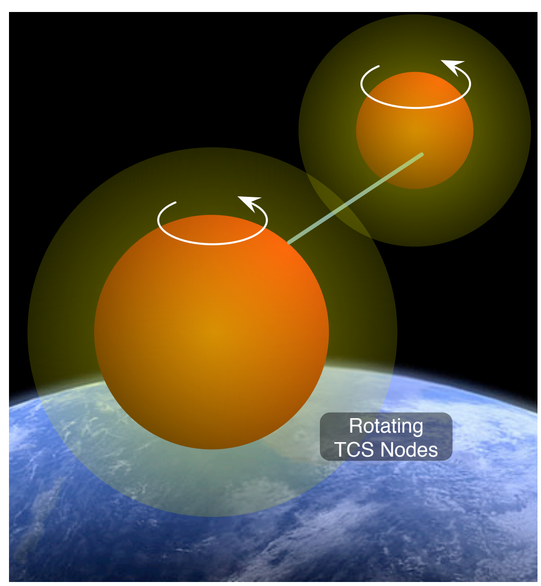

Figure 1.6: *Relative TCS rotational stiffness.*

The second relative motion challenge is the rotational stiffness of the TCS system illustrated in Figure 1.6. While the repulsive forces are sufficient to overcome differential gravitational forces, the question is how well the TCS nodes can resist rotational motion. The residual relative motion could be due to orbital perturbations such as differential solar radiation pressure, or due to the structure having been recently deployed. Of concern is how much initial TCS nodal rotation can be present without having the nodes wrap up in the thin tethers. The rotational stiffness will be a function of the nodal separation distance, where the tethers are attached, how many tethers are used to inter-connect two nodes, and of course, the TCS potential levels employed.

1.3.2 Networked Tether Dynamics

The network of thin filaments to interconnect the charged spacecraft components must be carefully considered. The required force levels to maintain a shape dozens of meters in size at GEO is on the order of micro- to milli-Newtons. To avoid significant wrinkling and twisting of the thin tethers, the material selection must be carefully coordinated with the tether thickness and strength. Significant wrinkling can be typically avoided with a sufficient force to cable cross-section area ratio. Because of the potentially large tether deflections that could occur, sophisticated finite element modeling methods must be employed that enable nonlinear tether deflections to be considered.

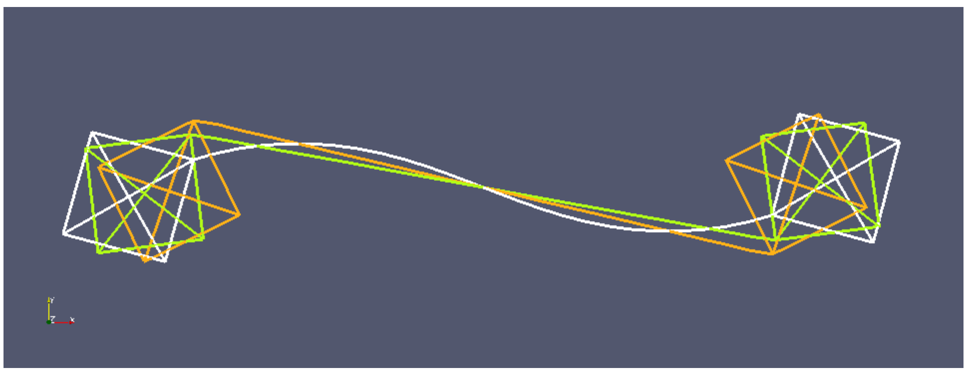

Figure 1.7: *Illustration of a continuous tether with end masses being modeled through finite element software simulations*

The higher-fidelity tether dynamics study provides insight into the conditions under which the tether motion can be modeled through a simpler nonlinear displacement model with proportional stiffness. This provides a verification and validation of the earlier charged astrodynamics study which uses a simplified tether model for computational efficiency. Further, the finite element tether model always allows studies into the impact of residual strain on the tether and TCS nodal motion, the influence of material property choices and tether diameters, as well as the impact of the tethers being charged. Careful study will prevent the TCS tether motion from causing significant nodal motion or TCS shape deformations.

1.3.3 Orbital Environment

The plasma environment about a spacecraft is influenced by the material and geometry, the ambient space plasma environment, and the presence of solar radiation. Most spacecraft charging research has investigated how a single vehicle will charge due to the plasma charge current and the photo-electron current. The coupled influence with another charged spacecraft remains an open area of research. The proposed work will investigate 1st order models of how the cluster craft with equal charge polarity will influence the local Debye shielding and associated plasma analytical properties.

Due to possible charge shielding from the local plasma environment it is necessary to operate a TCS at GEO altitudes (see Figure 1.8) or higher where the plasma is nominally hot and sparse. At GEO, a spacecraft can naturally charge to kilovolt potentials during periods of Earth eclipse. Such kilovolt charge levels are similar to the levels of charge that are considered for the TCS

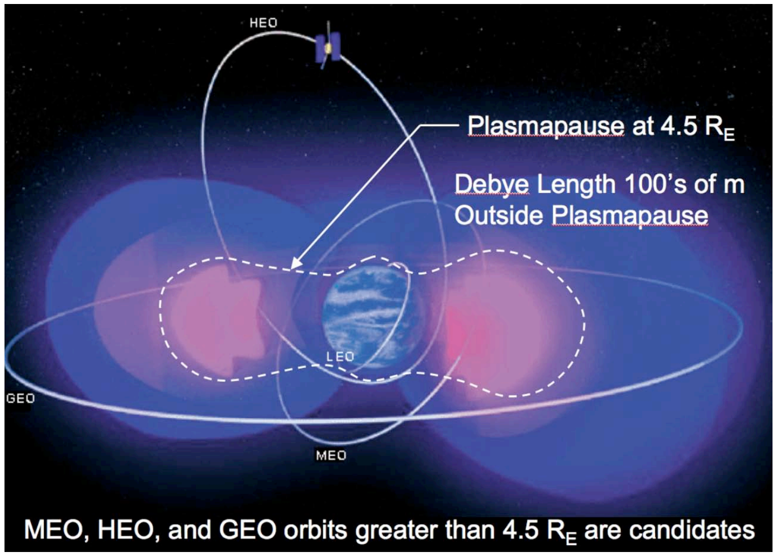

Figure 1.8: *Feasible TCS orbit altitude illustrations*

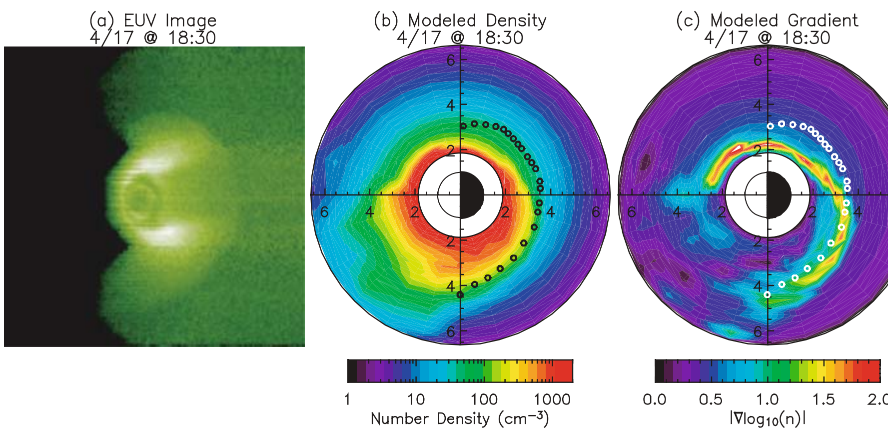

Figure 1.9: *IMAGE (Imager for Magnetopause to Aurora Global Exploration) space weather snapshot from April 17, 2002. (Image presented in Reference 37)*

concept in this paper.[32,33] This charge can be controlled with charge emission technology that is already space-proven. One example is the volt-level control the European CLUSTER mission demonstrates.[34,35,36] A charge emission device can be used on each of the TCS nodes or on a single node and distributed to other nodes via conducting tethers. The benefits and draw backs of either scenario are still being investigated.

The space weather will thus have a direct impact of the electrostatic forces that are experienced between charged TCS nodes, as well as the power requirements to maintain non-equilibrium TCS potentials. The Low-Earth-Orbit (LEO) regime is not practical for TCS because the plasma is too cold and dense, yielding Debye lengths on the order of centimeters. For the GEO regimen the nominal Debye length is on the order of 150-250 meters. However, at times the colder, lower altitude plasma environment can get pushed up into the geostationary regions as documented in Figure 1.9 of Reference 37. As a result the plasma parameter can fluctuate radically. This complicates the TCS design in that the tether tensions must not only be maintained during nominal, but also during worst case space weather conditions. The study will explore the impact of the space

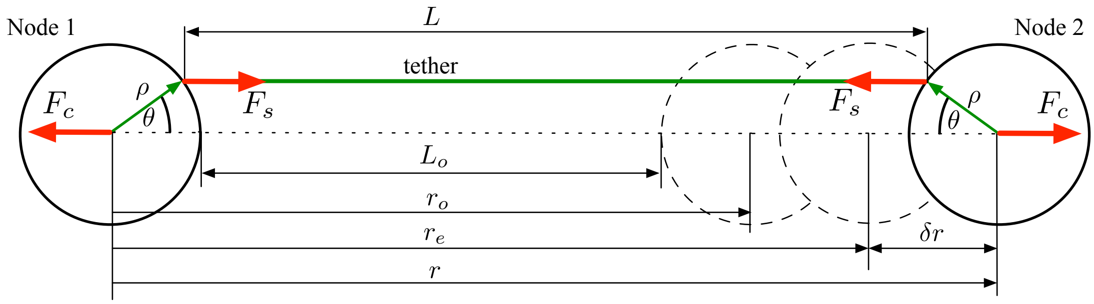

Figure 1.10: *Asymmetric two-node system with two degrees of freedom*

weather on the TCS expansion force creation, as well as on the associated power requirements to maintain desired potentials during space weather fluctuations.

1.4 Benchmark TCS Configuration

The dynamic analysis of the TCS nodes or the inter-connecting tether can quickly grow in complexity as the number of nodes increases. The TCS study uses the two-node setup shown in Figure 1.10 as a convenient benchmark.

By providing the nodes with an initial non-equilibrium separation distance r, and asymmetric rotations, the nodes undergo one-dimensional rotational motion and translation. This reduces the the complex six degree-of-freedom relative motion of a two-node TCS system to only 2. The benefit is that this allows for basic analytical insight into the voltage to translational and rotational stiffness relationship, as well as provides simple simulation cases that are used in both the TCS nodal dynamics and TCS tether dynamics simulations scenarios.

This setup will be used as the basic benchmark setup. Note that the two nodes are only interconnected via a single tether. Thus, as the simulation complexities are increased by considering other initial rotational motions, or considering multiple tethers interconnecting the nodes, this performance of the benchmark setup is used for relative performance comparisons.

1.5 Report Outline

The final technical report on the DII TCS study is organized as follows. Chapter 2 discusses the TCS nodal dynamics, taking into consideration both the translational and rotational stiffness of charged nodes. In particular, of interest is how constant TCS potentials influences the shape stiffness. Further, a shape study is presented where the coupled differential gravity and electrostatic force interactions are studied. Of interest is how differential gravity, or having particular three-dimensional nominal shape requirements, impacts the required charge levels, and if there are limitations on what types of shapes can be achieved with the TCS system. Next the orbital perturbations impact on the TCS nodal motion are studies. Finally, the chapter ends with a study of a particular two-node system where one element is much more massive (primary spacecraft) than the second node (sensor element).

Chapter 3 discusses how the tether dynamics is modeled through the use of nonlinear finite element simulation software. This work includes a validation study of the simplified tether dynamics model used in chapter 2, as well as a study on when the tether wrinkling effect significantly impacts the TCS nodal motion. The numerical tether dynamics simulation will consider deformation due to initial TCS nodal motions, residual strain within the tether material, as well as deformations due to the tethers being charged and mutually repelling.

Chapter 4 presents the findings on how cold and dense the geostationary space environment can become at worst case conditions. The resulting parameters are then used to study the impact on the electrostatic charge shielding. In particular, the effective Debye lengths are computed where the TCS potential exceed the Debye-Hückel assumptions. Further, numerical simulations are performed of the plasma environment about two nodes to obtain first order force and power variations due to having over-lapping Debye sheaths about equally charged objects. The space-weather related electrostatic forces are then used to revisit the translational and rotational TCS stiffness study and show the potential space weather storm impact. Finally, the TCS power and fuel estimates are studied for a range of space environmental conditions.

Chapter 2

Tethered Coulomb Structure Dynamics Modeling

This work utilizes a nonlinear numerical simulation that models a general number of spacecraft nodes which are tethered in a selectable configuration. Both the relative motion and rotation are modeled, providing each TCS node six degrees of freedom. The tethers are modeled here as proportional springs with nonlinear displacements. More detailed studies of the tether dynamics are performed with finite element simulations in chapter 3. This chapter examines the dynamics of TCS systems with the goal of obtaining qualitative and quantitative relationships between the TCS response and its system and nodal parameters and initial conditions. A description of the electrostatic force model used is given, as well as reasoning for its use. The system forces and the equations of motion for translation and rotation are given. The translational stiffness of a two-node TCS is examined for various system parameters. An analysis of rotational stiffness is conducted to examine the effects of system parameters, multiple tethers, and nodal properties. Orbital perturbations such as differential gravity and solar radiation pressure are analyzed and their effects are quantified. Finally, advanced TCS concepts are presented and simulated.

2.1 Electrostatic Force Modeling

A Coulomb force is generated from the electrostatic interaction of two charged bodies. If two bodies in a vacuum have charges q_1 and q_2, the Coulomb force between them is computed through

$$|\boldsymbol{F}_c| = k_c \frac{|q_1 q_2|}{r_{12}^2} \tag{2.1}$$

where $k_c = 8.99 \times 10^9\ \mathrm{Nm^2C^{-2}}$ is the vacuum Coulomb constant and r_{12} is the separation distance between bodies 1 and 2. If it is assumed that the spacecraft body is comprised of an outer spherical surface that maintains a constant charge q_1, then its potential in a vacuum is given as:

$$V_{sc1} = \frac{q_1 k_c}{\rho} \tag{2.2}$$

where ρ is the radius of the spherical craft.

Equation 2.2 is only valid in a vacuum, which is not true at geosynchronous orbits (GEO) altitudes. At GEO the Coulomb force will be partially shielded by free-flying charged particles of the local plasma environment. The Debye length, λ_D signifies the strength of the shielding due

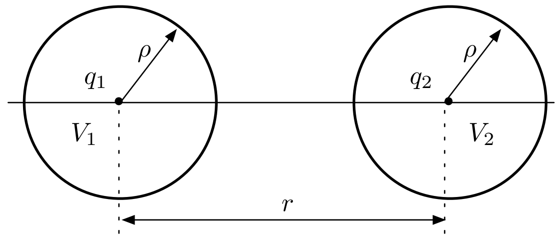

Figure 2.1: *Two closely separated charged finite spheres*

to the plasma. If a small spacecraft potential is assumed compared to the local plasma thermal energy

$$e_c V_{sc1} \ll \kappa T_e \tag{2.3}$$

where $e_c = 1.602176 \times 10^{-19}$ C is the elementary charge, $\kappa = 1.38065 \times 10^{-23}$ JK^{-1} is the Boltzmann constant and T_e is the plasma electron temperature in Kelvin, then the potential about this charged craft is represented by the Debye-Hückel equation:[38,39]

$$V = k_c \frac{q_1}{r} e^{-(r-\rho)/\lambda_D} \tag{2.4}$$

This potential equation incorporates plasma shielding and resembles a conservative bound of the charge interaction the nodes will experience.[40] At GEO, the $e_c V_{sc1} \ll \kappa T_e$ condition is no longer true if the spacecraft charges to 1-10 kV potentials. As discussed in Reference 40, the neglected higher order terms of Poisson's partial differential equation, which led to Equation (2.4), results in less plasma shielding of the electrostatic fields. Thus, the use of Equation (2.4) is considered a conservative estimate of the actual potential that might exist about a body. The benefit of using Equation (2.4) is that it allows for simplified analysis, and faster numerical simulations because the full Poisson-Vlasov equations do not need to be solved. Solving the full Poisson-Vlasov equations requires solving complex partial differential field equations and is discussed in more detail in section 4.2.

Taking the gradient of the potential in Equation (2.4) (assuming spherical symmetry) yields the resulting Coulomb force $\boldsymbol{F}_c$ relationship between charged craft 1 and 2:

$$|\boldsymbol{F}_c| = k_c \frac{q_1 q_2}{r_{12}^2} e^{-r_{12}/\lambda_D} \left(1 + \frac{r_{12}}{\lambda_D}\right) \tag{2.5}$$

The Coulomb force of Equation 2.5 is created between two isolate point charges and does not accommodate realistic electrostatic potential distributions from having two closely separated finite spheres. An improvement to the Coulomb force is made by modeling the effective charge between two finite spheres of fixed potential. This has a significant influence on the effective charge of each sphere when the center-to-center separation is low relative to the sphere radii (separations less than approximately 10 sphere radii, $r < 10\rho$). Figure 2.1 shows two close spheres that maintain a fixed potential, V_i.

In the absence of sphere 2, the point charge of 1 is computed using Equation 2.2. However, once sphere two is introduced the net potential of both spheres changes the effective sphere charge and consequently the Coulomb force. The potential at sphere 1 is computed including the charge of sphere 2 using the expression:[41,42]

$$V_1 = k_c \frac{q_1}{\rho} + k_c \frac{q_2}{r} \tag{2.6}$$

Similarly, there is an equivalent potential equation for sphere 2. With spheres 1 and 2 set to known and equivalent potential magnitudes $V_1 = V_2$, (a nominal TCS application characteristic) the two potential equations can be independently solved for the resulting equivalent charge of each sphere:

$$q_i^* = \frac{V_i}{k_c}\left(\frac{\rho r}{\rho + r}\right) \tag{2.7}$$

If the spheres have a large separation distance ($r >> \rho$) Equation 2.7 will reduce to the standard single sphere charge defined in Equation 2.2, as required. The effective charge and repulsive Coulomb force is reduced from the equivalent point charge model.

Generalizing Equation 2.6 for N spheres gives the potential equation:

$$V_i = k_c\left(\frac{q_i^*}{\rho_i} + \sum_{j=1}^{N}\frac{q_j^*}{r_{ij}}\right) \quad j \neq i \tag{2.8}$$

Equation 2.8 can be reduced a system of linear equations given by:

$$\boldsymbol{V} = k_c A \boldsymbol{q}^* \tag{2.9}$$

where A is given by:

$$A = \begin{bmatrix} \frac{1}{\rho_1} & \frac{1}{|r_{12}|} & \cdots & \frac{1}{|r_{1N}|} \\ \frac{1}{|r_{12}|} & \frac{1}{\rho_2} & & \vdots \\ \vdots & & \ddots & \vdots \\ \frac{1}{|r_{1N}|} & \cdots & \cdots & \frac{1}{\rho_N} \end{bmatrix} \tag{2.10}$$

This system of equations is what is used in simulation to solve for the charges of each node.

An additional improvement to the Coulomb force model is the inclusion of induced charge effects that occur when the spherical nodes are operating in very close proximity (separations less than approximately four sphere radii, $r < 4\rho$). This is relevant for the TCS during situations such as deployment. When the spheres are driven to a fixed potential, but in close proximity, the charge distribution on the sphere is no longer evenly distributed[43] and Equation 2.2 no longer provides an accurate potential prediction.

One method to account for close sphere induced effects is by representing the spheres' charge with an infinite series of charges computed using the method of images.[41,42,43] Figure 2.2 is used as an example to highlight the principle of the electrostatic method of images. In isolation, spheres 1 and 2 have a fixed potential that is represented with a respective charge q_1 and q_2 located at sphere center; however, at close separations a redistribution of charge occurs. This is modeled with a series of charges q_n, of decreasing magnitude and decreasing separations x_n ($n = a, b, c...$).

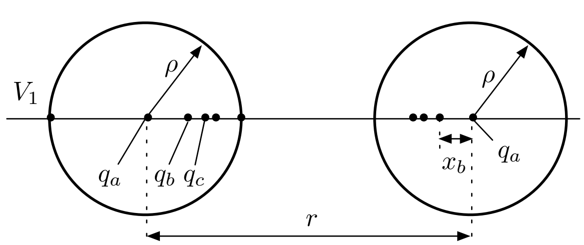

Figure 2.2: *Method of images to model induced charge effects of close spheres*

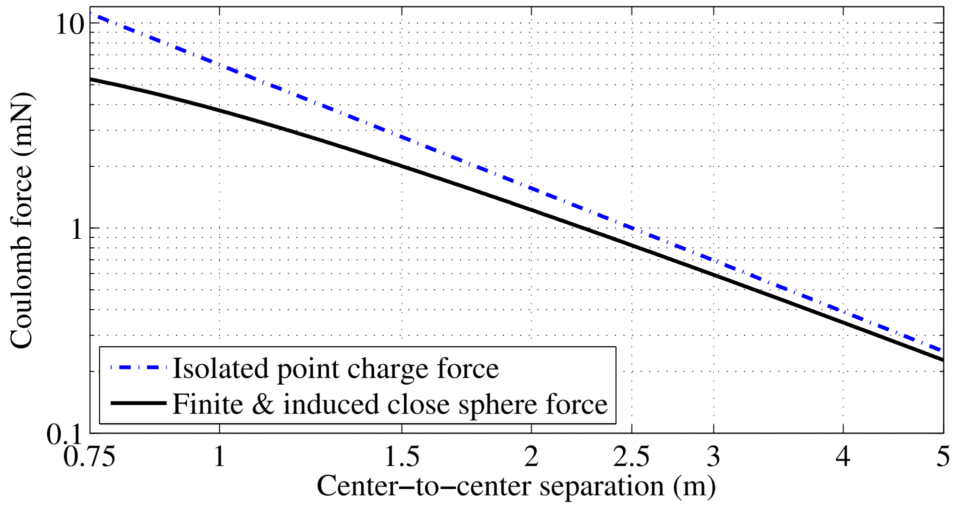

Figure 2.3: *coulomb force between spheres of radius (ρ = 0.25m) and 30 kV potentials for each model in a vacuum. Compares the force between the isolated point charge force model to the finite close sphere force model that includes induced effects.*

The values of q_n are computed for spheres of equivalent potential and polarity (repulsive force) using:

$$q_n = -\frac{r q_{n-1}}{d - x_{n-1}} \tag{2.11}$$

where $n > 1, q_a = q_1^*$ and $x_a = 0$. This results in an overall reduced net Coulomb force. The values of x_n are computed using:

$$x_n = \frac{r^2}{d - x_{n-1}} \tag{2.12}$$

Numerical computation is used to calculate the ratio of charges and locations for a finite series of charges. It is necessary to adjust the charge value to ensure the overall charge on each sphere is equal to that of the original sphere[43] (which can be the effective value for close finite spheres, computed with Equation 2.7). The net Coulomb force on the spheres is computed by summing the force between each charge image from within both spheres.

The effective repulsive force including both these effects is compared to the isolated point charge force model of Equation 2.1 in Figure 2.3. These force levels are computed for a two node TCS, with 0.25 m radii charged to |30| kV. For this force computation the induced charge affects are computed with a summation of 20 charge images. The results indicate that the effective repulsive Coulomb force is lower across all separation distances than the isolated point charge model in Eq. (2.1). However, because this study focuses on the TCS properties of deployed structures where the separation distances are at least 2 meters or more, the induced effect play a negligible role on the TCS stiffness properties. Future work considering the deployment dynamics would need to take induced effects into account.

An important consideration for the TCS study is that the magnitude of this force model reduction is low for the separation distances envisioned. Table 2.1 At a separation of 2.5 m center-to-center, (a common simulation example in this study) the effective Coulomb repulsive force is reduced 17.7% from the isolated point charge force. At a separation of 5 m the effective Coulomb force is reduced by only 9.3% from the isolated point charge force. This force magnitude decrease that is a result of having two charged finite spheres in close proximity requires the nodes to charge to slightly larger magnitudes to compensate and maintain desired repulsive forces and tether tension.

Table 2.1: *Reduction in the repulsive Coulomb force between two spheres using finite and induced close sphere model compared to the isolated point charge model. Spheres are 0.25 m radius and charged to 30 kV potential in a vacuum.*

Separation distance (m)	Force reduction (%)
1	40.15
1.5	27.94
2	21.61
2.5	17.68
3	14.99
4	11.50
5	9.35

For this example, the finite sphere effects are dominant and induced charge effects are minimal beyond separations of 1.25 m (5 radii). The range of separation distances used throughout this analysis are greater than 5 sphere radii. For this reason the inclusion of induced effects using the method of images are not included in the Coulomb force model. However, the effects of having close finite charged spheres are added to the TCS Coulomb force model with the conservative plasma shielding, resulting in the effective Coulomb force model between two spheres:

$$|\boldsymbol{F}_c| = k_c \frac{q_1^* q_2^*}{r_{12}^2} e^{-r_{12}/\lambda_D} \left(1 + \frac{r_{12}}{\lambda_D}\right) \tag{2.13}$$

where the charged q_i^* are evaluated using Equations 2.9 and 2.10 for a given TCS node potential V.

2.2 TCS Equations of Motion

The numerical simulation developed for this study solves for the six degree-of-freedom translational and rotational motion of TCS nodes. The only forces assumed acting on a TCS at GEO are Coulomb, tensile, gravity, and solar radiation pressure forces. The Coulomb force is given in the previous sections by Equation 2.13. The remaining forces are discussed next.

The tethers are modeled as a proportional spring with nonlinear end displacements. This allows for general tether stretching due to arbitrary node translation and/or rotation. The magnitude of the tensile force from a single tether is given by:

$$|\boldsymbol{F}_{\mathsf{s}}| = \begin{cases} k_{\mathsf{s}}\delta L & \delta L > 0, \\ 0 & \delta L \leq 0. \end{cases} \tag{2.14}$$

where k_s is the proportional spring constant and δL is the stretch in the tether. Thus, this simulation doesn't allow the tethers to carry any compression. Instead, the tether force is set to zero if any negative tether length displacements are computed due to the TCS nodal motion. The spring constant is given by:

$$k_s = \frac{EA_t}{L} \tag{2.15}$$

where E, A_t and L are Young's modulus, tether cross-sectional area and tether length, respectively.

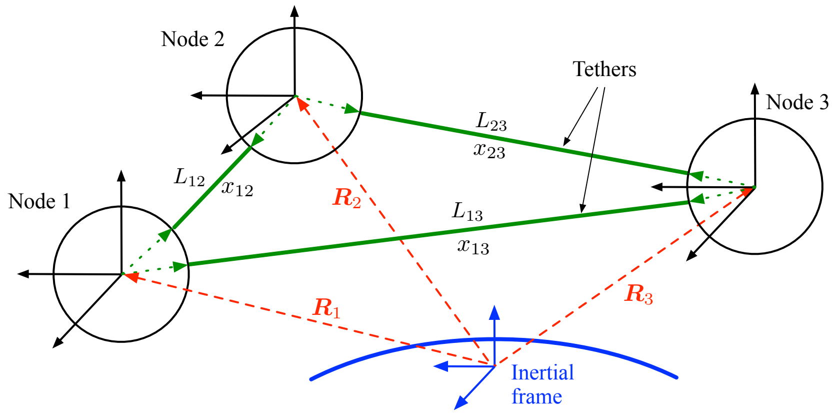

Figure 2.4: *Dynamic model setup for a three dimensional, three-node example*

If only a two-node TCS with a single tether is simulated, Equation 2.14 would give the total tether force on a node. However, the simulation is capable of simulating more than two nodes with multiple tethers between nodes. Figure 2.4 illustrates a simulation setup with 3 TCS nodes which are interconnected with single tethers. The NxN adjacency matrix, $[K]$, defines which nodes are connected and by how many tethers. The tether length increase of tether k between nodes i and j is defined by δL_{ijk}. Therefore, the resulting tensile force acting on node i from the tether(s) connected to node j is:

$$\boldsymbol{T}_{ij} = k_{\text{s}} \sum_{k=1}^{M} \delta L_{ijk} \hat{\boldsymbol{\tau}}_{ijk} \tag{2.16}$$

where M is the number of tethers between nodes i and j as defined by $[K_{ij}]$ and $\boldsymbol{\tau}_{ij}$ is the vector defining the k^{th} tether's connections between node i to j.

A two-body model for gravity is used in simulation to simulate TCS operating on orbit at GEO. The force from gravity is given as:

$$|\boldsymbol{F}_g| = \frac{\mu m_i}{|\boldsymbol{R}_i|^2} \tag{2.17}$$

where $\mu = 3.986 \times 10^{14}$ m^{3}s^{-2} is the gravitational coefficient for Earth, m_i is the spacecraft node mass and $\boldsymbol{R}_i$ is the inertial position of node i.

Solar radiation pressure is simulated using a simplified model. The SRP force magnitude is given by:

$$F_{\text{srp}} = P_{\text{srp}} C_r A_{sc} \tag{2.18}$$

where P_{srp}, C_r, and A_{sc} are the solar radiation pressure, surface reflectivity of the spacecraft and the cross-sectional area of the spacecraft, respectively.

2.2.1 Translational Equations of Motion

All four forces presented previously impact the translational motion of a TCS node. Including gravity and solar radiation pressure, then summing over all nodes, including the Coulomb force of Equation 2.13 and the tensile force of Equation 2.16, results in translational equations of motion of node i being calculated by:

$$\ddot{\boldsymbol{R}}_i = -\frac{\mu}{|\boldsymbol{R}_i|^2}\hat{R}_i + P_{\text{srp}} C_r A_{sc} \hat{S}_i + \sum_{j=1}^{N} K_{ij} \frac{\boldsymbol{T}_{ij}}{m_i} + \sum_{j=1}^{N} \frac{k_c q_i^* q_j^* (-\hat{\boldsymbol{r}}_{ij})}{m_i r_{ij}^2} e^{-r_{ij}/\lambda_D} \left(1 + \frac{r_{ij}}{\lambda_D}\right) \quad , \quad i \neq j \tag{2.19}$$

where $\hat{R}_i$ is the unit vector from the Earth to node i, $\hat{S}_i$ is the unit vector from the Sun to node i, N is the total number of nodes in the TCS model, and K_{ij} is a scalar based on the adjacency matrix which is 0 if no tethers are connected or 1 if any tethers are connected. Equation 2.19 is the full translational motion for a TCS in GEO. However, most of the simulations in this work use a simplified model for translational motion where gravity and solar radiation pressure are neglected. The simplified equation of motion is given by:

$$\ddot{\boldsymbol{R}}_i = \sum_{j=1}^{N} K_{ij}\frac{\boldsymbol{T}_{ij}}{m_i} + \sum_{j=1}^{N}\frac{k_c q_i^* q_j^*(-\hat{\boldsymbol{r}}_{ij})}{m_i r_{ij}^2} \quad , \quad i \neq j \tag{2.20}$$

Justification for this simplification is given in further sections.

2.2.2 Rotational Equations of Motion

It is assumed that the only forces that affects the rotational motion of the TCS nodes are the tether forces. Coulomb force induced torques are neglected because symmetric charge distribution is assumed, and the electrostatic forces are acting on the center of each node. Differential gravity torques are ignored because the spacecraft are spherical. Solar radiation pressure can induce torques but is not included early on. Solar radiation pressure disturbances are studied in section 2.6.

Therefore, the attitude of each spacecraft node is dependent on the torque acting on the node from each tether:

$$^{\mathcal{B}}\boldsymbol{\Gamma}_i = \sum_{j=1}^{N}\left[\sum_{k=1}^{M}\left(K_{ij}\,{}^{\mathcal{B}}\boldsymbol{p}_{ijk} \times [\mathcal{BI}]_i\,{}^{\mathcal{I}}\boldsymbol{T}_{ijk}\right)\right] \quad , \quad i \neq j \tag{2.21}$$

where $\boldsymbol{p}_{ijk}$ is the body fixed vector that defines the location of the k^{th} tether attachment point on node i that connects to node j and $[\mathcal{BI}]_i$ is the direction cosine matrix of the attitude of node i relative to the inertial frame. The angular acceleration of each node is defined in the body frame with Euler's rotational equations of motion:[44]

$$[I]\dot{\boldsymbol{\omega}}_i = -\boldsymbol{\omega}_i \times ([I]\boldsymbol{\omega}_i) + \boldsymbol{\Gamma}_i \tag{2.22}$$

The attitude of each node is represented with the Modified Rodrigues Parameters (MRP) which are integrated using the differential kinematic equation:

$$\dot{\boldsymbol{\sigma}}_i = \frac{1}{4}\left[(1-\sigma_i^2)[I_{3x3}] + 2[\tilde{\boldsymbol{\sigma}}]_i + 2\boldsymbol{\sigma}_i\boldsymbol{\sigma}_i^T\right]\boldsymbol{\omega}_i \tag{2.23}$$

The MRP set will go singular with a rotation of $\pm 360°$. To ensure a non-singular description, the MRP description is switched to the shadow set whenever $|\boldsymbol{\sigma}| > 1$.[44]

2.3 Translational Stiffness Study

Using the TCS equations of motion, a simplified two-node TCS configuration (benchmark two-node TCS problem shown in Figure 1.10) was simulated to study the effects of various system parameters on the translational stiffness of the TCS. The system parameters under review are the node separation distance, node mass, tether spring constant and node voltage. Table 2.2 shows the nominal parameters used in the numerical simulation sweeps. The spring stiffness reflects a value that is similar to that of Amberstrand fiber, a commercially available conducting wire. These parameters are the values used when varying the other parameters. Figure 2.5 shows the translational frequency and peak to peak oscillation amplitude for the various simulations conducted. For these simulations the nodes are started with the tensile and Coulomb forces in equilibrium and then each node is given and equal and opposite initial translational velocity of 0.1 mm/s.

Table 2.2: *Translational Simulation Parameters*

Separation Distance	5 m
Node Mass	50 kg
Spring Constant	35.8398 N/m
Node Voltage	30 kV

Figure 2.5 illustrates the common trends of a two-node configuration as the TCS parameters are varied. For example, Figures 2.5(a), 2.5(b), 2.5(c), and 2.5(d) show the frequency and amplitude response if the voltage and separation distance is varied and all other parameters are held fixed. Naturally the translational frequency and the amplitudes vary as the TCS equilibrium depends on the voltage and separation distance used. The figure shows that larger voltages and shorter separation distances increase the translational stiffness.

Figures 2.5(e) and 2.5(f) show how the translational stiffness increases if the nodal masses are kept small. Thus, for the TCS concept, it is beneficial to keep the support nodes as light as possible to increase the overall TCS stiffness. Additionally, Figures 2.5(g), 2.5(h) show that a stiffer tether provides more translational stiffness.

The tether displacements for varying voltages in Figure 2.5(b) remain low, unless the potentials are very low, making is easier for the tethers to go slack. The low-voltage deflections in Figure 2.5(b) illustrate the large compressions that occur with the weak electrostatic restoring forces. Also, note that the tether displacements generally remain small on the order of sub-millimeters for the other parameter variation sweeps. For all cases the translation oscillation periods are on the range of 10-20 seconds.

2.4 Rotational Stiffness Study

A TCS system stiffness of more interest than the translational is that of rotational stiffness. Rotation of individual nodes is of specific interest for TCS systetms because this will have a direct impact on the deployment and orbital maneuvers of TCS systems. The aim of this section is to determine the allowable rate and direction of node rotation that that will return the node to its original attitude and that does not result in the tether becoming entangled with the node. A TCS configuration must be robust towards initial conditions and perturbations. Therefore the rotational stiffness of a two-node configuration in deep space is examined. Figure 2.6 details an asymmetric rotation scenario that is considered. This scenario is chosen because there is no net angular momentum, thus isolating the effects of TCS system parameters. Please note that this 2-node, single-tether configuration provides the worst possible rotational stiffness of a TCS system. As such, it is a good system to study to examine lower performance bounds. This section examines the two-node TCS for various TCS parameters and initial rotation rates. Additionally, the rotational stiffness of a two-node TCS configuration with multiple tethers is analyzed. Lastly, the impact of nodal properties such as inertia, radius and multiple tether attachment angles is examined.

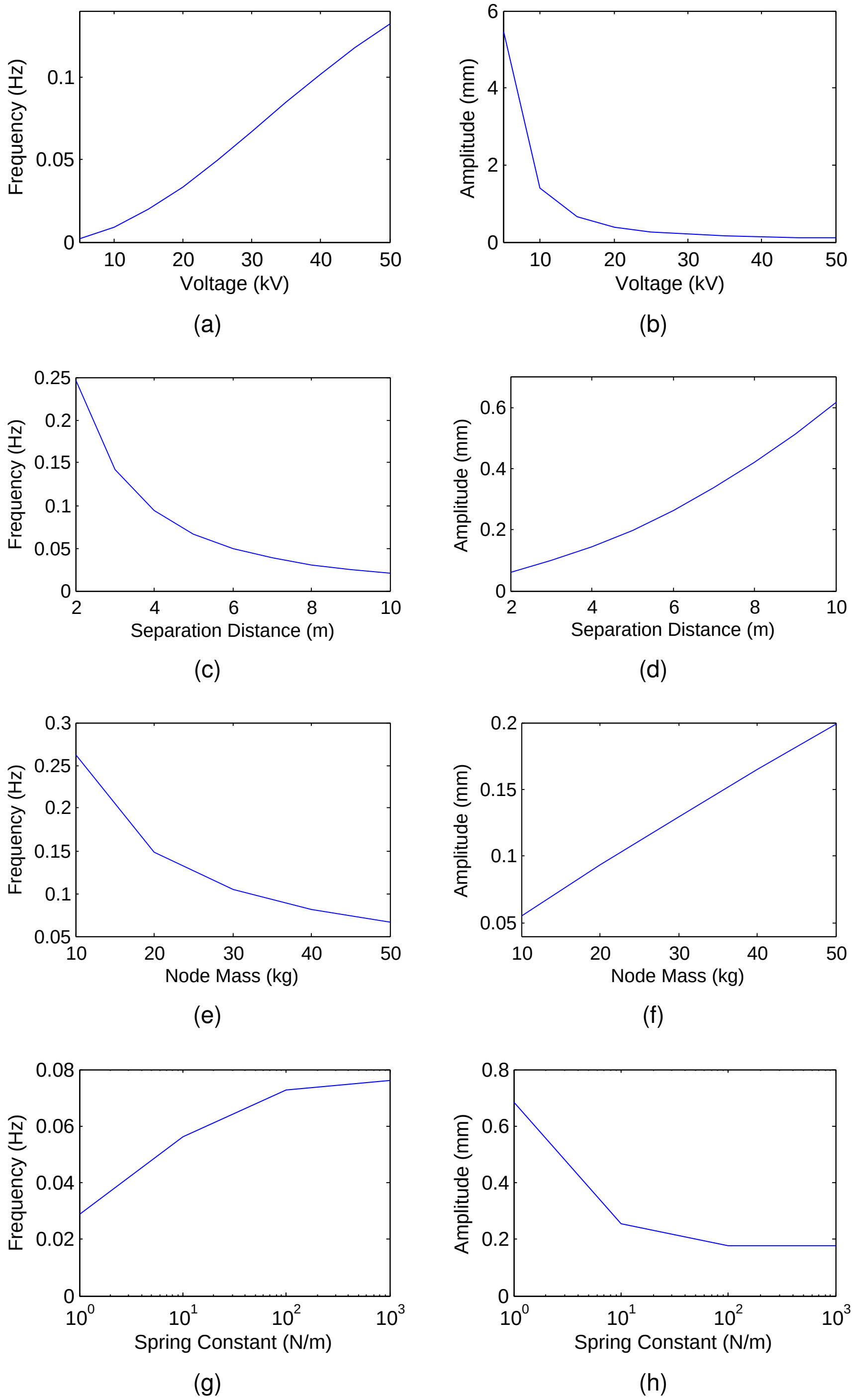

Figure 2.5: *TCS nodes translational motion behaviors*

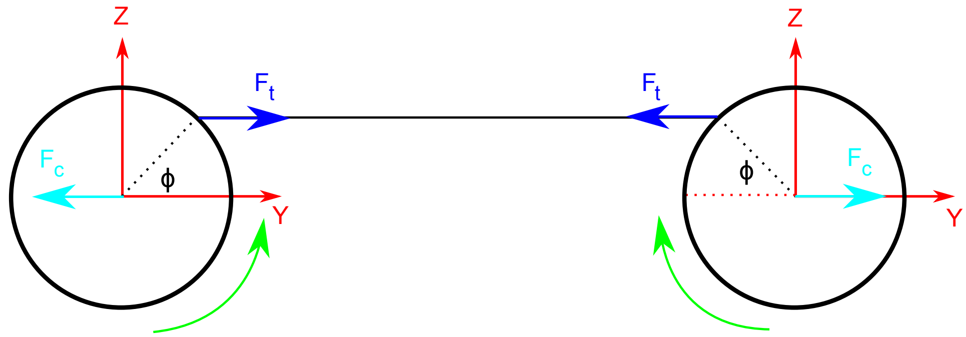

Figure 2.6: *Asymmetric rotational motion*

Table 2.3: *Rotational Stiffness Simulation Parameters*

Separation Distance	5 m
Node Mass	50 kg
Spring Constant	35.8398 N/m
Node Charge	30 kV
Node Radius	0.5 m
Inertia Distribution	Solid Sphere
Initial Spin	10 deg/min

2.4.1 System Parameter Effects

Similar to the translational stiffness analysis, a two-node TCS is examined for various voltages, masses, separation distances and spring constants. The rotational case shown in Figure 2.6 is simulated with the parameters shown in Table 2.3, and the resulting rotational frequencies and maximum angular deflections are shown in Figure 2.7. For these simulations the nodes are started at a TCS equilibrium with an initial angular spin rate of 10 deg/min.

Figures 2.7(c) and 2.7(e) show that the rotational stiffness of a TCS configuration can be increased by decreasing either the node mass and/or decreasing the node separation distance. Additionally, Figures 2.7(d) and 2.7(f) show that decreasing the separation distance and/or node mass also decreases the maximum deflection of the nodes. From Figures 2.7(g) and 2.7(h) it can be seen that the spring constant has little effect on the rotational stiffness of a TCS configurations. Finally, Figures 2.7(a) and 2.7(b) show that increasing the node voltage effectively increases the TSC system rotational stiffness. Note that the rotational oscillations now have a period on the order of hundreds of seconds, where in contrast the translational motion was faster on the order of tens of seconds. The TCS dynamics studies indicate that the translational and rotational mode experience little cross-coupling due to this frequency separation.

Even though these cases are a lower bound on TCS performance, Figure 2.8 shows that the spacecraft are still capable of withstanding moderate initial rotation rates of 10's of degrees per minute without the tether wrapping up around the spacecraft. For this single tether spherical two-node TCS, tether wrap up would occur when a node is rotated 90 degrees from the vector connecting the two nodes. Figure 2.8(a), 2.8(b) and 2.8(c) show the maximum angular deflection of nodes over various ranges for 2.5m, 5m, and 10m separation distances. The results from Figure 2.8 also agree with the results from Figure 2.7, which show that larger voltages and shorter separation distances increase the rotational stiffness of the TCS configuration.

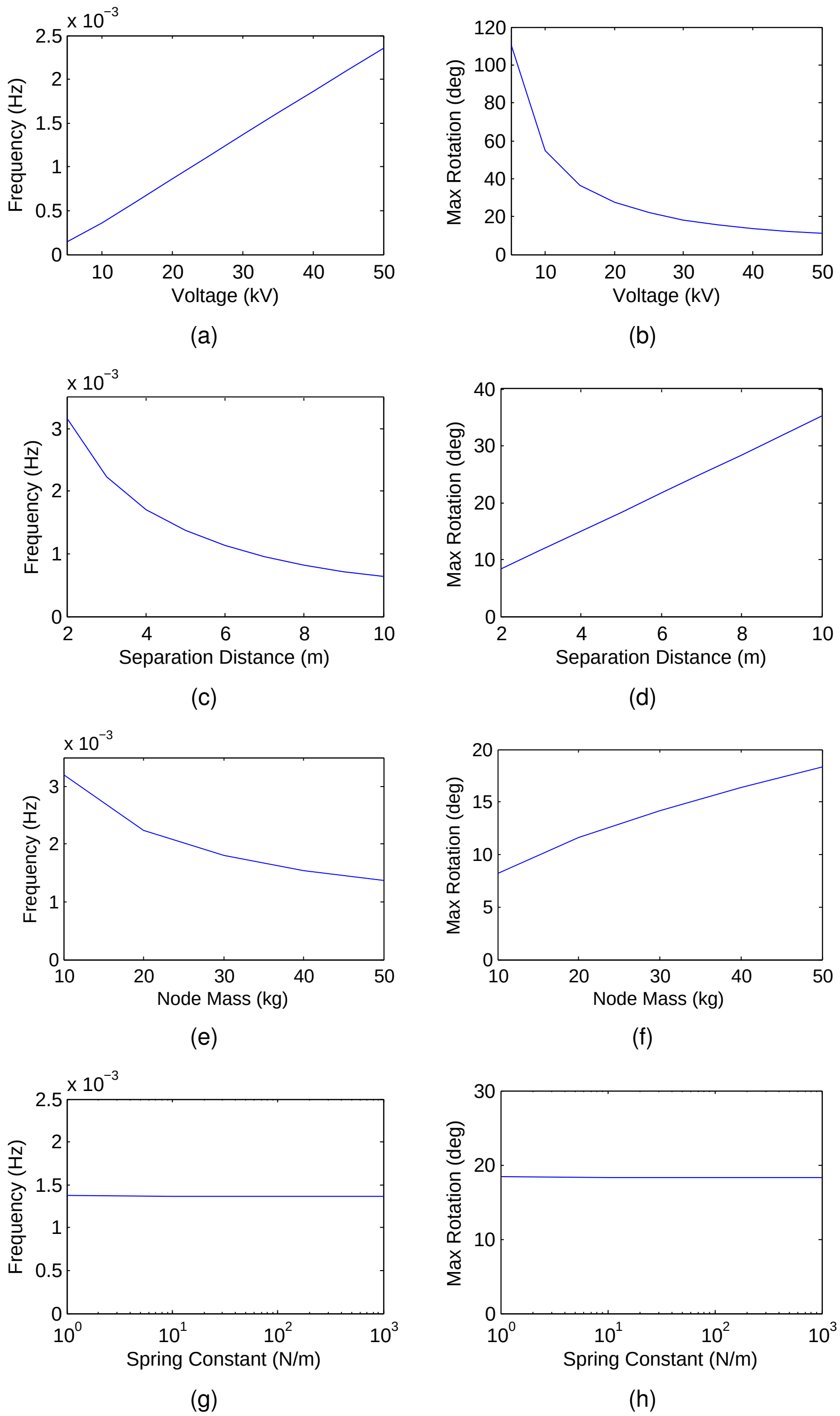

Figure 2.7: *Rotational motion dependencies*

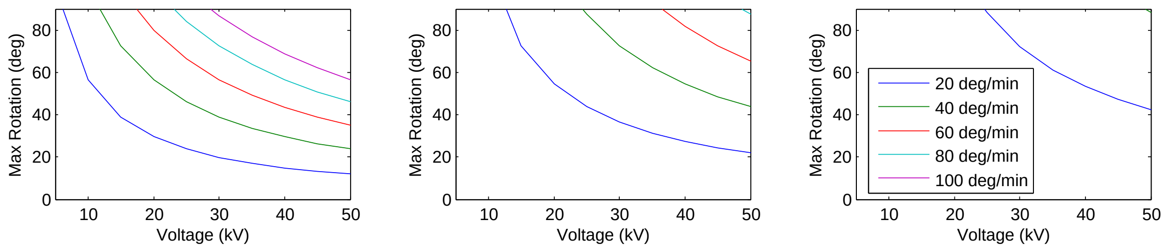

(a) 2.5 m (b) 5 m (c) 10 m

Figure 2.8: *Stiffness towards initial spin rates*

Table 2.4: *Spherical Node Rotation Causing Tether Entanglement (for Single-Axis, Asymmetric Rotations)*

Rotation Axis	Single-Tether (deg)	Double-Tether (deg)	Triple-Tether (deg)
X-axis (Node 1 Positive)	90	90 - ϕ	90 - θ
X-axis (Node 1 Negative)	90	90 - ϕ	90 - ϕ
Y-axis	N/A	90	90
Z-axis	90	90	90 - ψ

2.4.2 Multiple Tethers

A key thing to note about rotation of single-tether two-node TCS is that it does not provide full three-dimensional stiffness. From Figure 2.6 it can be seen that initial rotations about the Y-axis would have no restoring torque. One way to provide the desired three-dimensional stiffness is to connect the nodes with two or three tethers. The connections for these scenarios are shown in Figure 2.9.

However, the additional tethers do affect the rotation angle at which a node will become entangled with a tether. The variation in entanglement angles can be seen for the double- and triple-tether TCS configurations in Figure 2.9. Table 2.4 lists the nodal rotation angles at which each TCS configuration will reach the entangled state. The entanglement rotations in Table 2.4 are based upon geometry, where $\theta = \tan^{-1}(2\cot\phi)$ and $\psi = \tan^{-1}\left(2\cot\phi/\sqrt{3}\right)$. However, one should note that nodes are not likely to be spherical and the tether attachment points could be attached away from the nodes on booms, thus increasing the possible absolute rotations.

2.4.2.1 Nodal Motion

A single-tether connection yields the simplest and most intuitive dynamics for a two-node TCS configuration under the disturbance of an initial angular velocity. Figure 2.10(a) shows the resulting dynamics of the single-tether system under an initial asymmetric nodal rotation about the X-axis using the simulation conditions in Table 2.3. It is important to note that for all results the translational motion is only due to the rotational coupling, as the node is initially at translational equilibrium. Figure 2.10(a) shows the smooth and sinusoidal nodal separation, the asymmetric nodal rotations and the tether tension of a single-tether TCS. Under this small initial rotation disturbance (10 deg/min) the nodes rotate a maximum of approximately 20 degrees about the X-axis and the tether remains under tension at all times. Larger initial disturbances can make the single-tether configuration go slack and cause the motion to no longer be sinusoidal. In contrast

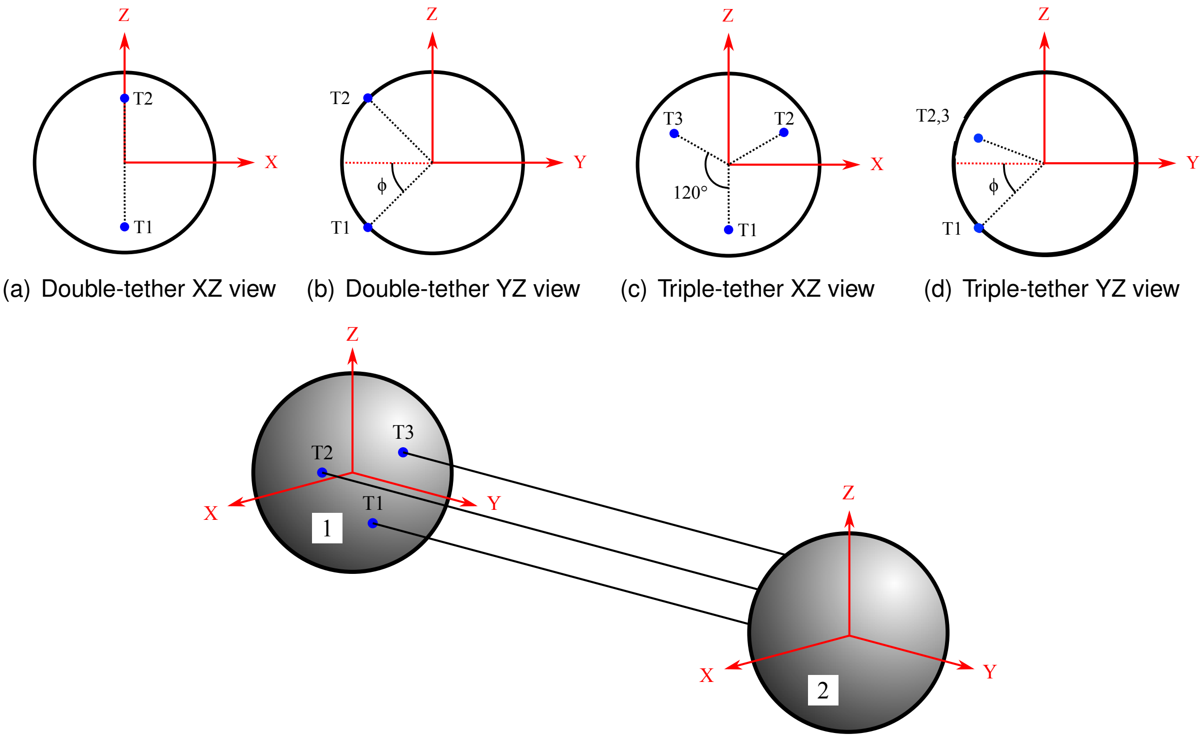

(a) Double-tether XZ view (b) Double-tether YZ view (c) Triple-tether XZ view (d) Triple-tether YZ view

(e) Triple-tether 3D configuration

Figure 2.9: *Two-node TCS tether configurations and connections*

to the single-tether configuration, Figure 2.10(b) shows the translational and rotational motion for the double-tether configuration with initial rotations about the X-axis. The nodal motion is now piecewise linear. The nodes rotate, only about the X-axis, at a constant rate until the tethers become taught and reverse the direction of rotation. The piecewise linearity of a multiple-tether TCS configuration is due to the tethers no longer remaining continuously taught. This is shown by the plot of tether tension for each tether (T1 and T2). Maintaining a taught tether is not a required dynamic property, although there is concern of a tether reaching a buckled or tangled state. In these simulations each tether only reaches a slightly loose state on the order of millimeters over its entire 4 meter length.

The triple-tether configuration for this X-axis rotation results in similar dynamics to that shown for the double-tether in Figure 2.10(b). Although the triple-tether demonstrates similar separations and X rotations to the double-tether it adds another unique complexity to the two-node TCS configuration. The 3D spread of the triple-tether attachment points adds coupled off-axis rotational motions that is most apparent with rotations about the Z-axis. Figure 2.11 shows the three axes rotational motion of a triple-tether node with an initial rotation about the Z-axis. From the figure it can be seen that there is no longer pure rotation about the Z-axis. Figures 2.9(c) and 2.9(d) highlight the cause, showing that the connections for tethers 2 and 3 are no longer on a nodal axis and rotation leads to tether force moments and off-axis rotations. Figure 2.11(b) shows the resulting tensions for each tether, reiterating the coupling effect.

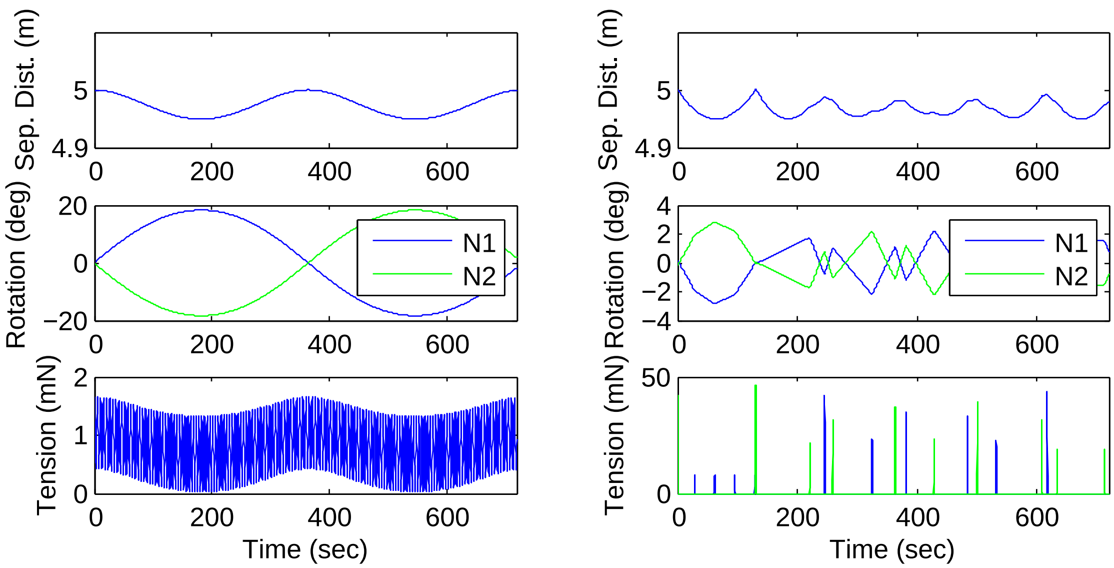

(a) Single-tether configuration (b) Double-tether configuration

Figure 2.10: *TCS nodal dynamic response to asymmetric nodal rotation about the X-axis*

2.4.2.2 Multiple Tether Advantages

As shown in the prior sections, additional tethers in a two-node configuration adds complexity to the nodal dynamics. However, there are rotational stiffness advantages that multiple tethers provide. With the inability of a tether to hold torsional loads there is no stiffness in the Y-axis (for a single-tether) and only restoring torques for rotations about the X and Z axes are feasible. Using a TCS configuration with two or three tethers allows for there to be a restoring torque for rotations about any axis.

Additional tethers not only provide added system robustness to initial rotations, but they also reduce the maximum deflection a node can incur. The maximum angular deflection of the node is a measure of the TCS configuration rotational stiffness to an angular rate disturbance. Figure 2.12 demonstrates this by showing the maximum principal rotation angle reached as a function of initial

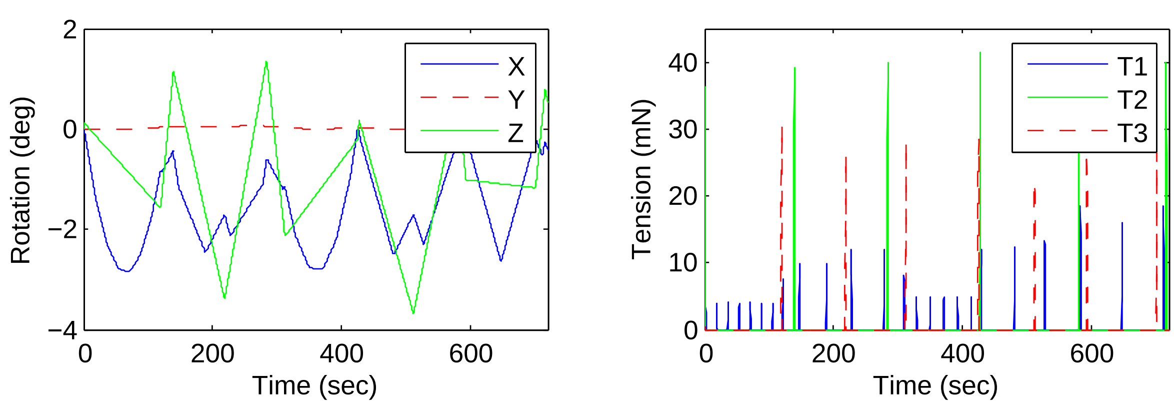

(a) Three axes rotations (b) Tether tensions

Figure 2.11: *Triple-tether nodal dynamic response to asymmetric nodal rotation about the Z-axis*

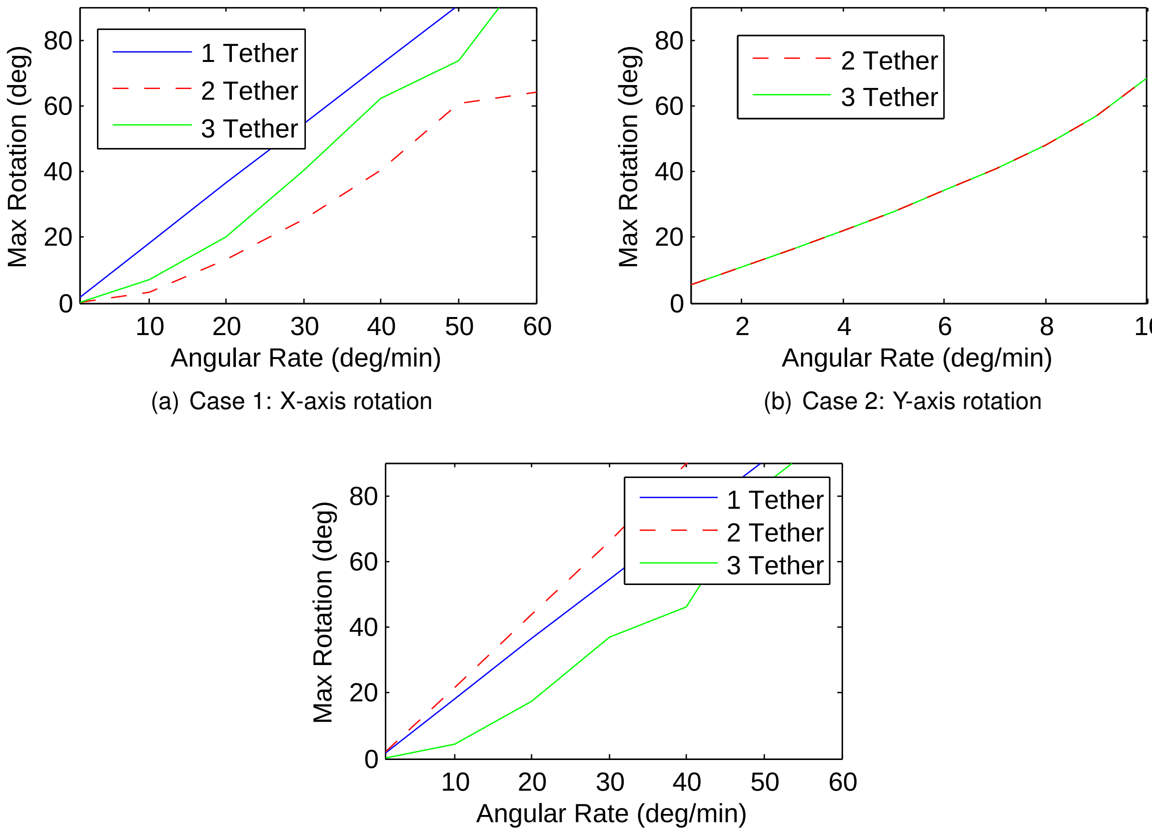

(a) Case 1: X-axis rotation

(b) Case 2: Y-axis rotation

(c) Case 3: Z-axis rotation

Figure 2.12: *Maximum absolute principal rotation as a function of initial initial angular rate*

angular rate. The maximum rotation is shown for each of the tether number configurations and shown for three cases, each with an initial rotation about a different axis. Note the difference in the angular rate axis of each of these figures. Angular rates about the Y-axis result in large rotations much faster than the other two axis rotations. It is shown in Table 2.4 that the multiple tether nodes have a reduced absolute rotation before entanglement occurs. For this reason Figure 2.13 shows the maximum rotation of the nodes relative to their corresponding entanglement rotation angle. Additionally, Figure 2.14 reiterates the effect of multiple tethers on node rotation by showing the absolute maximum rotations as a function of node potential. The rotation about each axis is now analyzed for the three rotation cases using the results of Figures 2.12-2.14.

Case 1: Figure 2.12(a) shows that for asymmetric rotation about the X-axis, the addition of tethers reduces the maximum absolute angle reached from the single-tether case. The double-tether does, however, perform better than the triple-tether configuration. This is due to the moment arms provided by the tethers. From Figures 2.9(b) and 2.9(d) it can be seen that the attachment points in the positive Z direction for the two tether configuration are further away from the X-axis than the three tether configuration. This difference provides a larger moment arm for the restoring torques and is one reason the multiple tether configurations are stiffer at higher rates for this rotation. Additionally, the double-tether has larger moment arms than the triple-tether and that is why the double tether performs the best for X-axis rotation.

While the addition of tethers certainly reduces the absolute rotational deflection of the node, the increased tether attachment locations places the node closer to the entanglement rotation. This

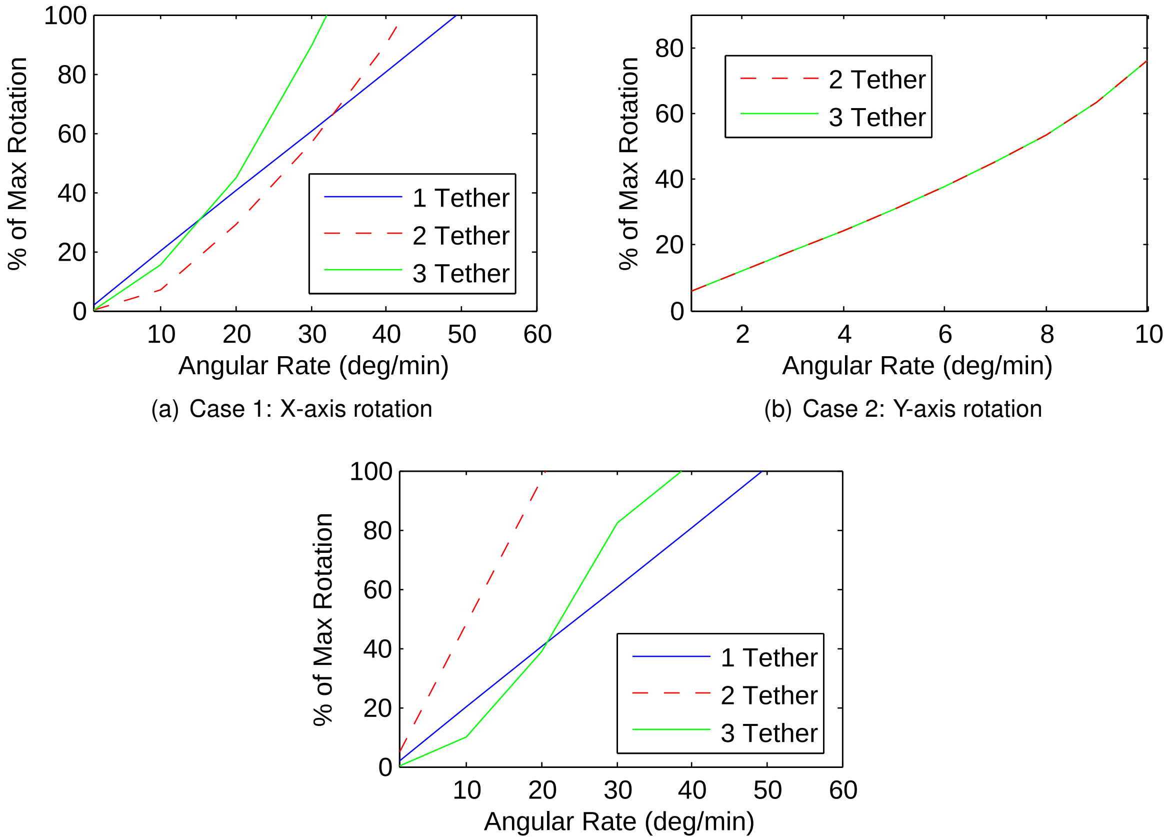

(a) Case 1: X-axis rotation

(b) Case 2: Y-axis rotation

(c) Case 3: Z-axis rotation

Figure 2.13: *Maximum principal rotation relative to maximum entanglement rotation (Table 2.4)*

is demonstrated in Figure 2.13(a) which shows the maximum angular deflection as a percentage of the entanglement rotation, which is a function of each tether configuration and rotation axis (as defined in Table 2.4). The result is that each tether configuration has a similar proximity to entanglement. The double-tether keeps the node further from entanglement than the single-tether, while the triple-tether results in entanglement with disturbances above 30 deg/min.

The effect of multiple tethers on X-axis rotation as a function of node potential is seen in Figure 2.14(a). The double- and triple-tether both provide more rotational stiffness across all node potentials than a single-tether TCS configuration. The double-tether does provide a slightly more stiff system than the triple-tether configuration.

Case 2: Rotational stiffness about the Y-axis for a two and three tether configuration is shown in Figure 2.12(b). The single-tether configuration is omitted because it has no rotational stiffness for Y-axis rotations. From the Figure it can be seen that the double- and triple-tether configurations provide equal rotational stiffness about the Y-axis, because the moment arms about the Y-axis are equal. Figures 2.9(a) and 2.9(c) show how the moment arms are all the same radial distance from the Y-axis.

Figure 2.13(b) shows how close the Y-axis angular deflection comes to reaching the entanglement angle. The Y-axis has a reduced disturbance angular rate as the nodes have less rotational stiffness, however the inclusion of additional tethers provides prevention of entanglement for the disturbance range analyzed. In this case the single-tether entanglement rotation is undefined as the tether is bound about itself.

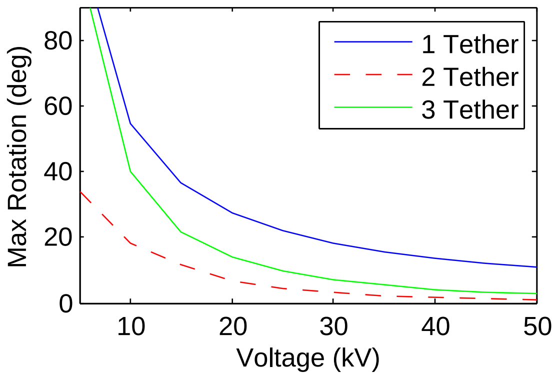

(a) Case 1: X-axis rotation

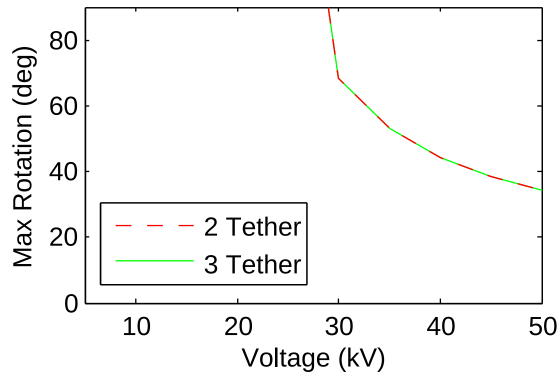

(b) Case 2: Y-axis rotation

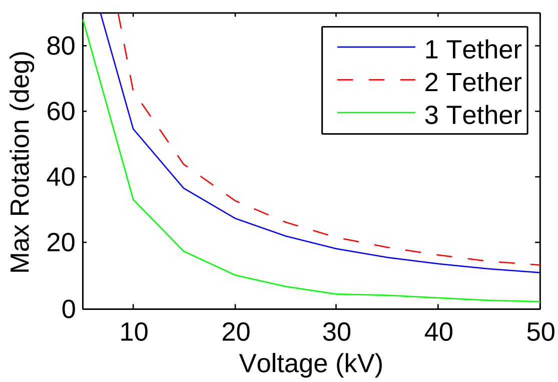

(c) Case 3: Z-axis rotation

Figure 2.14: *Maximum absolute principal rotation as a function of nodal potential*

Figure 2.14(b) provides additional evidence of the effects of multiple tethers on Y-axis rotation. Again the double- and triple-tether configurations perform identically. However, at lower potentials the nodes reach undesirable rotation angles. The lower rotation rates and the large node rotation agrees with Figure 2.12(b) and shows that for a two-node TCS configuration the Y-axis has the least rotational stiffness.

Case 3: For a single-tether the Z-axis rotation is identical to X-axis rotation. However, Figure 2.12(c) shows that a double-tether configuration provides less stiffness than a single-tether for rotations about the Z-axis. Again the moment arm is the cause for this reduced stiffness. The moment arm about the Z-axis in Figure 2.9(b) is less than what the moment arm of a single-tether provides. The moment arm for this configuration is only in the Y direction and is reduced proportionally to the attachment angle ϕ. A triple-tether configuration also has a moment arm that is dependent on ϕ but the maximum rotation is less than that of a single-tether. The additional stiffness in a three tether configuration is because tethers 2 and 3 in Figure 2.9(d) provide a larger moment arm about the Z-axis. The larger moment arm arises because tethers 2 and 3 are not located in the ZY plane, which adds additional length to the moment arm.

The relative angular deflection about the Z-axis is shown in Figure 2.13(c). These results indicate that the double-tether system will reach entanglement at disturbances above 20 deg/min. The triple-tether however performs significantly better than than the double- and single-tether configurations at keeping the node away from entanglement.

The rotational stiffness for rotations about the Z-axis and dependence on node potential is shown in Figure 2.14(c). The figure shows that a triple-tether configuration provides more rotational stiffness than a single-tether. Also, a double-tether configuration again provides lower stiffness than a single-tether for rotations about the Z-axis.

Case Summary: The results of Figure 2.12 indicate that there is up to a 75% decrease in the absolute maximum angular rotation about the X-axis by using a triple-tether over a single-tether. Similarly, there is up to a 60% decrease in the Z-axis rotation with a triple-tether over the single. As the single-tether offers no Y-axis rotational stiffness the addition of tethers does provide rotational stiffness. These values are approximate and are calculated for an initial rotation rate of 20 deg/min and a node voltage of 30 kV. The actual quantitative increase in stiffness is a function of the initial rotation rate and node potential.

The multiple tether configurations have a geometry that places the tether attachment point closer to the entanglement rotation prior to any rotational motion. The results of Figure 2.13 indicate that the multiple tethers offer minimal advantage in reducing the chances of entanglement, and sometimes perform worse than a single-tether. The advantage of using multiple tethers is that it reduces the absolute nodal rotation for an equivalent initial disturbance as well as introducing 3D rotational stiffness.

In addition, from these results it would appear that a equally spaced quad tether would offer all axis rotational stiffness as well as symmetric moment arms. This combination may provide an advantageous rotational stiffness capability over the tether configurations used in this study. However, a quad tether configuration is no longer statically determinate and any slight discrepancy in tether length results in asymmetric motions. This concept is to be investigated in future studies.

2.4.3 Spacecraft Nodal Properties

To further expand the TCS capabilities it is advantageous to explore other system parameters that affect the rotational stiffness of the system. Spacecraft nodal parameters such as radius, mass distribution and tether attachment angle are critical components in determining the rotational stiffness of a TCS configuration. Figure 2.15 shows the effect of varying these nodal parameters on the maximum absolute rotation of a two-node configuration, disturbed about the X-axis.

Figures 2.15(a) and 2.15(b) show the results for a single-tether TCS as a function of mass distribution and nodal radii respectively. Similar trends can be shown for multiple tether configurations. The results of multiple tethers are shifted in maximum angle in the same ratio as the comparison shown in Figure 2.12(a). Figure 2.15(c) shows the results of a double-and triple-tether TCS configuration as a function of the tether attachment angle ϕ. All other simulation parameters are listed in Table 2.3.

With a node of a certain mass and radius, the shell model provides the largest possible nodal inertia. This scenario then shows the lower bound on the rotational stiffness that can be achieved. The solid sphere (homogeneous mass distribution throughout the sphere) will have a lower inertia, and thus increased rotational stiffness. However, even the solid sphere model is very conservative. Ideally the TCS nodes would have most of their mass near the node center, and thus obtain an even lower moment of inertia. As Figure 2.15(a) indicates, compared to the shell model, a 2-3 fold increase in the rotational stiffness can be achieved by designing the TCS nodes to have their most massive components near the nodal center, and thus a lower inertia. Additionally, for a constant mass distribution, solid sphere, Figure 2.15(b) shows that larger node radii increase the rotational stiffness. Even though the inertia is increasing for larger radii, the larger moment arms for the tethers dominates and thus increases the stiffness. Therefore, Figures 2.15(b) and 2.15(c) indicate that the ideal TCS would have its attachment points the furthest away from the center of the craft. Additionally, Figure 2.15(c) shows that as the tether attachment angle increases (moment

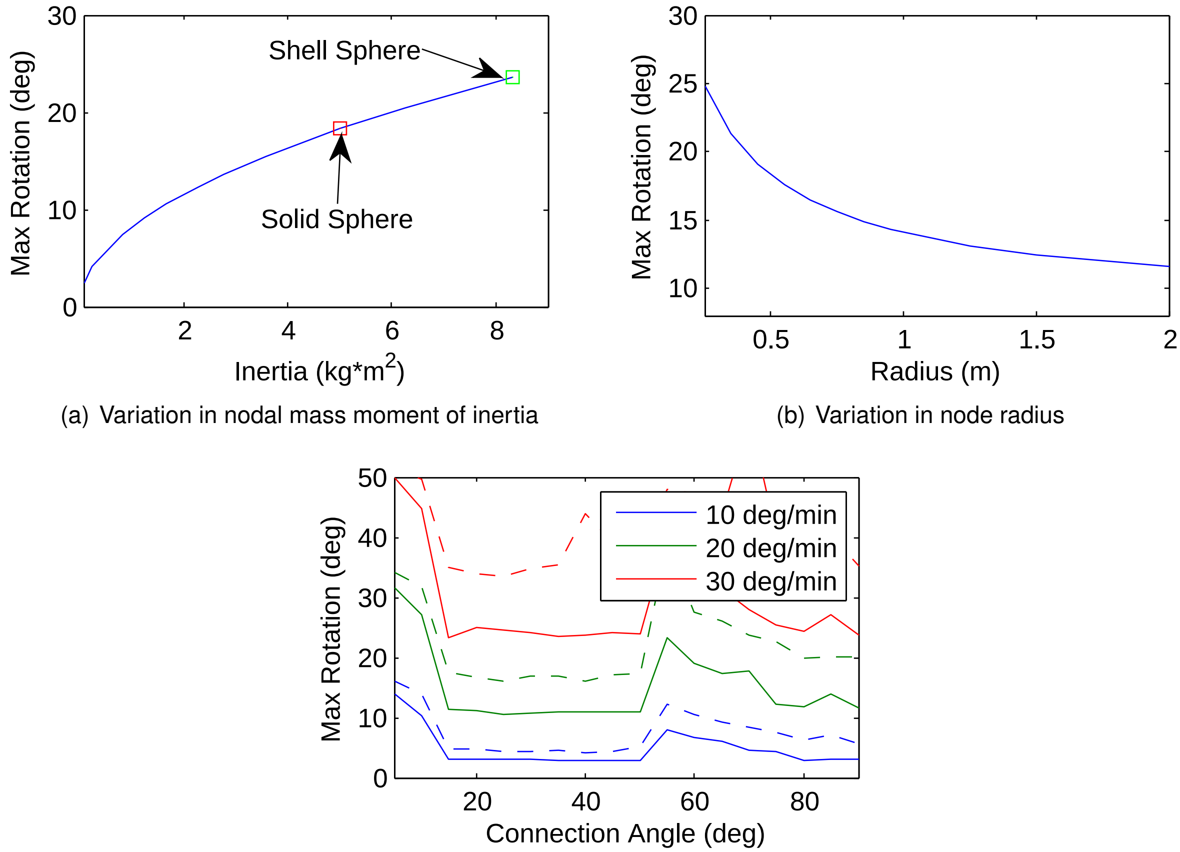

(c) Variation in tether attachment angle (Solid: double-tether, Dashed: triple-tether)

Figure 2.15: *Maximum principal rotation as a function of nodal parameters*

arm increases) the maximum absolute rotation decreases. Based on the results of this figure an ideal tether attachment angle is approximately between 20-45 degrees.

Taking into consideration the previous results of nodel parameters an ideal TCS spacecraft node design may appear similar to the conceptual illustration of Figure 2.16. This design maximizes the spacecraft rotational stiffness, increases nodal wrap-up angles and provides a spherical conductive surface for even Coulomb force generation. The mass moment of inertia is minimized by placing the spacecraft components within a low-mass exterior conducting shell. The tethers are connected to attachment arms that extend beyond the shell increasing the tether moment arms and consequently rotational stiffness. This attachment arm design also increases the maximum angle before nodal wrap up.

2.5 Shape Configuration Study

For the shape configuration study, four TCS configurations are analyzed. The primary goal of the shape configuration study is to determine what charge levels would be necessary to overcome differential gravity effects experienced by a TCS in orbit. As such, only differential gravity forces in circular orbits and electrostatics are assumed to be acting on the structures. Each configuration is analyzed as a static structure, and analytic expressions are determined for all tether forces. These

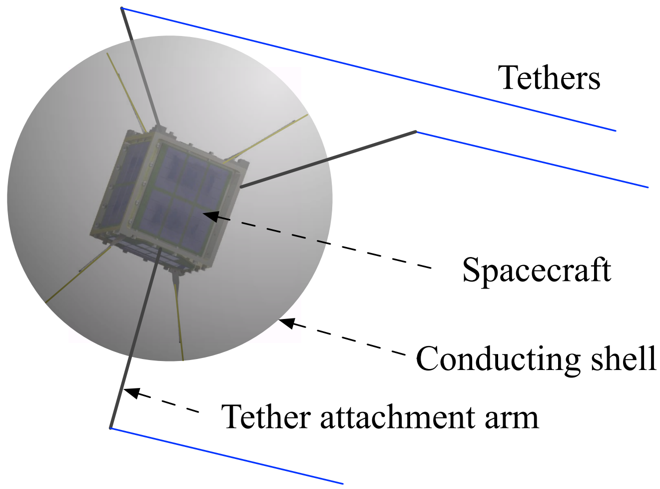

Figure 2.16: *Illustration of conceptual TCS spacecraft node design*

expressions are all determined assuming that each of the nodes in the TCS are of equal mass, m. Simplifying assumptions are made in order to yield conditions that would guarantee tension in all the tethers (neglecting dynamic effects). This section seeks to determine how the TCS shape impacts the minimum necessary charge level required to maintain tension, and it electrostatic inflation can be used to ensure tension for all types of shapes.

2.5.1 Method of Analysis

For the structural analysis, we assume that the tethers do not deflect under the forces considered. As such, dynamic effects of node motion are not considered. Instead, a static analysis is performed using the method of joints. Applying Newton's second law at each of the nodes yields

$$m_i \ddot{\mathbf{r}}_i = \mathbf{F}_i, \tag{2.24}$$

where m_i is the mass of the node, $\ddot{\mathbf{r}}_i$ is the inertial acceleration of the node, and $\mathbf{F}_i$ is the total force acting on the node which consists of tether, Coulomb, and differential gravity forces. Since a static assumption is made, no node motion is present. Thus, Eq. 2.24 is reduced to

$$\mathbf{F}_i = \mathbf{0}. \tag{2.25}$$

Contained in Eq. 2.25 are three equations for each node (one for each direction). If we define the reference coordinate frame as the orbital frame, we can expand Eq. 2.25 to obtain

$$\hat{\mathbf{o}}_\mathbf{r} : \quad T_r + C_r + F_{g,r} = 0 \tag{2.26}$$
$$\hat{\mathbf{o}}_\mathbf{t} : \quad T_t + C_t + F_{g,t} = 0 \tag{2.27}$$
$$\hat{\mathbf{o}}_\mathbf{n} : \quad T_n + C_n + F_{g,n} = 0, \tag{2.28}$$

where the subscript r represents the along track direction, t the along-track direction, and n the orbit normal direction. The forces T_r, T_t, and T_n represent the tether forces projected in each of the three directions. Similarly, C_j is used to represent Coulomb forces, and $F_{g,j}$ is the differential gravitational forces. To determine the components of the forces in each of the three directions, the dot product identity can be used. For example, the projection of the tether force between craft 1 and 2 on the $\hat{\mathbf{o}}_\mathbf{r}$ axis can be obtained for node 1 by

$$T_{r,12} = T_{12} \hat{\mathbf{e}}_{\mathbf{12}} \cdot \hat{\mathbf{o}}_\mathbf{r}, \tag{2.29}$$

where $\hat{\mathbf{e}}_{\mathbf{12}}$ is the unit vector pointing from craft 1 to craft 2. To obtain the forces for all tethers in the TCS, Eqs. 2.26 - 2.28 are applied to multiple nodes until all tethers have been solved for.

2.5.2 Differential Gravity Model

For the differential gravity model, the linearized gravitational force model from Reference 1 is used. To compute the differential gravitational forces acting on each node, the center of mass of the TCS is used as the reference position. The linearized gravity effects are only present in the orbit radial and orbit normal directions. In the radial direction, the linearized force is

$$\delta F_r \approx m\frac{3\mu}{r_c^3}L, \tag{2.30}$$

where m is the node mass, μ is the gravitational constant, r_c is the orbit radius of the TCS center of mass, and L is the distance of the node above or below the center of mass in the radial direction. For any node above the center of mass, L will be positive. This means the force will be directed away from the earth. If the node is below the center of mass, L will be negative and the force will be directed towards the earth.

The differential gravity force for the orbit normal direction is expressed as

$$\delta F_n \approx -m\frac{\mu}{r_c^3}L, \tag{2.31}$$

where for this case L represents the magnitude of the distance of the node from the center of mass in the orbit normal direction. The orbit normal differential gravity effects will always tend to compress the craft inwards towards the center of mass.

2.5.3 Three-craft TCS Analysis

Two configurations are analyzed which both consist of three craft in an isosceles triangle arrangement, as shown in Figure 2.17. The difference between the two configurations is how they are arranged with respect to the TCS orbit frame $\mathcal{O}$ direction. The first of the two configurations is aligned such that craft 2 and 3 are aligned in the orbit along-track direction, $\hat{\mathbf{o}}_{\mathbf{t}}$. Craft 1is centered above craft 2 and 3 in the orbit radial direction. It is this arrangement which is pictured in Figure 2.17. The only dimensions needed to describe the geometry of this configuration are the lengths L and b.

To determine the tether tensions, a static analysis is applied to the three craft structure. For the configuration depicted in Figure 2.17, the tensions in each of the three tethers are

$$\begin{aligned} T_{12} &= k_c\frac{q_1q_2}{L_{12}^2}e^{-\frac{L_{12}}{\lambda}}(1+\frac{L_{12}}{\lambda})+m\mu\frac{L_{12}}{r_c^3} && \text{(2.32a)}\\ T_{13} &= k_c\frac{q_1q_3}{L_{13}^2}e^{-\frac{L_{13}}{\lambda}}(1+\frac{L_{13}}{\lambda})+m\mu\frac{L_{13}}{r_c^3} && \text{(2.32b)}\\ T_{23} &= k_c\frac{q_2q_3}{b^2}e^{-\frac{b}{\lambda}}(1+\frac{b}{\lambda})-m\mu\frac{b}{2r_c^3}, && \text{(2.32c)}\end{aligned}$$

where μ is the earth gravitational parameter, k_c is the Coulomb constant, and r_c is the distance from the center of the earth to the TCS center of mass. It is evident that if $q_2 = q_3$ the tensions in tethers T_{12} and T_{13} will be equal, due to the symmetry of the shape. Furthermore, electrostatic inflation is not needed to ensure tension in T_{12} or T_{13}, as these two tethers will naturally experience

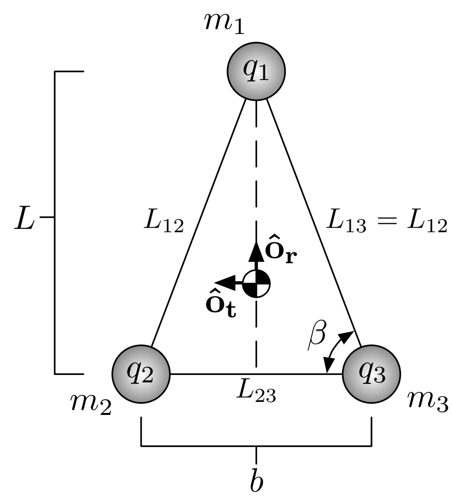

Figure 2.17: *Triangular 3-craft TCS configuration aligned with orbit along-track direction*

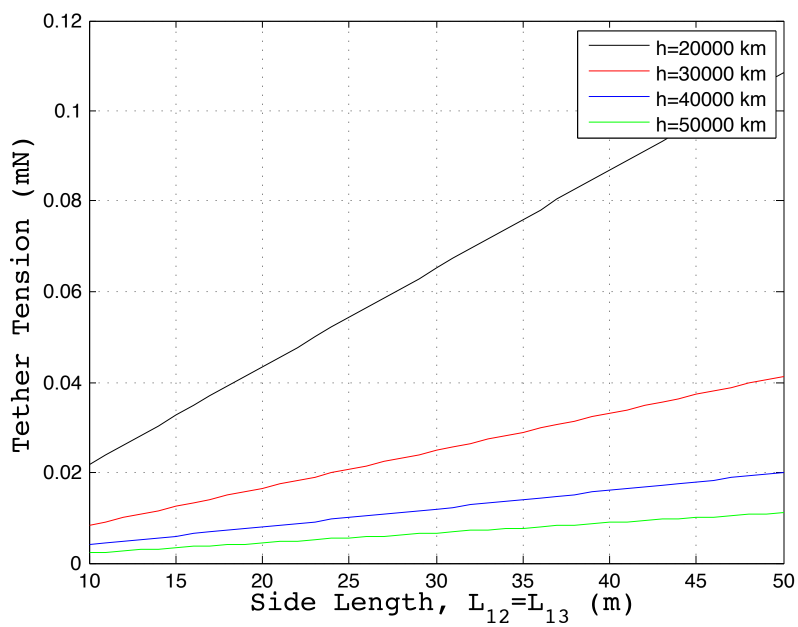

Figure 2.18: *Tension due to differential gravity only for tethers T_{12} and T_{13} at different altitudes. With $q_1 = 0$, the tethers maintain tension.*

tensile forces due to differential gravitational effects. This is illustrated in Figure 2.18, which shows the tether tensions due solely to gravity at different altitudes. For the simulations, the structure is assumed to be in orbit at an altitude ranging between 20,000 and 50,000 km, and in a plasma environment with a Debye length of $\lambda = 200$ m. All craft in the structure were assumed to be of equal mass, with m=100 kg.

Tether T_{23}, on the other hand, **does** require charging of craft 2 and 3 to ensure the tether will be in tension, due to the natural compressive effects of differential gravity for this particular geometry. For tension, it is required that $T_{23} > 0$. Thus, the required charge product $q_2 q_3$ can be determined as

$$q_2 q_3 > \frac{m\mu b^3}{2k_c r_c^3 (1 + \frac{b}{\lambda})} e^{\frac{b}{\lambda}}. \tag{2.33}$$

Values for q_2 and q_3 can be determined by taking the square root of Eq. (2.33). This yields a result where $q_2 = q_3$. Note that the right hand side of Eq. (2.33) will always be positive, so there is no chance of obtaining imaginary charges using this method. The minimum necessary charges to ensure tension, assuming $q_2 = q_3$, for a range of altitudes are presented in Figure 2.19 as solid lines. Interestingly, Eq. (2.33) is independent of L. What this means is that we may place craft 1 arbitrarily high above craft 2 and 3 without affecting the necessary charges to maintain tension in tether T_{23}. The distance L could be increased to maximize the gravity induced tension in tethers T_{12} and T_{13}, so that craft 1 could remain uncharged.

The second configuration considered has the same geometry as in Figure 2.17. Instead of craft 2 and 3 being aligned in the along track direction, however, they are arranged in the cross track direction. This arrangement provides an additional compressive force to tether T_{23} due to differential gravity. In this configuration, the tensions in tethers T_{12} and T_{13} are equal to the expressions in Eqs. (2.32a) and (2.32b). The tension in tether T_{23}, however, is now computed as

$$T_{23} = k_c \frac{q_2 q_3}{b^2} e^{-\frac{b}{\lambda}} (1 + \frac{b}{\lambda}) - m\mu \frac{b}{r_c^3}. \tag{2.34}$$

The compressive forces acting on T_{23} for this configuration are twice that of the previous case, due to the additional differential gravity effects. To ensure that tension is maintained, craft 2 and 3 must be charged so that

$$q_2 q_3 > \frac{m\mu b^3}{k_c r_c^3 (1 + \frac{b}{\lambda})} e^{\frac{b}{\lambda}}. \tag{2.35}$$

The charges required, again assuming $q_2 = q_3$, to maintain tension are shown in Figure 2.19 as dashed lines for different altitudes. As expected, the necessary charges for the cross-track alignment are higher than those for the along-track alignment. Note that at higher altitudes, less charge is needed to maintain tension. This is due to the fact that gravitational effects are smaller at higher altitudes. The comparison of these two similar structures yields a clear picture that the effect of orbital alignment can have on tether tensions. By selecting certain nominal arrangements (along-track alignment in this case), required charges can actually be lower for the same structure than would be needed in a different alignment.

2.5.4 Four-craft TCS Analysis

The third case under consideration is a 4-craft tetrahedron, as depicted in Figure 2.20. Craft 1, 2, and 3 make up the base, which is an equilateral triangle with side length L. Craft 4 is positioned above the base center of mass at a height b in the orbit radial direction. Craft 3 lies in the orbit along-track direction, and craft 2 and 3 are aligned in the orbit cross-track direction relative to the TCS center of mass. In this configuration, the geometry is determined entirely by the dimensions L and b.

The tensions in the six tethers for the tetrahedron arrangement are

$$T_{12} = k_c \frac{q_1 q_2}{L^2} e^{-\frac{L}{\lambda}} (1 + \frac{L}{\lambda}) - \frac{3}{4} m\mu \frac{L}{r_c^3} \tag{2.36a}$$

$$T_{13} = k_c \frac{q_1 q_3}{L^2} e^{-\frac{L}{\lambda}} (1 + \frac{L}{\lambda}) - \frac{1}{4} m\mu \frac{L}{r_c^3} \tag{2.36b}$$

$$T_{14} = k_c \frac{q_1 q_4}{L_{14}^2} e^{-\frac{L_{14}}{\lambda}} (1 + \frac{L_{14}}{\lambda}) + \frac{3}{4} m\mu \frac{L_{14}}{r_c^3} \tag{2.36c}$$

$$T_{23} = k_c \frac{q_2 q_3}{L^2} e^{-\frac{L}{\lambda}} (1 + \frac{L}{\lambda}) - \frac{1}{4} m\mu \frac{L}{r_c^3} \tag{2.36d}$$

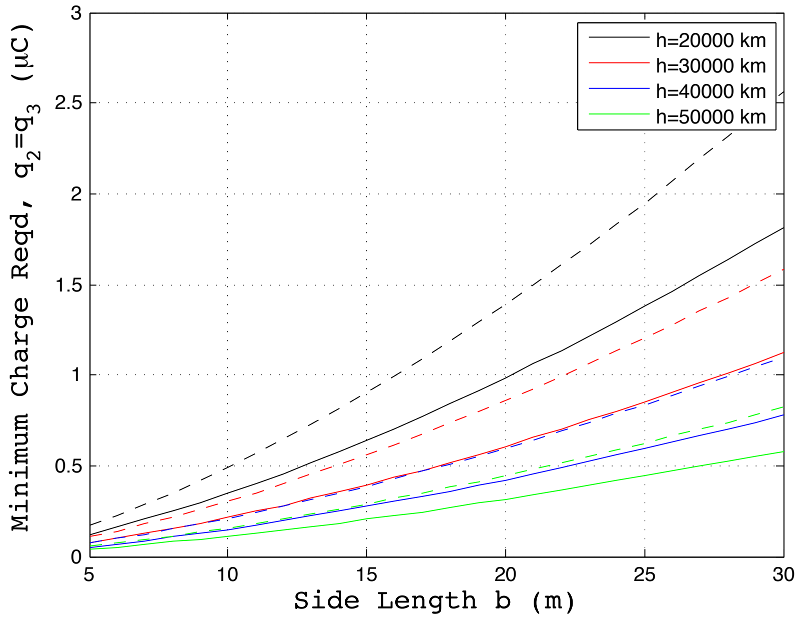

Figure 2.19: *Necessary charges on craft 2 and 3 to maintain tension in tether T_{23} at different altitudes, assuming $q_2 = q_3$. Solid lines represent along-track alignment and dashed lines represent cross-track alignment.*

$$T_{24} = k_c \frac{q_2 q_4}{L_{24}^2} e^{-\frac{L_{24}}{\lambda}} (1 + \frac{L_{24}}{\lambda}) + \frac{3}{4} m\mu \frac{L_{24}}{r_c^3} \tag{2.36e}$$

$$T_{34} = k_c \frac{q_3 q_4}{L_{34}^2} e^{-\frac{L_{34}}{\lambda}} (1 + \frac{L_{34}}{\lambda}) + \frac{3}{4} m\mu \frac{L_{34}}{r_c^3}. \tag{2.36f}$$

The symmetry of the tetrahedral configuration leads to similarities in several of the tethers. If $q_1 = q_2 = q_3$, the tensions in tethers T_{14}, T_{24}, and T_{34} will be the same. Also, if $q_1 = q_2$, the tensions in tethers T_{13} and T_{23} will be equal. In this tetrahedral configuration, the tethers connected to craft 4 will be in tension, even when $q_4 = 0$. Differential gravity effects are enough to ensure that the tethers T_{14}, T_{24}, and T_{34} will be in tension without craft charging. This is illustrated in Figure 2.21, which shows the tensions in these three tethers solely due to differential gravity effects. With no spacecraft charging, the forces in the tethers will be on the order of 0.1 mN or less. Spacecraft charging is required, however, to ensure tension in the base tethers T_{12}, T_{13}, and T_{23}. Without the use of Coulomb forces, the tethers will naturally go slack due to differential gravitational effects. To

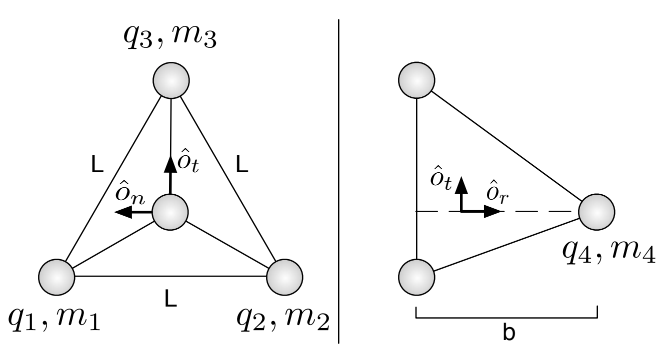

Figure 2.20: *Tetrahedral 4-craft TCS configuration*

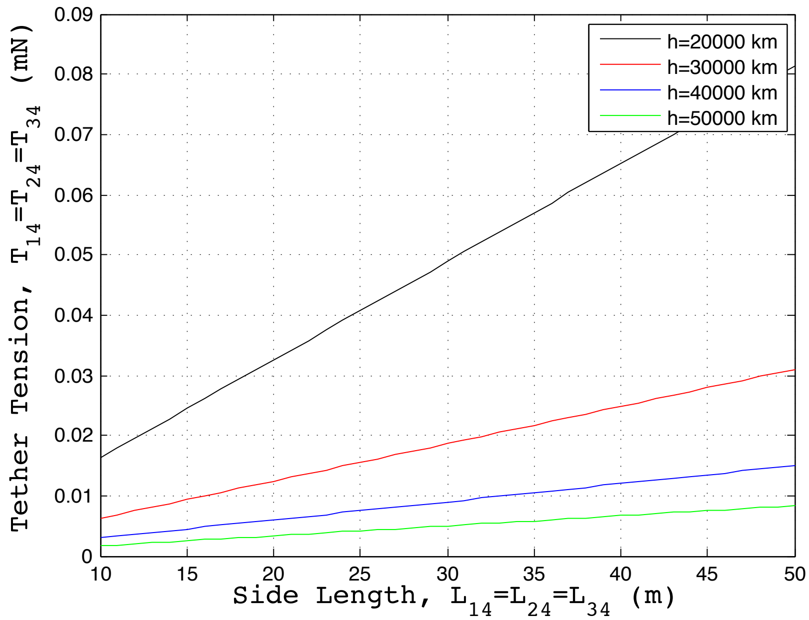

Figure 2.21: *Tension in tethers connected to craft 4 due only to differential gravity. From symmetry,* $T_{14} = T_{24} = T_{34}$.

guarantee rigidity of the three base tethers, it is required that

$$q_1 q_2 > \frac{3m\mu L^3}{4k_c r_c^3 (1 + \frac{L}{\lambda})} e^{\frac{L}{\lambda}} \tag{2.37}$$

$$q_1 q_3 > \frac{m\mu L^3}{4k_c r_c^3 (1 + \frac{L}{\lambda})} e^{\frac{L}{\lambda}} \tag{2.38}$$

$$q_2 q_3 > \frac{m\mu L^3}{4k_c r_c^3 (1 + \frac{L}{\lambda})} e^{\frac{L}{\lambda}}. \tag{2.39}$$

These three inequalities correspond to the three base tethers. Note that if $q_1 = q_2$, satisfying Eq. (2.38) also guarantees that Eq. (2.39) will be satisfied. Determining acceptable ranges for the three craft charges that satisfy these inequalities can be done by first ensuring that $q_1 = q_2$ by taking the square root of Eq. (2.37). This gives the minimum necessary charges on craft 1 and 2. With $q_1 = q_2$, the minimum required charge for craft 3 can be found by satisfying either Eq. (2.38) or Eq. (2.39), since they are equal. The results of this procedure are shown in Figure 2.22. The minimum needed charges on craft 1 and 2, assuming $q_1 = q_2$ are shown as solid lines. These values were then used to determine the minimum charges needed on craft 3, which are shown as dashed lines. It should be said that there is no reason why these particular assumptions need to be made; rather, they were used merely to provide a simple way to compute charges required to maintain tension. Note that, similar to the three-craft structure, the tensions in the base tethers are independent of the height of craft 4, b. Again, this means craft 4 may be placed arbitrarily high above the base without causing extra compression in the base tethers.

2.5.5 Six-craft TCS Analysis

The fourth structure under study is a six craft TCS, pictured in Figure 2.23. Unlike the three previous tethered Coulomb structures analyzed, the six-craft configuration does not feature fully

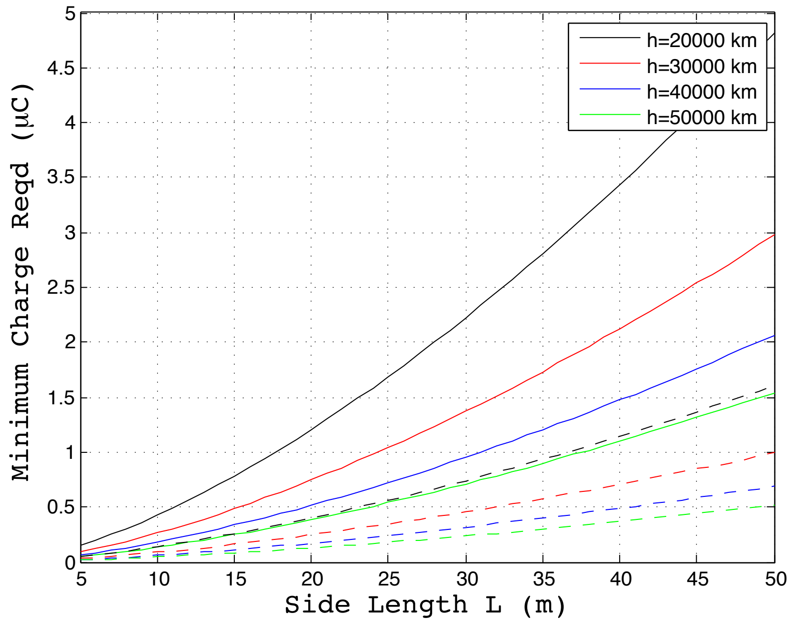

Figure 2.22: *Minimum charges required for tension for three base craft. Charges on craft 1 and 2 ($q_1 = q_2$) are shown as solid lines, while charges needed for craft 3 are shown as dashed lines.*

interconnected nodes. This means that a single node does not have a tether connection to all other nodes. As a result, inter-craft Coulomb forces affect more than only one tether at a time. This means that when charging the craft, careful consideration must be taken to avoid inducing unmanageable compressive forces in the structure. The other cases examined only exhibit compressive forces due to gravity, but with the six craft TCS inter-craft Coulomb forces may cause compression in the tethers.

The shape of the structure under investigation is presented in Figure 2.23. Four craft are arranged in a square with a side length of $2L$. A craft is placed above and below the center of this square at a distance of h in the orbit radial direction. The dimensions are thus defined by the lengths h and L, with the side length S computed as

$$S = \sqrt{h^2 + 2L^2}. \tag{2.40}$$

If we define the magnitude of the Coulomb force between two craft as

$$F_{ij} = k_c \frac{q_i q_j}{r_{ij}^2} e^{-\frac{r_{ij}}{\lambda_D}} \left(1 + \frac{r_{ij}}{\lambda_D}\right), \tag{2.41}$$

and recall our equal mass assumption, then the resulting tether forces are expressed as

$$T_{12} = F_{12} - F_{14} \tag{2.42a}$$

$$T_{13} = F_{13} + F_{14} + \frac{S}{2}\left(\frac{F_{16}}{h} + 3\frac{m\mu}{r_c^3}\right) \tag{2.42b}$$

$$T_{15} = F_{15} + F_{14} + \frac{S}{2}\left(\frac{F_{16}}{h} + 3\frac{m\mu}{r_c^3}\right) \tag{2.42c}$$

$$T_{23} = F_{23} + \frac{F_{24}}{\sqrt{2}} + L\left[\frac{F_{14}}{S} - \frac{F_{56}}{S} - \frac{1}{2}\left(\frac{F_{16}}{h} + 3\frac{m\mu}{r_c^3}\right)\right] \tag{2.42d}$$

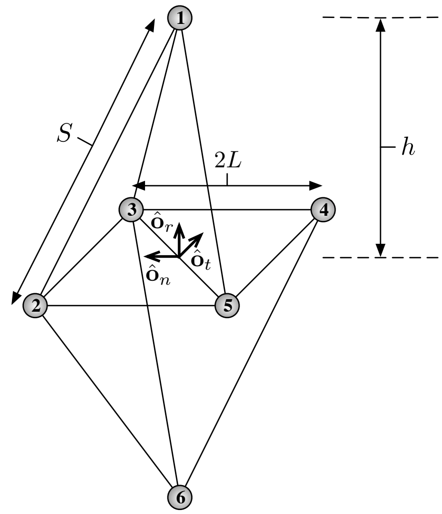

Figure 2.23: *Six-Node TCS System*

$$T_{25} = F_{25} + \frac{F_{24}}{\sqrt{2}} + L\left[\frac{F_{14}}{S} - \frac{F_{56}}{S} - \frac{1}{2}\left(\frac{F_{16}}{h} + 5\frac{m\mu}{r_c^3}\right)\right] \tag{2.42e}$$

$$T_{26} = F_{26} + F_{56} + \frac{S}{2}\left(\frac{F_{16}}{h} + 3\frac{m\mu}{r_c^3}\right) \tag{2.42f}$$

$$T_{34} = F_{34} + \frac{F_{24}}{\sqrt{2}} + L\left[\frac{F_{14}}{S} - \frac{F_{56}}{S} - \frac{1}{2}\left(\frac{F_{16}}{h} + 5\frac{m\mu}{r_c^3}\right)\right] \tag{2.42g}$$

$$T_{35} = F_{35} - F_{24} + 2\sqrt{2}\frac{L}{S}\left(F_{56} - F_{14}\right) \tag{2.42h}$$

$$T_{36} = F_{36} - F_{56} \tag{2.42i}$$

$$T_{45} = F_{45} + \frac{F_{24}}{\sqrt{2}} + L\left[\frac{F_{14}}{S} - \frac{F_{56}}{S} - \frac{1}{2}\left(\frac{F_{16}}{h} + 3\frac{m\mu}{r_c^3}\right)\right] \tag{2.42j}$$

$$T_{46} = F_{46} + F_{56} + \frac{S}{2}\left(\frac{F_{16}}{h} + 3\frac{m\mu}{r_c^3}\right). \tag{2.42k}$$

Because F_{ij} are positive forces of arbitrary value (due to the choices of q_i in Eq. (2.41)), is apparent that spacecraft charging can lead to compressive forces in more than one tether. In fact, this is the case in tethers $T_{12}, T_{23}, T_{25}, T_{34}, T_{35}, T_{36},$ and T_{45}, which is seven out of the eleven tethers in the structure. Also, we make note that for the six craft TCS, the forces in the base tethers are dependent on the vertical distance h, unlike with the previous three cases examined. This can be attributed to the fact the structure is no longer fully interconnected.

A quick examination of tethers T_{12} and T_{36} shows that for tension, it is required that $q_2 > q_4$ and $q_3 > q_5$. Also, if we assume $q_1 = q_6$ and $q_4 = q_5$, tether T_{35} requires that $q_3 > q_2$. If these assumptions are made, and the inequalities are satisfied, tethers T_{12}, T_{36} and T_{35} will always experience tensile forces. This leaves four tethers which may experience compressive forces, depending on the charges. It is important to develop a way to ensure tension in the remaining tethers. This can be done by determining which tether will experience the minimum tensile forces. The similarity of the tether force expressions makes this a relatively straightforward task. Consider the similarities of tethers T_{25} and T_{34}, where the only difference between the two is the first term. Because we have already assumed that $q_4 = q_5$ and $q_3 > q_2$, we know that $T_{25} < T_{34}$ because $F_{25} < F_{34}$. That is, if we select charges to ensure tension in T_{25}, T_{34} will also be in tension. A similar analysis can be performed to compare tethers T_{23} and T_{45} with the result that $T_{45} < T_{23}$. Thus, we know which two tethers will experience the smallest tensile forces out of T_{23}, T_{25}, T_{34}, and T_{45}. What remains is to determine which tether, T_{25} or T_{45}, will have the minimum tension. Unfortunately, this is not immediately clear. While it is true that $F_{45} < F_{25}$ due to the fact that $q_4 < q_2$, it is not clear whether or not this difference is enough to make up for the additional compressive forces due to gravity experienced by T_{25}. Thus, we must consider both of the tethers when determining a set of charges that will ensure tension. If we define the value of $q_4 = q_5$ as some fraction, f, of q_2 such that

$$q_4 = q_5 = fq_2, \tag{2.43}$$

we can develop two relationships that must be satisfied in order to ensure tension in all tethers. Using tether T_{25}, charge requirements for q_2 can be determined as

$$q_2^2 > 8e^{\frac{2(1+\sqrt{2})L}{\lambda_D}} L^3 \lambda_D \left(\frac{k_c q_1^2 r_c^3 e^{\frac{-2h}{\lambda_D}} (\frac{2h}{\lambda_D} + 1) + 20h^3 m\mu}{4fk_c h^3 r_c^3 \left[4e^{\frac{2\sqrt{2}L}{\lambda_D}} (2L + \lambda_D) + e^{\frac{2L}{\lambda_D}} (4L + \sqrt{2}\lambda_D) \right]} \right). \tag{2.44}$$

Likewise, consideration of tether T_{45} yields

$$q_2^2 > 8e^{\frac{2(1+\sqrt{2})L}{\lambda_D}} L^3 \lambda_D \left(\frac{k_c q_1^2 r_c^3 e^{\frac{-2h}{\lambda_D}} (\frac{2h}{\lambda_D} + 1) + 12h^3 m\mu}{4fk_c h^3 r_c^3 \left[4fe^{\frac{2\sqrt{2}L}{\lambda_D}} (2L + \lambda_D) + e^{\frac{2L}{\lambda_D}} (4L + \sqrt{2}\lambda_D) \right]} \right) \tag{2.45}$$

With a few assumptions, the charge requirements can be reduced to satisfying only a few conditions. In sum, tension can be ensured in all tethers by satisfying the following:

1. $q_1 = q_6$
2. $q_4 = q_5 < q_2$
3. $q_3 > q_2$
4. Satisfaction of the greater of Eqs. (2.44) and (2.45)

There are no explicit requirements on the magnitudes of the charges q_1 and q_6, only that they be positive to make sure that tethers T_{12} and T_{36} are not slack. There is a direct impact on the necessary magnitude of charges q_2 and q_3, however. Assigning too high of a charge for q_1 and q_6 could necessitate an unimplementable charge level on craft 2 and 3.

Regarding which of Eq. (2.44) and (2.45) will be greater, there are two factors which will affect the result for a given shape: the fraction value, f, and the Debye length, λ_D. As an example, consider a six craft TCS formation at GEO with the dimensions $h = 25$ m and $L = 7.5$ m, with $q_1 = q_6 = 1$ μC. The effects of varying λ_D and f on the requirements for such a shape are illustrated in Figure 2.24. To examine the effects of varying f, the Debye length is set at a constant $\lambda_D = 100$ m. Likewise, when considering the effects of varying Debye lengths, f is held at a constant 0.5. Figure 2.24 shows that the values of both parameters affect which of T_{25} and T_{45} requires a higher magnitude of q_2. This is the reason why both inequalities must be checked when determining charges for the craft.

To ensure that the outlined assumptions and inequality constraints do yield tension in all tethers, a range of Debye lengths are tested using the above assumptions. At each different value

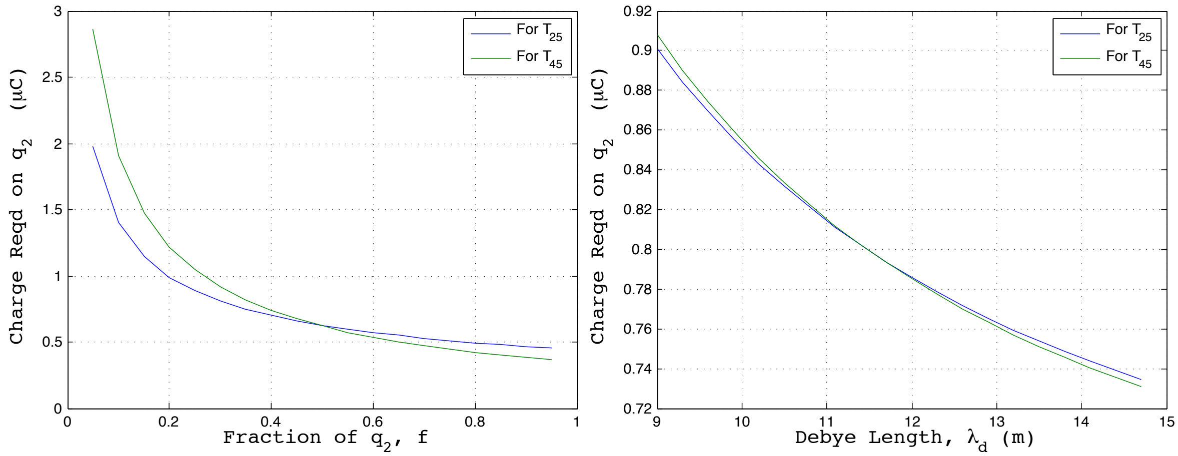

(a) $\lambda_D = 100$ m

(b) f=0.5

Figure 2.24: *Effect of varying a) f and b) λ_D on Eqs.* (2.44) *and* (2.45)

of λ_D the required q_2 is calculated and all tether tensions are computed. For these calculations, the values in Table 2.5 were used. The resulting tether tensions using these parameters and the value of q_2 calculated using Eqs. (2.44) and (2.45) are presented in Figure 2.25 for a range of Debye lengths. All of the tethers are positive except one, which is zero, at each Debye length computed. At small Debye lengths, it is tether T_{45} that is slack. For the larger Debye lengths, tether T_{25} is slack. This is a result of the effect demonstrated in Figure 2.24(b). The reason these tethers experience zero tension is because q_2 was computed as the greater of the right hand sides of Eqs. (2.44) and (2.45). To actually satisfy the inequality, q_2 would have to be increased above the value used here. In doing this, tethers T_{25} and T_{45} would be in tension. The craft charges corresponding to the tensions calculated in Figure 2.25 are presented in Figure 2.26. The necessary charges are on the order of 2 μC or less, even at worse-case Debye lengths of 5 meters.

The method described here for ensuring tension in all tethers is simply one approach to the problem. There is no reason why certain assumptions must be made; they were only done to simplify the problem and arrive at useful analytical solutions to the problem. In fact, there are an infinite number of potential charge combinations which would yield tension in all tethers, with no clear direction towards an "ideal" solution. The analysis performed for the six-craft TCS clearly indicates the complexities of designing structures with large numbers of craft. Not only are there many different conditions which must be met to guarantee tension, there are also the added concerns of inducing tension in the tethers due to inter-node electrostatic forces.

2.5.6 Compressive Forces due to Electrostatics

The existence of compressive electrostatic forces in the six-craft TCS is unique compared to the other three configurations analyzed. This is an intriguing result, as it implies that in complex tethered Coulomb structures careful design consideration must be given to ensure that compressive

Table 2.5: *Parameter values used in tension calculations*

$q_1 = q_6$	q_3	f	h	L	r_c
1 μC	1.1q_2	0.5	25 m	7.5 m	42164 km

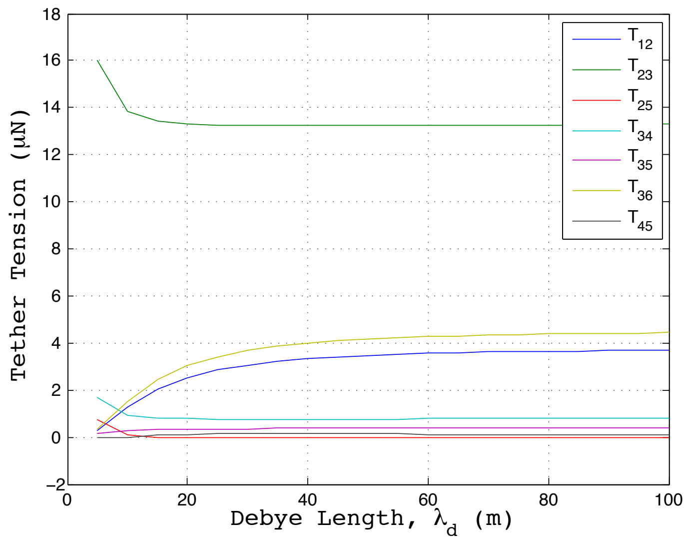

Figure 2.25: *Tensions computed in each of the tethers using inequality constraints to define q_2*

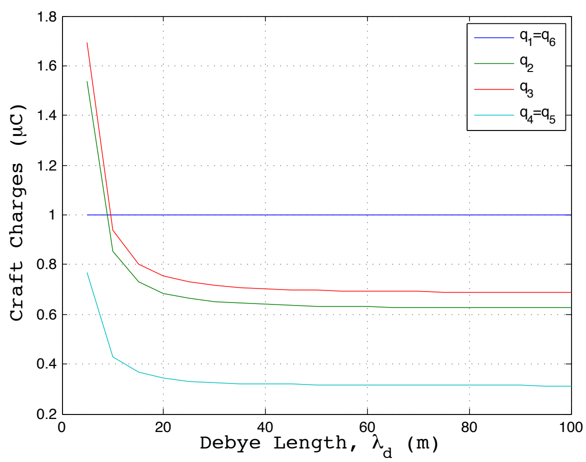

Figure 2.26: *Craft charges computed using inequality constraints to ensure tension in TCS tethers*

forces are not generated by electrostatics which cannot be overcome. Naturally, it is of interest to determine when such cases may or may not be possible. That is, what kinds of structures may exist where electrostatic forces **cannot** cause compression in **any** tethers, assuming all craft are charged to the same polarity (positive or negative)?

While, in general, large and complex structures consisting of many nodes (5 or more) need to be analyzed on a case by case basis to determine potential compressive forces caused by electrostatics, we can return to the case of completely interconnected structures and demonstrate that, at least for statically determinate structures, no compression can occur in any of the tethers due to electrostatics. By completely interconnected, we mean that each node is connected to all other nodes with a tether. This is illustrated in Figure 2.27. For comparison, a structure that is not completely interconnected is also presented.

For a statically determinate structure, we can apply the method of joints at each node to determine the tether tensions. In order for the structure to be statically stable, the forces acting on a particular node must satisfy

$$\sum \mathbf{C} + \sum \mathbf{T} = \mathbf{0}, \tag{2.46}$$

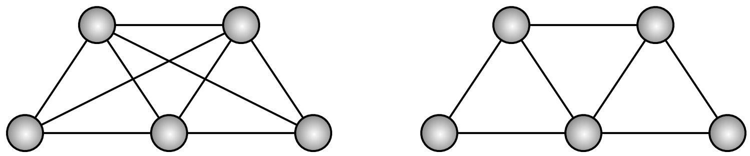

Figure 2.27: *Example of a completely connected (left) and non-completely connected (right) truss structure*

where $\mathbf{C}$ is the Coulomb force vector acting on the node, and $\mathbf{T}$ is the tether force acting on the node. Because we are concerned with electrostatic compressive effects, differential gravity is omitted from this analysis. This has no effect on how the Coulomb forces affect the tethers, as gravitational forces are decoupled from the electrostatic forces. To proceed further, we first define an orthogonal coordinate frame described by

$$\mathcal{N} : (\hat{\mathbf{n}}_\mathbf{1}, \hat{\mathbf{n}}_\mathbf{2}, \hat{\mathbf{n}}_\mathbf{3}).$$

If we define a unit vector $\hat{\mathbf{e}}_\mathbf{ij}$ as a vector from craft i to craft j in the formation, we can express the forces acting on craft i as

$$\mathbf{F}_\mathbf{i} = \sum_{j=1, j\neq i}^{k} (T_{ij} - C_{ij})\hat{\mathbf{e}}_\mathbf{ij}, \tag{2.47}$$

where T_{ij} represents the tether force between craft i and j, and C_{ij} represents the Coulomb force generated between craft i and j. In our three-dimensional coordinate system, we obtain three equations using Eq. (2.46):

$$\hat{\mathbf{n}}_\mathbf{1} \ : \ F_{i1} = \sum_{j=1, j\neq i}^{k} T_{ij}\hat{\mathbf{e}}_\mathbf{ij} \cdot \hat{\mathbf{n}}_\mathbf{1} - \sum_{j=1, j\neq i}^{k} C_{ij}\hat{\mathbf{e}}_\mathbf{ij} \cdot \hat{\mathbf{n}}_\mathbf{1} = 0 \tag{2.48}$$

$$\hat{\mathbf{n}}_\mathbf{2} \ : \ F_{i2} = \sum_{j=1, j\neq i}^{k} T_{ij}\hat{\mathbf{e}}_\mathbf{ij} \cdot \hat{\mathbf{n}}_\mathbf{2} - \sum_{j=1, j\neq i}^{k} C_{ij}\hat{\mathbf{e}}_\mathbf{ij} \cdot \hat{\mathbf{n}}_\mathbf{2} = 0. \tag{2.49}$$

$$\hat{\mathbf{n}}_\mathbf{3} \ : \ F_{i3} = \sum_{j=1, j\neq i}^{k} T_{ij}\hat{\mathbf{e}}_\mathbf{ij} \cdot \hat{\mathbf{n}}_\mathbf{3} - \sum_{j=1, j\neq i}^{k} C_{ij}\hat{\mathbf{e}}_\mathbf{ij} \cdot \hat{\mathbf{n}}_\mathbf{3} = 0.. \tag{2.50}$$

To determine the tether forces this process must be repeated for each tether until enough expressions have been derived such that the tether forces may be solved for algebraically. If we denote the number of tethers in the TCS as t, we will need to obtain t independent equations using Eqs. (2.48)-(2.50). With these t equations, the problem can be expressed in matrix form as

$$[A_{t\times t}]\mathbf{T} = [B_{t\times t}]\mathbf{C}, \tag{2.51}$$

where $\mathbf{T} = [T_{12} \ \ T_{13} \ \ ... \ \ T_{ij}]^T$ and $\mathbf{C} = [C_{12} \ \ C_{13} \ \ ... \ \ C_{ij}]^T$. The $[A]$ and $[B]$ matrices are populated using Eqs. (2.48)-(2.50). The form of these equations, however, guarantees the every row of the $[A]$ and $[B]$ matrices will be identical. Thus, $[A]$=$[B]$, and solving for $\mathbf{T}$ yields

$$\mathbf{T} = [A]^{-1}[A]\mathbf{C} = \mathbf{C}. \tag{2.52}$$

Thus, for a completely interconnected TCS, the tether force component due to electrostatics between craft i and j will equal the Coulomb force between the two craft.

This result has important implications regarding compressive forces generated by electrostatics in a TCS. Recalling that the force between any two craft is given as

$$C_{ij} = k_c \frac{q_1 q_2}{r_{ij}^2} e^{-r_{ij}/\lambda_D} \left(1 + \frac{r_{ij}}{\lambda_D}\right), \tag{2.53}$$

it is immediately clear that all tether force components due to inter-craft Coulomb forces will be tensile so long as all craft have the same polarity, irregardless of the TCS size or shape. This is directly applicable to **all** three and four craft TCS formations. Any formation of three or four craft **must** be completely interconnected in order for it to be statically stable (that is, tethers can balance all other forces and prevent dynamic motion of any node). Thus we can conclude that **for any 3 or 4 craft TCS, it is impossible to generate compressive forces in any tether due to the inter-craft electrostatic forces, so long as all craft have the same polarity**. This conclusion also applies to 5-craft completely interconnected structures. Beyond five craft, the system becomes statically indeterminate, and such structures have not yet been analyzed.

2.5.7 Discussion of Shape Configuration Study Results

The shape analyses presented here were done using basic static analysis techniques, assuming no deflection in the tethers. Careful consideration must be taken when observing the charge results required for tension. Actual implementation of the charges presented in the analysis would yield ideal tether tensions on the order of μN. In practice, tensions on this order would be too low to ensure rigidity of the structure. The important results of the shape configuration study concern the magnitude of the gravitational forces within the tethers, and the minimum amount of craft charges needed to offset those forces. Furthermore, we have observed possible issues which may be present when designing complex tethered Coulomb structures, such as induced compressive forces due to craft charging. Lastly, our analysis has demonstrated that for completely interconnected tethered Coulomb structures of five craft or less, craft charging will only cause tensile forces within the tethers so long as all craft have the same polarity.

2.6 Orbital Perturbation Study

The full translational equations of motion, Equation 2.19, for a TCS models a system that is affected by differential gravity and solar radiation pressure (SRP). However, both forces have been neglected in previous sections to isolate effects on translational and rotation motion. This section examines both perturbations separately and provides justification for using the simplified equations of motion of Equation 2.20. The benchmark two-node TCS will be used for this analysis. Since the rotational and translational equations of motion are coupled, both the translation and rotation of a two node TCS are investigated.

2.6.1 Differential Gravity

Previous simulations examine TCS rotational motion with no gravitational effects. However, TCS systems are envisioned to be operated at GEO where differential gravity can affect the nodal dynamics. A two node TCS system will be only be stable on orbit if the two nodes are in an orbit radial configuration. This condition is also stable if the nodes undergo initial asymmetric rotations. Table 2.6 shows the percent difference between the max principal rotations of a two-node TCS system with 10 deg/min asymmetric initial rotations in deep space as compared to GEO.

From the table it can be seen that putting the benchmark problem into GEO has minimal effect on the rotation of the TCS system. Therefore, differential gravity can be excluded from simple rotational simulations so that the TCS system dynamics can be isolated and analyzed. However, it is important to note that with differential gravity effects, rotations are no longer purely about a single axis for single- and double-tether TCS but they are very small respectively.

Table 2.6: *Maximum Rotation Percent Difference Between Deep Space and GEO Simulations*

Initial Rotation Axis	Single-Tether	Double-Tether	Triple-Tether
X-Axis	-0.0839%	0.6780%	-1.1596%
Y-Axis	N/A	-0.1514%	-0.1514%
Z-Axis	1.5793%	1.3376%	-2.2354%

2.6.2 Solar Radiation Pressure Compression

Solar radiation pressure is the only other prominent external force for spacecraft at GEO. The force on a spacecraft due to solar radiation is given in Equation 2.18. The worst case SRP compression force for a two spacecraft system is when the two TCS nodes are aligned relative to the sun and one node shields the other from the SRP. This worst case configuration is shown in Figure 2.28.

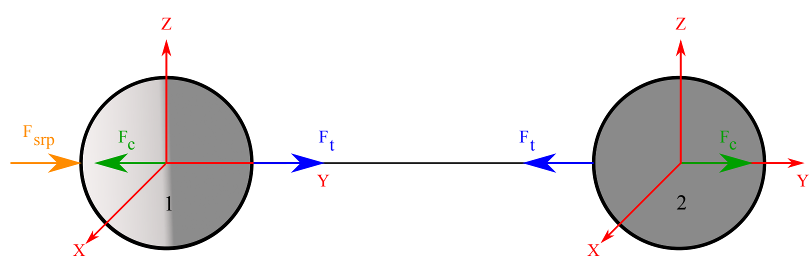

Figure 2.28: *Worst case, two-node solar radiation pressure orientation*

The key concern with SRP and TCS is if it will cause the TCS to loose tension. For the worst case scenario, loss of tension will occur when Coulomb inflationary force between nodes 1 and 2, Equation 2.5, is equal to the SRP force on node 1. Dividing Equation 2.18 by Equation 2.5 yields a percent of lost Coulomb force. Simplifying and letting $K = \pi P_{\text{srp}} C_r k_c$ be a constant, results in the percent of lost Coulomb force

$$\%LCF = K \frac{r_{12}^2}{V^2 e^{-r_{12}/\lambda_D} \left(1 + \frac{r_{12}}{\lambda_D}\right)} 100 \tag{2.54}$$

which only depends on the node voltage(V), separation distance (r_{12}) and the Debye length (λ_D). However, if the nodes are not the same radius, the ratio of the crafts radii must be added to the numerator of Equation 2.54. The simulation is started at TCS equilibrium with the parameters of Table 2.7. As long as the percent of lost Coulomb force is less than 100, there will be no loss of tension in the TCS. Figure 2.29 shows the percent of lost Coulomb force for the plausible operating regions for a two identical node craft in deep space.

It is important to note that this is for the worst case configuration with a worst case debye length of 4m. Even so, the SRP force only overcomes the Coulomb force for low potential values at high

Table 2.7: *Rotational Simulation Parameters*

Separation Distance	5 m
Node Mass	50 kg
Spring Constant	35.8398 N/m
Node Charge	30 kV
Node Radius	0.5 m
P_{srp}	4.56e-6 N/m
C_r	1

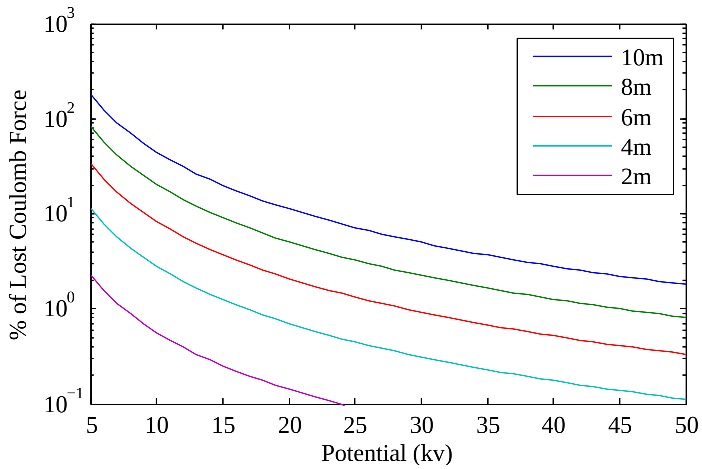

Figure 2.29: *Percentage of lost Coulomb force*

separation distances. Looking at the typical operating regions of 30 kilovolt potentials and 5 meter separation, Figure 2.29 shows that the SRP force is less than a percent of the Coulomb force and thus can be considered negligible.

Note that this plot shows this force ratio percentage on a logarithmic scale. For the voltages (20-40kV) and separation distances (2-5m) that are being considered between the nodes, the solar radiation force is 2-3 orders of magnitude smaller than the Coulomb force. For smaller TCS configurations the solar radiation pressure will have a negligible impact. However, as larger TCS node clusters are considered, the differential solar could contribute to large scale flexing of the TCS shape.

2.6.3 Solar Radiation Pressure Torques

The effects of solar radiation pressure on TCS compression is not the only way SRP can affect a TCS. SRP may also cause torques on a TCS. Two different worst case SRP torque scenarios are examined for a single tether two node TCS in deep space. The first scenario is a SRP torque about the system center of mass. This can arise when one craft is experiencing the effects of SRP and the other is not, due do some external shielding of a craft. The SRP torque about the center of mass scenario is shown in Figure 2.30.

Assuming the two craft are identical and that the SRP force is given in Equation 2.18, then the

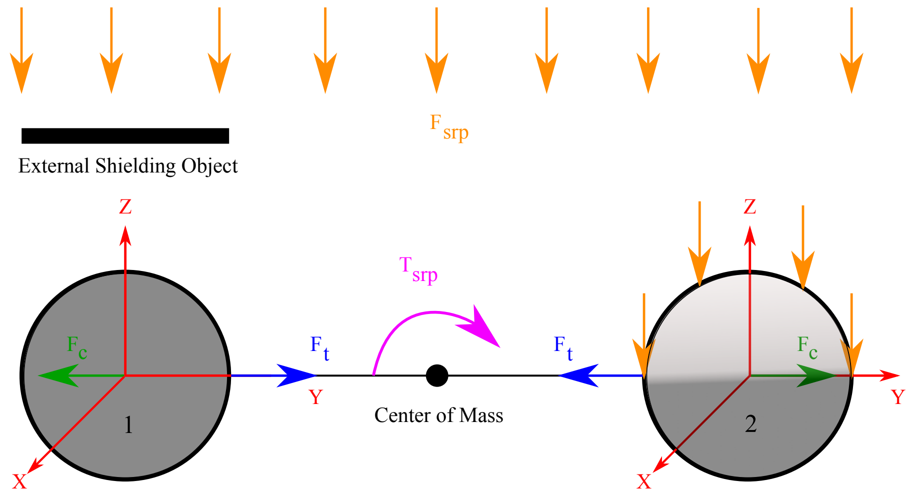

Figure 2.30: *SRP center of mass torque scenario*

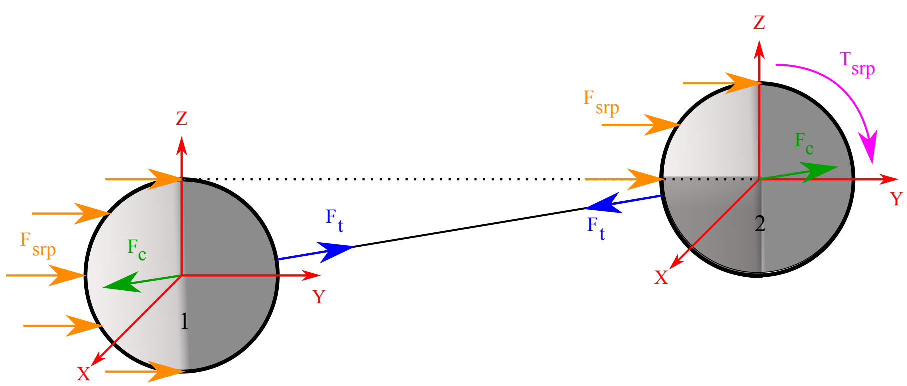

Figure 2.31: *SRP body torque scenario*

torque on the system will be given by

$$T_{\text{srp}} = F_{\text{srp}} \frac{r}{2} \tag{2.55}$$

where r is the node separation distance. Since this scenario is considered a worst case it is not envisioned to last for long durations. A three-hour simulation for the SRP center of mass torque was conducted to examine the effects of the torque. The simulation was started with the Coulomb and tensile forces in equilibrium. The parameters for the simulation are shown in Table 2.7. The simulation shows that as expected, the two craft TCS begin to rotate about their center of mass due to the external torque. After the three hour simulation the TCS was rotating at 1.5e-4 rad/s about the center of mass. However, when working with formations of spacecraft the relative positions and rotations are often of more importance. The change in relative position and rotation for the simulation was less that 1e-15 deg, effectively zero. Therefore the only concern with having a SRP torque around the system center of mass is that the system will begin to rotate as a whole.

The second SRP torque of interest is an SRP body torque. This type of torque can occur if a only a portion of a spacecraft is shielded. Figure 2.31 show a possible scenario. The figure shows that node one shields approximately half of node two from the SRP force. Therefore the SRP force on node two is given by

$$F_{\text{srp}_2} = P_{\text{srp}} C_r \frac{A_{sc}}{2} \tag{2.56}$$

This force is simplified by assuming the SRP only acts on a half sphere instead of the crescent

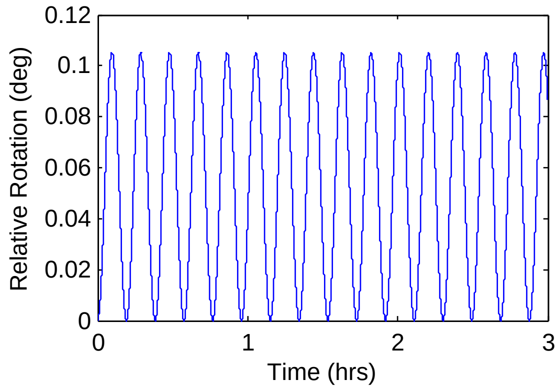

Figure 2.32: *SRP body torque relative rotation*

shape that most likely would occur with spherical craft. This total force is applied at the centroid of the cross-section half-circle of node two and results in the body torque

$$T_{\text{srp}} = F_{\text{srp}} \frac{4r}{3\pi} \tag{2.57}$$

where r is the radius of the node. This type of SRP torque that arises when nodes shield other nodes, will become more prominent working with TCS that have many nodes. A simulation is run where the only SRP force applied is on half of node two. The force on node one is neglected to isolate the effects of the body torque on one node. The nodes are started at equilibrium and all parameters are listed in Table 2.7. The change in relative position between the two nodes is again less than 1e-15 m. However, there is a change in relative rotation, which is shown in Figure 2.32. From the figure it can be seen that there is max relative rotation of 0.1 deg between the two craft. The rotation due to SRP body torques is minimal and the effects of these torque will not be the dominating perturbation.

The results of both SRP induced torque scenarios show that SRP will only have negligible effects on a TCS. The relative positions and rotation between TCS will be negligibly affected. The key effect from solar radiation pressure is that it will rotate a TCS system as a whole. This, like most other space systems affected by SRP, could be counteracted using thrusters or momentum wheels.

2.7 Advanced Dynamic Concepts

Previously, the two-node TCS is the only configuration that has been examined in the shape stiffness studies. This section provides a preliminary study of advanced TCS concepts to further show its capabilities. Work with a two-node TCS is expanded upon by examining a similar two-node TCS, but with one craft much larger and massive than the other such as in a mother-child configuration of having a primary craft deploy a small sensor sub-vehicle. Additionally, a three-node TCS with the nodes in an equilateral triangle is examined. Lastly, the topic of damping is introduced and a simple control law is simulated to show the further prospects of a TCS.

2.7.1 Mother/Child Configuration Study

One envisioned use of a TCS is to provide situational awareness for a geostationary satellite. Here one large spacecraft (the mother) has a smaller spacecraft (the child) tethered to it as illustrated

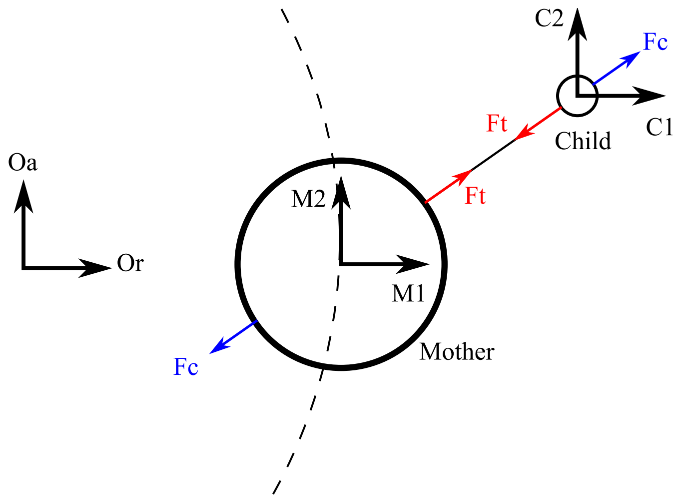

Figure 2.33: *Illustration of mother/child spacecraft scenario*

Table 2.8: *Mother Child Simulation Parameters*

Parameters	Mother	Child
Mass (kg)	2000	50
Radius (m)	2	0.5
Voltage (kV)	30	30
Separation (m)	5	5

in Figure 2.33. This type of TCS configuration can provide a unique vantage point for on-orbit inspection of the mother craft, rendezvous, docking and refueling operations and space environment measurements. The key advantage that a TCS can provide for situational awareness at GEO is that it can hold a child spacecraft at a relatively fixed position and angle with respect to the mother craft with minimal use of control and propulsion.

Free Mother-Craft Scenario: The trivial set up for a TCS mother child craft configuration is when the two craft are in the orbit radial configuration. This type of system would even be effective for spacecraft without charge, but less robust to perturbations. Charging the spacecraft allows for additional configurations with negligible relative translation and rotation. For example, using the parameters in Table 2.8, the maximum relative translation and rotation of the two craft after one orbit when the craft are oriented in either of the principal local vertical local horizontal directions is less than 1 mm and 0.001 deg, respectively. These simulations use a one tether TCS where the spacecraft started with initial Coulomb and tensile forces in equilibrium.

A configuration of more interest is when the child craft is placed at an arbitrary position relative to the mother craft. One such example would be placing the child craft where it would have positive radial and along track components relative to the mother craft. Figure 2.34 shows time elapsed snapshots of a tethered structure (TS) and TCS for this set up with the system parameters given in Table 2.8. From the figure it can be seen that for a TS the relative position and attitude of the two craft varies over an orbit. The tether is mostly slack and the child craft only rotates the mother craft after approximately 5 hours. The TCS however, maintains a reasonably fixed relative position and rotation between the two craft and the changes in relative position and rotation from the initial conditions can be seen in Figure 2.35. The reason for this consistency is that tether between the

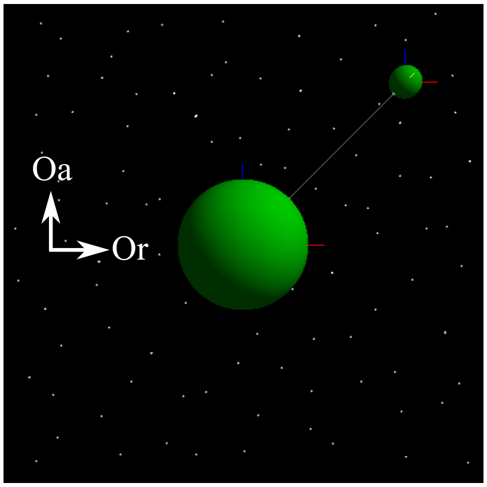

(a) TS at t = 0 hrs

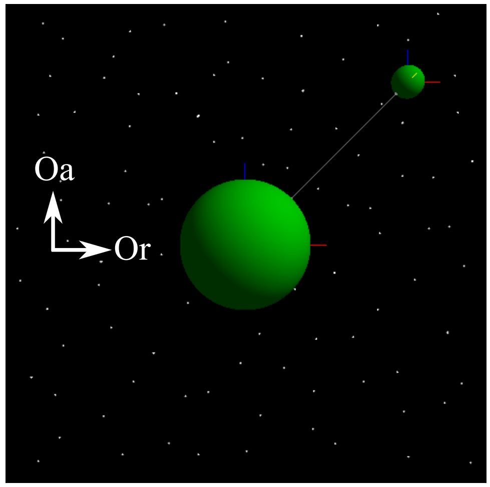

(b) TCS at t = 0 hrs

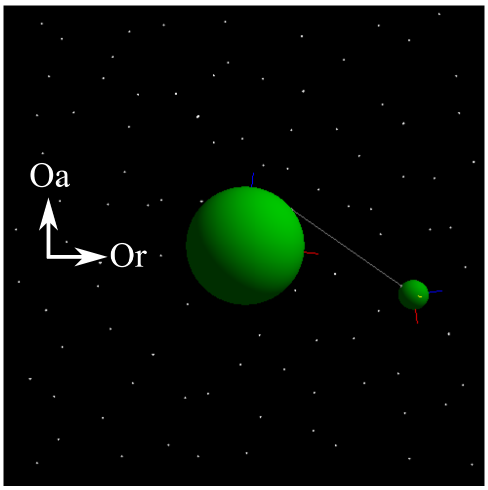

(c) TS at t = 5.5 hrs

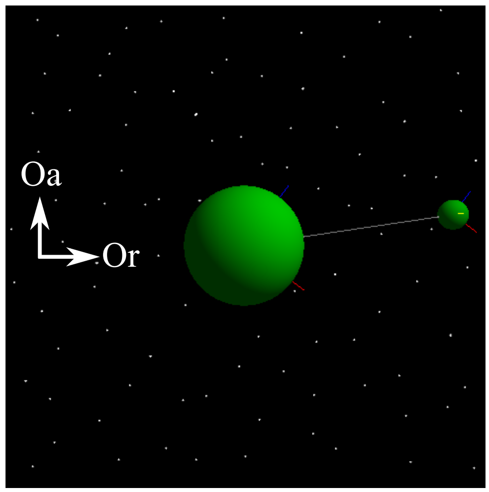

(d) TCS at t = 5.5 hrs

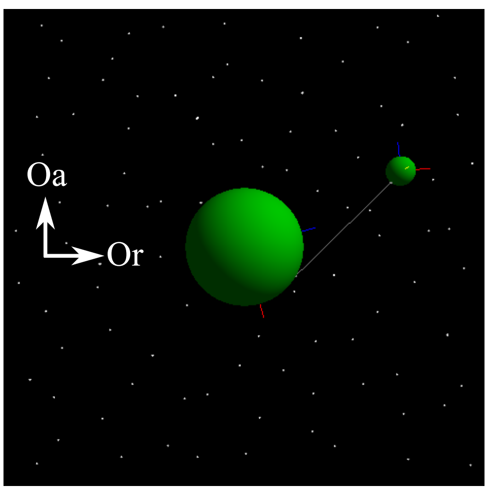

(e) TS at t = 14 hrs

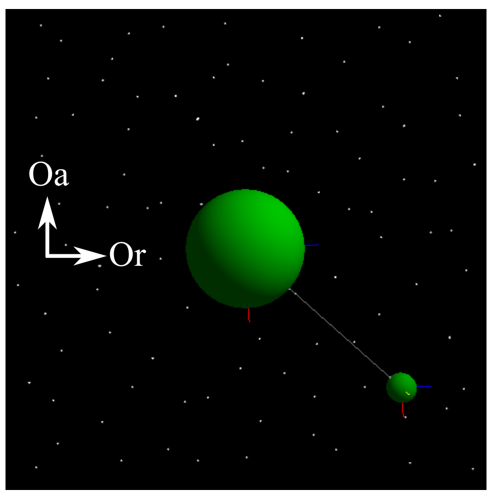

(f) TS at t = 14 hrs

Figure 2.34: *TS and TCS comparison of mother child configuration*

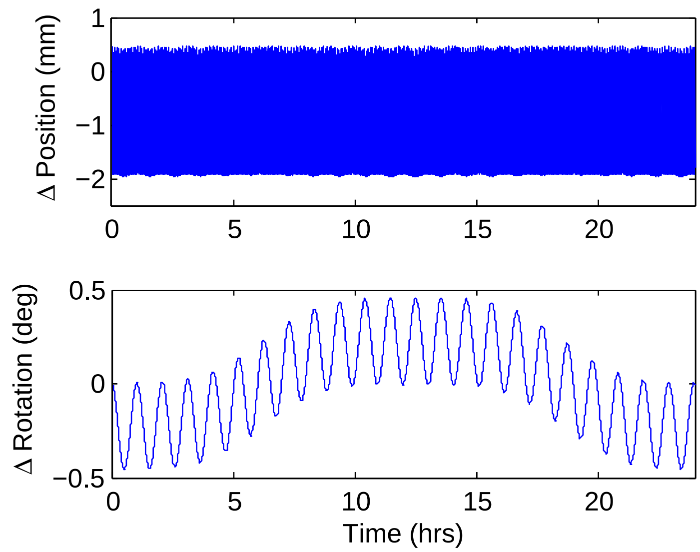

Figure 2.35: *TCS mother child relative position and rotation considering a freely rotating mother craft*

two craft remains almost always in tension throughout the orbit. These results are also typical if the child craft has an out of plane component, relative to the mother craft.

Fixed Mother-Craft Scenario: Even though a mother child TCS keeps relative positions and rotations nearly constant for an arbitrary set up, it does cause the system as a whole to rotate relative to the orbit frame. This is typically not desired, but can be easily fixed by implementing a simple attitude control solution. Figure 2.36 shows the relative values for a mother child configuration with a control that zeros the torque on the mother craft by applying an equal and opposite torque to that which is applied by the tether. In this scenario the mother craft orientation is held fixed, while the tethered child spacecraft is free to rotate due to the differential gravity influence. Of interest are how much the child spacecraft will move relative to the mother craft in this scenario. The parameters for this simulation are given in Table 2.8 and the control was updated at 10Hz.

The top figure in Figure 2.36(b) shows the relative rotation between the child and mother craft, while the bottom plot illustrates the rotation of the mother craft relative to the orbit frame. From the figure it can be seen that this simple control can hold a child craft almost fixed relative to a mother craft while keeping the formation aligned with the orbit frame. The relative motion is larger, as expected, than with the free-mother craft scenario. However, in this constrained mother craft orientation scenario the relative motions are still held very small with the constant electrostatic force.

2.7.2 TCS Triangle Configuration

Three-axis stiffness of a two-node TCS is achievable using a configuration with multiple tethers. The two-node configuration is considered the worst case scenario. Adding additional nodes increases the stiffness. A configuration examined here is a three-node TCS configuration in an equilateral triangle distribution. This three-node configuration was simulated with two nodes having initial asymmetric rotations as shown in Figure 2.37.

The configuration in Figure 2.37 was simulated for various initial asymmetric spin rates about all three axes. The maximum rotation of the initially rotating nodes results are shown in Figure 2.38.

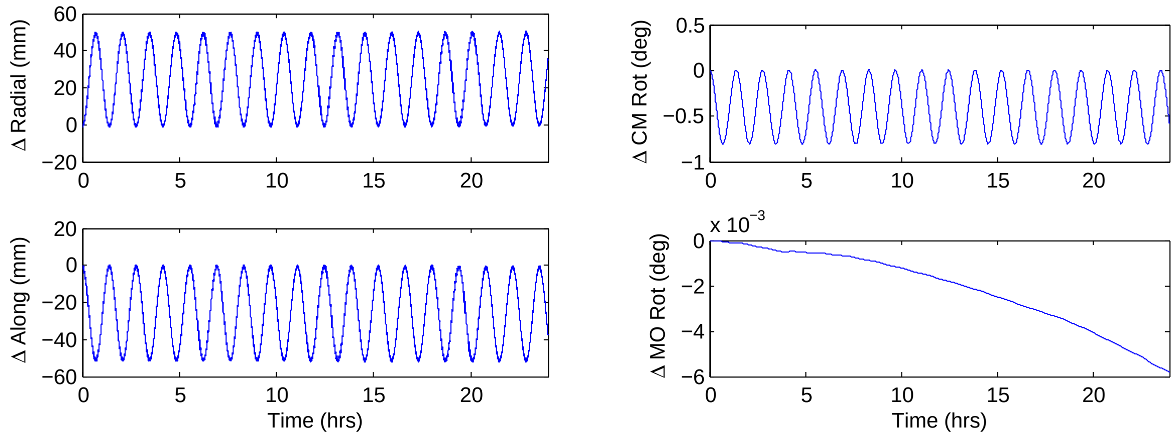

(a) Relative change in position

(b) Child/mother & mother/orbit relative change in rotations

Figure 2.36: *TCS mother child relative position and rotation with control considering a mother craft with a fixed/controlled orientation*

Additionally, the figure shows the maximum rotations for a similar two-node configuration.

As one would expect from the geometry of the three-node TCS the rotational stiffness is increased relative to the two-node TCS for rotations about the X-axis. However, the Z-axis rotational stiffness is decreased, relative to the two-node configuration. The important thing to note from Figure 2.38 is that there is now three dimensional rotational stiffness. A two-node single-tether TCS with rotation about the Y-axis has no restoring torque, but with an additional node now there is a restoring torque. This simulation shows that additional nodes can increase rotational stiffness depending tether orientation. Future work could look at multiple tether configurations with more than two nodes as well as TCS configurations with more than three nodes.

2.7.3 Two Node Damping Control

From the results of the previous sections it can be seen that there is no natural damping of translation or rotation for a TCS. In reality there may be loss of energy in the tether or other structure deformations which leads to damping of motion. This section examines a control to damp out rotations of a two node TCS undergoing initial asymmetric rotations. Since the translational and rotational motion of a TCS are coupled, both will damp out as long as the system is always removing energy.

For this work it is assumed that the nodes have a means of applying an internal torque with a momentum wheel or other control device. A control to damp out rotations of a single spacecraft is given in Reference 44 and is:

$$\boldsymbol{U}_i = -[P]\,\boldsymbol{\omega}_i \tag{2.58}$$

where $[P]$ is a symmetric, positive-definite feeback gain matrix and $\boldsymbol{\omega}_i$ is the rotation rate of node i. Combining this control with Equation 2.22 yields the following rotational equation of motion.

$$[I]\dot{\boldsymbol{\omega}}_i = -\boldsymbol{\omega}_i \times ([I]\boldsymbol{\omega}_i) + \boldsymbol{\Gamma}_i + \boldsymbol{U}_i \tag{2.59}$$

Figure 2.39, shows the results of the control in Equation 2.58 applied to both nodes of the TCS scenario in Figure 2.6 with the parameters of Table 2.9. Figure 2.39 shows that initial rotations can be quickly nullified and leave minimal translational motion.

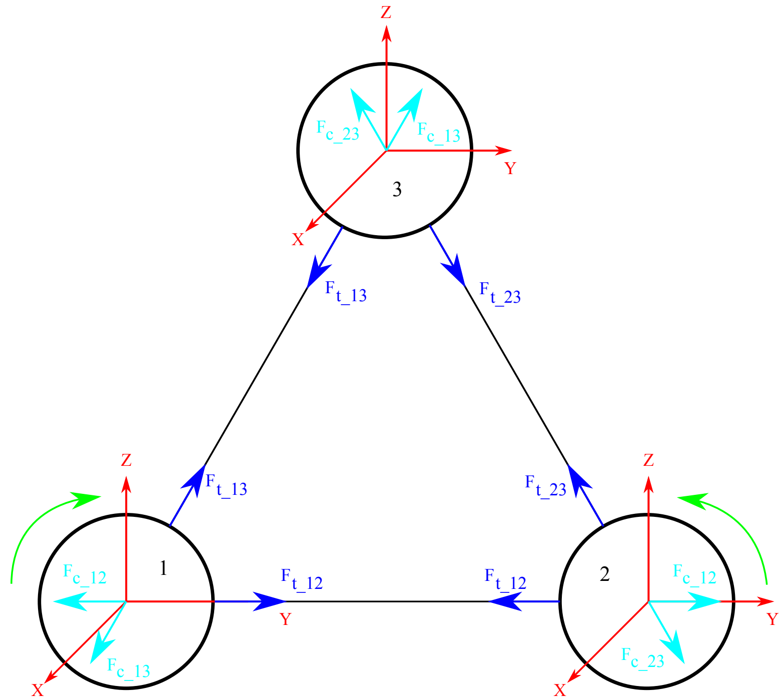

Figure 2.37: *Three-node equilateral triangle configuration*

The control in Equation 2.58 is useful in that is shows that TCS systems can cope with rotations. However, TCS nodes should be as simple as possible and it is not desirable to have a control mechanism on each node. Figure 2.40 shows the results of an identical simulation to that of Figure 2.39, but with only one node implementing the control of Equation 2.58. Figure 2.40 shows that the rotation of the node with the control device is reduced and remains low. The rotation of the other is slowly decreasing as energy is transfered and then removed by the node with a control. Additionally, the translational motion is also being reduced by the control. If this control is combined with a charge control to dampen out translational motion, it is believed the rotation of both nodes will quickly diminish. The results of this simulation show that a control mechanism does not need to be on every node. However, the control used has not been optimized and improvements should be considered in future work.

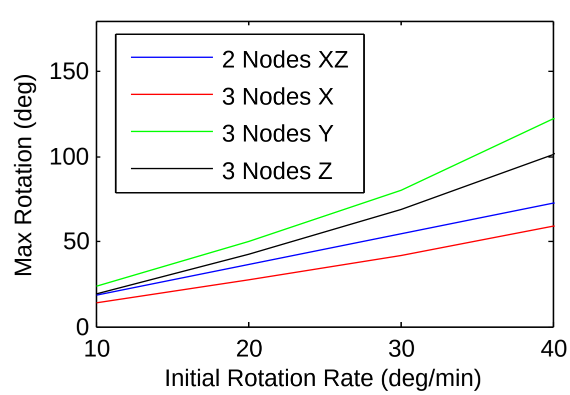

Figure 2.38: *Three-node equilateral triangle maximum rotations*

Table 2.9: *Controlled Rotational Simulation Parameters*

Parameter	Value
Separation Distance	5 m
Node Mass	50 kg
Spring Constant	35.8398 N/m
Node Charge	30 kV
Initial Rotation Rate	30 deg/min
Node Radius	0.5 m
Inertia Distribution	Solid Sphere
Gain	0.1

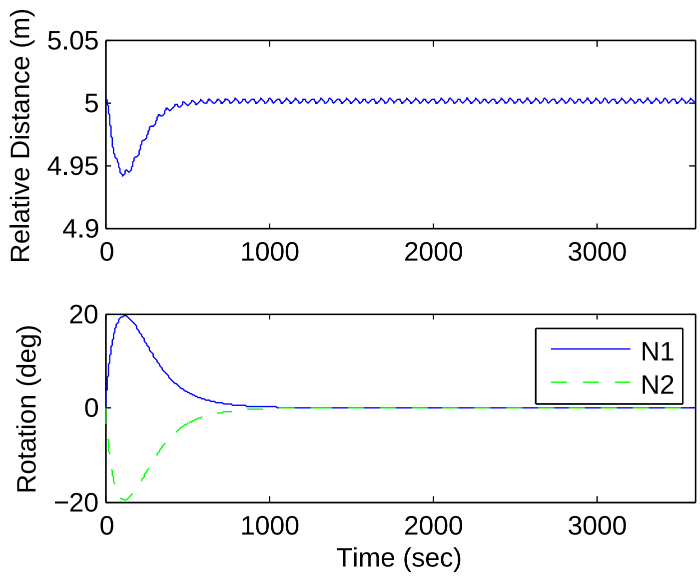

Figure 2.39: *System response to two-node rotation control*

2.8 Discussion of TCS Dynamics Modeling

This chapter examines the dynamics of TCS systems. Force models and equations of motion are given. Simulations are conducted to examine the effects of varying system parameters on translational and rotational stiffness. It is found that systems with nodes of low mass and high potential that are close together provide the highest translational and rotational stiffness. Additionally, it is shown that tether properties have negligible effects on rotational motion.

Rotational analysis of a two-node TCS configuration shows that this configuration can withstand moderate initial rotations up to around 1 deg/sec before the tether would become entangle with the spacecraft. Also, adding additional tethers yields full three-dimensional stiffness and increases the maximum allowable initial rotation by 60-70%. However, tether entanglement will now occur at lower absolute values of rotation, if the nodes are spherical. Finally, for optimal rotational stiffness it is found that the ideal node configuration should have most of its mass at the center of the structure with the largest possible radius for the tether attachment points and if multiple tethers are used, the optimal connection angle is 45 degrees.

The shape configuration study illustrates how the TCS shape influences the viability for electro-

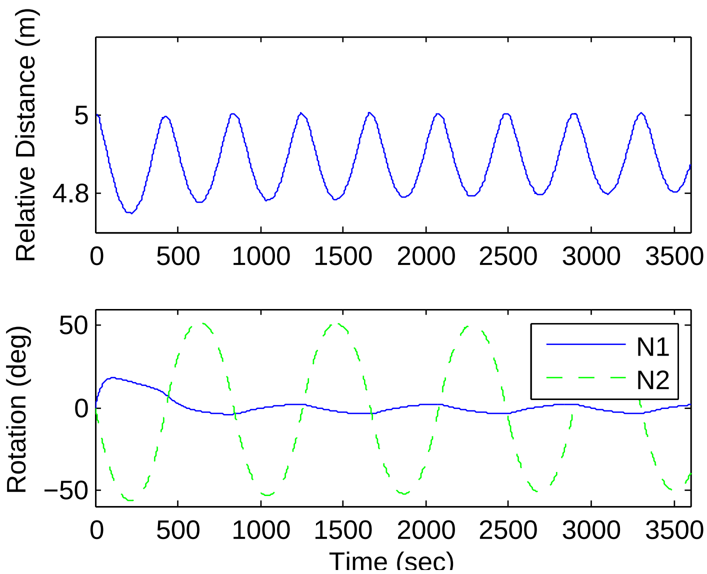

Figure 2.40: *System response to one-node rotation control*

static forces to ensure tether tension at all time. For fully inter-connected systems charge solutions with equal polarity will result in repulsive nodal forces. However, with more open structures the study illustrates the existence of shapes where a set of node charges could lead to the loss of tether tension.

The effects of orbital perturbations caused by differential gravity and solar radiation pressure are analyzed. Simulations show that differential gravity has minimal effect on the rotations of two-node TCS. Compression of a TCS system due to solar radiation pressure can be considered negligible because it only has noticeable effects for low potentials ($<$10kV) and large separation distances ($>$10m). Nodal torques due to SRP shown that only when there is partial shielding of a node will the torques affect relation position and rotation of TCS. However, SRP can cause TCS systems to rotate as a whole.

Lastly, advanced TCS concepts are presented to show TCS wide applicability. Mother child simulations show that a TCS can be used to hold a small craft relatively fixed to a large craft in any orbit configuration. A three-node TCS shows that larger structures provide full three-dimensional stiffness. Furthermore, a control was presented to show that basic damping of initial rotations is feasible for TCS but must be examined further.

Chapter 3

Finite Element Tethered-Dynamics Modeling

3.1 Introduction

In this section we refine our tether model and consider a higher-fidelity model that accounts for large displacements and rotations as well as local structural instabilities. The motion of the tether is predicted by a nonlinear transient finite element approach. The finite element model accounts for the inertia of spacecraft and the electrostatic forcing.

The goal of our study is to establish a feasible design space for the tether and to identify potential failure modes of the TCS caused by undesirable tether behavior and spacecraft-tether interaction. We study the influence of various design parameters on the TCS dynamics. Based the observed stress levels in the tether for nominal load scenarios we identify a range of material suitable for the tether design.

3.2 Structural and Electrostatic Force Modeling

To gain insight into the structural behavior of the tether-spacecraft system we model the motion of the tethers via a nonlinear two-dimensional elastic model, assume that the spacecraft are perfectly rigid, and approximate electrostatic forces via a lumped model. Starting with the equations of motions of the overall system, we describe the individual models.

3.2.1 Equations of Motion of the System

The transient response of the tether-spacecraft system due to electrostatic forcing and initial perturbations is modeled in the time domain. The equations of motion of the system are derived from the kinetic and potential energies using Lagrange's method.

Assuming a system of N_S spacecraft and N_T tethers the total kinetic energy is given by:

$$T_{System} = \sum_{N_S} T_{S,i} + \sum_{N_T} T_{T,i} \tag{3.1}$$

where $T_{S,i}$ and $T_{T,i}$ are the kinetic energies of the individual spacecraft and tethers. The total potential energy of the system is composed of:

$$U_{System} = \sum_{N_S} U_{S,i} + \sum_{N_T} U_{T,i} + U_{ES} \tag{3.2}$$

where $U_{S,i}$ and $U_{T,i}$ are the potential energies of the individual spacecraft and tethers; U_{ES} is the potential energy of the electrostatic field. In the following we neglect gravity. Assuming a rigid spacecraft the potential energy $U_{S,i}$ vanishes and $U_{T,i}$ equals the strain energy of a deforming tether.

Assuming a conservative system, i.e. $T_{System} + U_{System} = const.$, the equations of motions are derived via Lagrange's method as follows:

$$\frac{\mathrm{d}}{\mathrm{d}t}\Big(\frac{\partial T_{System}}{\partial \dot{q}_i}\Big) - \frac{\partial T_{System}}{\partial q_i} + \frac{\partial U_{System}}{\partial q_i} = 0, i = 1, 2, \ldots, N_q \tag{3.3}$$

where q_i denote the N_q generalized coordinates. Using a finite element method to spatially discretize the above equations, the generalized coordinates are the degrees of freedom of the finite element model. The system response is advanced in time via a numerical time integration scheme.

3.2.2 Tether Models

The main goal of the study presented in this section is to capture the dynamics of tethers and their interaction with the spacecraft. Therefore selecting an accurate tether model is of crucial importance. Due to the slenderness of the tether, the model needs to account for large displacements and rotations. Large strain effects are neglected as the TCS operates in a low-force environment and the tethers are assumed to be designed under small strain requirements.

A literature survey shows that beam models are often used to model tethers for space applications.[45,46,47] However, in contrast to most application scenarios considered in the literature, the low-force environment of the TCS allows for extreme slenderness. Therefore, we study the accuracy of both, bar and beam models in the following.

Assuming a linear kinematics and formulating the equations of motions in the undeformed configuration, bar models predict that the tether provides axial stiffness in tension and compression. Beam models also account for bending stiffness. Limiting the following study to two-dimensional models, torsion is neglected. To account for the loss of stiffness under compression due to local buckling, geometrically nonlinear bar or beam models are needed. Nonlinear models formulate the equations of motions in the deformed configuration. Assuming small deformations, i.e. small strains, but accounting for large displacements and rotations, we describe the tether kinematics with a corotational approach.[48] This formulation utilizes a corotated frame that is attached to the rigid body motions of the element base configuration. Element deformations are then defined with respect to the corotated frame. An explicit representation of the corotated configuration is not necessary but the motion is decomposed into a rigid body and elastic displacement. An illustration of the base and corotated frames are given in Fig. 3.1. Details on the corotational finite element formulation of bar and beam models are given in.[48]

3.2.3 Spacecraft Model

The spacecraft are assumed to be rigid. To facilitate the integration of the resulting rigid body models into the finite element framework used to analyze the motion of the flexible tethers, two models are considered: (a) a rigid disk model which allows attaching a single tether, and (b) a pseudo-rigid beam model which allows for an arbitrary connectivity of tethers and spacecraft.

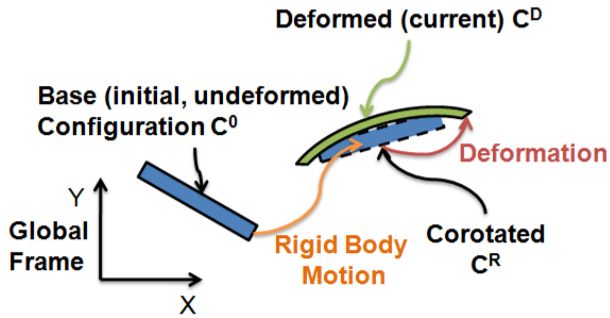

Figure 3.1: *Corotational Configuration.*[48]

3.2.3.1 Rigid Disk Model:

The spacecraft is modeled by a rigid two-dimensional disk made of a homogeneous material. The tether is pinned at an attachment point along the perimeter of the disk. The equations of motion are derived using Lagrange's method considering the kinetic energy of the spacecraft. To facilitate the integration of the spacecraft model into the finite element tether model, the motion of the spacecraft is expressed in terms of the motion of the attachment point and the rotation of the spacecraft about this point. The kinematics of the disk model is shown in Fig. 3.2 and is given by:

$$x_p = X_t + r\cos(\theta) R_D \cos(\alpha) \tag{3.4}$$

$$y_p = Y_t + r\sin(\theta) R_D \sin(\alpha) \tag{3.5}$$

where R_D is the radius of the disk, α defines the location (X_t, Y_t) of the attachment point t, and θ and r are the rotation angle and the distance from the center of an arbitrary point p with the coordinates x_p and y_p on the disk.

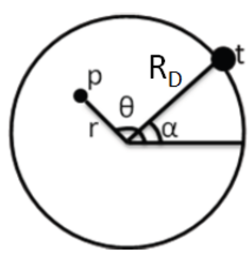

Figure 3.2: *Rigid disk model.*

The kinetic energy T_D of the disk is:

$$T_D = \int_0^{2\pi} \int_0^{R_D} \frac{1}{2}\, \rho_D\, h_D\, (\dot{x}^2 + \dot{y}^2)\, r\, \mathrm{d}r\, \mathrm{d}\theta \tag{3.6}$$

where ρ_D and h_D are the density and thickness of the disk, respectively. Note that since point t and an arbitrary point p are on a rigid disk, the angular velocities θ and α are equal. Applying Lagrange's Method to the kinetic energy defined above yields the contributions of the spacecraft to the overall equations of motion of the tether-spacecraft system. The disk model is integrated into the finite element framework via a rigid disk element.

The disk model presented above allows for attaching tethers only at a single attachment point. To allow for multiple attachment points additional kinematic constraint equations need to be considered. However, this complicates the integration of the rigid spacecraft model into a finite element framework.

3.2.3.2 Pseudo-Rigid Wheel Model:

In order to facilitate the integration of a rigid spacecraft model with multiple attachment points into a finite element model, the spacecraft is modeled by a spokes-wheel-type structure shown in Fig. 3.3. Spokes and rim are modeled by corotational beam elements described in section 3.2.2. The number of beam elements in the structure can easily be varied, allowing different connection angles for multiple tethers.

The geometry of the spokes-wheel and the density of the beams are chosen such that this model has identical mass, radius and polar moment of inertia as the rigid disk model. Note, for a two-dimensional model, only the polar moment needs to be considered and moments about in-plane axis play no role.

For a given disk radius R_D and disk mass m_D, the densities of spoke and rim elements are calculated by solving the following equations:

$$m_D = N_p \cdot (m_{Spoke} + m_{Rim}) = N_p \cdot (\rho_{Spoke} A_{Spoke} R_D + \rho_{Rim} A_{Rim} L_{Rim}) \tag{3.7}$$

$$I_{z,D} = N_p \cdot (I_{z,Spoke} + I_{z,Rim}) = N_p \cdot (\frac{m_{Spoke} R_D^2}{3} + \frac{m_{Rim} L_{Rim}^2}{12} + m_{Rim} h_{Rim}^2) \tag{3.8}$$

with

$$\begin{aligned} I_{z,D} &= \frac{1}{2} m_D R^2 \\ L_{Rim} &= 2R_D^2 (1 - \cos(\frac{2\pi}{N_p})) \\ h_{Rim} &= \sqrt{R_D^2 - \frac{L_{Rim}^2}{4}} \end{aligned} \tag{3.9}$$

where N_p is the number of sides of the polygon, and m_{Spoke} and m_{Rim} are the masses of each spoke and rim elements. The moments of inertia of the disk, and spoke and rim elements with respect to the disk or wheel center of mass are denoted by $I_{z,Disk}$, $I_{z,Spoke}$ and $I_{z,Rim}$. For given geometry parameters R_D, N_p, and disk mass m_{Disk} and setting the areas of spoke and rim elements, A_{Spoke} and A_{Rim} Eqs. 3.8 is solved to obtain the densities.

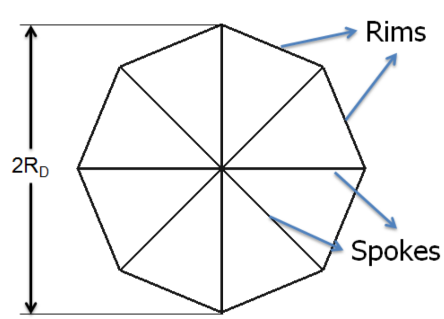

Figure 3.3: *Wheel model with n=8.*

While the spokes-wheel model would be able to capture elastic deformations of the spacecraft, in this study we assume a rigid spacecraft. Therefore we set the material stiffness and the cross-sectional areas of the spokes-wheel such that the spacecraft deformations are negligible. Using a higher stiffness ratio between spacecraft and tether models leads to numerical problems when time-integrating the transient response (see Section 3.2.6).

3.2.4 Electrostatic Force Modeling

The TCS concept inherently relies on the electrostatic forces acting between spacecraft and tether. These forces depend on the geometry of the overall system and therefore depend on the motion of the individual components relative to each other. The electrostatic pressure acting on a body is proportional to the strength of the electrostatic field surrounding the body. Therefore, to accurately determine the electrostatic forces as the spacecraft and tethers move the electrostatic field needs to be determined. For complex geometric configurations, such as multi-spacecraft-tether configurations, this can be done only numerically using boundary or finite element methods.

To bypass the complexity of such an approach we use a simplified electrostatic force model which is integrated into the finite element framework used to predict the tether and spacecraft motion. For this model we assume that the charge density on the surface of the spacecraft and tethers is uniform and does not change as the system deforms. This simplification is appropriate as long as the distance between bodies is sufficiently large, e.g. larger than the radius of the spacecraft, but may lead to noticeable errors as the distance is decreases. To understand the influence of electrostatic forces on the motion of the spacecraft-tether system the approximation errors are considered acceptable. The components of the simplified force model are summarized in the following.

3.2.4.1 The Coulomb Force Element:

The electrostatic pressure acting between two charged bodies is approximated by a lumped force model which is derived from Coulomb's law for forces between two point charges. The potential energy of an electrostatic field between two point charges is given by:

$$U = k_c \frac{q_1 \, q_2}{d} \tag{3.10}$$

where q_1 and q_2 are the charges of the two points, k_c is the Coulomb's constant, and d is the distance between the points. For a spherical body with radius R_i, the charges are related to the electric potential, V_i by the following equation:

$$q_i = \frac{V_i R_i}{k_c} \tag{3.11}$$

Applying Lagrange's Method to the potential energy defined above yields the contributions of the Coulomb forces to the overall equations of motion of the tether-spacecraft system. The resulting force term is integrated into a finite element model via a Coulomb Force (CF) element.

3.2.4.2 Spacecraft Charging:

The electrostatic pressure acting on a charged spacecraft is approximated by a force acting on the spacecraft area center. Accounting for the kinematic of the rigid disk model, a specialized CF element is developed. Given a spacecraft potential V_S the charge Q_S of a spherical spacecraft wit radius R_S is given by Eq. (3.11) with $V_i = V_S$ and $R_i = R_S$.

3.2.4.3 Tether Charging:

In the case of charged tethers, electrostatic forces between the spacecraft and tether and between tether segments are accounted for. The forces are approximated with the CF computing the equivalent nodal charges as follows:

For a straight tether with a circular cross-section the capacitance is given as:[49,50,51]

$$C_T = \frac{4\pi\epsilon L_T}{\Lambda}\left[1+\frac{1}{\Lambda}(1-\ln(2))+\frac{1}{\Lambda^2}\left\{1+(1-\ln(2))^2-\frac{\pi^2}{12}\right\}\right], \tag{3.12}$$

with

$$\Lambda = \ln\left(\frac{L_T}{R_T}\right), \tag{3.13}$$

where L_T and R_T are the length and radius of the tether, respectively. Setting the permittivity ϵ of the surrounding medium to that of vacuum (i.e. $\epsilon = \epsilon_0$), Eq. (3.12) can be written as follows:

$$C_T = \frac{L_T}{\Lambda k_c}\left[1+\frac{1}{\Lambda}(1-\ln(2))+\frac{1}{\Lambda^2}\left\{1+(1-\ln(2))^2-\frac{\pi^2}{12}\right\}\right], \tag{3.14}$$

The total charge Q_T on the tether is given by:

$$Q_t = V_T\, C_T \tag{3.15}$$

where V_T is the potential of the tether which is assumed to be constant along tether.

The total charge of the tether is distributed to the nodes of the tether elements. Note that the charge of end nodes is half of charge of the mid nodes.

To model the forces between spacecraft and tethers CF elements connect each charged node (including the spacecraft central node) to every other charged node in the model. This model can be broken down to 3 components, as shown in Fig. 3.4 in the case of charged spacecraft and tethers. Note that the nodal charges along the tether differ from the charge values for the spacecraft.

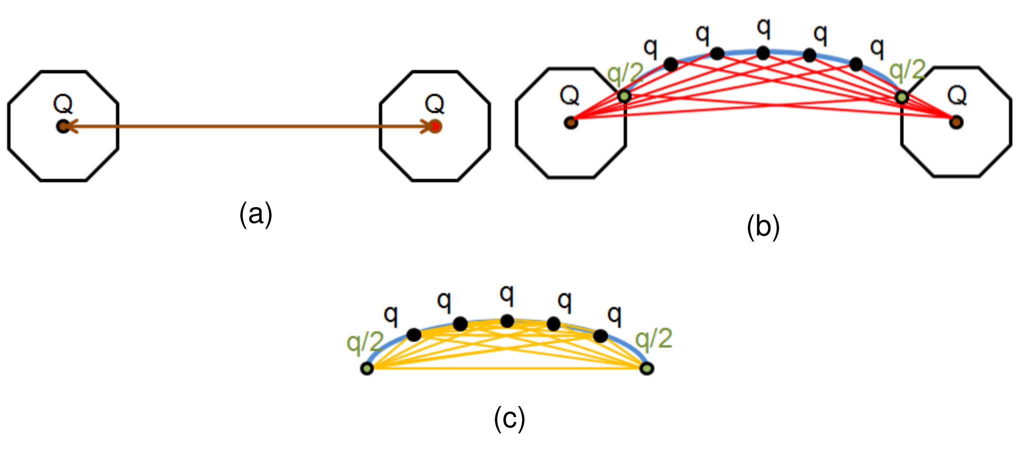

Figure 3.4: *Electrostatic force model: (a) CF element between spacecraft, (b) CF elements between spacecraft and tether nodes, and (c) CF elements between tether nodes.*

3.2.5 Inelastic Strain Effects

Environmental effects, material processing, and material aging are likely to generate inelastic strains in the tether. Inelastic strains are often referred to as eigenstrains; this expression is used in the following. Owing to the slenderness of the tether these eigenstrains may cause large displacements and rotations of the tether and the spacecraft.[52] Accurately predicting the magnitude and distribution of eigenstrains along tether requires precise knowledge of the space environment, manufacturing processes, and storage of the tether before deployment. In the absence of such information, we develop a simplified model to study the effects of eigenstrains on the motion of the spacecraft-tether system. Our model is built upon a thermal strain analogy, i.e. we assume that all eigenstrains are caused by a fictitious thermal gradient in the tether. Note that the thermal strain analogy is used only for modeling purposes and all mechanisms generating eigenstrains are approximated via this model.

The thermal strain is given by:

$$\epsilon_{thermal} = \alpha_{thermal}\, T \tag{3.16}$$

where $\alpha_{thermal}$ is the coefficient of thermal expansion and T is the temperature measured with respect to an arbitrary reference temperature. Assuming that the temperature varies across the cross-section, the thermal strains generate a bending moment which is calculated by:

$$M_z = \int_{A_T} E_T\, \alpha_{thermal}\, T(y)\, y\, \mathrm{d}A. \tag{3.17}$$

where A_T and E_T are the tether cross-sectional area and modulus of elasticity. The spatial coordinate y is pointing in thickness direction; the origin of the associated coordinate system is in the neutral axis and the x-axis is aligned with the axial direction of the tether. For simplicity reasons, we assume that the temperature varies linearly across the cross-section of the tether and that the tether has a cross-section that is symmetric with respect to the y-axis. For a circular cross-section, the bending moment M_z is:

$$M_z = \int_{-R_T}^{R_T} E_T\, \beta\, \frac{y^2}{R_T}\, \sqrt{R_T^2 - y^2}\, \mathrm{d}R = E_T\, I_T\, \frac{\beta}{2\, R_T}. \tag{3.18}$$

where R_T is the radius of the tether, and I_T is the second area moment of inertia about the z-axis. The differential eigenstrain between the hot and cold face of the beam is denoted by $\beta = \alpha_{thermal}\, (T_{hot} - T_{cold})$.

3.2.6 Numerical Solution Procedure

The tether, spacecraft, and electrostatic force models are implemented into an in-house finite element platform. The system response is analyzed in time via a numerical time integration scheme. The key components of the numerical analysis procedure are outlined in the following.

Applying a finite element approach to spatially discretize the spacecraft-tether system, the equations of motion in semi-discrete form are given by:

$$\mathbf{M}\ddot{\mathbf{u}} + \mathbf{R}(\mathbf{u}, \dot{\mathbf{u}}) = \mathbf{0} \tag{3.19}$$

where $\ddot{\mathbf{u}}$, $\dot{\mathbf{u}}$, $\mathbf{u}$ denote the acceleration, velocity and displacement vectors; $\mathbf{M}$ is the mass matrices and $\mathbf{R}$ is the residual of internal and external forces.

Given initial conditions for displacement and velocities, the system response is integrated in time by the Newmark - β method. In each time step, this scheme approximates the displacements by a cubic polynomial and solves a nonlinear problem via Netwon's method.[53] The size of the time step is selected such that all oscillatory modes that effect the transient response of the system are computed accurately.[54] As the systems considered in this study exhibit strong nonlinearities, numerical stability requirements impose further constraints on the size of the time step.

In the present study, numerical stability issues are significant as the tether undergoes large displacements and rotations, including buckling, and the spacecraft-tether model consists of flexible and (pseudo-)rigid components leading to wide spectrum of modes. Resolving the contributions of all modes in the time response of the system would require an impractically small time step; omitting high-frequency contributions may cause the time-integration scheme to diverge. To be able to use a larger time-step while mitigating numerical stability issues, we introduce numerical damping via algorithmic parameters of the Newmark - β method.[55]

3.3 Model Verification

To study the robustness and accuracy of the tether, spacecraft and electrostatic models introduced above, we perform numerical simulations with bar and beam tether models. This study provides insight into the conceptual mechanical behavior of the system and guides the selection of the tether model. In particular, we study whether bending effects are of any relevance for the tether dynamics. The slenderness of the tether may suggest that its bending stiffness is negligible and a bar model is sufficient. However, as the external forces are also small, bending may still play a role.

The following simulations are preformed for a two spacecraft / single tether configuration whose parameters are defined in Table 3.1. Note that this configurations differs from the nominal tether design studied later (see Section 3.5).

Table 3.1: *Two spacecraft / single tether configuration – Verification study.*

Spacecraft mass	$50\ kg$
Spacecraft radius	$0.5\ m$
Spacecraft potential	$30\ kV$
Distance between spacecraft centers	$5\ m$
Tether cross-sectional area	$5.60\ 10^{-7}\ m^2$
Tether area moment of inertia	$2.46\ 10^{-13}\ m^4$
Tether density	$1.56\ g/cm^3$
Tether modulus of elasticity	$9.5\ GP$

To gain insight into to the dynamics of the spacecraft-tether system we perturb the system which is initially in static equilibrium. We impose initial angular velocities of the spacecraft. Two cases are studied (see Fig. 3.5): in the asymmetric case the spacecrafts are rotating in opposite directions, in the symmetric case the spacecrafts are rotating in the same direction.

3.3.1 Comparison of Eigenfrequencies

In order to obtain conceptual insight into the dynamics of a slender tether we first compare the lowest eigenfrequencies of the axial mode of a linear bar model and the bending mode of a linear beam model with the first eigenfrequency of a string pre-stressed by the electrostatic force T acting

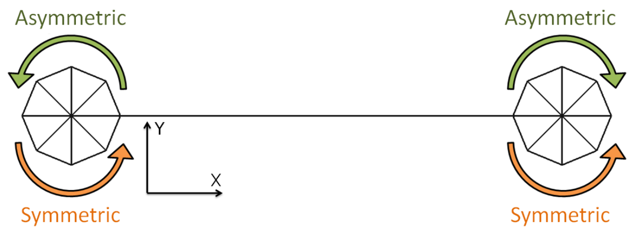

Figure 3.5: *Asymmetric and symmetric perturbations.*

between the two spacecraft. Here, the tether is assumed to be uncharged. The eigenfrequencies for the three models are:

$$\begin{aligned} w_{bar} &= \frac{\pi}{L_T}\sqrt{\frac{E_T}{\rho_T}} && = 1.9382 \cdot 10^3 \text{ rad/s} \\ w_{beam} &= (\frac{\pi}{L_T})^2\sqrt{\frac{E_T I_T}{\rho A_T}} && = 1.0095 \text{ rad/s} \\ w_{string} &= \frac{\pi}{L_T}\sqrt{\frac{T_T}{\rho_T A_T}} && = 0.8403 \text{ rad/s} \end{aligned} \quad (3.20)$$

where I_T is the tether area moment of inertia, A_T is the tether area, L_T is the tether length, E_T is the modulus of elasticity, and ρ_T is the tether density. The results show that the eigenfrequency of the bar is significantly higher than the eigenfrequency of the string and the beam. The string and the beam vibrate in bending-type modes, while the bar vibrates in axial modes. This result points out the inaccuracy of a linear bar model for slender tethers.

3.3.2 Dynamic Response

To further down select the tether model, the displacements at the spacecraft attachment point are compared for linear and nonlinear bar and beam models. The simulations are performed with the spacecraft represented by the disk model and the parameters given in Table 3.1. The system is perturbed by imposing initial angular rotations of $40°/min$ such that spacecraft rotate in opposite directions. The displacements are monitored over a time period of $2000\ s$.

Figure 3.6 shows the displacement and forces for different models. Here, the tether is discretized by 25 elements in the case of beam and nonlinear bar models. Only one element is used in the case of a linear bar model. Both linear models predict similar forces. As the linear models cannot capture instabilities, in particular buckling of the tether due to compression, the compressive forces in the tether are over predicted. Both nonlinear models predict a similar, rapidly oscillating response and higher tensile forces. The prediction of noticeable compressive forces is due to insufficient mesh refinement. This issue is illustrated in Fig. 3.7 and Fig. A.3.

Increasing the number of tether elements reduces the magnitude of the compressive forces as local buckling is better resolved. Both models predict that the tether can resist a small amount of compressive forces due to inertia effects. While nonlinear bar and beam models show similar trends as the mesh is refined there remains a distinct difference between both models which suggests that bending effects play some role in the tether dynamics.

The above numerical studies suggest that the motion of the tether is dominated by geometrically nonlinear phenomena, such as large displacement and rotations as well as local buckling

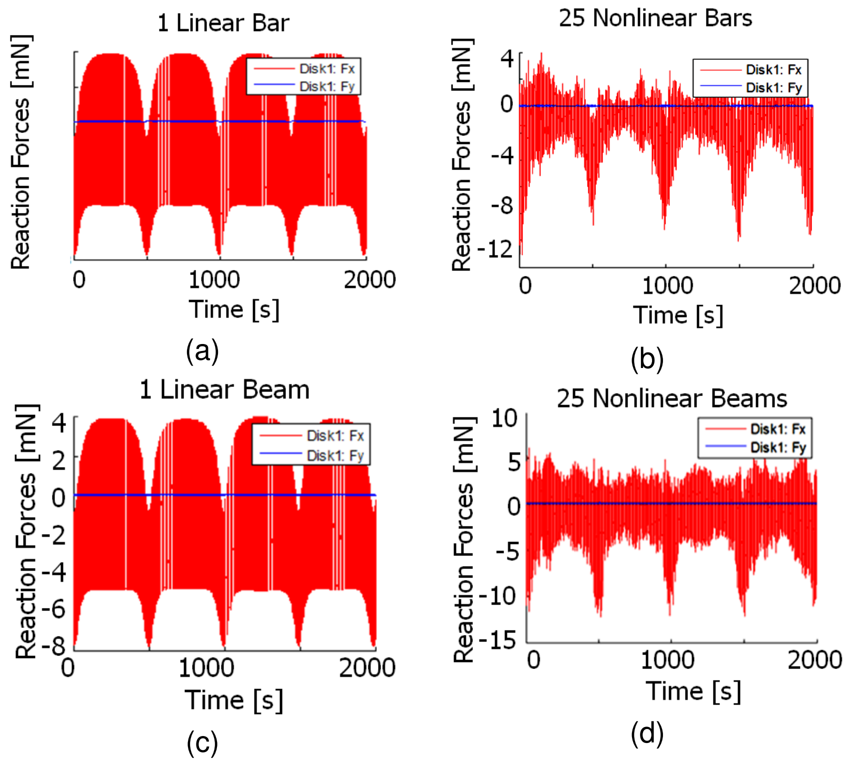

Figure 3.6: *Forces at the tether attachment point for linear and nonlinear bar and beam models.*

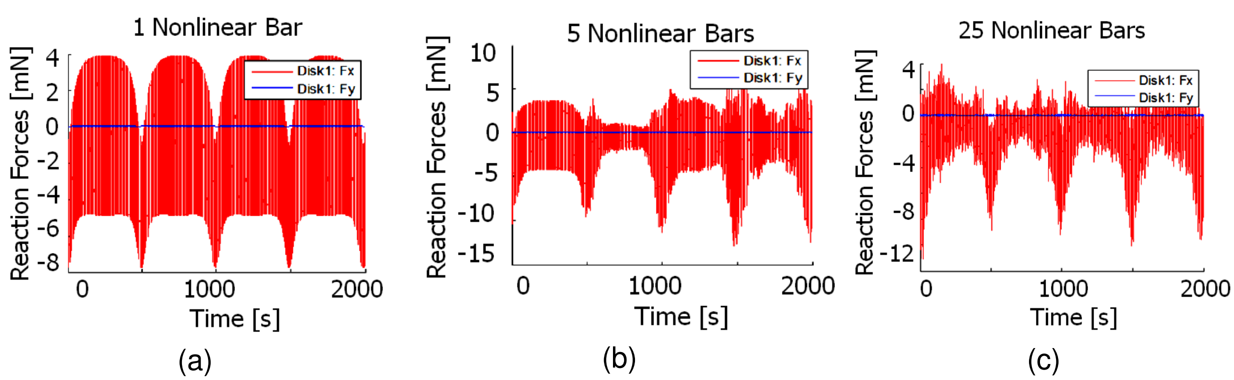

Figure 3.7: *Mesh refinement study for nonlinear bar model - Reaction forces at attachment point over time.*

phenomena. Nonlinear bar and beam models yield similar results. As the beam model, which also accounts for axial deformation, features an overall greater accuracy, we model the tether by nonlinear beam elements in the following.

3.3.3 Mesh Refinement Study

To determine the number of nonlinear beam elements needed to predict accurately the motion of the spacecraft-tether system, a detailed mesh refinement study is performed. We consider the asymmetric and symmetric perturbations with an initial angular velocity of $30^o/min$ and simulate the response of the system for $500\ s$.

The displacements of the spacecraft center in x-direction and the rotation of the left spacecraft are shown in Figs. 3.8 and 3.9 for the asymmetric and symmetric perturbation scenarios, respectively. These figures compare simulations with $n = [1, 5, 25, 30, 40, 50, 100]$ tether elements. The simulations agree well for number of elements larger than 25. The results for both perturbation scenarios show that the simulations are well converged for 30 elements. Using more elements has little effect on the displacements.

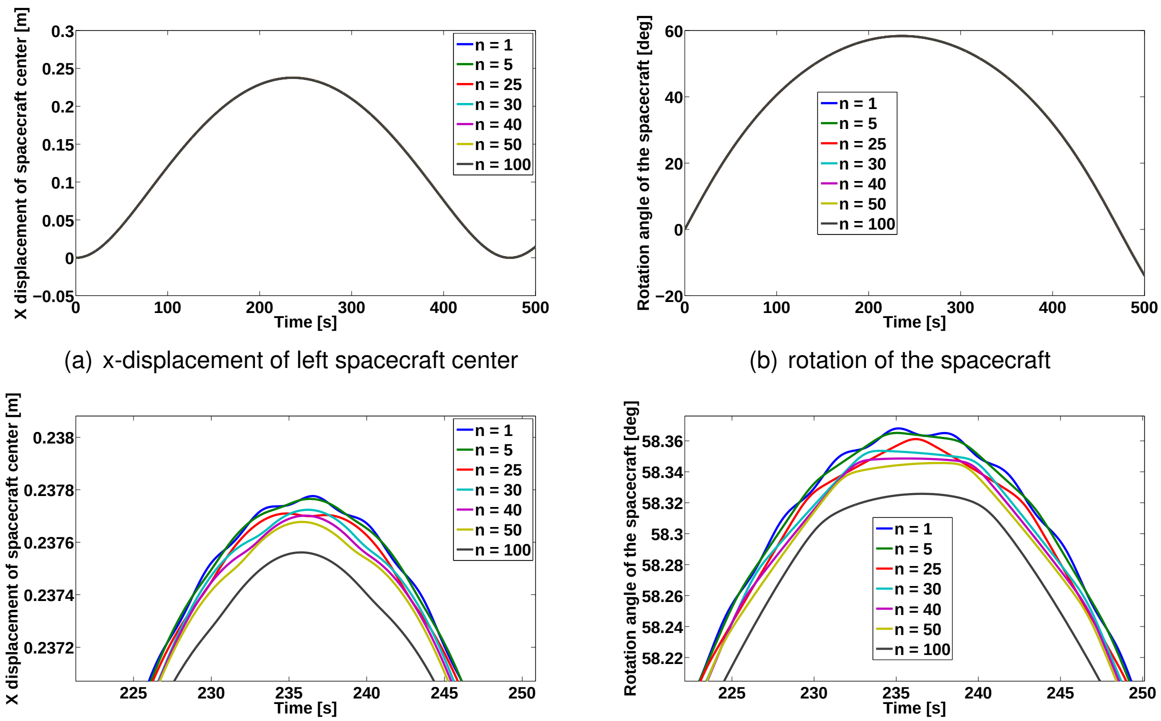

(a) x-displacement of left spacecraft center

(b) rotation of the spacecraft

(c) x-Displacement - magnified

(d) rotation - magnified

Figure 3.8: *Mesh Refinement for asymmetric perturbation.*

3.3.4 Accuracy of Spacecraft Models

In our numerical simulations we use two models to represent the spacecraft inertia. Here we demonstrate the equivalence of these spacecraft models and validate it with analytical results. We analyze two cases with forces and moments applied to the spacecraft respectively.

In the first case, we apply a moment M_z to the center node of the spokes-wheel model and the attachment node of the disk model, and observe the rotation of the spacecraft. Fig. 3.11a compares the rotation angle over time of the disk model, a quadrilateral spokes-wheel, an octagonal spokes-wheel, and the analytical solution. Relative errors with respect to the analytical solution are given in Table 3.2. The solutions of all numerical models agree well with the analytical solution. The errors of the spokes-wheel models are slightly larger than for the disk model and are caused by the oscillations in the spokes-wheel due to the finite stiffness of the beam elements.

In the second case, we apply a force in x-direction to the center node of the wheel and the tether attachment point of the disk, as shown in Fig. 3.10. As the attachment point and the center of the disk are both on the x-axis the force does not generate a moment about the z-axis. Fig. 3.11b shows the translation in x direction versus time of the disk model, a quadrilateral spokes-wheel, an

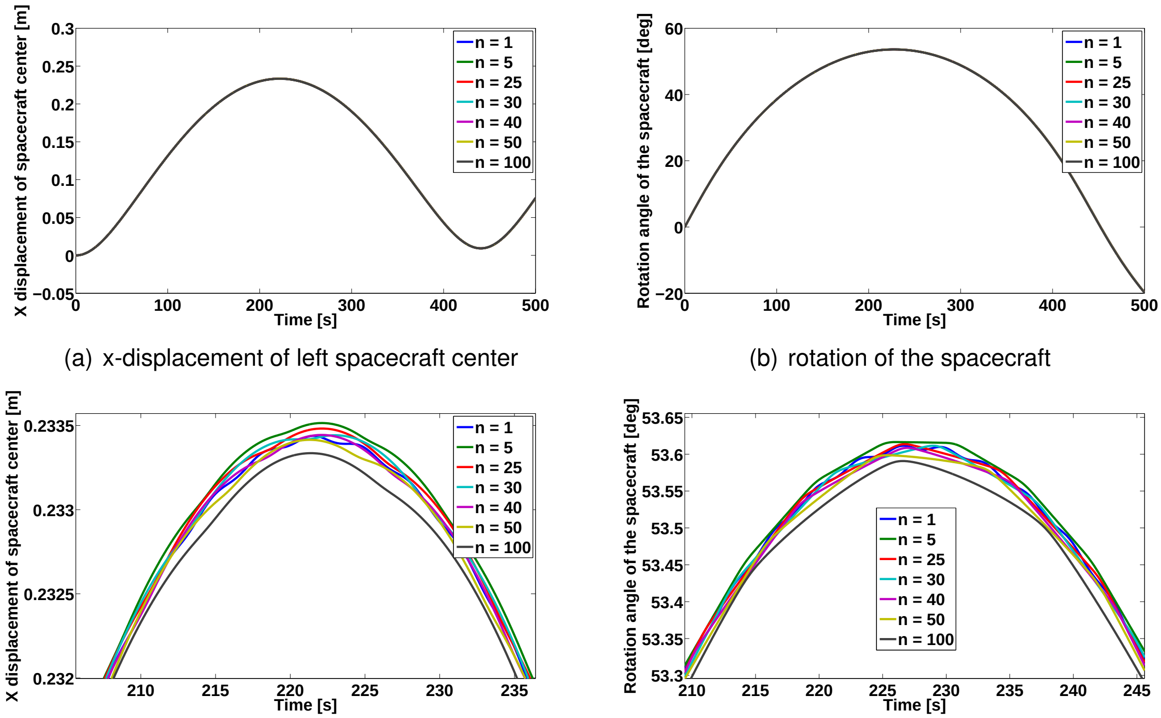

(a) x-displacement of left spacecraft center

(b) rotation of the spacecraft

(c) x-Displacement - magnified

(d) rotation - magnified

Figure 3.9: *Mesh Refinement for symmetric perturbation.*

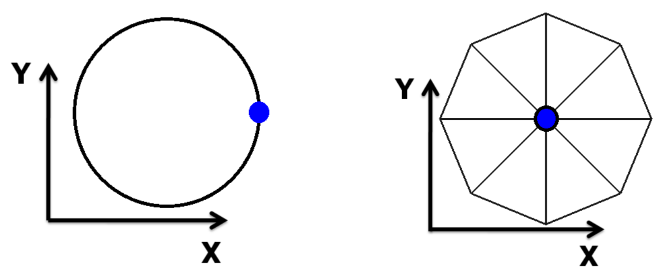

(a)

(b)

Figure 3.10: *Force and moment application points (blue) on disk and wheel models.*

Table 3.2: *Relative Errors for different models at time $t = 100\ s$.*

Model \ Motion	Rotation $\epsilon_{Relative}$	X-displacement $\epsilon_{Relative}$
Wheel 4	$1.4176 \cdot 10^{-2}$	$6.9780 \cdot 10^{-6}$
Wheel 8	$1.9836 \cdot 10^{-2}$	$6.9771 \cdot 10^{-6}$
Disk	$6.6326 \cdot 10^{-3}$	$6.6320 \cdot 10^{-3}$

octagonal spokes-wheel, and the analytical solution. Relative errors with respect to the analytical solution is given in Table 3.2. Again the numerical results are in good agreement with the analytical solution.

The above study suggests that both spacecraft models used in the present study are accurate.

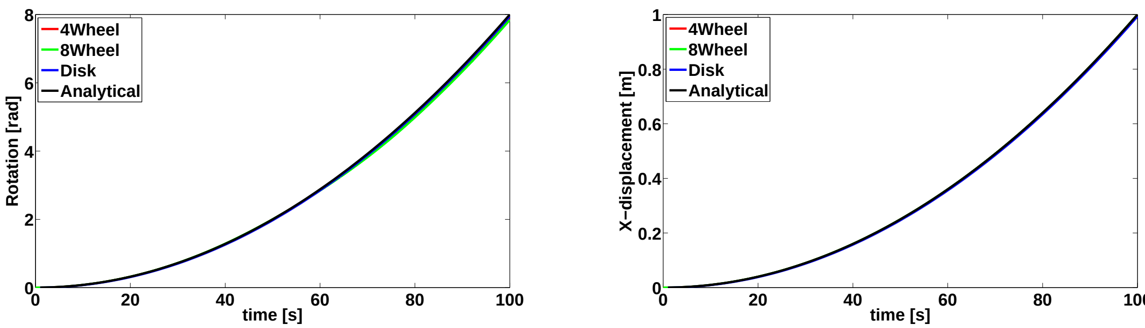

(a) Rotational Comparison (b) Translational Comparison

Figure 3.11: *Comparison between Analytical, Quadrilateral Wheel, Octagonal Wheel and Disk models.*

As the spokes-wheel model allows for configurations with multiple tethers this models is used in the following numerical studies.

3.4 Tether Material Consideration

3.4.1 Material Selection

The simulations results presented above are used to identify a class of materials suitable for the design of tethers. Although the expected force levels are small ($\leq 100mN$), high-strength materials are desirable as they allow for small tether cross-sections which aid in mitigating eigenstrain effects (see Section 3.7). A high material stiffness is beneficial to reduce the motion of the system. Properties of existing high-strength, high-stiffness materials, such as Spectra 1000, Zylon, and Magellan M5, are given in Table 3.3.

Table 3.3: *Candidate Materials*[56,57,58,59]

Material	Density ρ kg/m^3	Strength σ_u GPa	Young's Modulus E GPa
Magellan M5	1700	5.7	271
Zylon HM	1560	5.8	270
Spectra 1000	970	2.57	120
T1000G	1810	6.37	294
Kevlar 49	1440	3.6	120

Besides mechanical considerations effects of space environment on materials need to be accounted for. At low earth orbits, atomic oxygen (AO) reacts with most materials and protective coatings are needed to protect the tether against deterioration under AO exposure.[60] Ultra-violet light affects in particular polymers and may cause mass and strength loss as discussed in.[61,62] A study by[56] shows that, after being exposed to visible and UV light for 100 hours, Zylon fibers lost 35% of the fiber strength, while Magellan M5 fibers retained their original strength. Again protective coatings exist to reduce radiation effects. Materials may also experience significant changes in strength with exposure to high temperatures. It is shown in Reference 56 that after being exposed to 180 degrees Fahrenheit for 11 weeks, a 20 % loss in strength was observed in Zylon yarns, while Magellan M5 yarns retained their original strength.

The above studies render Magellan M5 a promising candidate material for TCS tethers. It combines good mechanical properties, such as high stiffness and strength, with high damage tolerance, low specific weight and good temperature resistance. Therefore the mechanical properties of Magellan M5 are used in the following studies. The properties of M5 listed in Table 3.4 are conservative estimates and are subject to change as the Magellan M5 is still in development.

Table 3.4: *Magellan M5 properties.*[56,57]

Density	1700 kg/m^3
Fracture strain	1.4 (%)
Tensile Modulus	271 GPa
Tensile Strength	5.7 GPa

For the studies on charged studies we assume that tethers made of Magellan M5 can be modified to be electrically conductive. Such modification exist, for example, for AmberStrand-Z-series fibers with nickel, copper, silver or gold plated Zylon.

3.4.2 Tether Dimensioning

Using Magellan M5 as candidate material for the tether design, we determine the cross-sectional area of the tether via the following procedure. For simplicity reasons, a uniform cross-section along the tether is used.

Neglecting bending stress the cross-sectional area is determined based on the maximum axial stress and the ultimate strength of the material:

$$A_T = n_{safety} \frac{F_{max}}{\sigma_u} \qquad \text{with} \quad n_{safety} = 4. \tag{3.21}$$

where F_{max} is the maximum axial force in the tether observed for asymmetric and symmetric perturbations with an initial angular velocity of $\omega = 40°/min$. The geometric parameters of the two spacecraft / single tether configuration and the spacecraft potential considered in the design study are given in Table 3.1. A safety factor of $n_{safety} = 4$ is used to account for the technology readiness level of Magellan M5.

Due to inertial effects, the forces in the tether implicitly depend on the cross-sectional area. Therefore, an iterative design process is used to determine the cross-sectional area. The design process converges to $A_T^\star = 5.2878 \cdot 10^{-12}\, m^2$. Assuming a circular cross-section, this corresponds to a diameter of about $2.6\mu m$.

As storing and deploying a tether with such a small cross-section may impose significant challenges, for the following studies we increase the cross-section by a factor of 100, i.e. $A_T = 5.29 \cdot 10^{-10} m^2$ and a diameter of about 26 μm. Furthermore, the increased tether cross-section amplifies potential issues due to eigenstrains and thus is a conservative choice.

3.5 Nominal Configuration

In the previous subsections, we have presented and verified models for analyzing the dynamics of a spacecraft-tether system. We have further identified candidate tether materials and dimensioned the tether cross-section. In the following, we study the behavior of spacecraft-tether systems.

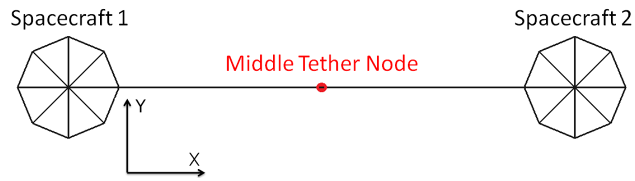

Figure 3.12: *Nominal TCS configuration for finite element tether response study.*

The geometric and material parameters of the nominal configuration for these studies are defined in Table 3.5. The tether is assumed to have a uniform circular cross-section and is discretized by 30 nonlinear beam elements. The tethers are uncharged. The spacecraft are models by an octagonal spokes-wheel model with 8 rim and 8 spoke nonlinear beam elements. The modulus of elasticity of the spokes-wheel is 100 that of the tether and the cross-sectional area of the rim and spokes elements is 10^4 times that of the tether. The system is initially at rest in static equilibrium. The motion of the spacecraft tether system is not constraint, i.e. no boundary conditions are imposed. Unless otherwise stated, this configuration is used for the following studies.

Table 3.5: *Geometric and material properties of nominal configuration.*

Spacecraft mass	$50\ kg$
Spacecraft radius	$0.5\ m$
Spacecraft Surface Potential	$30\ kV$
Distance between spacecraft centers	$5\ m$
Tether area	$5.29\ 10^{-10}\ m^2$
Tether density	$1700\ kg/m^3$
Tether modulus of elasticity	$271\ GP$
Initial angular velocity	$30°/min$

3.6 Influence of Spacecraft Potentials

The TCS concept fundamentally relies on the electrostatic force between the spacecraft to maintain shape and control the relative position of the spacecraft. The earlier chapter 2 discussed a nonlinear simulation model which uses spherical rigid nodes, and linear tether spring models with nonlinear end-point displacements. The benefit of this simulation is that parametric sweeps can be readily performed in much less time than it takes to perform a single FEM simulations (minutes versus multiple hours). However, any nonlinear tether deformations such as buckling and twisting cannot be modeled with such a simulation setup. Instead, the FEM approach is taken to study the complex tether dynamics in more detail in this chapter.

Here, we study the influence of the flexibility of the tether in dependence of the spacecraft potential. We predict the system response of the nominal configuration for the symmetric and asymmetric perturbation scenarios for $V_S = [0, 1, 10, 30, 50, 100]\ kV$ spacecraft potentials over $500\ s$. In Figs. 3.13 and 3.14 the horizontal displacements and rotation of the left spacecraft as well as the distance between the spacecraft centers and the vertical displacement of the tether center over time are shown. Note that the results for $0kV$ and $1kV$ coincide. Snapshots of the system motion at $t = 250s$ and $t = 500s$ are shown in given in Fig. 3.15.

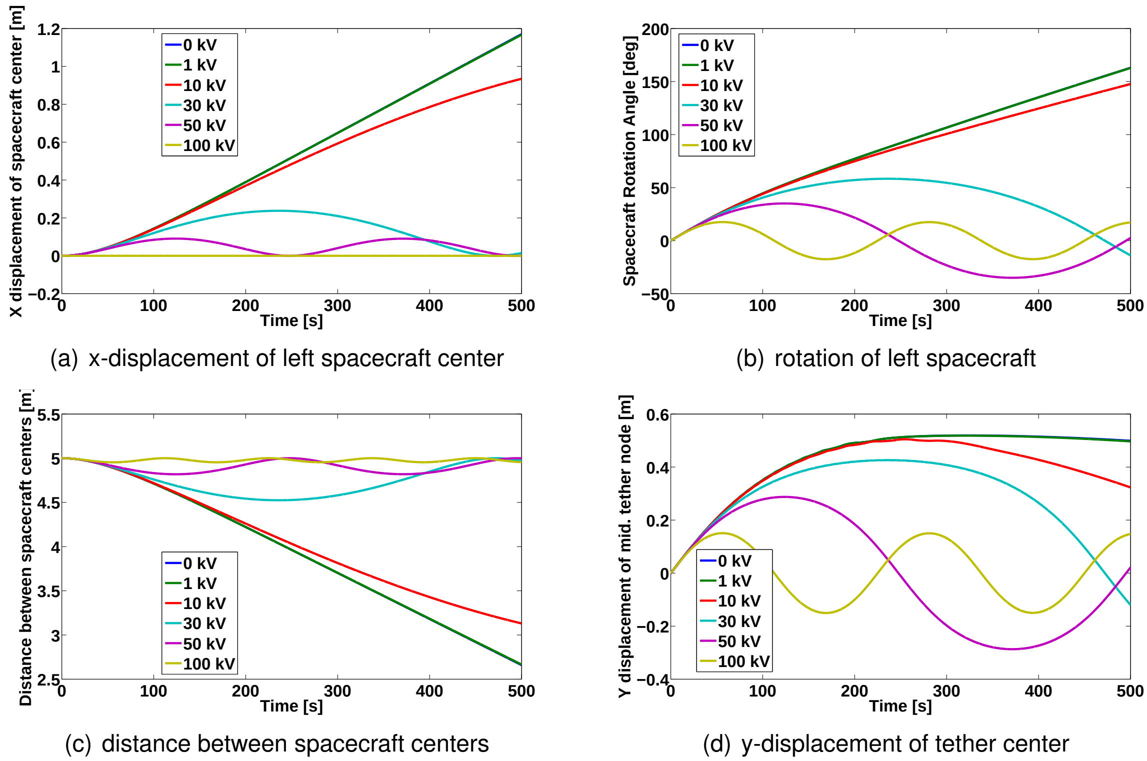

(a) x-displacement of left spacecraft center (b) rotation of left spacecraft

(c) distance between spacecraft centers (d) y-displacement of tether center

Figure 3.13: *Effects of spacecraft potentials on the system motion for asymmetric perturbation scenario.*

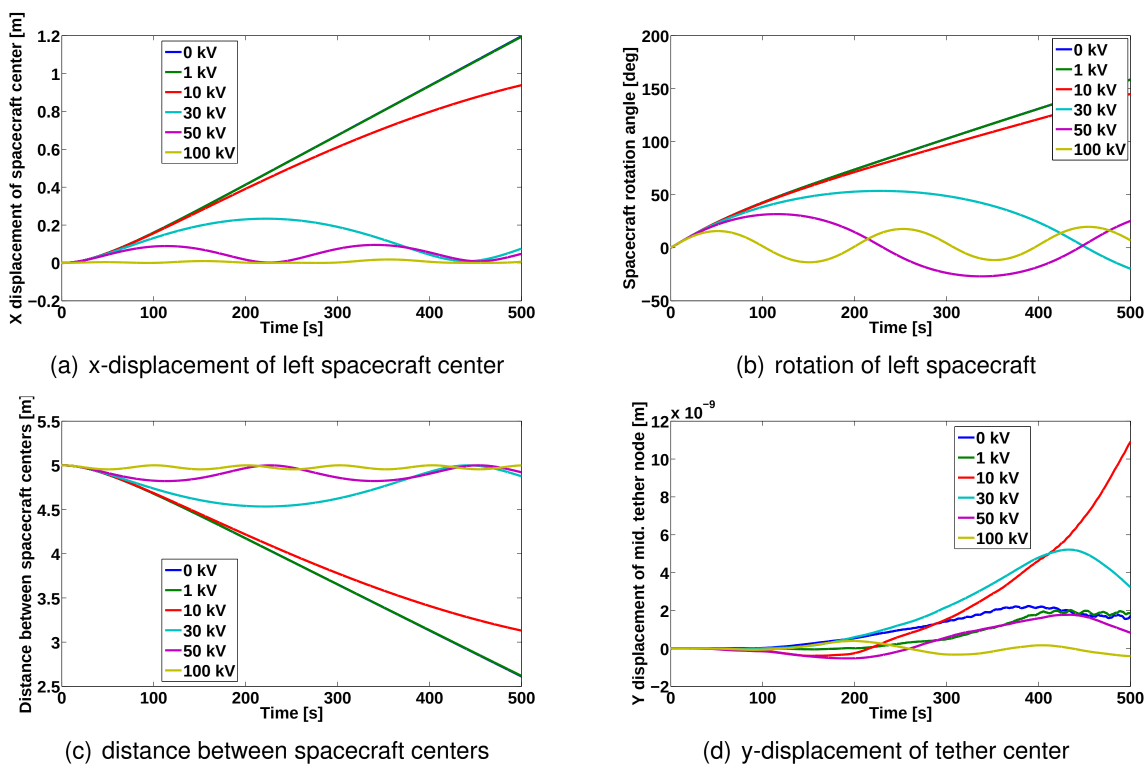

(a) x-displacement of left spacecraft center (b) rotation of left spacecraft

(c) distance between spacecraft centers (d) y-displacement of tether center

Figure 3.14: *Effects of spacecraft potentials on the system motion for symmetric perturbation scenario.*

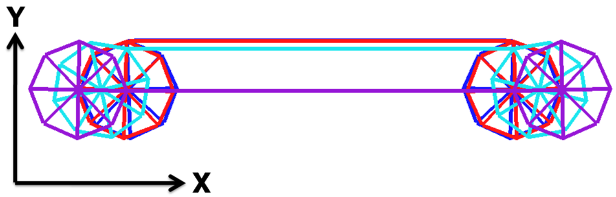

(a) $t = 250s$, asymmetric

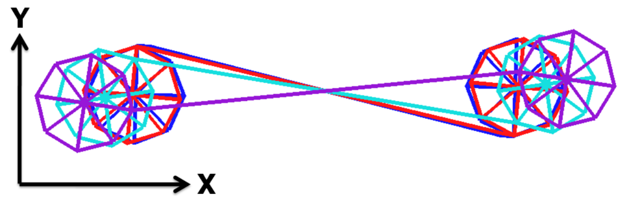

(b) $t = 250s$, symmetric

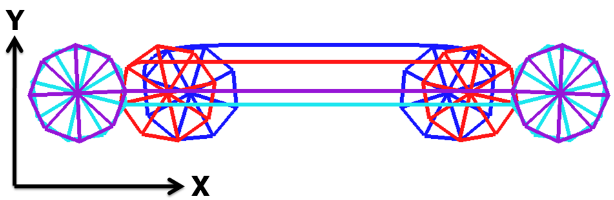

(c) $t = 500s$, asymmetric

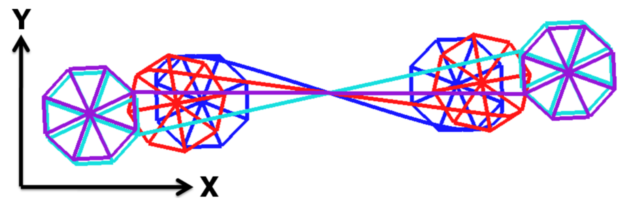

(d) $t = 500s$ symmetric

Figure 3.15: *Snapshots of spacecraft-tether motion for different spacecraft potentials:* $0kV$ *(blue),* $10kV$ *(red),* $30kV$ *(cyan), and* $50kV$ *(purple).*

The results suggest that for the perturbation scenarios considered the spacecraft undergo undesirable large displacements and rotations for spacecraft potentials below $30kV$. The snapshot plots show that for spacecraft potentials of $10kV$ and below the rotation of the spacecraft exceed 90^o and the tether would wrap around the spacecraft. Note that since contact is not modeled in our simulations, the tether passes through the spacecraft. A spacecraft potential of $30kV$ is sufficient to generate a low-amplitude oscillation about the static equilibrium. The amplitude decreases as the spacecraft potential is increased. This overall behaviors compare well with the earlier simulation results in chapter 2.

3.7 Influence of Eigenstrains

If the external forces on a slender structure are small, eigenstrain may have a significant effect on the dynamics of the structure. Space tethers have been observed to undergo large displacements and rotation due to eigenstrains.[52] However, unlike most other architectures the electrostatic forces between the spacecraft apply a tensile force to the tether which is expected to reduce the motion caused by the eigenstrains.

Here we study the effect of eigenstrains on the motion of the spacecraft-tether system. We employ the thermal strain analogy described in Section 3.2.5 to model eigenstrains. As the magnitude and distribution of the eigenstrain can only be approximated roughly, we consider a range of eigenstrain magnitudes. First we assume a uniform eigenstrain distribution. Bending moments due to eigenstrains increase with the radius of the circular cross-section of the tether, so do the tether stiffness and inertia. Thus the influence of eigenstrains on the system dynamics may be non-intuitive and we therefore perform a study of the spacecraft-tether dynamics for a range of tether cross-sections. Finally we impose a non-uniform eigenstrain distribution to gain insight into the effect of spatially varying eigenstrains on the system dynamics.

To obtain an initial estimate of the magnitude of eigenstrains that one may expect in a tether, we set the temperature difference between hot and cold faces to $250\ K$ (see[63]) and assume a thermal expansion of $\alpha_{thermal} = 6 \cdot 10^{-6}$ K^{-1}. This yields a differential eigenstrain of $\beta = 0.0015$. Note that this magnitude about 10 % of the fracture strain of Magellan M5 (see Table 3.4).

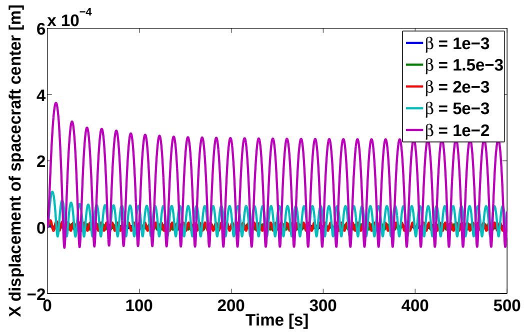

(a) x-displacement of left spacecraft center

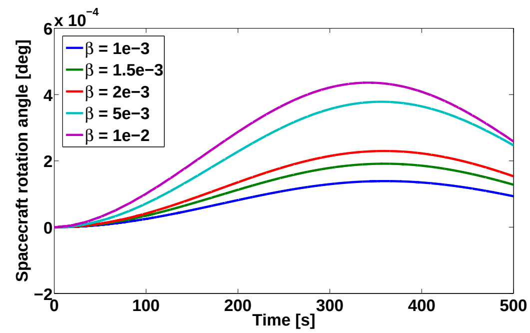

(b) rotation of left spacecraft

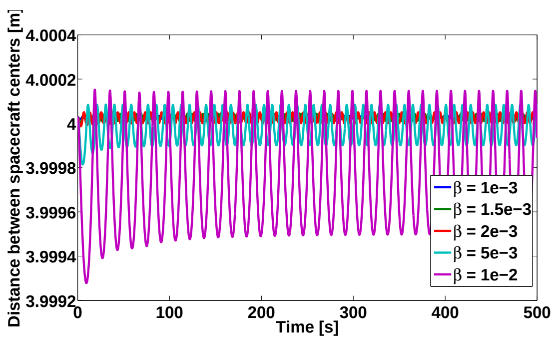

(c) distance between spacecraft centers

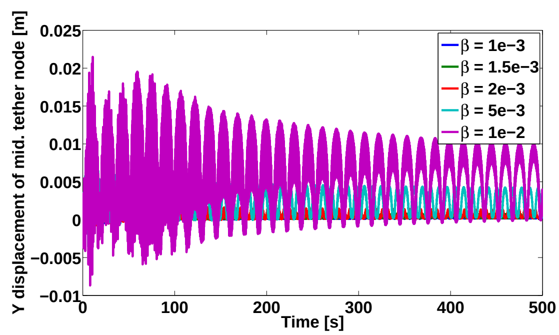

(d) y-displacement of tether center

Figure 3.16: *System response to uniformly distributed eigenstrains.*

3.7.1 Variation of Eigenstrain Magnitude

As the eigenstrain model is based on several assumptions we consider a range of values: $\beta = [0.001, 0.0015, 0.002, 0.005, 0.01]$. Note the maximum value is about 70 % of the fracture strain and can be considered a conservative estimate.

In order to study the effect of eigenstrains on the system dynamics, we analyze the system response for the range of eigenstrain values specified above assuming a uniform eigenstrain distribution. Starting from a spacecraft-tether system at static equilibrium we impose the bending moments generated by the eigenstrains at time $t = 0$ and observe the system response for $500\ s$.

Figure 3.16 shows the effects of different residual strains on the system. The system oscillates as the electrostatic forces between the spacecraft counteract the bending moments due to eigenstrains. The graphs show that even for the largest eigenstrain considered the overall motion is rather small: the maximum x-displacement of the spacecraft is $3.8 \cdot 10^{-4}\ m$ meters, the maximum y-displacement of the tether center is $2.2 \cdot 10^{-2}\ m$, and the maximum rotation of the spacecraft is $4.2 \cdot 10^{-4\ o}$. Thus the simulation results suggest that the effects of residuals strains can be ignored for the given configuration.

3.7.2 Variation of Tether Cross-Sectional Area

The bending moments caused by eigenstrains depend strongly on the tether cross-sectional area. Therefore we perform simulations with the maximum strain value of $\beta = 0.01$ for a range of tether cross-sectional areas: $A_T = [5.6 \cdot 10^{-7}, 5.6 \cdot 10^{-8}, 5.6 \cdot 10^{-9}, 5.6 \cdot 10^{-10}, 5.29 \cdot 10^{-10}]m^2$. The simulation results are given in Fig. 3.17. As the tether area increases, the eigenstrains generate larger moments, which cause larger displacements in the system. Eventually, the electrostatic force between the spacecraft is insufficient to counteract the bending moments and the system undergoes a large, non-oscillatory motion.

Figures 3.17a and b show that tether cross-sectional areas of $A = 5.6 \cdot 10^{-8} m^2$ and larger cause severe displacements and rotations. Figure 3.17e illustrates that in these cases the distance between the spacecraft falls below $1\ m$, i.e. the spacecraft collide. Reducing the cross-sectional area to $A = 5.6 \cdot 10^{-9} m^2$ and lower leads to acceptable displacement and rotations levels (see Figs. 3.17c and d).

These results illustrate the strong influence of the tether cross-sectional area on the dynamics of the system in the presence of eigenstrains.

3.7.3 Non-Uniform Eigenstrains

In the above studies on eigenstrains we assumed a uniform eigenstrain distribution. In the absence of measurements on the eigenstrain distribution in space tethers, we study the influence of non-uniform eigenstrain distributions on the tether dynamics by assuming that eigenstrains are present only in the center section of the tethers. We consider two cases with the length of the center section being $L_c = [0.66, 0.80]\ L_T$ (see Fig. 3.18). Within the center section the eigenstrain is assumed to be uniform. Using the thermal strain analogy, the eigenstrain distributions generate bending moments that act at a distance of $[0.17, 0.10]$ from the tether end points. Note that the magnitude of the bending moment does not change in comparison to eigenstrains are present along the entire tether.

For a cross-sectional area of $A = 5.29\ 10^{-10}\ m^2$ we apply bending moments for two eigenstrains magnitudes, $\beta = [0.01, 0.001]$, and observe the system response over $500\ s$, starting from system at static equilibrium. The results are shown in Fig. 3.19 for $L_c = [0.66, 0.80]\ L_T$. Note that the results for $\beta = 0.001$ coincide in sub-figures (a), (c) and (d).

The responses for the non-uniform eigenstrain distributions are comparable to the ones obtained for the uniform case and suggest that also the effect of eigenstrains on the nominal configuration are negligible, independent of their spatial distribution.

3.8 Tether Charging

The TCS architecture allows for using electrically conductive and non-conductive tethers. In the studies presented above we considered only uncharged tethers and electrostatic forces acting between the spacecraft. If the tether is charged electrostatic forces are acting also between the spacecraft and tether as well as between points on the tether.

Here we study the dynamics of the nominal configuration assuming that the tether is electrically conductive and at the same potential as the spacecraft. First we analyze the response of the system due to initial perturbations. Then we study the influence of tether charging in the presence of eigenstrains.

3.8.1 Influence on Nominal Configuration:

In Fig. 3.20 we compare the system response due to initial perturbations for a charged and uncharged tether. The results show that tether charging decreases the motion of the spacecraft. However, the systems response is less smooth and the spacecraft are subject to larger accelerations if the tether is charged. Note the kinks in the time evolution of the displacements. Moreover, Fig. 3.20d shows that tether charging increases the displacement of the middle tether node.

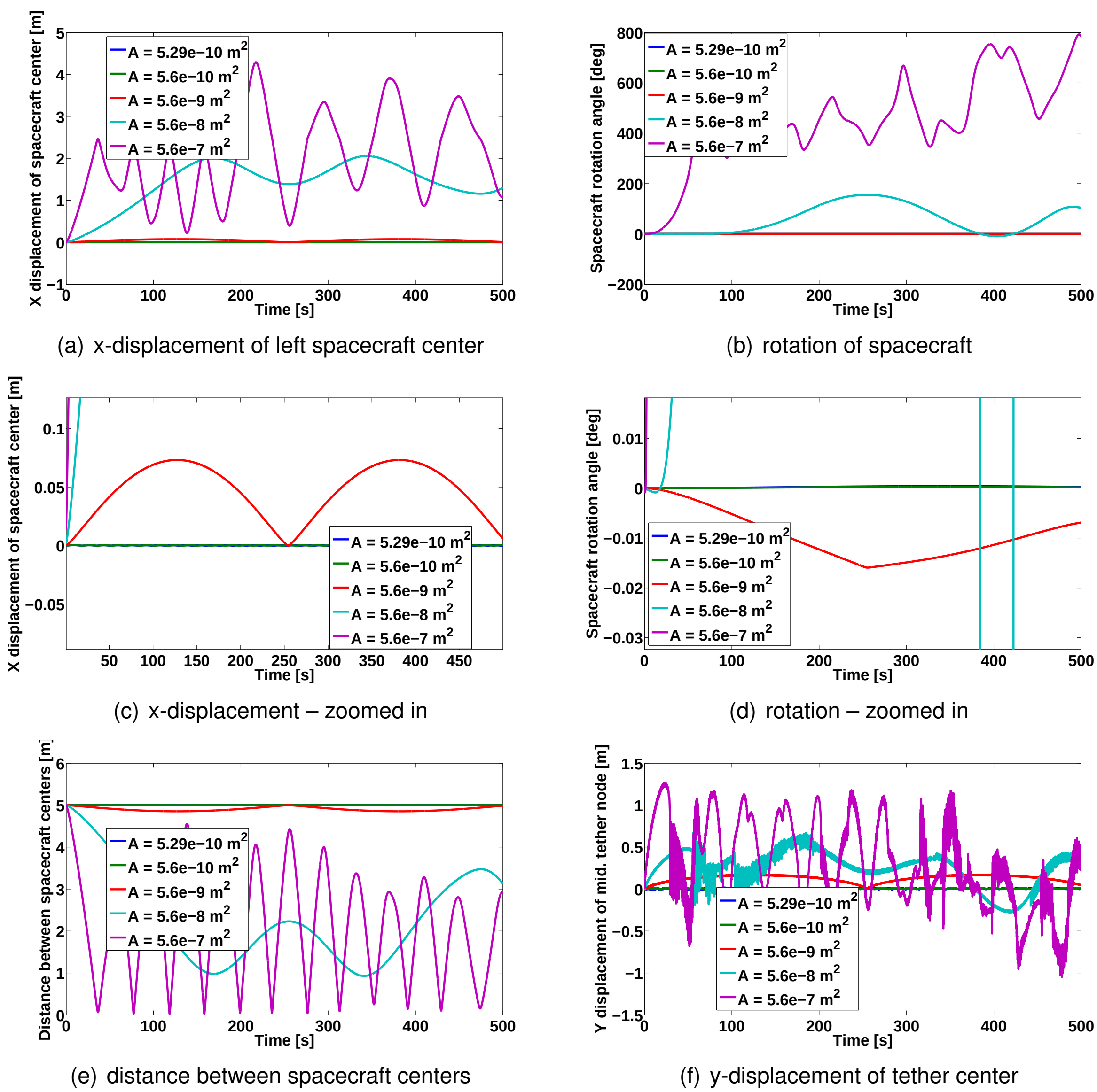

(a) x-displacement of left spacecraft center

(b) rotation of spacecraft

(c) x-displacement – zoomed in

(d) rotation – zoomed in

(e) distance between spacecraft centers

(f) y-displacement of tether center

Figure 3.17: *System response to non-uniform residual strains.*

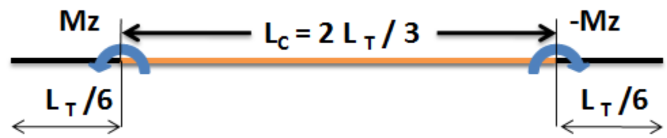

(a)

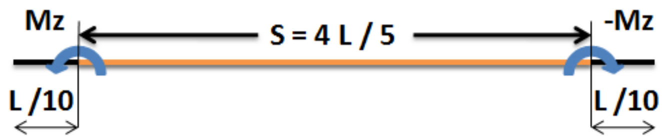

(b)

Figure 3.18: *Non-uniform eigenstrains. a)* L_c *= 0.66* L_T *. b)* L_c *= 0.80* L_T

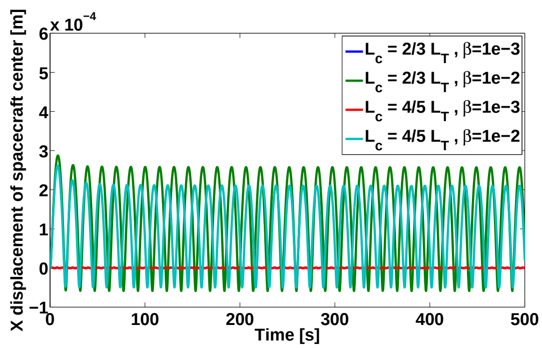

(a) x-displacement of left spacecraft center

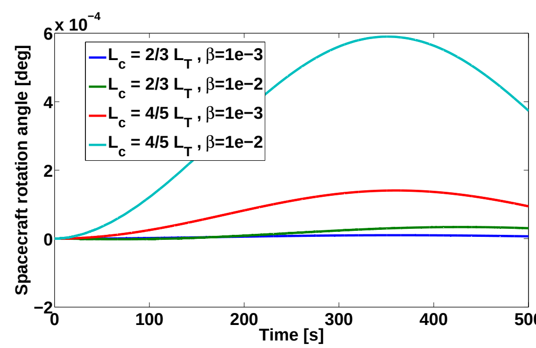

(b) rotation of spacecraft

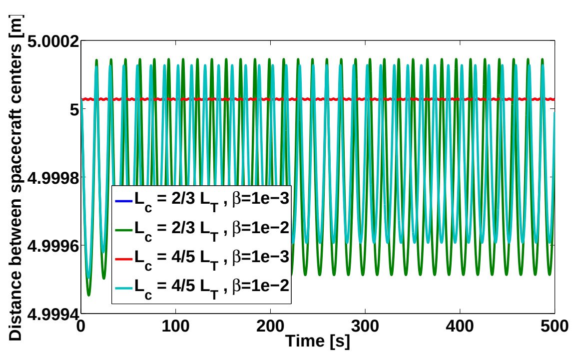

(c) distance between spacecraft centers

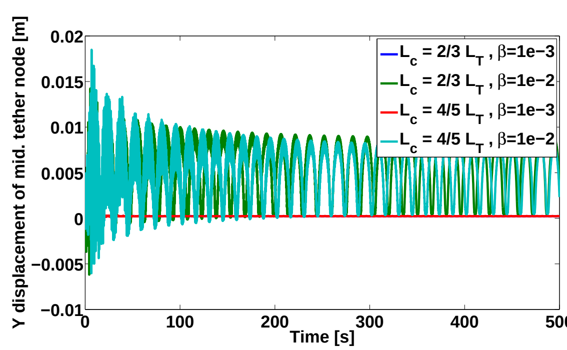

(d) y-displacement of tether center

Figure 3.19: *System response to non-uniform residual strains.*

These effects are due to the nonlinearity of the electrostatic force model whose impact on the system dynamics is stronger when considering electrostatic forces between spacecraft and tether and between points along the tether.

To illustrate the transient response of the system, snapshots of the system are shown in Fig. 3.21. The series of snapshots in Fig. 3.21a show a snap-through-type motion.

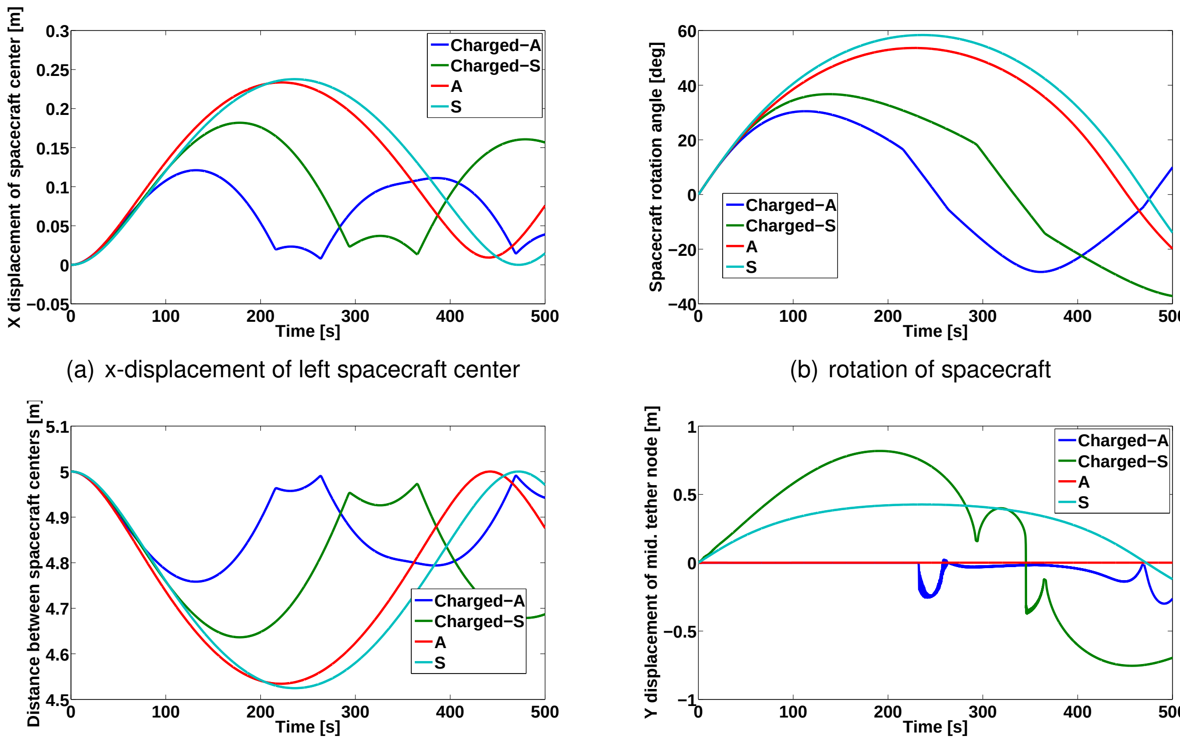

(a) x-displacement of left spacecraft center (b) rotation of spacecraft

(c) distance between spacecraft centers (d) y-displacement of tether center

Figure 3.20: *System response to asymmetric and symmetric perturbations for uncharged and charged tether.*

3.8.2 Tether Charging in the Presence of Eigenstrains

The previous study has shown that tether charging reduces the spacecraft motion and, thus, may aid in counteracting the influence of eigenstrains. Here we investigate the combined effects of tether charging and eigenstrains. Considering a uniform eigenstrain of $\beta = 0.01$, we compute the system responses for a charged tether with $V_T = V_S = 10, 30, 50, 100]\ kV$ potentials, and compare these results again the nominal configuration with an uncharged tether. The results are given in Fig. 3.22. For the same potential tether charging reduces slightly the motion of the tether in comparison to the uncharged tether.

Due to simplified electrostatic force model these results on tether charging should be used only in a qualitative fashion. A higher-fidelity force model is needed to more accurately predict the influence of tether charging on the spacecraft-tether dynamics in the presence of perturbations and eigenstrains.

3.9 Conclusions

In this Section we have used a high-fidelity finite element model to study the transient response of a two-spacecraft / single tether system. We have identified models to adequately describe large displacements and rotations of spacecraft and tether and to approximate electrostatic forcing between the components of the overall system. Comparing the simulation results of this section with the results presented in Section 2 suggests that inertia and bending stiffness of the tether play a minor role for the overall motion of the spacecraft-tether system. However, eigenstrains due

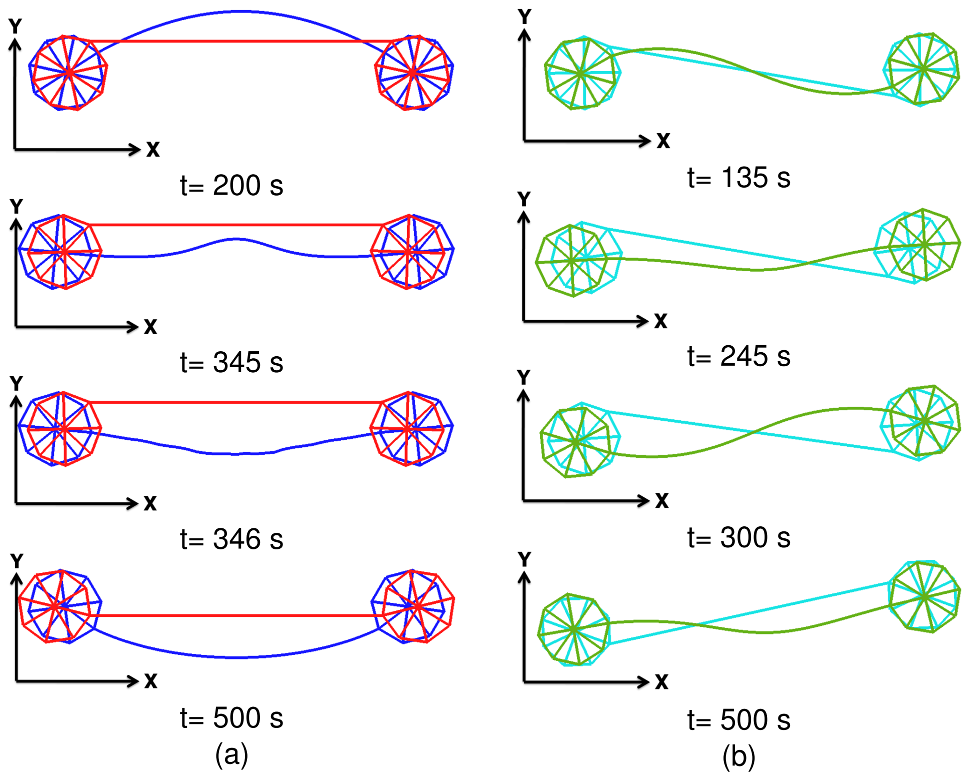

Figure 3.21: *Snapshots of system motion with charged and uncharged tethers: (a) asymmetric perturbation – uncharged tether (red) and charged tether (blue) at* $t = 135s$ *(top) and* $t = 245s, 300s, 500s$ *(bottom), and (b) symmetric perturbation – uncharged tether (cyan) and charged tether (green) at* $t = 200s$ *(top) and* $t = 345s, 346s, 500s$ *(bottom).*

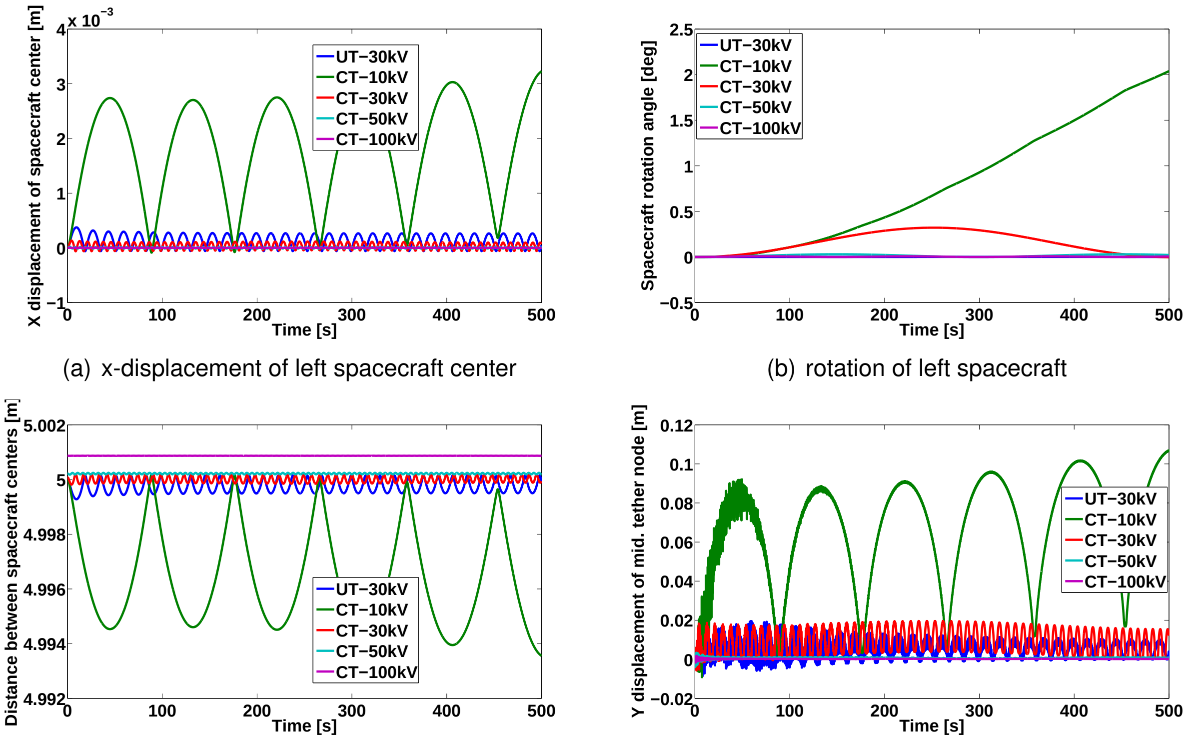

(a) x-displacement of left spacecraft center

(b) rotation of left spacecraft

(c) distance between spacecraft centers

(d) y-displacement of tether center

Figure 3.22: *System Response for combined tether charging and eigenstrain effects. UT – Uncharged Tether with Charged Spacecraft; CT – Charged tether with Charged Spacecraft.*

to fabrication, storage, and environmental effects, such as partial heating, radiation, may lead to large undesirable displacements and rotations. Our study suggests that the electrostatic forces between the spacecraft and the tether can mitigate eigenstrain effects if a sufficiently small tether diameter and the sufficiently large potential are chosen.

In regards of material selection, the above numerical studies suggest that high-performance fibers should be used for the tether. While the forces in the tether are small, eigenstrain issues require using tethers with smaller cross-sectional areas which, in turn, requires a larger strength of the tether material. Furthermore, electrically conducting, charged tethers aid in mitigating large displacements.

While the models for spacecraft and tether are sufficient to accurately capture the motion of the spacecraft-tether system in two-dimensions, further studies are needed to study three-dimensional phenomena. The simple lumped Coulomb model used to approximate the electrostatic forces between different components relies on several assumptions, such as displacement-independent, uniform charge distribution. Higher-fidelity models are needed to predict more accurately electrostatic force effects. The above study indicates that eigenstrains may play an important role in the motion of the overall system. Refined eigenstrain models need to be developed.

Chapter 4

Space Environment Impact

The space environment that the tethered Coulomb spacecraft will operate in is a highly variable plasma. This plasma plays two key effects on the functionality of the TCS nodes. Firstly, the plasma directly interacts with the nodes inducing natural spacecraft charging that can either hinder or aid the desired charge levels required to maintain TCS tether tensions and resistance to deformation. The second environmental impact is the partial charge shielding of the repulsive Coulomb forces from the local plasma.

In this chapter the space environmental parameters and impact on TCS operations are explored. This includes characterization of the plasma at Geosynchronous Earth Orbit (GEO), an envisioned application altitude, and modeling of the current interaction with the nodes. Also studied is the extent of Coulomb force partial shielding as well as the additional effects of over-lapping charge sheaths. These effects are then extended to analyze the electrostatic zones of influence and the impact on rotational stiffness. Finally, an investigation into the required power and fuel estimates to maintain the required charges in a plasma environment are performed.

4.1 Space Weather Parameters

The GEO plasma environment will affect the functionality of the charged nodes of a TCS system. The intent here is to characterize the GEO plasma environment. The free-flying charged particles of the plasma impact the nodes and result in a net current flow as illustrated in Figure 4.1. This current flow leads to natural spacecraft charging. The extent of charging is dependent on the plasma temperature, density, and the spacecraft potential and material properties.

A spacecraft, such as a TCS node, operating at GEO will experience a highly dynamic plasma environment. The local GEO magnetosphere is typically dense and hot, but can undergo quiet periods or experience rapid fluctuations where it is flooded with high energy particles (mean values as high as a few tens of keV).[64] The local plasma conditions are heavily dependent on the local time as well as the geomagnetic levels which are driven by solar activity. The highest levels of natural charging occur during eclipse and between the local hours of midnight through 6 am.[65] However, at GEO the TCS nodes may only be in eclipse for up to minutes at a time during an orbit and a charge control device can overcome these naturally occurring charge scenarios.

4.1.1 Debye Length

The attraction of oppositely charged particles to a charged spacecraft node results in a net shielding effect that screens the apparent potential of the spacecraft. A measure of this electric field

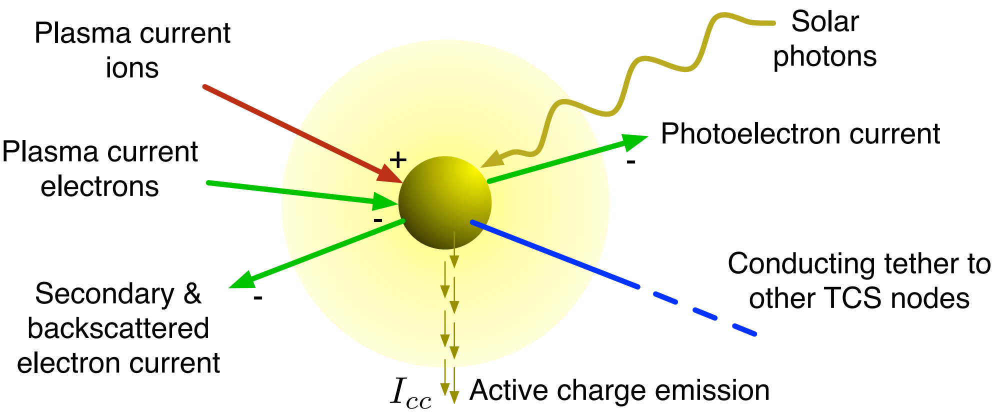

Figure 4.1: *Illustration of spacecraft/plasma environmental current interactions*

reduction, and consequently local plasma environment activity, is the Debye length (λ_D). For the plasma conditions analyzed here it is assumed that there is a equal density of electrons and protons (H^+), a good assumption at GEO.

The Debye length is calculated with the single-Maxwellian densities of the plasma electrons and singly ionized species (n_e & n_i [m^{-3}]), as well as their respective temperatures (T_e & T_i [K]), using the general expression:[66]

$$\lambda_D = \sqrt{\frac{\frac{\epsilon_0 \kappa}{e_c^2}}{\frac{n_e}{T_e} + \sum_i \frac{n_i}{T_i}}} \tag{4.1}$$

where $\epsilon_0 = 8.854187817 \times 10^{-12}$ [C^{2}N^{-1}m^{-2}] is the permittivity of vacuum, $\kappa = 1.38065 \times 10^{-23}$ [JK^{-1}] is the Boltzmann constant, and $e_c = 1.602176 \times 10^{-19}$ [C] is the elementary charge. Due to the large mass of ions in comparison to electrons, their acceleration is significantly less in the presence of a charged object. For this reason it is common to neglect the influence of ions species altogether and have a Debye length that is purely a function of the local plasma electrons, which is used in this study:

$$\lambda_D = \sqrt{\frac{\epsilon_0 \kappa T_e}{n e_c^2}} \tag{4.2}$$

4.1.2 Representative GEO Plasma Environment

Three representative plasma conditions will be used for this TCS analysis (quiet, nominal, and disturbed). These three plasma conditions define the extreme bounds and nominal operating regimes TCS spacecraft will encounter on-orbit. The single-Maxwellian parameters used to describe each of these GEO plasmas along with the corresponding Debye lengths (λ_D) are shown in Table 4.1. These values are based on models and data interpreted from measurements obtained on-orbit from the SCATHA and ATS-6 spacecraft during the 1970-80s.[65,67,68,69,70]

The nominal plasma conditions represent the typical operating environment for the TCS system. The disturbed plasma conditions corresponds to injections of low density, highly energetic particles. The quiet plasma (λ_D = 4 m) coincides to a cold and dense plasma that can occur during times of low solar activity when the Earths magnetosphere expands raising the outer plasmasphere to synchronous altitudes.[37] The resulting drastic temperature reductions can significantly decrease the Debye length to multiple meters at times as illustrated in Figure 1.9.

Table 4.1: *GEO Representative Single-Maxwellian Plasma Parameters and Debye Lengths*

Conditions	T_e [keV]	n_e [cm^{-3}]	T_i [keV]	n_i [cm^{-3}]	λ_D [m]
Quiet	0.003	10	0.003	10	**4**
Nominal	0.9	1.25	0.9	1.25	**200**
Disturbed	10	1	10	1	**743**

These rare, quiet plasma bound the 'worst-case' conditions the TCS will encounter at GEO. The quiet plasma conditions result in the maximum net plasma currents and consequently high natural charging events. In order to maintain a charged spacecraft node in this plasma will require the highest charge control current and electrical power. This quiet plasma also corresponds to the most detrimental Coulomb force shielding for TCS applications.

4.2 Debye Shielded Force Evaluation

This section describes the physics of the interaction between the geosynchronous orbit plasma environment, the magnetosphere, and a charge-conducting sphere. If the spherical TCS node potential is small compared to the local plasma temperature, than the Debye charge shielding can be modeled through an exponentially decaying function as shown in Eq. (2.4). At GEO this condition is exceeded with kilo-Volt levels of potentials, depending on the plasma temperature and density properties. Of interest to this study is how the electrostatic shielding changes if the potentials exceed this simplifying analytical assumption. To study this, the force computation focuses on an elemental 2-node interaction. These results are incorporated into the force computations of the nonlinear TCS simulation.

The symmetric potentials around a sphere satisfy Poissons equation in 1-D:

$$\frac{1}{R^2}\frac{\partial}{\partial R}R^2\frac{\partial}{\partial R}V = -\frac{Ne_c}{\epsilon_0} \tag{4.3}$$

where the net number density, N, is the difference between the ion and electron densities:

$$N = n_i - n_e \tag{4.4}$$

For simplicity in all the equations, we assume that plasma ions are singly charged. This is a good approximation in the GEO magnetosphere, where most of the ions are H^+. In order to write Poisson's equation in a non-dimensional form, the following definitions are required:

$$\begin{aligned}
\zeta &= \frac{R}{\rho} \\
\phi &= \frac{V}{T_e} \\
n &= \frac{N}{N_\infty} \\
\gamma &= \left(\frac{\rho}{\lambda_D}\right)^2
\end{aligned} \tag{4.5}$$

Where N_∞ is the electron density at infinity under no influence of foreign charges. Using these definitions, the non-dimensionalized Poisson equation is as follows:

$$\frac{1}{\zeta^2}\frac{\partial}{\partial\zeta}\zeta^2\frac{\partial}{\partial\zeta}\phi = -\gamma n \tag{4.6}$$

This non-dimensional Poisson's equation in Equation (4.6) is in general used to analyze both the range of potentials and electric fields, and also to calculate the currents collected by a sphere. To find the potentials it is necessary to solve Poissons equation along with the collision-less Vlasov equation for ions and electrons, shown in Equation (4.7), over the range of plasma parameters found in the GEO magnetosphere.

$$\mathbf{v}\cdot\nabla_x f - q\mathbf{E}\cdot\nabla_v f = 0 \tag{4.7}$$

where the distribution function depends on both position and velocity:

$$\begin{aligned} f &= f\left(\mathbf{x},\mathbf{v}\right) \\ \nabla_x &= \left(\frac{\partial}{\partial x},\frac{\partial}{\partial y},\frac{\partial}{\partial z}\right) \\ \nabla_v &= \left(\frac{\partial}{\partial v_x},\frac{\partial}{\partial v_y},\frac{\partial}{\partial v_z}\right) \end{aligned} \tag{4.8}$$

The particle densities are given by:

$$\begin{aligned} n_i\left(\mathbf{x}\right) &= \int f_i\left(\mathbf{x},\mathbf{v}\right)\mathrm{d}^3\mathbf{v} \\ n_e\left(\mathbf{x}\right) &= \int f_e\left(\mathbf{x},\mathbf{v}\right)\mathrm{d}^3\mathbf{v} \end{aligned} \tag{4.9}$$

The solution of the Poisson-Vlasov system of equations for the special case of a charged sphere in an isotropic Maxwellian plasma has been studied extensively and reported in literature.[71,72] In spherical symmetry, the distribution functions depend only on the radius, the kinetic energy, and angular momentum. As reported by Laframboise, the solution depends strongly on the ratio of the sphere size to the Debye length. When γ is much less than unity (large Debye lengths) the motion of charged particles is limited by the angular momentum, Orbit Motion Limited (OML). The OML limit provides an upper bound on the charge density surrounding and the current collected by a conducting sphere. For this study, a computer code was written that solves the Poisson-Vlasov equations in the OML limit. In the OML limit for a positively charged sphere collecting electrons, the charge densities of the electrons and ions species are respectively:

$$\begin{aligned} n_e &= \left(1-\frac{1}{2\zeta^2}\right)\left(e^{\phi}\left(1-\mathrm{erf}\left(\sqrt{\phi}\right)\right)+\frac{2}{\sqrt{\pi}}\sqrt{\phi}\right) \\ n_i &= \left(1-\frac{1}{2\zeta^2}\right)e^{-\phi} \end{aligned} \tag{4.10}$$

This computer code allows for the electrostatic forces to be computed for a range of plasma conditions and TCS node potentials. Compared to the earlier analytical results, a key aspect of this study is that the small node potential assumption is not required. Instead, the full, coupled nonlinear field equations about a sphere are solved subject to the plasma interactions. For the scope of this project, the complexity of the simulation runs is reduced by looking only at spherical

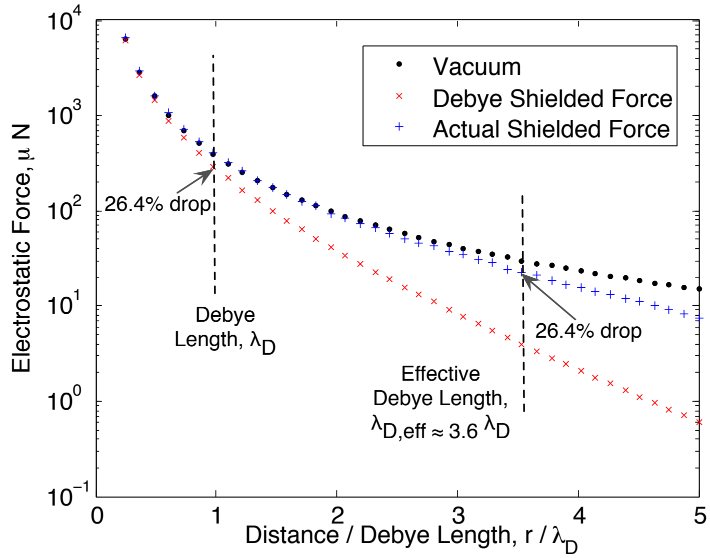

Figure 4.2: *Comparison of analytical and numerical predictions of electrostatic force experienced in a cold plasma at GEO due to a 0.5 m radius sphere, V = 30 kV, λ_D = 4.1 m*

bodies for which the field equation can be solve in a 1-D fashion. This is sufficient to provide an improved electrostatic force model for high TCS potentials to be used in the nonlinear TCS simulation. Potentials as a function of density are found by solving the dimensionless Poissons equation, Eq.(4.6), with the expressions in Eq.(4.10) for the dimensionless electron and ion densities. The ambient plasma densities and temperature in Eq.(4.6) enter through γ, the square of the sphere radius divided by the Debye length. The spheres in this study have diameters between 0.5 m and 1 m. For most magnetospheric conditions, the Debye length is much greater than the radius of the largest sphere. Only for a combination of the lowest plasma temperature and the highest plasma density, does the Debye length approach the sphere radius. For those cases, the calculations performed in this study are conservative; that is, they overestimate both the plasma shielding and the currents needed to maintain the potentials on the system.

4.2.1 Effective Debye Length

4.2.1.1 Effective Debye Length Modeling

The analytical solution to Poisson's equation is based upon the assumption that $(eV \ll \kappa T)$. This condition is quickly violated as craft potentials become large, especially in the cold plasma conditions of LEO. The full numerical solution of Poisson's equation yields electrostatic forces larger than predicted by Equation (2.5). Equation (2.5) therefore serves as a lower bound for the actual force that will be experienced in a plasma. The vacuum force model, which was given in Equation (2.1), is the largest amount of force that can be produced. The actual electrostatic force is close to the vacuum force values for a larger range of separation distances. The end result is an increased effective sphere of influence of an electrostatic object. These effects are illustrated in Figure 4.2 for cold GEO conditions. This figure also illustrates the concept of the effective Debye length, the length at which the numerical solution for the electrostatic force has been shielded to the amount of shielding analytically predicted at one Debye length. The effective Debye length, $\hat{\lambda}_D$, is defined

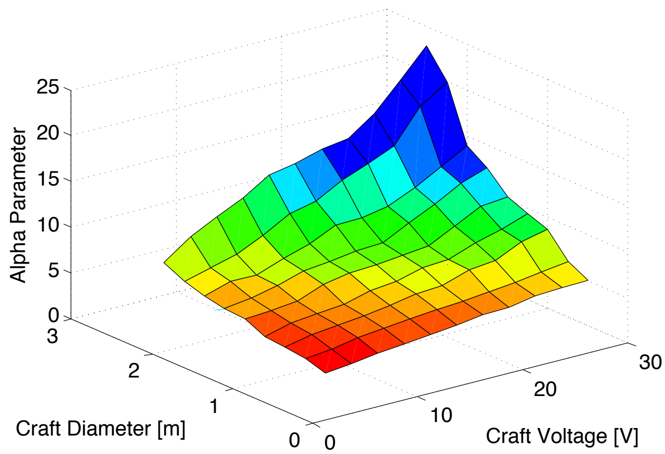

Figure 4.3: *Alpha parameter for effective Debye lengths in a plasma,* $\lambda_D = 4$

by a scaling parameter, α, as shown:

$$\hat{\lambda}_D = \alpha \lambda_D \tag{4.11}$$

An analytical relationship of the partial charge shielding is desirable for quick modeling of this phenomena. One approach is to model the nonlinear plasma force function using the effective Debye length through the relationship:

$$F = k_c \frac{q_1 q_2}{r^2} e^{-r/\hat{\lambda}_D} \left(1 + \frac{r}{\hat{\lambda}_D} + f_1(r, \rho, \hat{\lambda}_D)\right) \tag{4.12}$$

where the term f_1 is depends on the separation distance r, TCS node radius ρ, as well as the effective space plasma Debye length $\hat{\lambda}_D$. The later parameter is a scaled parameter which indicates the true influence range of a large potential in a plasma. Here $f_1 \to 0$ if the potentials are small.

Murdock et. al discuss the effective Debye length for the electrostatic astroid tug application in Reference 40. For their application of electrostatic astroid deflections, the effective Debye lengths can reach values 100 times greater than the Debye length. This result is especially useful for cold plasma conditions which can limit the feasibility of using electrostatics for tensioning a tethered Coulomb structure. Trends of the effective Debye length as a function of the plasma conditions, craft size, and craft voltage are discussed in the following subsections.

4.2.1.2 Effective Debye Length Trends

Factors that affect the effective Debye length include the plasma Debye length, craft radius, and the voltage level on craft. Numerical simulations were performed using ranges of each of these parameters to understand the trends. Curve fitting was used on the numerical solutions of electrostatic forces from charged craft to determine the approximate α parameter for each solution. Note that $\alpha(V, d, \lambda_D)$ is a function of three parameters, namely the voltage V, the TCS nodal diameter d, as well as the local space weather's actual Debye length λ_D. The following study will illustrate the α values by studying cross-sections of the three-dimensional parameter sub-space.

Figure 4.3 displays the variation of the α factor over a range of TCS node sizes and voltages. These important results will allow more realistic values to be used for partial charge shielding modeling in the numerical TCS simulations. Figure 4.3 clearly illustrates that larger craft radii and

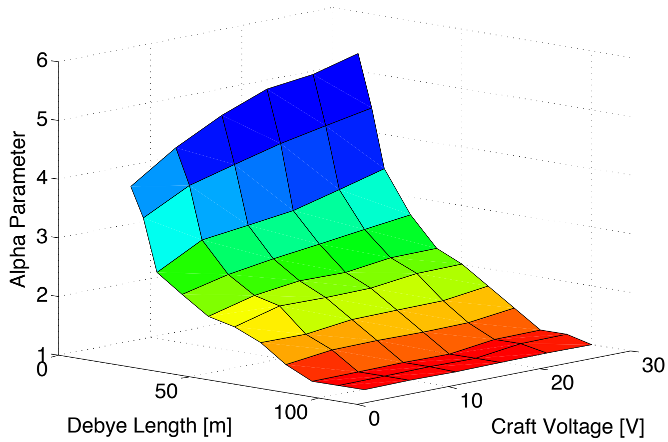

Figure 4.4: *Alpha parameter for effective Debye lengths in a plasma, 1m craft diameter*

higher potentials yield larger effective Debye lengths. The craft voltage trend occurs because as the assumption $(eV \ll \kappa T)$ is further violated, the shielding is reduced. There exist limitations on craft voltage due to power requirements and limitations of craft size due to launch constraints, but this study shows that electrostatic tensioning of a tethered structure is more effective with larger craft and higher potentials.

Figure 4.4 shows the variation of the effective shielding parameter as a function of Debye length and craft voltage for a sphere with a 1 m diameter. The extreme case of a cold GEO plasma Debye length near 10 m and a high craft voltage of 30 kV, the effective Debye length is more than 5 times the predicted Debye length. As the Debye length approaches the order of 100 m, the effective Debye length is nearly the analytically predicted Debye length, therefore α approaches a value of one. With a Debye length of 100 m, the Debye shielded force is nearly the same as the vacuum force at distances on the order of a few tens of meters. The effective Debye length, therefore, is approximately one Debye length. Interpolation of the data shown on these plots can be used to determine the effective Debye lengths for different combinations of craft voltage, Debye lengths, and craft sizes.

4.2.1.3 Linear Regression Analysis

Using data from numerical solutions of the Poisson-Vlasov equation, linear regression was used to find a parametric relationship between the effective Debye length alpha parameter and each input parameter: Debye length, craft voltage, and craft diameter. The coefficient of determination, $\mathcal{R}^2$, was used to measure the goodness of fit for each regression performed on the data. Due to large sensitivities in the Debye length, a logarithmic transformation was performed on this data for the fitting. The benefit of this transformation was clear in examining a linear fit to the raw data and the transformed data, which had $\mathcal{R}^2$ values of 0.562 and 0.916, respectively. Using the logarithm of the craft radius also improved the fit, but transforming the craft voltage data had a negligible effect on the goodness of fit.

To illustrate the effect of the logarithmic transformation on the data, plots are shown in Figure 4.5 for linear fits of the transformed data (represented by the white surface) versus raw data (shown by the colored surface). Figures 4.5(a) and 4.5(b) of the transformed data show a fit which is clearly a closer match to the data than the fit to the raw data shown in Figures 4.5(c) and 4.5(d).

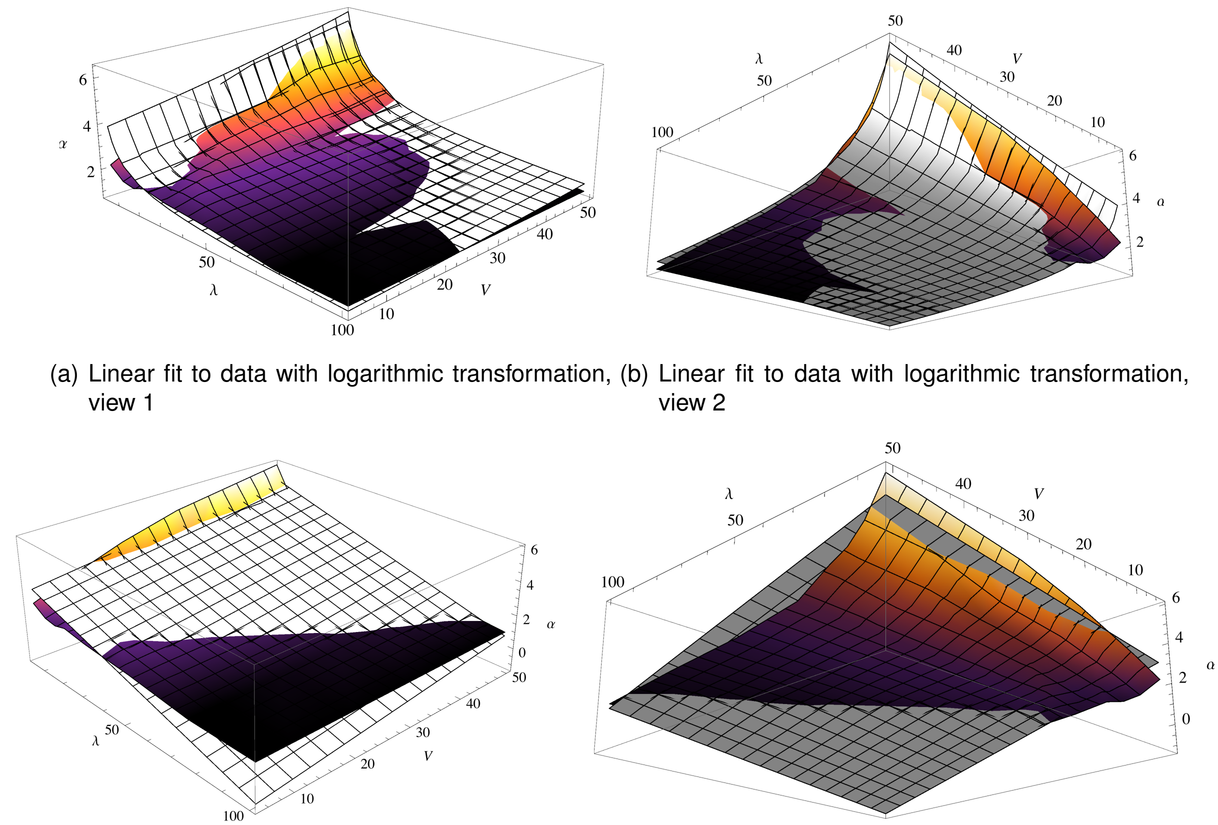

(a) Linear fit to data with logarithmic transformation, view 1 (b) Linear fit to data with logarithmic transformation, view 2

(c) Linear fit to data without logarithmic transformation, view 1 (d) Linear fit to data without logarithmic transformation, view 2

Figure 4.5: *Illustration of the effect of the logarithmic transformation alpha parameter data with a Craft Diameter of 0.5 m*

A cubic fit of the alpha parameter data is shown in Equation (4.14) as a function of Debye length, λ_D, craft voltage, V, and craft diameter, d. The $\mathcal{R}^2$ value of this fit is 0.968, which is very near the maximum value of 1, therefore this model was considered a satisfactory prediction of the alpha parameter for effective Debye lengths. For comparison, the $\mathcal{R}^2$ value for the linear, quadratic and cubic fit models are: 0.916, 0.947, and 0.968 respectively.

The following variables are defined for the parameters on which the logarithmic transformation was performed:

$$\begin{aligned} \bar{\lambda}_D &= \ln(\lambda_D) \\ \bar{d} &= \ln(d) \end{aligned} \tag{4.13}$$

Using these variables, the regression equation is as follows:

$$\begin{aligned} \alpha = \exp[&1.47 - 0.566\bar{\lambda}_D + 0.242\bar{\lambda}_D^{\,2} - 0.406\bar{\lambda}_D^{\,3} + 0.0987V - 0.0337\bar{\lambda}_D V \\ &+ 0.00283\bar{\lambda}_D^{\,2}V - 0.00102V^2 + 0.000202\bar{\lambda}_D V^2 + 2.90e^{-6}V^3 - 2.37e^{13}\bar{d} \\ &- 0.361\bar{\lambda}_D\bar{d} + 0.0538\bar{\lambda}_D^{\,2}\bar{d} - 0.00112V\bar{d} + 0.0000236V^2\bar{d} \\ &- 0.741\bar{d}^2 + 0.185\bar{\lambda}_D\bar{d}^2 + 0.00354V\bar{d}^2 + 4.94e^{13}\bar{d}^3] \end{aligned} \tag{4.14}$$

4.2.2 Illustration of Results of Effective Debye Length

To illustrate the results of the cubic parametric relationship of Equation (4.14), surface plots are shown in Figures 4.6, 4.7, and 4.8 for three fixed values of craft diameter: 0.5, 1.0, and 2.0 m. These plots display the alpha parameter data as a colored surface, with the fit model shown as a white mesh surface. In Figures 4.6 - 4.8, it can be seen that the model closely matches the behavior of the data.

4.2.3 Discussion of Effective Debye Length Results

These results are used for obtaining a more accurate value of the effective Debye length in a range of plasma conditions and craft scenarios. There are limitations in the applicability of the determined regression relationship due to the assumptions made. The numerical simulation assumes that the two tethered craft are of the same size and same voltage. Also, the solutions do not take into account effects of overlapping Debye sheaths. If the assumptions are satisfied, such as for the tethered Coulomb application, these results provide an improved representation of the effects of the plasma environment.

4.3 Over-Lapping Plasma Sheath Study

A charged spacecraft immersed in a plasma will generate a local sheath of charged particles. SPEAR-1 is one such experimental spacecraft that demonstrated, on-orbit, the accumulation of local charges, producing over-lapping plasma sheaths.[73] For a single spacecraft with even charge distribution, this natural effect has minimal consequences. However, for charged spacecraft in close proximity, such as the TCS application, this may cause the sheaths to over-lap and that alters the local plasma interaction and produced Coulomb force. The intent here is to investigate any electrostatic force and associated power changes due the local over-lapping of plasma sheaths of closely separated charged spacecraft. This force change is computed in addition to the plasma shielding, using finite element type particle-in-cell numerical simulations. In particular, of interest if the GEO space weather plasma environment and the TCS related nodal separation distance will yield appreciably different results if over-lapping Debye sheaths are considered.

4.3.1 Numerical Simulation Parameters

An analytic expression of the Coulomb force between two charged spheres with partial shielding from the plasma environment is derived from the Debye-Hückel potential model and shown in Eq. (2.5):

$$|\boldsymbol{F}_c| = k_c \frac{q_1 q_2}{r_{12}^2} e^{-r_{12}/\lambda_D} \left(1 + \frac{r_{12}}{\lambda_D}\right)$$

This Coulomb force model is most appropriate when the combinations of spacecraft charge and the plasma conditions abide Eq. (2.3):

$$eV_{sc1} \ll \kappa T_e$$

In addition to this natural shielding, when charged spheres are in close proximity, the force can be further reduced due to the over-lapping of the local plasma sheaths. In order to calculate the extent of this over-lapping plasma sheath shielding a 3D electrostatic numerical solver is used. The

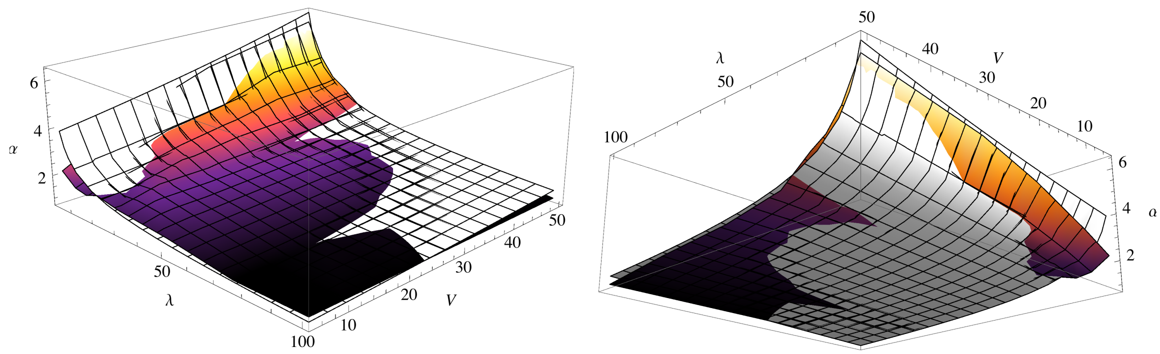

(a) (b)

Figure 4.6: *Alpha parameter values of regression (Equation* (4.14)*) for Diameter = 0.5 m*

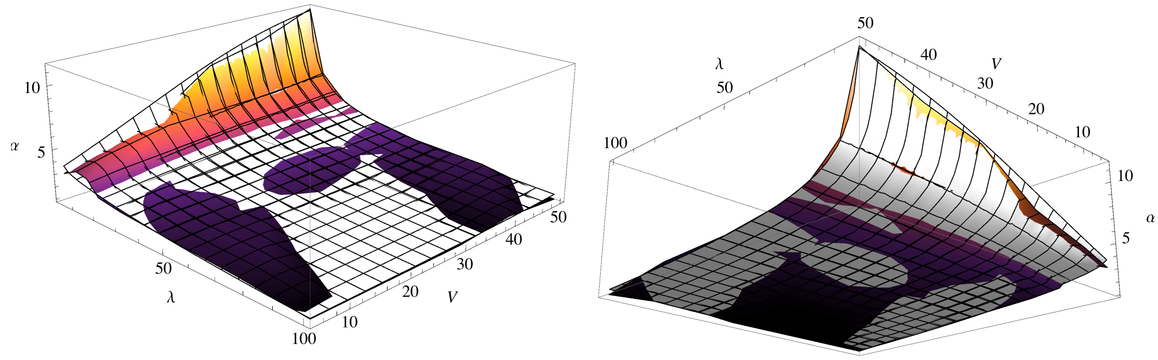

(a) (b)

Figure 4.7: *Alpha parameter values of regression (Equation* (4.14)*) for Diameter = 1.0 m*

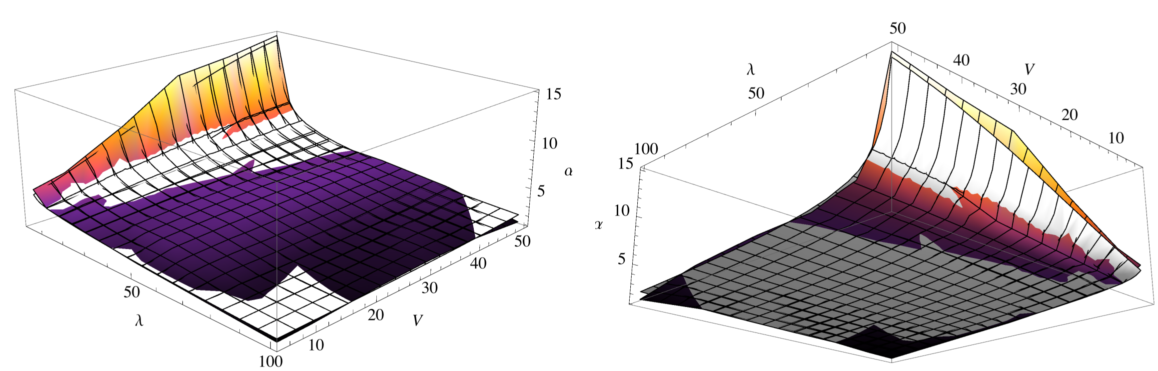

(a) (b)

Figure 4.8: *Alpha parameter values of regression (Equation* (4.14)*) for Diameter = 2.0 m*

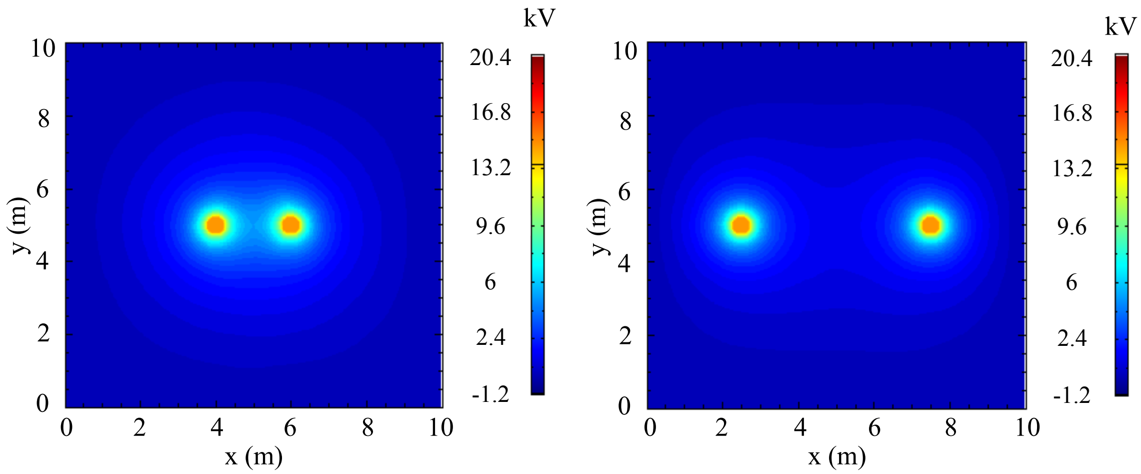

Figure 4.9: *Electric potential distribution for 2 m and 5 m separated spheres (0.25 m radii) charged to 15 kV in a representative plasma (λ_D = 74 m) using VORPAL.*

numerical computations are performed using Tech-X's plasma simulation code VORPAL[1]. VORPAL is designed as a highly flexible and computationally efficient modeling tool for computational electromagnetics and plasma physics.

A two-node TCS example is used to determine the over-lapping Debye sheath effects on repulsive Coulomb forces. For the simulation, spheres with radii 0.25m are placed in a grounded rectangular box with 40 m side along tether axis and 20 m by 20 m in perpendicular directions. The grid size for the simulations is 0.1 m in each direction and time step equal to 2 ns. The effect of the plasma is obtained by comparing the force between the spheres for both vacuum conditions and two extreme GEO plasma conditions.

For the plasma simulation cases, the electron and ion densities are ramped up during the 1000 time-steps to GEO plasma values and then the simulated plasma evolution runs for 9000 time-steps. The ramp-up of the density is used to avoid unnatural triggering of plasma oscillations. All particles that impact the boundaries are reflected off the walls.

4.3.2 Two-Node Simulation Potentials and Densities

A preliminary simulation for VORPAL electric potential verification is performed. The simulation placed two spheres in a ground 10x10x10 m box, containing a representative GEO plasma. The plasma conditions are; electron and ion temperatures of 100 eV, and densities of 1 cm^{-3}, which equates to a Debye length λ_D = 74 m. Two cases are simulated with 2 m and 5 m separations, with the spheres charged to a surface potential of 15 kV. The distribution of the electric potential of the local plasma around the spheres is shown in Figure 4.9.

Figure 4.10 shows the ion number density during the simulation. This is a snapshot of the plasma conditions between the two charged spheres 60 ns and 80 ns after simulation start, for the 2 m and 5 m sphere separations respectively. These figures show the development of the local plasma sheaths and their over-lapping characteristics for the 2 m separation case.

For this two-node example the electric potential solution in the λ_D = 74 m plasma is very similar to the vacuum numerical solution as there is ultimately minimal plasma (shielding) between the spheres. In order to verify the limits of the VORPAL solution an extremely dense plasma is

[1]VORPAL Product Page, Tech-X Corporation, http://vorpal.txcorp.com

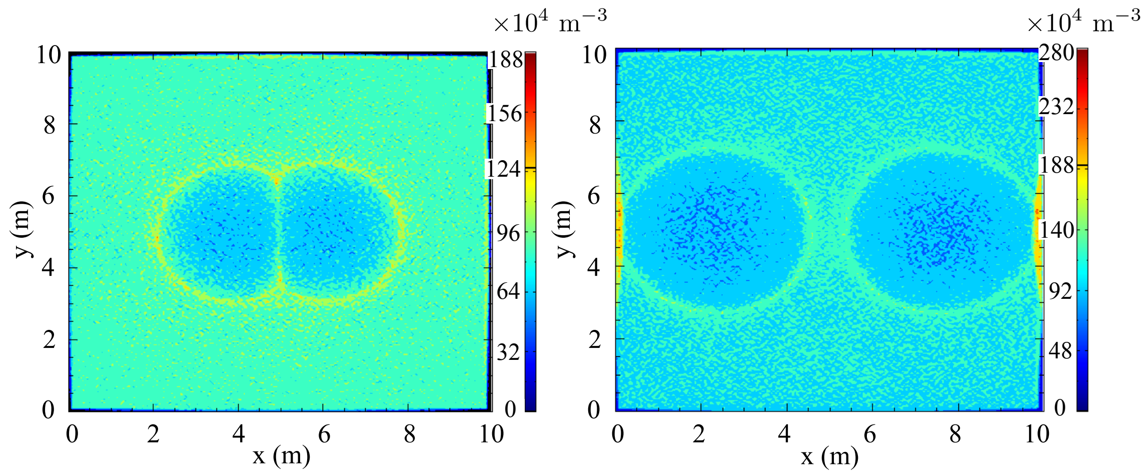

Figure 4.10: *Ion number density for 2 m (left) and 5 m separated spheres (0.25 m radii) charged to 15 kV in a representative plasma (λ_D = 74 m) using VORPAL. This is a simulation snapshot at 60 ns (left) and 80 ns after simulation start.*

simulated. This plasma has properties of electron and ion temperatures of 100 eV, and densities of 1×10^5 cm^{-3}, which equates to a Debye length $\lambda_D \approx$ 0.2 m. This is well beyond the worst case conditions anticipated at GEO, however it is used to push the limits of the numerical solution for comparison purposes. The two dimensional (along the tether axis) electric potential around the two spheres charged to 15 kV and separated by 2 m is shown in Figure 4.11.

Figure 4.11 also shows the electric potential numerical solutions for the alternate plasma case (λ_D = 74 m) and vacuum case as well as the analytic solutions. The analytic solution of the electric potential to first-order is given by the Debye-Hückel equation (Eq. (2.4)):

$$V = k_c \frac{q_1}{r} e^{-(r-\rho)/\lambda_D}$$

The analytic electric potentials match the numerical solutions well, however offer a conservative reduction in the electrical potential from the spheres. This is due to the sphere potential of 15 kV violates the conditions of Eq. (2.3) that is the basis of the Debye-Hückel approximation as well as including the increased force shielding from the over-lapping Debye sheaths. In addition, the boundaries of this plasma box are grounded in the simulation which is lower than the true potentials at these distances. This indicates that the VORPAL Coulomb force that is derived from the electric potential solution is a viable comparison tool.

4.3.3 Two-Node Numerical Coulomb Force Calculation

In order to use VORPAL to compute the Coulomb force acting on the spheres in a vacuum the following technique is implemented. First, the electric potential distribution from one charged sphere is computed, as shown in Figure 4.12. From this simulation, the electric field at the projected center of the second sphere (coordinates [4 5 5] here) is given. The Coulomb force is computed by multiplying the electric field at this location by the charge of the sphere. The charge of the sphere is computed using Eq. (2.7) that accounts for close sphere charge effects:

$$q_i^* = \frac{V_i}{k_c} \left(\frac{\rho r}{\rho + r} \right)$$

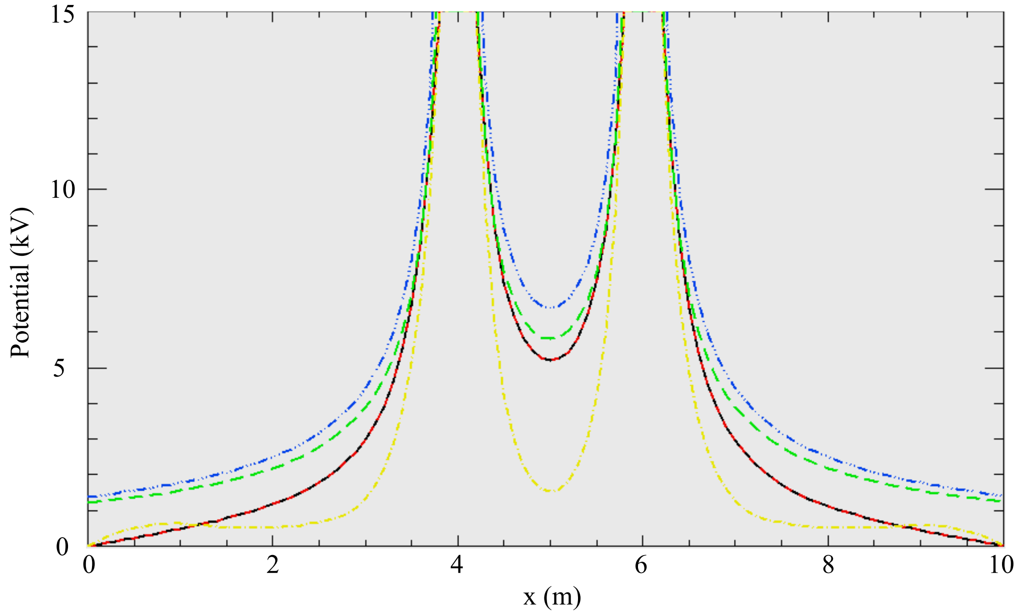

Figure 4.11: *Electric potential distribution along tether axis between two spheres (0.25 m radii) charged to 15 kV using VORPAL. Blue corresponds to zero-order accurate analytical solution. Green first order accurate analytical solution. Black numerical solution for vacuum case. Red numerical solution for low-density (λ_D = 74 m) plasma case. Yellow numerical solution for extreme high-density ($\lambda_D \approx$ 0.2 m) plasma case.*

Extending this Coulomb force calculation to a simulation with a plasma requires a more complex procedure.

First, the plasma is evolved in the presence of the two charged spheres. This plasma distribution is then frozen and one of the spheres is removed from the simulation domain. The electric potential and the electric field is obtained at the projected center of the removed sphere based on the plasma distribution and contribution from another sphere. The Coulomb force is computed by multiplying the electric field at this location by the charge of the sphere. Figure 4.13 shows both the distribution of the electric potential (left) and electric field (right) from one charged sphere. In order to highlight the plasma distribution effects this is shown for the extremely dense plasma with a 0.2 m Debye length.

The challenge here is the computation of the sphere charge. In an electrostatic simulation, the potential of the sphere is a boundary condition on the charge. An indirect method of computing the sphere charge to maintain the required potential on the sphere is required. In the presence of a plasma, the potential of each sphere is defined as:

$$V = k_c \frac{q}{\rho} + k_c \frac{q}{r} + \sum_i k_c \frac{q_i}{r_i} \tag{4.15}$$

where the summation accounts for the potential contribution from each plasma particle in the simulation box. With the removal of one sphere an expression for the remaining spheres potential (that is kept constant) is given by:

$$V = k_c \frac{\tilde{q}}{\rho} + \sum_i k_c \frac{q_i}{r_i} \tag{4.16}$$

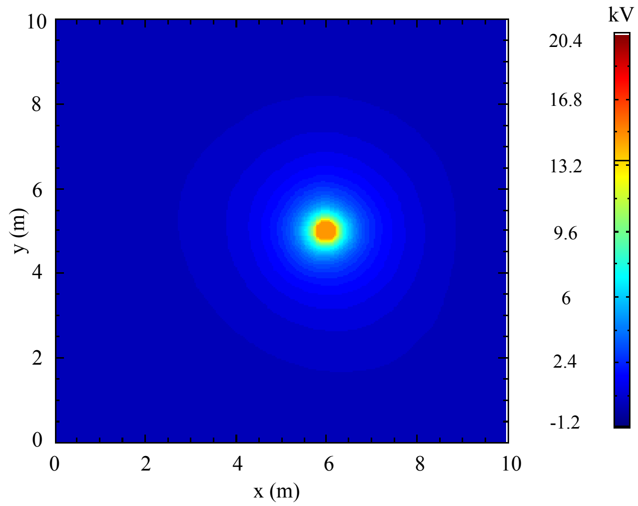

Figure 4.12: *Electric potential distribution about a single sphere (0.25 m radius) charged to 15 kV in a vacuum using VORPAL.*

where $\tilde{q}$ is the charge required on the remaining sphere to maintain the potential V constant. The potential at the center of the removed sphere is computed numerically in VORPAL using:

$$\tilde{V} = k_c \frac{\tilde{q}}{r} + \sum_i k_c \frac{q_i}{r_i} \tag{4.17}$$

Solving Equations (4.16) and (4.17) for the required charge $\tilde{q}$ gives the two equations:

$$\begin{aligned} \tilde{q} &= \frac{(V - \tilde{V})\rho r}{k_c(r-\rho)} \\ \sum_i k_c \frac{q_i}{r_i} &= \frac{\tilde{V} r - V\rho}{(r-\rho)} \end{aligned} \tag{4.18}$$

which can be substituted into Eq. (4.15) to give the numerically-solved charge on the spheres in the plasma:

$$\acute{q} = \frac{r^2 \rho (V - \tilde{V})}{k_c(r^2 - \rho^2)} \tag{4.19}$$

With this expression for the sphere charges it is possible to compute the correction to the electric field at the center of the removed sphere. The correction is equal to:

$$\Delta E = k_c \frac{\tilde{q} - \acute{q}}{r^2} \tag{4.20}$$

The resulting numerical solution Coulomb force acting on the spheres is given by:

$$F_{\text{numeric}} = (E + \Delta E)\acute{q} \tag{4.21}$$

where E is the electric field component in the tether axis direction, located at the center of the removed sphere. In addition, by modeling the charge evolution on the spheres, it is possible to compute the necessary current to the sphere in order to keep the potential constant.

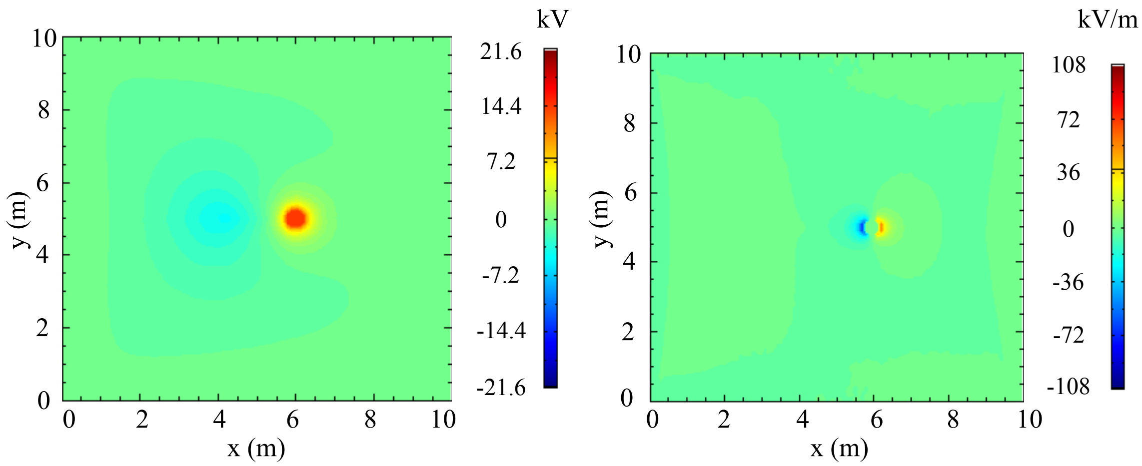

Figure 4.13: *Distribution of electric potential (left) and electric field (right) from one charged sphere (0.25 m radius) in the extreme high-density plasma λ_D = 0.2 m using VORPAL.*

The numerical force solution computed in a plasma with VORPAL gives the total force with plasma shielding and over-lapping plasma sheath effects. Of interest here is solely the reduction in force due to the over-lapping plasma sheath. In order to isolate this effect the numerical force solution of Eq. (4.21) is subtracted from the charged close sphere analytic force model in a vacuum:

$$F_{\text{close}} = k_c \frac{q_1^* q_2^*}{r_{12}^2} \tag{4.22}$$

to give the numerical force reduction percentage:

$$\%F_{\text{Nreduce}} = \frac{(F_{\text{close}} - F_{\text{numeric}})100}{F_{\text{close}}} \tag{4.23}$$

This force reduction is directly compared to the force reduction due to the plasma shielding from the Debye-Hückel model which is computed as:

$$\%F_{\text{Mreduce}} = \left[1 - e^{-r_{12}/\lambda_D}\left(1 + \frac{r_{12}}{\lambda_D}\right)\right]100 \tag{4.24}$$

The difference between the numeric and model force reductions gives a measure of the shielding due to the over-lapping Debye sheaths ($\%F_{\text{Nreduce}} - \%F_{\text{Mreduce}}$).

4.3.4 Numerical Force Calculation Results

The analytical model shielding that results in the force reduction of Eq. (4.24) is only valid for comparison if Eq. (2.3) is not violated. It is therefore necessary to select both the plasma conditions and spacecraft charges that will abide Eq. (2.3). Two representative plasma conditions (λ_D = 33 m & λ_D = 50 m) are used for this study with parameters shown in Table 4.2. Both these example plasma conditions are colder and more dense than the quiet (worse-case) plasma conditions of Table 4.1, indicating an extreme and unexpected GEO environment. This is used purely to identify the effects of over-lapping Debye sheaths.

With these two plasma conditions defined the corresponding spacecraft potentials that violate Eq. (2.3) are 0.5 kV and 0.9 kV for the λ_D = 33 m & λ_D = 50 m plasmas respectively. For this

Table 4.2: *Plasma Properties for Over-Lapping Debye Sheath Study*

Debye (m)	Temperature [eV]	Density [cm^{-3}]
33	500	25
50	900	20

Table 4.3: *Analytic Plasma Shielding Based on Debye-Hückel Force Model (Eq.* (4.24)*)*

Debye (m)	5 m separation	10 m separation
33	1.02 %	3.71 %
50	0.47 %	1.76 %

reason the selected potentials used in this study will be [-10, -1, -0.5, 0.5, 1, 10, 25] kV. The two-node example features spacecraft with 0.25 m radii and separations of 5 and 10 m. At these separations the expected Coulomb force reduction based on the analytic Debye-Hückel plasma shielding model is shown in Table 4.3.

The model force reduction due to plasma shielding and the numerical total force reduction between the two nodes is shown in Figure 4.14. The discrepancy between the two solutions for each plasma and spacecraft potential gives an indication of the effects of the over-lapping plasma sheath. For low magnitude potentials [-1, -0.5, 0.5, 1] kV in these dense/cold plasmas the over-lapping plasma sheaths cause a slight increase in the force reduction (except for the 10 m separation in the λ_D = 33 m plasma). This stronger shielding is an expected result as there is an enhanced plasma interaction between the closely separated nodes and their over-lapping plasma sheaths.

For the higher level potentials [-10, 10, 25] kV the force reduction from the numerical solution is lower than the model prediction, indicating that the over-lapping Debye sheaths have little effect. However, at these operating potentials the analytic model properties violate Eq. (2.3), reducing the validity of comparing these solutions and also suggesting there are numerical computation limitations in these regions. What is important is that the numerical solution demonstrates similar force magnitudes and reductions at these operating potentials and extreme GEO plasma environments. The final conclusion drawn from this comparison is that the force shielding due to over-lapping plasma sheaths are minimal in comparison to the plasma shielding and close sphere finite effects. The over-lapping plasma sheaths are an important and real characteristic of multiple craft charging, however the net result has minimal consequence on the overall production of TCS repulsive forces.

4.4 Electrostatic Zones of Influence Study

In the analysis of the six craft TCS in the shape configuration study (see Figure 4.15), the tether expressions are found to be functions of inter-craft Coulomb forces which occur between nodes not connected by any tethers. Some of these electrostatic forces actually act to cause compression in the tethers, an undesirable consequence of the geometry of the structure. Naturally, it is of interest to determine whether or not certain TCS sizes may decouple some of the electrostatic forces from the tethers. As an illustrative example, we will examine the forces in tether T_{34} of the six craft TCS.

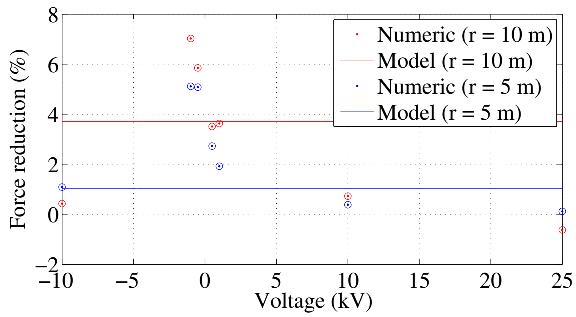

(a) Plasma Debye Length of 33 m

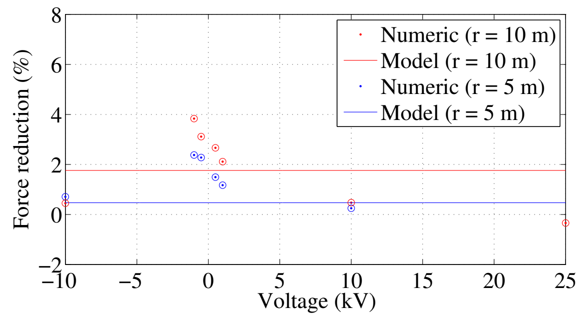

(b) Plasma Debye Length of 50 m

Figure 4.14: *Coulomb force reduction comparing analytic model, Eq.* (2.5) *to the VORPAL numerical solution. This is computed for spheres of 0.25 m radii. The analytic model captures only the close finite sphere and Debye shielding effects, while the numeric model also captures the effects of over-lapping plasma sheaths.*

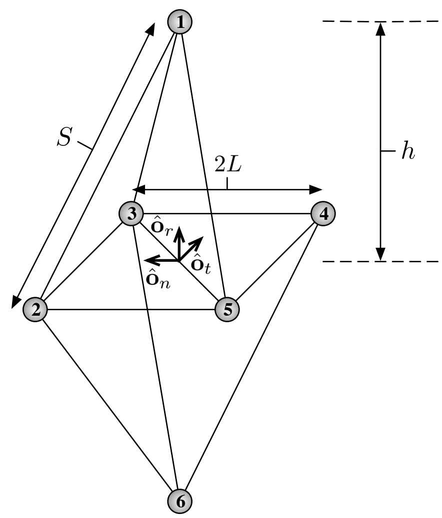

Figure 4.15: *Six-Node TCS System*

The expression for the tether tension is

$$T_{34} = F_{34} + \frac{F_{24}}{\sqrt{2}} + L\left[\frac{F_{14}}{S} - \frac{F_{56}}{S} - \frac{1}{2}\left(\frac{F_{16}}{h} + 5\frac{m\mu}{r_c^3}\right)\right]. \tag{4.25}$$

It is immediately apparent due to $F_{ij} > 0$ that compressive forces components result from the electrostatic forces F_{16} and F_{56}. What we would like to ascertain is whether or not increasing the length of h relative to the local plasma environment may cause these electrostatic forces to become so small relative to F_{34} that they no longer affect the tension in T_{34}. Note that tether T_{34} is not the only tether that experiences electrostatic compressive forces; it is arbitrarily chosen from the TCS to serve as the example.

Before proceeding further, we must first define a force component, denoted as $F_{c_{ij}}$. The force component provides an expression for the contribution to the tether tension of electrostatic and gravitational forces, including all scaling factors present in Eq. (4.25). As an example, the force

Table 4.4: *Charges Used for Decoupling Simulations*

$q_1 = q_2 = q_6$	q_3	$q_4 = q_5$
5 μC	1.2q_1	0.5q_1

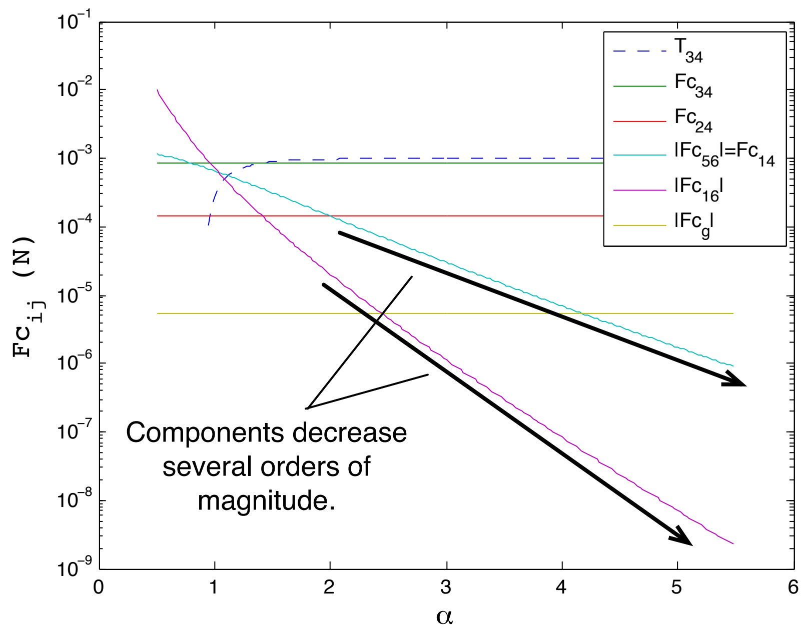

Figure 4.16: *Force components for $\lambda_D = 4$ m. The magnitude of the negative force components is plotted.*

components for F_{16} and F_{56} are

$$F_{c_{16}} = -\frac{L}{2h}F_{16}$$
$$F_{c_{56}} = -\frac{L}{S}F_{56}, \tag{4.26}$$

while the force component due to gravity is

$$F_{c_g} = -\frac{5m\mu L}{2r_c^3} \tag{4.27}$$

Because Debye shielding effects are the primary reason for electrostatic force decoupling, the Debye length will be used to define TCS lengths for the investigation. Returning to Figure 2.23, the length L will be set at λ_D; the 6-node TCS height measure h in Figure 4.15 will be varied linearly as a function of the Debye length so that

$$h = \alpha\lambda_D$$

The scaling parameter α will be varied to demonstrate the decoupling effect. To provide an illustration of how the decoupling can directly affect tether tension, the charges on the craft will be held constant as α is varied. The charges used for the simulations are presented in Table 4.4. The TCS is assumed to be located at GEO, with $r_c = 42,164$ km.

The results for the change in force components as α is varied are presented in Figure 4.16 for the case where $\lambda_D = 4$ m. Note that for the negative force components $F_{c_{56}}$, $F_{c_{16}}$, and F_{c_g} the magnitudes are plotted. This enables a clear picture of which force components are influencing the tether tension the most. Up to around $\alpha = 1$, the compressive force component $F_{c_{16}}$ is the dominating force. Indeed, the tether will experience compression up until this point. It is not until the distance h has been increased enough and the tensile force component F_{34} dominates that the tether experiences tension. It is clear that as α is increased further, the magnitudes of the force components which incorporate the length h drop off to orders of magnitude several times lower than the dominating force component. This is what is meant by force decoupling. Essentially, these tether components have become so small as to be insignificant. In this case, the gravitational force component F_{c_g} is also at an order of magnitude that is insignificant. As α increases, the tether tension approaches the value of $F_{c_{34}} + F_{c_{24}}$, as these are the only remaining significant force components.

This illustrates that for large structures that may consist of tens of nodes, the Coulomb forces between two craft at either ends of the structure will have a minimal impact on tether tensions in the structure due to the effects of Debye shielding. Consider a large truss structure that is 100 meters long. In an environment with a Debye length of 4 m, the force between two nodes spaced 100 meters apart would be very small. While the force would appear in expressions for tether tensions in the structure, it would be multiple orders of magnitude smaller than forces generated between nearer neighbors. Ultimately, we would expect that the expressions for tether tensions connected to a single node would be dominated by the Coulomb forces generated between craft separated by distances on the order of the Debye length. This is in fact what we see in Figure 4.16 as α increases. When the distance h becomes large relative to λ_D, the tether tension T_{34} is influenced only by $F_{c_{34}}$ and $F_{c_{24}}$. The separation distance between craft 3 and 4 is $2\lambda_D$, and the separation distance between craft 2 and 4 is $2\sqrt{2}\lambda_D$. If we consider the case when $\alpha = 5$, the separation distance between craft 1 and 6 is $10\lambda_D$, while the separation distance between craft 5 and 6 is $5.1\lambda_D$.

To illustrate the effects these separation distances have on the amount of Debye shielding that occurs, let us introduce a shielding coefficient υ_{ij}, defined as

$$\upsilon_{ij} = e^{-r_{ij}/\lambda_D}\left(1 + \frac{r_{ij}}{\lambda_D}\right). \tag{4.28}$$

This coefficient allows us to directly compare the magnitude of Debye shielding effects as a function of separation distances. The lower the shielding coefficient, the more the force between two craft has been reduced due to the Debye length. The values of the shielding coefficients for the case when $\alpha = 5$ are presented in Table 4.5. The amount of shielding between craft 2 and 4 is on the same order of magnitude as that between craft 3 and 4. It is these two force components that dominate the tether forces when $\alpha = 5$. The reason why is clear when examining the values of υ_{16} and υ_{56}. The amount of shielding between craft 1 and 6 is three orders of magnitude more intense than that between craft 3 and 4. Similarly, the shielding effects between craft 5 and 6 are a full order of magnitude below that between craft 2 and 4. This illustrates the manner in which the TCS dimensions relative to the Debye length can reduce intercraft Coulomb forces to the point that they no longer influence tethers in the structure.

Thus far, we have examined the case of a fixed Debye length with varying structural dimensions. Alternatively, we may consider the case of fixed structure dimensions with a varying Debye length, which is more applicable to what a real structure would experience while in orbit. For this simulation, we will set the TCS dimensions to $L = 4$ m and $h = 8$ m and vary the Debye length. The results are shown in Figure 4.17. All of the force components decrease as λ_D decreases, but

Table 4.5: *Shielding Coefficient Values for* $\alpha = 5$

r_{ij}	$r_{34} = 2\lambda_D$	$r_{24} = 2\sqrt{2}\lambda_D$	$r_{16} = 10\lambda_D$	$r_{56} = 5.1\lambda_D$
υ_{ij}	4.06×10^{-1}	2.26×10^{-1}	4.99×10^{-4}	3.72×10^{-2}

the rate of decrease is not the same for all components. If we compare $F_{c_{16}}$ to $F_{c_{34}}$, we see that the force component $F_{c_{16}}$ decreases more rapidly than $F_{c_{34}}$. This is evidenced by the fact that the separation in orders of magnitude between the force components grows as λ_D decreases. At the upper bound on the Debye length, the force components are separated by slightly more than an order of magnitude. At the lower end of the Debye length, however, the craft are separated by four orders of magnitude. This large difference between the force components means that at the lower Debye lengths $F_{c_{16}}$ has minimal influence on the tether relative to $F_{c_{34}}$. Practically, the influence of the Coulomb force between craft 1 and 6 has decoupled from the tether.

These cases illustrate what is meant by a zone of influence. Beyond some certain dimensions of the TCS or Debye lengths of the surrounding environment, certain force components grow so small that they negligibly affect the tether tension. Once they no longer significantly impact the tether forces, they have exited the zone of influence of the tether. Because this is the first time this effect has been noted and analyzed, it is appropriate to formalize a definition for the idea of a zone of influence. Providing a geometric based definition does not make sense in this case, because the geometry of each TCS is different; the definition would need to be reworked for each particular configuration. Rather, the definition will be based on force component magnitudes, and is provided as follows:

Zone of Influence - A force component is said to be within the zone of influence of a particular tether at some instant in time, t_0, if its magnitude is greater than one percent of the largest positive (tensile) force component in said tether for a particular TCS geometric configuration, charge configuration, and Debye length of the local plasma environment.

Thus, a force component may be within the zone of influence for a tether at time t_0, but not within it at some later time $t_0 + \Delta t$. This effect is illustrated in Figure 4.17 where decoupling due to Debye length changes is demonstrated. Because the Debye length is a time variant quantity, decoupling may exist at one point in time but not at another.

If we return to the two cases examined here, we can illustrate how the change in parameters causes force components to enter or exit the zone of influence of T_{34}. For both cases the largest positive force component is $F_{c_{34}}$. Thus, the zone of influence is defined based on the magnitude of this force component. If we compare the magnitudes of the two compressive electrostatic force components $F_{c_{16}}$ and $F_{c_{56}}$ to $F_{c_{34}}$, we can see clearly at which points they are within the zone of influence of tether T_{34}. The results for the first case where α is varied are presented in Figure 4.18(a). The results for the second case, where the dimensions are fixed as the Debye length varied, are shown in Figure 4.18(b). For the first case, we see that $F_{c_{16}}$ exits the zone of influence at $\alpha \approx 2.3$, while $F_{c_{56}}$ remains within the zone of influence until $\alpha \approx 3.9$. This particular case illustrates the importance of considering TCS dimensions relative to anticipated Debye lengths. At certain dimensions, the compressive electrostatic force components significantly impact the overall forces in T_{34}. However, the magnitude of these compressive elements can be rendered insignificant if the dimension h is chosen to be large enough. With a smaller magnitude of compressive elements in the tether force expression, less charge would be needed on the nodes to maintain tension.

In the second case, only the force component $F_{c_{16}}$ exits the zone of influence over the range of Debye lengths investigated. This exit occurs around $\lambda_D = 2.8$ m. This case illustrates how

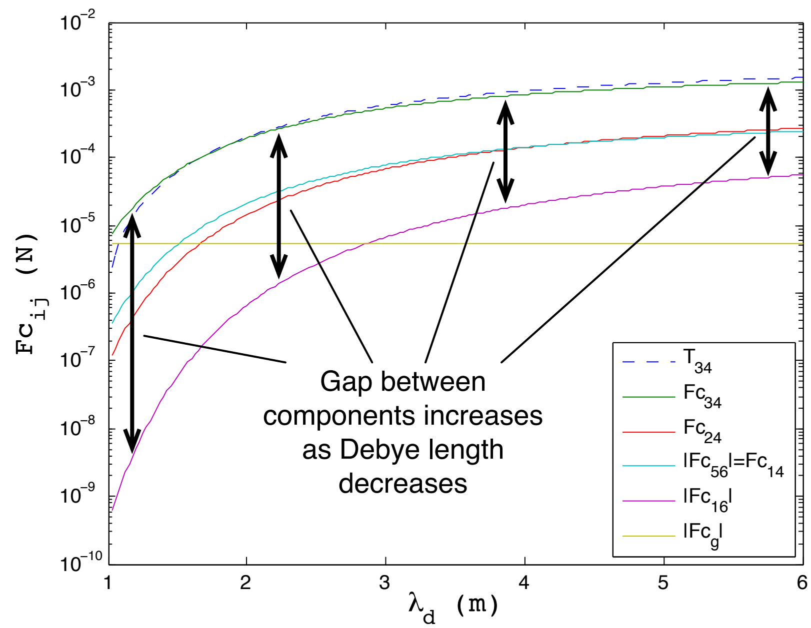

Figure 4.17: *Force components for $L = 4$ m and $h = 8$ m with varying Debye length. The magnitude of the negative force components is plotted.*

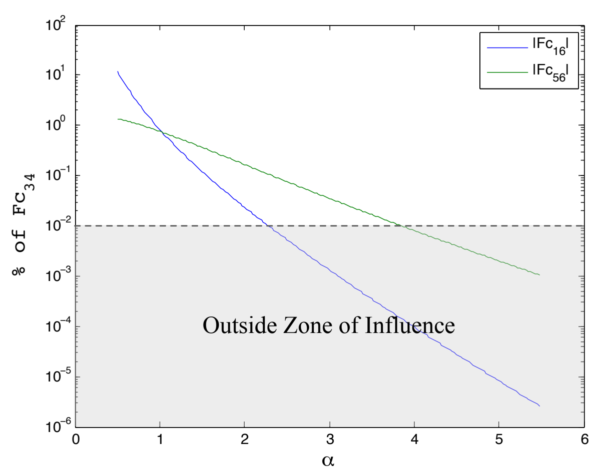

(a) Case 1: Varying α

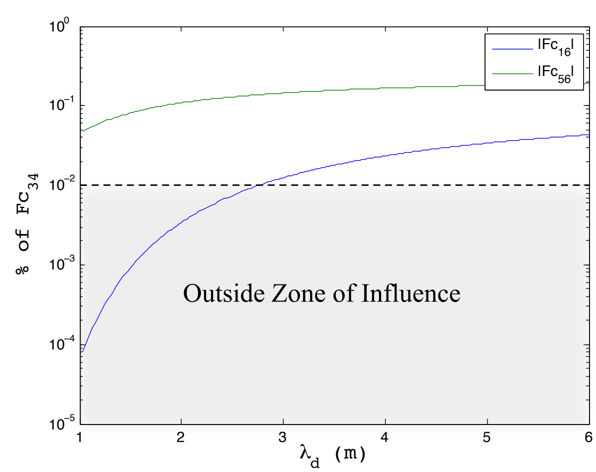

(b) Case 2: Varying λ_D

Figure 4.18: *Illustration of zones of influence for a) case where α is varied and b) case where λ_D is varied.*

different force components could enter or exit the zone of influence over time. If at some point in time the Debye length is 6 meters, $F_{c_{16}}$ would be within the zone of influence of T_{34}. At a later time the Debye length could be 2 m, in which case $F_{c_{16}}$ would no longer be within the zone of influence for the tether. As Figure 4.18(b) clearly illustrates, the magnitude of the compressive force elements in this particular TCS is much more significant for larger Debye lengths.

The concept of zones of influence is important for structures which may have overall distances larger than the local Debye length. While the force between two nodes at either end of the structure

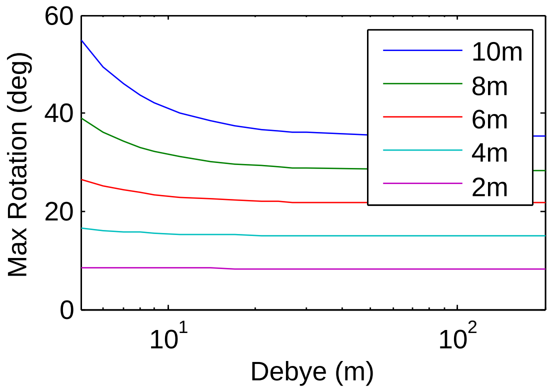

(a) Variation in nodal separation

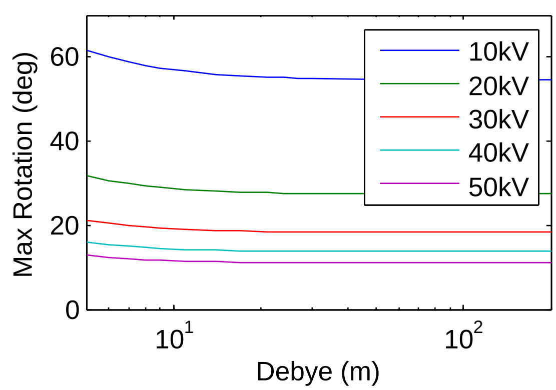

(b) Variation in nodal potential

Figure 4.19: *Maximum absolute principal rotation as a function of environmental conditions (Debye length)*

may appear in many tethers throughout the structure, the magnitude of this force may be so small that it does not noticeably impact the tensions in said tethers. Additionally, the decoupling effects observed as the Debye length varies provide a clear picture of why space weather variations must be carefully considered when designing a TCS. While a structure may be properly inflated under large Debye lengths, one or more tethers could shift into compression if the Debye length decreases. Consider a case where a certain force component is being used to ensure tension in some tether T_{ij}. If the Debye length decreases such that the tensile force component is no longer within the zone of influence of T_{ij}, the tether could go slack. These results indicate that a structural design must be simulated across the range of all expected Debye lengths, from large to small, to ensure that inflation can be maintained during all space weather conditions.

4.5 Space Weather Impact on Rotational Stiffness

Analyzed here is the plasma effect of charge shielding which reduces the inflationary Coulomb force and stiffness capabilities of the system.[2] The charge reduction is examined for a range of Debye lengths from nominal to worst-case conditions. Figure 4.19 shows the effect of these plasma conditions on the rotational stiffness of a single-tether TCS configuration with disturbance about the X-axis. The results shown are for the conservative partial charge shielding force model of Eq. (2.5). For spacecraft charges to these magnitudes the effective Debye length will in fact be larger improving the rotational stiffness results.

Figure 4.19 shows that environmental conditions have minimal impact on the dynamics of a closely-operated TCS system until Debye lengths on the order of 10 meters or smaller are considered. The maximum absolute rotation lines in the figures converge to the maximum rotation values with no plasma shielding. Nominal values of Debye lengths (far right of figure) have no effect, but as the plasma Debye length reduces to the worst case value the rotational stiffness decreases. When designing for the worst case plasma conditions consideration must be made for TCS nodal separations larger than 5 meters. Considering a TCS system with a large number of nodes spanning 100 meters, the shorter Debye length plasma shielding will also impact the overall rigidity of this system. The results in Figure 4.19 are specific to a simple two-node system and short separations.

4.6 TCS Power Requirements

The goal of this section is to compute the power required for a single TCS node to maintain a fixed potential as it operates in the representative GEO plasma conditions given in Table 4.1. Firstly, the net plasma current flow to the node (that is charged to a fixed potential) is computed. It is necessary to emit the equivalent current to offset the plasma and maintain the desired node potential, and the power required is the product of these two values. In addition, the resulting fuel (electron/ion ejection current) is estimated for these charging conditions.

4.6.1 Net Plasma Current Flow

Without charge control the GEO plasma environment will cause the spacecraft potential to vary uncontrolled between positive (sunlit) and negative (shaded) values. The resulting currents drive the spacecraft to charge equilibrium with the local plasma where the net current is zero, which can occur at kiloVolt-level potentials. For a TCS node, an active charge control device is implemented to enhance or offset this natural equilibrium and drive the node to desired charge levels regardless of the local plasma conditions. Presented here is a model of the current flow between a spacecraft and its operating plasma. The plasma interaction to the spacecraft is modeled with the net current flow equation, (with the notation that all currents to the spacecraft are negative):

$$I_{\text{net}} = I_e - I_i - [I_{Pe} + I_{Se} + I_{Si} + I_{BSe}] \pm I_{cc} \tag{4.29}$$

where

I_e = incident electrons
I_i = incident ions
I_{Pe} = photoelectrons
I_{Se} = secondary emitted electrons due to I_e
I_{Si} = secondary emitted electrons due to I_i
I_{BSe} = backscattered electrons due to I_e
I_{cc} = charge control (electrons or ions)

4.6.2 Primary Electron and Ion Current Density

It is assumed the plasma is comprised of two populations (electrons, protons) that are modeled with single-Maxwellian distributions. A spacecraft at GEO is stationary relative to the plasma (no ram currents) and the two primary current contributions are from electron and ion bombardment. The net current density J_{net} [Am^{-2}], is developed for both positive and negatively charged spacecraft with a Boltzmann factor representation and exponential repulsion and Mott-Smith and Langmuir attraction:[74,75]

$$J_{\text{net}}(V_{sc} < 0) = J_{0e} \exp\left[\frac{-e_c|V_{sc}|}{\kappa T_e}\right] - J_{0i}\left(1 + \frac{e_c|V_{sc}|}{\kappa T_i}\right) \tag{4.30a}$$

$$J_{\text{net}}(V_{sc} > 0) = J_{0e}\left(1 + \frac{e_c V_{sc}}{\kappa T_e}\right) - J_{0i} \exp\left[\frac{-e_c V_{sc}}{\kappa T_i}\right] \tag{4.30b}$$

where V_{sc} [V] is the spacecraft potential and J_{0e} & J_{0i} are the electron/ion saturation currents:

$$J_{0e} = e_c n_e \sqrt{\frac{T_e}{2\pi m_e}} \tag{4.31a}$$

Table 4.6: *Example Photoelectron Current Densities and Particle Energies*

Source	J_{0pe} [μA/m^2]	T_{Pe} [eV]
Grard[76,77]	4-42	3.9-4.8
Whipple[39]	7.2-48	1-2
King[14]	10	4.5
Nakagawa[78]	85	2.1
DeForest[79]	8.2	-
Samir[80]	30	-

$$J_{0i} = e_c n_i \sqrt{\frac{T_i}{2\pi m_i}} \tag{4.31b}$$

A spacecraft will reach current equilibrium with the plasma when $J_{\text{net}} = 0$. Depending on the plasma conditions this solution exists for a specified spacecraft potential, known as the floating potential. With a single Maxwellian plasma distribution and no photoelectron or secondary particle effects the equilibrium will occur at a negative potential.

4.6.3 Inclusion of Photoelectron Current

In sunlight a spacecraft is hit with solar radiation that leads to a net outflow of photoelectrons. This occurs during sun-lit conditions when the photons impacting the spacecraft surfaces cause an electron to be emitted. This is an important contributor to the net current flow for a GEO spacecraft as this is the majority of on-orbit conditions and the magnitude of the current can be relatively high. The photoelectron current is modeled using:

$$J_{Pe}(V_{sc} < 0) = -J_{0pe} \tag{4.32a}$$

$$J_{Pe}(V_{sc} > 0) = -J_{0pe} \exp\left[\frac{-e_c V_{sc}}{\kappa T_{Pe}}\right]\left(1 + \frac{e_c V_{sc}}{\kappa T_{Pe}}\right) \tag{4.32b}$$

where T_{Pe} [K] is the mean energy of the photoelectrons leaving the spacecraft surface and J_{0pe} [Am^{-2}] is the constant photoelectron current density for a spacecraft at zero potential. The photoelectron current is dependent on the surface materials of the spacecraft. Emitted photoelectrons leave the spacecraft surface isotropically with a Maxwellian energy distribution that has a mean energy T_{Pe}. This mean energy value is computed both with space and laboratory experiments and is constant regardless of the incoming photon spectrum.[65] Table 4.6 lists a range of representative photoelectron currents (J_{0pe}) as well as the mean energy T_{Pe} of emitted photoelectrons.

The photoelectron current is computed at a distance of 1 AU and with a impact trajectory that is normal to the surface. Torkar in Reference 81 presents the use of an active charge control device emitting a current of 10-50 μA to overcome the photoelectron current of the TC-1 spacecraft. Samir in Reference 80 demonstrates that the photoelectron current on the Ariel 1 satellite was as high as 300 μA/m^2 but reduced as a result of changing surface conditions such as outgassing.

For this study a photoelectron current of $J_{0pe} = 20$ μAm^{-2} will be used along with a mean energy, $T_{Pe} = 2$ eV.[76,77,39,14] These values are chosen to represent typical spacecraft materials and give a conservative indication of the effect of photoelectron currents on TCS power requirements. The photoelectron current is computed from only the sun-lit surface (half-sphere).

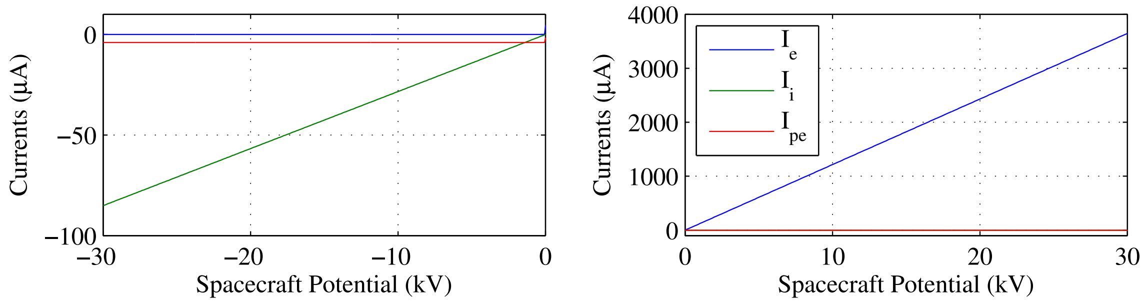

Figure 4.20: *Current flows to spacecraft during quiet plasma conditions, λ_D = 4 m (worst-case)*

4.6.4 Inclusion of Secondary Electrons and Backscattering

Additional current sources considered are the outgoing electrons from secondary emissions and backscattering.[82] The secondary yield (that can be higher than the incoming primary particle flux)[83] is a function of the surface material and the primary particle energy. The mean energy of the secondary electron leaving the surface is very low, $T_{\text{Se}} \approx$ 2-3 eV[65,84,85] and will return to the surface of a positively charge craft (no net current effect).

The electron current I_e is low for a negatively charge craft, so the secondary electron and backscattered current from electron impacts is omitted in this study. The backscattering of ions is generally very low and is also omitted.[65,79] The secondary electron yield from ion impacts is only larger than unity for high primary energies (> 10 keV)[65] and will only be considered for the higher energy plasmas of the nominal and disturbed conditions. A simple linear model of the secondary electron current is given by Francis in Reference 84:

$$J_{Se}(V_{sc} < 0) = -b|J_i| \tag{4.33}$$

where $b \approx 3$ is computed from a study of ATS-5 and ATS-6 data.[84]

4.6.5 Dominant Plasma Currents

The natural net current flow between the plasma and a spacecraft operating at a given potential is computed. The range of spacecraft potentials used in this analysis is -30 to 30 kV, a reasonable range that is anticipated for TCS operations. The currents impacting the spacecraft during the quiet plasma conditions ($\lambda_D = 4$ m) is shown in Figure 4.20.

The currents are shown for a single spherical craft of 0.25 m radius. In this cold and dense plasma a negatively charged spacecraft will attract a current of ions. During positive charging electrons will be attracted to the craft and the relative ion current is zero.

The plasma currents for nominal conditions ($\lambda_D = 200$ m) is shown in Figure 4.21. In this plasma, the dominant current for a negatively charged spacecraft are the escaping photoelectrons. For a positively charged spacecraft the electron current bombardment dominates both the ion current and the low energy photoelectrons that are attracted back to the craft.

The plasma currents for the hotter and sparser disturbed plasma conditions ($\lambda_D = 743$ m) is shown in Figure 4.22. The dominant current for negative charge is the escaping photoelectrons while a positive charge has a dominant electron current bombardment.

The consequence of these resulting charging schemes in all environments is that to maintain a negative spacecraft potential it will be necessary to emit ions to compensate for either the ion impacts and/or escaping photoelectrons. Alternatively, to maintain a positive spacecraft potential it will be necessary to emit electrons to compensate for the impacting electrons from the plasma.

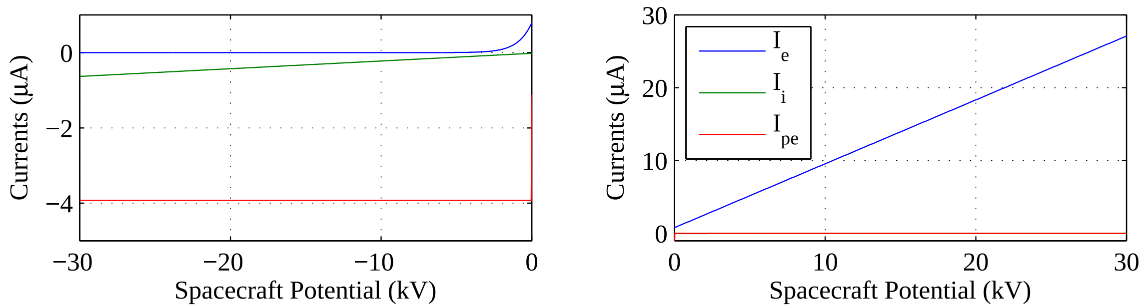

Figure 4.21: *Current flows to spacecraft during nominal plasma conditions, λ_D = 200 m*

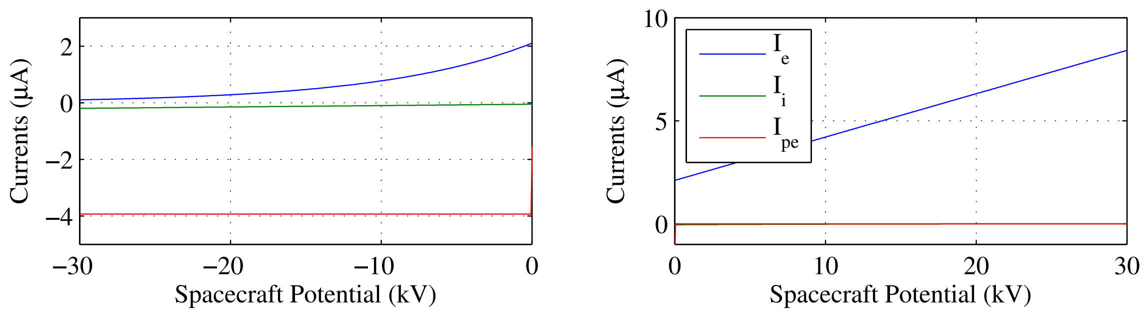

Figure 4.22: *Current flows to spacecraft during disturbed plasma conditions, λ_D = 743 m*

4.6.6 Net Plasma Current

The plasma current levels shown in Figures 4.20-4.22 can be summated to compute the net plasma current and dictate the equilibrium potential each craft will reach in each plasma environment. The net current flow to a spacecraft that is in eclipse (no photoelectrons) is shown in Figure 4.23 for each of the plasma conditions. The maximum net current occurs in a quiet plasma for a positively charged spacecraft.

The net current flow to a spacecraft that is in sun light (includes photoelectron current) is shown in Figure 4.24, for each of the plasma conditions. The addition of the photoelectron current has minimal affect on the quiet plasma (λ_D = 4 m) however does contribute to a negatively charged craft in the nominal and disturbed plasmas as predicted from Figures 4.21 & 4.22.

4.6.7 Net Plasma Current Verification

The VORPAL 3D electrostatic numerical simulation code is also used to compute the net plasma current to two nodes. This allows comparison to the analytic current models, providing a means of verification. The current to the charged spheres is computed in VORPAL by tracking the number of electrons in the simulation domain at each time step. The average current is computed by taking the total number of electrons lost to the craft divided by the corresponding simulation time interval.

The plasma conditions used are the extreme cold/dense properties given in Table 4.2 that are used for the over-lapping plasma sheath study. These properties along with spacecraft potentials of [-10, -1, -0.5, 0.5, 1, 10, 25] kV cover the ranges of validity of Eq. (2.3). The comparison of the plasma current model to the numerical solution for a single node of 0.25 m radius is shown in Figure 4.25.

Overall, the comparison of the net current flow to a single craft indicates the analytic model

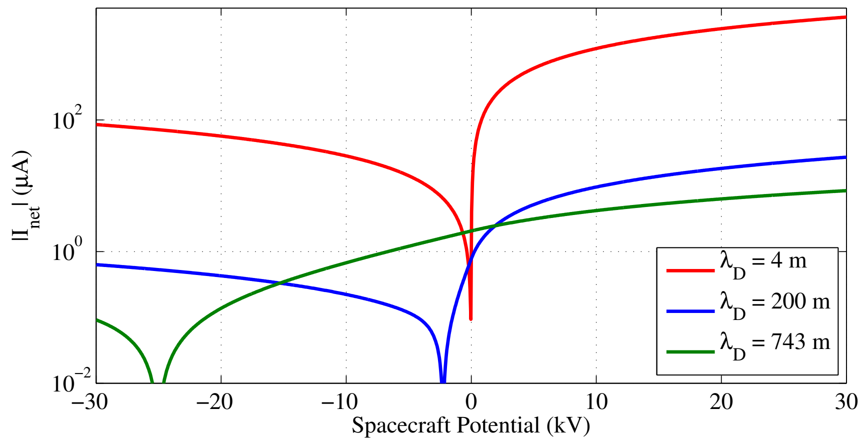

Figure 4.23: *Net current flow to spacecraft in eclipse for each plasma*

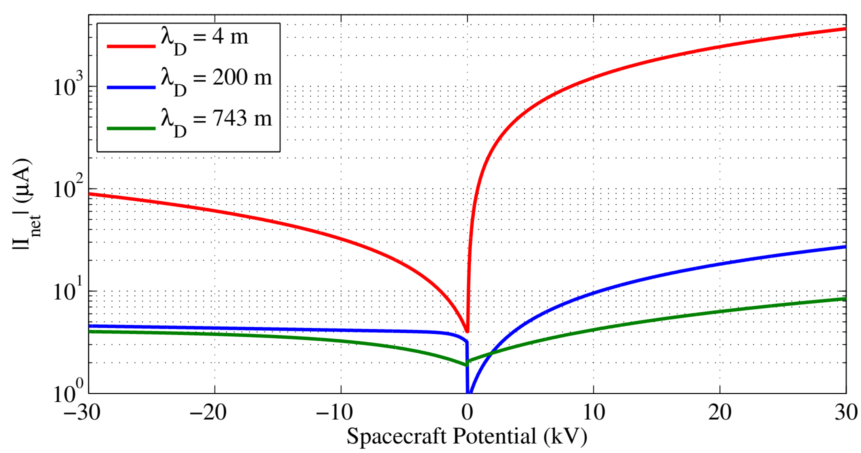

Figure 4.24: *Net current flow to spacecraft in sun light for each plasma*

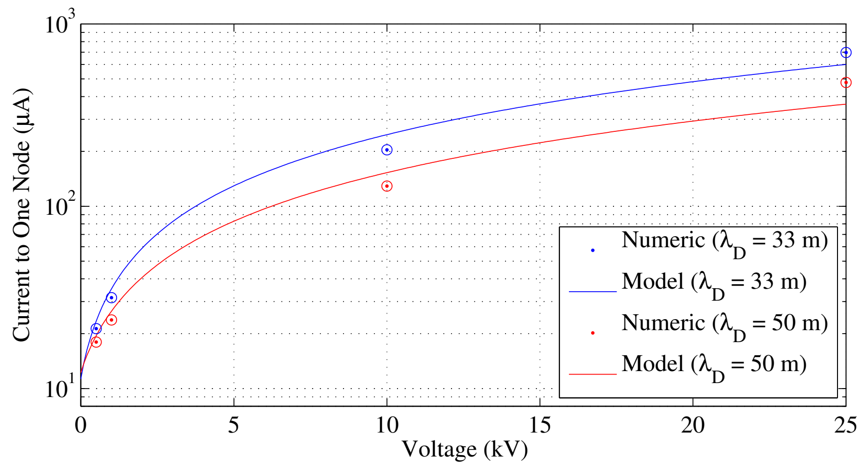

Figure 4.25: *Net current flow to one spacecraft in eclipse comparing analytic model to VORPAL numerical solution*

matches the numerical solution well for the positive potentials. In the low positive potentials [0.5, 1] kV the numeric solution yields slightly larger currents as a result of the increased force shielding due to the over-lapping plasma sheath, (an effect that is not captured in the analytic model). At higher positive potentials [10, 25] kV it is harder to make a direct comparison due to the violation of Eq. (2.3), however the numerical results still agree well with the analytic model current.

The numerical current solution of VORPAL also captures the equilibrium currents and floating potentials close to the model predictions. The numeric solutions indicate equilibrium occurs at potentials of $\approx$-0.5 kV and $\approx$-0.85 kV for the 33 m and 50 m plasma conditions respectively. This is close to the model prediction of -1.2 kV and -2.3 kV.

4.6.8 Net Power Requirements

The net current is used to compute the power necessary to maintain a fixed potential. It is assumed that the charge control current can be either positive or negative charge and equal the net plasma current $I_{\text{net}} = I_{cc}$. For a given spacecraft potential the power is calculated using $P = |V_{sc}I_{\text{net}}|$.

For a spacecraft in eclipse (no photoelectrons) the power required to maintain a fixed potential is shown in Figure 4.26 for each plasma condition. The nominal (λ_D = 200 m) and disturbed plasma conditions require realistic Watt-levels of power, while the quiet plasma power remains less than 100 W.

For a spacecraft in sun light the power required to maintain a fixed potential is shown in Figure 4.27 for each plasma condition. The inclusion of photoelectrons has very little effect on the power for a quiet plasma (λ_D = 4 m). The inclusion of photoelectrons and ion secondary emissions for negative potentials in nominal and disturbed plasmas slightly raises the required power, however the magnitude is still an order of magnitude lower than the quiet plasma.

The net current and consequent power required by an onboard charge control device to maintain a fixed potential is computed for three representative plasma conditions. A summary of the maximum power requirements for each plasma condition and spacecraft potential polarity is shown in Table 4.7. Each of the maximum power requirements occurs at the maximum potential level studied (|30| kV), except for the eclipse case, in the disturbed environment that occurs at -8 kV.

For the nominal TCS GEO plasma conditions the power requirements for this single 0.25 m radius craft is less than 1 W to charge between $\pm$ 30 kV. This power requirement increases linearly

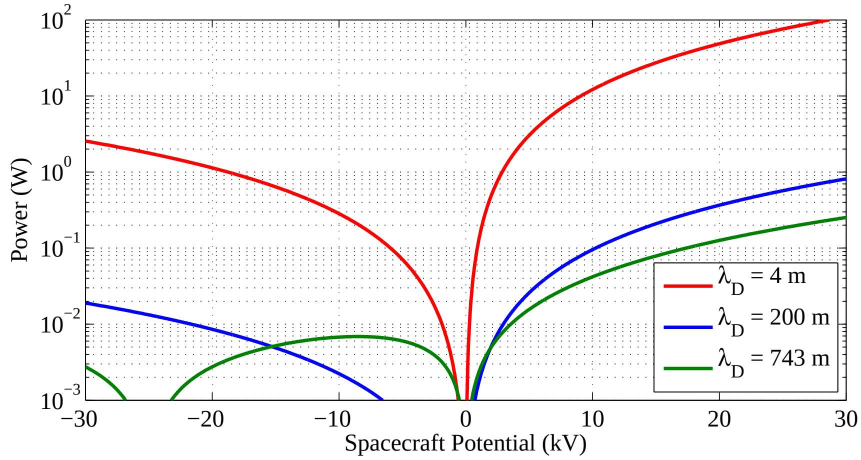

Figure 4.26: *Power required in eclipse to maintain fixed spacecraft potential for each plasma*

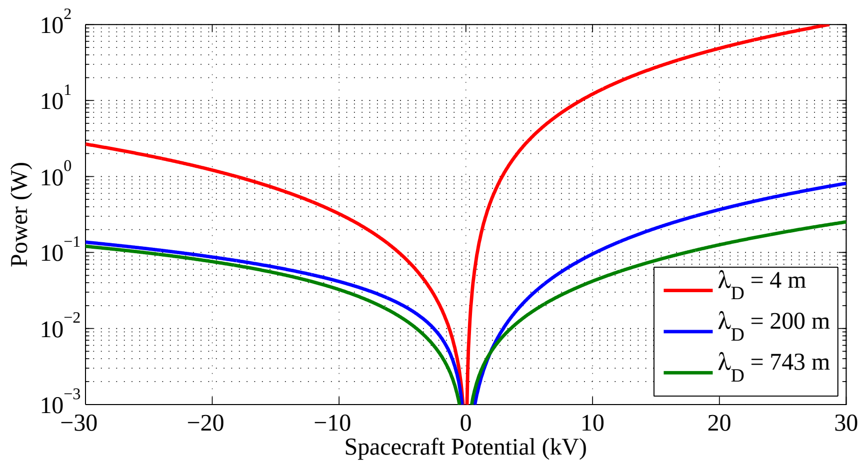

Figure 4.27: *Power required in sun light to maintain fixed spacecraft potential for each plasma*

with the number of Nodes in the TCS configuration. Operations in a quiet (worst-case) requires at least an order of magnitude greater power than the nominal conditions. The TCS spacecraft concept can use either charge polarity, however a negatively charged craft (emitting ions) will require less power than a positively charged spacecraft. This is because the electrons that have the same temperature as the ions (model assumption), but significantly smaller mass, are attracted and impact the charged craft during positive charging. Therefore for the same magnitude of charge the electron current will be higher than the ion current if the same particles have the same temperature (i.e. energy).

4.6.9 Plasma Equilibrium Currents and Floating Potentials

The low magnitude dips in the net current flow and power figures correspond to natural equilibrium conditions where $I_{\text{net}} = 0$. The location of this root occurs at the spacecraft floating potential. For a single-Maxwellian plasma there is a single root to the net current equation and consequently a sole equilibrium condition. At GEO this solution will typically produce a spacecraft floating potential that is slightly negative for sun-lit conditions and can go highly negative during eclipse. The single-Maxwellian floating potentials are shown in Table 4.8 for each of the plasma environment

Table 4.7: *Maximum Power [W] for Each Plasma and Spacecraft Potential Polarity Between the Range of Charging (-30 kV to 30 kV)*

Conditions	Polarity	Quiet (λ_D = 4 m)	Nominal (λ_D = 200 m)	Disturbed (λ_D = 743 m)
Eclipse				
	negative	2.55	0.02	0.007
	positive	109	0.81	0.25
Sun-lit				
	negative	2.67	0.14	0.12
	positive	109	0.81	0.25

Table 4.8: *Spacecraft Equilibrium Floating Potentials for Each Plasma Condition*

Conditions	Eclipse [V]	Sun-lit [V]
Quiet (λ_D = 4 m)	-8	5.3
Nominal (λ_D = 200 m)	-2250	6.0
Disturbed (λ_D = 743 m)	-25000	3.2

conditions studied here. These equilibria are advantageous to the TCS concept that can utilize these naturally occurring spacecraft potentials for very low power requirements.

It is also possible to have multiple roots (and floating potential solutions) with the inclusion of additional plasma currents. Using a single-Maxwellian plasma that includes secondary electron currents produces two roots that are a function of the plasma electron temperature and the material properties. The low temperature plasma root is typically not experienced at GEO.[65] As the plasma temperature increases to the second root (critical temperature) the spacecraft will go from slight positive charge to high negative potentials.[65,86] This occurs in eclipse with no photoelectrons and is a potentially hazardous scenario for a TCS application as the nodes could abruptly change charge polarity and magnitude losing required repulsive forces.

A double-Maxwellian can also be used to represent a GEO plasma. Although more complex, this can be more advantageous as it provides a more accurate fit to GEO plasma data and allows for analysis of high energy charging affects.[87] A double-Maxwellian is also more accurate in representing a GEO spacecrafts floating potential characteristics as it allows for multiple equilibrium roots to the net current equation.

With a double-Maxwellian plasma it is possible to have one, two or three roots depending on the plasma conditions. The low energy plasma determines the number of roots and the respective spacecraft charge.[65] A changing single-Maxwellian plasma will cause the spacecraft potential to change continuously. With the presence of a triple root represented with a double-Maxwellian it is possible to capture the abrupt spacecraft potential jumps that can occur in a changing plasma.[88,87] This is also an undesired charging situation for a TCS, that must be considered during future design and implementation stages.

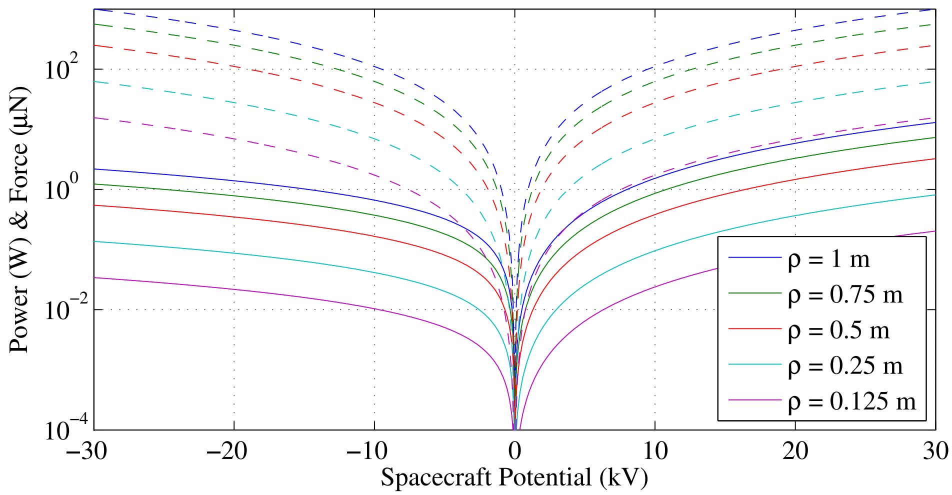

Figure 4.28: *Force generated and power required in sunlight [Solid = Power, Dashed = Force] as a function of sphere potential and radius. This is computed in a nominal plasma (λ_D = 200 m).*

4.6.10 Effect of Spacecraft Radius on Force Generation and Power Requirements

The power requirements of a TCS spacecraft also has an impact on the selection of the nodes radial size. A larger node will generate a greater Coulomb repulsive force (for a given potential level) while also requiring a larger power requirement due to a larger surface area interacting with the plasma. Analyzed here is the relationship between spacecraft radius and the magnitudes of force generation and power requirements to determine if there is an optimal TCS nodal size.

The Coulomb force generated between two spherical TCS nodes of potential V_{sc} is computed using the force of Eq. (2.1). This is an ideal force that ignores plasma shielding and true charge interactions of close spheres, however it is appropriate for the scaling comparison performed here.

The net power required for a spherical node is computed for the nominal plasma condition (λ_D = 200 m) in sunlight (photoelectrons included). The force and power is shown as a function of spacecraft potential for a range of possible spacecraft radii and shown in Figure 4.28. In this figure the solid lines represent the required power, the dashed lines are the Coulomb force generated.

Both the force and power are a function of $f(r^2)$, hence at a given voltage the proportional increase between each radial line is equivalent. Ultimately, there is no optimal radii, TCS nodal size should be selected based on total power limitations, mass and size constraints or minimum force required for a given potential.

The Coulomb force is a function $F = f(V_{sc}^2)$ which dictates the shape of the curves, and is equivalent magnitude for both positive and negative potentials. The power required during positive charging is a function $P(V_{sc} > 0) \approx f(V_{sc}^2)$ and hence has a similar profile to the force. However during negative charging in this nominal plasma, the dominant current is the constant photoelectrons and the resulting power is a function $P(V_{sc} < 0) \approx f(V_{sc})$. The result is that for negative charging lower power is required to achieve the equivalent force at a given potential.

To demonstrate the relationship between force and power, Figure 4.29 shows the ratio $\frac{F}{P}$. A large ratio value indicates more force is obtained per power required. This figure shows that for positive charging the ratio is constant. Figure 4.29 also shows that it is more advantageous to use negative charge as an equivalent force can be generated for less power than the same positive charge. This ratio value is independent of the craft radii used as force and power values are a function of $f(r^2)$.

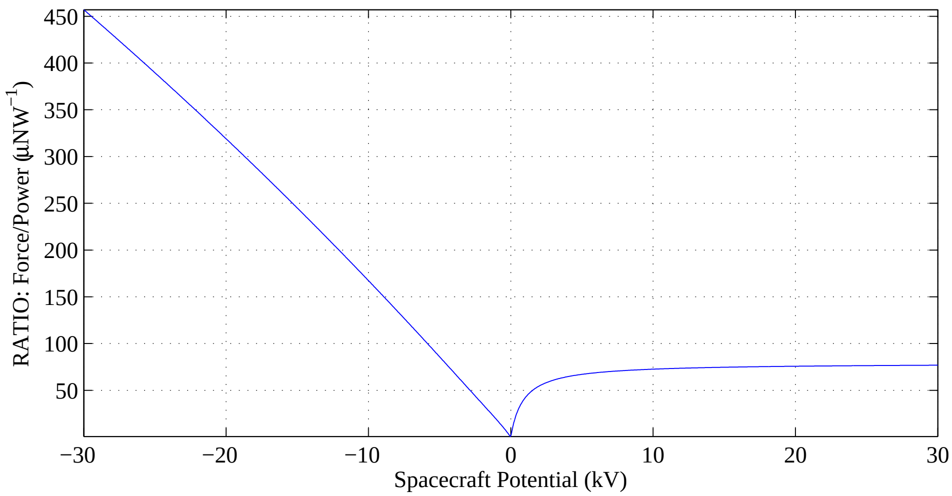

Figure 4.29: *Ratio between force generated and power required in sunlight and a nominal plasma (λ_D = 200 m) for a sphere of radius 0.25 m*

4.7 TCS Propellant Mass Estimates

An important consideration for a TCS node using a charge control device is the mass flow rate (ion emission) and total propellant mass required to maintain the desired surface potentials. Given an example two-node TCS with 0.25 m radii spheres operating in sunlit conditions in three representative plasma conditions (quiet, nominal, disturbed) the propellant mass requirements are computed. The propellant mass requirements of a Coulomb charge control system are compared to the propellant requirements of alternate electronic propulsion systems. An important consideration that is also analyzed here is the momentum exchange force from the emission of the charge control device.

4.7.1 Coulomb Thrust Propellant Mass Flow Rate

For a TCS maintaining a fixed potential in a plasma, the required propellant is the charged particles emitted as a current to offset the net plasma current. To charge to negative potentials positive ions from an onboard propellant source are emitted. For positive nodal charging, electrons that are either stored or obtained from solar energy are emitted.

The mass flow rate of propellant is the charge control emission current. For this study the mass flow rate, during negative charging, is computed using Xenon gas ions (Xe^+). For charge control emission it is most advantageous to use the lowest mass particles (ideally H^+ ions), however Xenon is used as it is a common hollow cathode propellant (See Appendix B) and it results in the largest (worst-case) mass flow rate, with a higher ion mass than Indium (a common field emission propellant).[75,89] The mass flow rate, during negative charging, is computed using:[14]

$$\dot{m} = \frac{|I_{\text{net}}| m_{\text{ion}}}{e_c} \tag{4.34}$$

where m_{ion} is the mass of the emitted ion species assuming it has a single charge. For positive charging, m_{ion} is replaced with m_{electron}, the mass of an electron, which is 5 orders of magnitude less than Xenon gas ions. An advantage of using electrons is that they are essentially free propellant as they can be obtained on-orbit from solar energy. Figure 4.30 shows the total mass flow rate

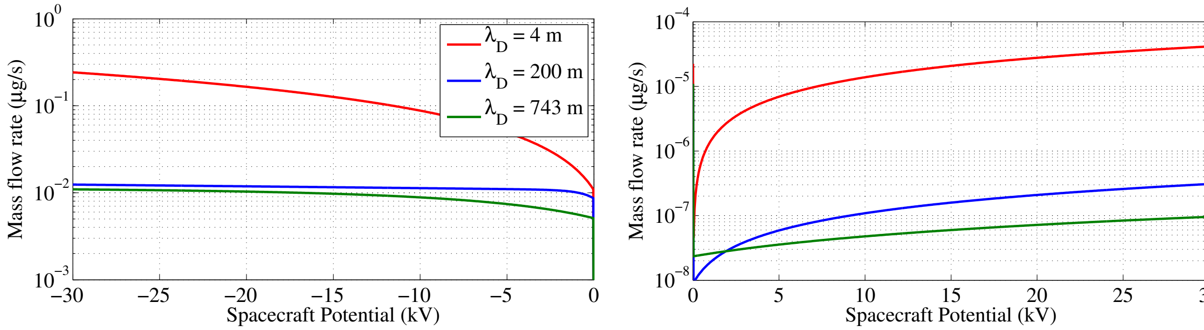

(a) Negative potentials emitting Xenon ions (b) Positive potentials emitting electrons

Figure 4.30: *Charge control mass flow rate in sunlight for a sphere of 0.25 m radius*

Table 4.9: *Maximum Mass Flow Rate [μgs^{-1}] for Each Plasma at a Given Spacecraft Potential*

Spacecraft potential	Quiet (λ_D = 4 m)	Nominal (λ_D = 200 m)	Disturbed (λ_D = 743 m)
-30 kV	0.24	0.012	0.011
+30 kV	4.2×10^{-5}	3.1×10^{-7}	9.6×10^{-8}

required by the two-node example TCS operating a charge control device(s) in sunlight. During eclipse, the mass flow rate is equivalent for positively charged craft and lower magnitudes for negatively charged craft, due to the lower net current. Table 4.9 lists the maximum mass flow rates for each of the plasma conditions. The maximum rates correspond to the extremes of the analyzed spacecraft potentials of $\pm$30 kV.

The maximum mass flow rate occurs during the worst case, quiet plasma conditions ($\lambda_D = 4$ m) as the net plasma current to the craft is at its highest level then. In a nominal plasma ($\lambda_D = 200$ m) mass flow rates are reduced by at least an order of magnitude. The mass flow rates are orders of magnitudes lower for positive charging as low mass electrons are emitted. The currents here are still higher, so a higher electrical power is required compared to the negative charging.

The highest expected mass flow rate for this two node system are below 0.24 μg/s for all expected plasma conditions. The current spacecraft charge control technology can produce mass flow rates as high as 0.1 A at 100 μg/s and 10 A at 200 μg/s.[90,91] The fact that the mass flow rates required by a TCS system are significantly lower, indicates that they can be achieved with current technology. Also, the mass flow rate analysis conducted here does not account for any inefficiencies in the charge control device. In addition, the charge control accuracy for a TCS node system is not important, rather that the overall charge is significant to maintain tether tension and overcome external disturbances. For this reason, a higher mass flow rate will increase the nodal charge and ultimately stiffness of the system.

4.7.2 Total Propellant Mass Comparison

For the two-node TCS example case it is beneficial to estimate the total propellant mass required by the charge control system. The propellant mass is compared to the mass requirements of alternate electric propulsion systems performing an equivalent node repulsive force. The example

Table 4.10: *Propellant Mass Requirements for a Two Node System Operating in a Orbit Normal Configuration at GEO for Ten Years; [10 m Separation, 0.25 m Radii, Nominal Plasma]*

Propulsion technology	I_{sp} (s)	Propellant mass (g)
PPT	500	684
Colloid	1000	342
FEEP	10000	34.2
Coulomb (Xe^+)	2×10^6	3.9
Coulomb (e^-)	∞	9.8×10^{-5}

used is the two-node TCS with spheres of 0.25 m radii. The nodes are operating in an orbit normal configuration at GEO with a desired separation of 10 m. Under these conditions a differential gravity force of 5.32 μN is compressing the 100 kg craft. In this naturally compressive orbit scenario, the repulsive Coulomb force maintains a taut tether.

To achieve this force in a nominal plasma requires the nodes to be charged to |9.0| kV. Charging to negative potentials occurs by emitting Xenon ions, while positive charging is achieved with electron emission. Both these propulsion emission options for the Coulomb system are computed. The first is negative spacecraft charging that emits Xenon ions (Xe^+) and the alternate is for positive spacecraft charging that emits electrons (e^-).

This two-node configuration could also be implemented with free-flying craft that utilize continuous electric propulsion with a thrust opposing the compressive differential gravity. The three electric propulsion methods analyzed are a micro Pulsed Plasma Thruster (PPT), a Colloid thruster, and a Field Emission Electric Propulsion (FEEP) thruster. An important implementation consideration with all of these propulsive methods is that they have possible plume contamination given the close operating proximity for this two-node example.

The total propellant mass requirements for each electric propulsion system is computed for a single node using the relationship:

$$m_{\text{propellant}} = \frac{t|T|}{g I_{\text{sp}}} \tag{4.35}$$

where t is the duration of propulsive maneuver, g is the gravitational constant and T is the desired thrust from a single node, which is equal to the differential gravity force. Table 4.10 gives a representative value of the specific impulse (I_{sp}) of each of the propulsion systems.

The propellant mass is calculated based on the propulsive system applying a continuous thrust to oppose the differential gravity force. This is computed to maintain a 10 m separation for 10 years. The required propellant mass of each of the propulsive methods for this two-node example is shown in Table 4.10. For the Coulomb system, the propellant mass flow rate is computed for a nominal plasma, λ_D = 200 m, in sunlit conditions from Figure 4.30. The propellant mass requirements of each of the propulsion systems is also shown in graphical form in Figure 4.31.

As shown in the Figure 4.31, the total propellant mass requirements are extremely low for a Coulomb system. If operating in a nominal GEO plasma environment, the TCS system requires less than 4 g of Xenon propellant for positive charging. This propellant mass will increases considering inefficiencies of the system and variable plasma environments, however it is still a significantly low requirement that is very competitive compared to alternate systems.

Another important consideration is the inert mass requirements of the charge control system. As an example, charge control devices for current space missions have masses ranging from 19

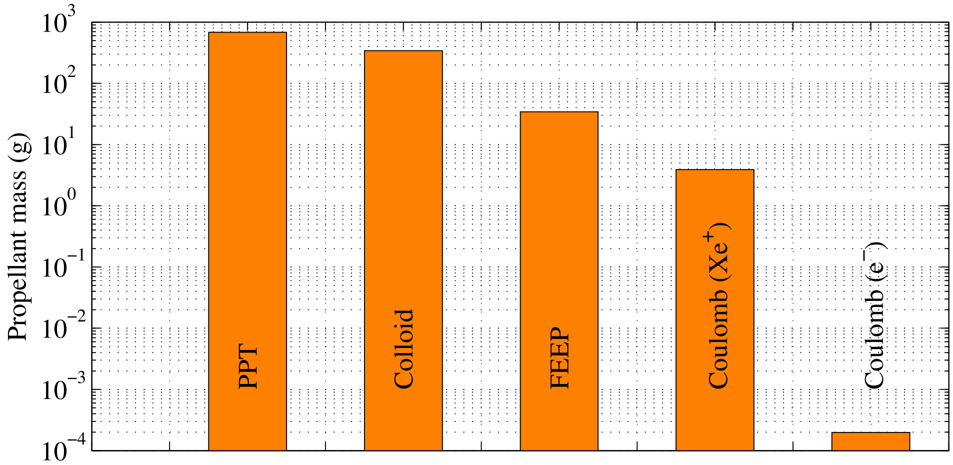

Figure 4.31: *Propellant mass estimates for each propellant system operating in an orbit normal configuration at GEO for ten years; [10 m separation, 0.25 m radii, nominal plasma conditions]*

kg on ATS-6[94] through to the more recent CLUSTER devices weighing only 1.85 kg each.[75,36]

4.7.3 Emission Current Net Force

The charge current required to maintain a fixed potential is emitted under electrostatic acceleration. An emission current of ions (negative craft potential) will result in a net momentum exchange and consequently force on the TCS nodes that feature charge control. In the earlier studies this force was shown to be negligible for the free-flying charged spacecraft study where the Debye lengths were assumed to be at least 80 meters or larger.[14] However, as Section 4.1 illustrates, these Debye length values are not sufficiently conservative, hence the use of the worst case plasma conditions of this study (λ_D = 4 m). This section investigates the magnitude of the charge-thrust force and compares it to the electrostatic force for the TCS application.

The charge-thrust force is computed for each of the plasma conditions and compared to the magnitude of the Coulomb force produced for a given two node system. The force on a single node from the emission current is computed using:[95]

$$F_{cc} = \dot{m} u_{ion} \tag{4.36}$$

where $\dot{m}$ is the mass flow rate and u_{ion} is the emission speed of the ions. The mass flow rate is computed using Eq. (4.34) the emitted ion species is assumed to be Xenon here. The emission speed is proportional to the spacecraft potential V_{sc} and is calculated using electrostatic repulsion:[95]

$$u_{ion} = \sqrt{\frac{2e_c V_{sc}}{m_{ion}}} \tag{4.37}$$

Combining Equations 4.34-4.37 the net charge control force is computed with:

$$F_{cc} = I_p \sqrt{\frac{2m_{ion} V_{sc}}{e_c}} \tag{4.38}$$

The extent of the charge emission force is compared to the Coulomb force of the two node system, separated by 2 m in Figure 4.32. The charge emission force (solid) is shown as a function of spacecraft nodal potential for each of the three representative plasma conditions (designated by Debye length). The emission force is computed for a single node of 0.25 m radius. Each node would require this calculated emission force to maintain equivalent potentials. The Coulomb force magnitude (dashed) is computed between two craft in each plasma and includes shielding and close sphere effects using the model of Eq. (2.13). The partial shielding is minimal for spacecraft in a nominal and disturbed plasma and the resulting Coulomb forces are approximately equal.

For a spacecraft to charge to negative potentials positive, ions are emitted. For this study the emission force is computed using Xenon gas ions, a common propellant that results in the largest (worst-case) mass flow rate. For positive charging, electrons are used as the emission charge as they are readily and freely obtainable from solar power in space.

Due to the lower power requirements to charge to negative potentials the Coulomb force is approximately three orders of magnitude greater than the charge emission force for the nominal ($\lambda = 200$ m) and disturbed ($\lambda = 743$ m) plasmas (a desired attribute). For the worst-case plasma ($\lambda = 4$ m) the Coulomb forces still dominate but with a lower margin. For a positively charged node the emission force is significantly reduced due to the emission of low-mass electrons. Only in the worst-case plasma is the charge emission force high, but still at least two orders of magnitude less than the corresponding Coulomb force. During the nominal and disturbed plasmas the charge emission force is below 2 μN.

As the separation distance between the spacecraft increases the Coulomb force magnitude reduces. For this two-node example, Figure 4.33 compares the force magnitudes for a center to center separation of 5 m. The results shown in this figure indicate that the Coulomb forces dominate the potentially disturbing charge emission forces. For all charge polarities and environments the Coulomb forces are at least two orders of magnitude larger, except for negative charging in a worst-case (quiet) plasma where there is approximately an order of magnitude difference.

Extended the two nodes out to 10 m separation causes the Coulomb forces reduce again to the levels shown in Figure 4.34. In this case, the Coulomb forces dominate in all regimes except for conditions of negative charging in the worst-case plasma environment. Here the charge emission force is slightly larger magnitude than the charge emission force from a single-stream current.

4.7.4 Discussion on Propellant and System Mass Requirements

The propellant mass flow requirements for a TCS system charge control device are low (μA levels) and easily achievable with space proven technology. A list and small description of charge control technology is given in Appendix B. The charge control device inert mass is estimated to be low, in the low kg range, which matches well with current charge control technology. The Coulomb propellant mass is also estimated to be very low, being hundreds of grams for a 10 year mission, with two nodes in a nominal plasma.

An advantage of the Coulomb thrust technique for a TCS is that the required inert system mass and propellant mass are estimated to be lower than the three electric propulsion methods analyzed. The overall propulsion mass requirements will be in the low kilogram level, which could be easily implementable on small TCS nodes. The Coulomb concept also eliminates the concern for exhaust plume impingement that is present with the alternate electric propulsion methods.

The two node example used for the comparison does not distinguish how the TCS system achieves and maintains charge. Depending on the mission application and number of nodes it is possible to have a single large charge control device that conducts charge to all nodes in the configuration through conducting tethers or use a small device on each node.

One consideration for the implementation of a charge control device to a TCS configuration is the force from the momentum of the charge emission current. Depending on the relative orientation of the charge emission current from the node, this may apply a perturbation to the TCS

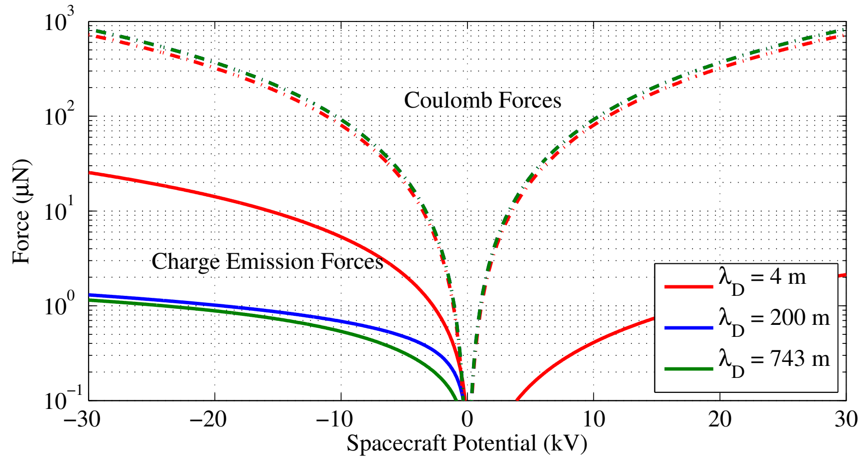

Figure 4.32: *Force magnitude comparison for two craft of 0.25 m radius and 2.5 m separation in each plasma. Charge control emission forces (solid) and Coulomb forces (dashed).*

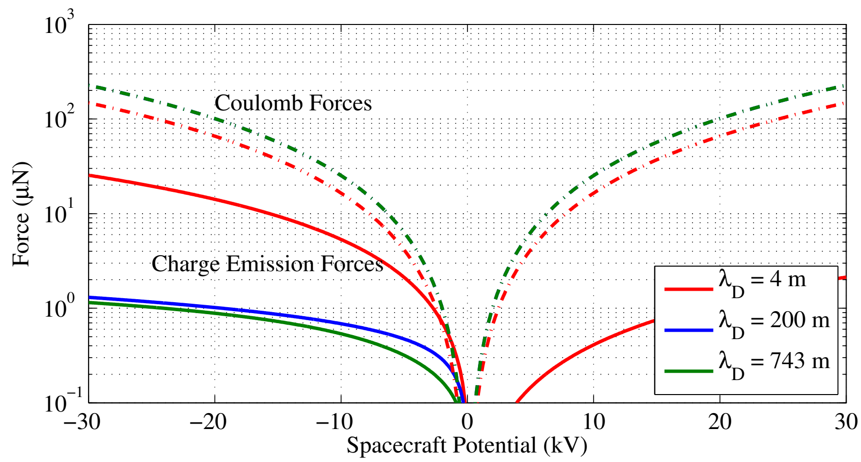

Figure 4.33: *Force magnitude comparison for two craft of 0.25 m radius and 5 m separation in each plasma. Charge control emission forces (solid) and Coulomb forces (dashed).*

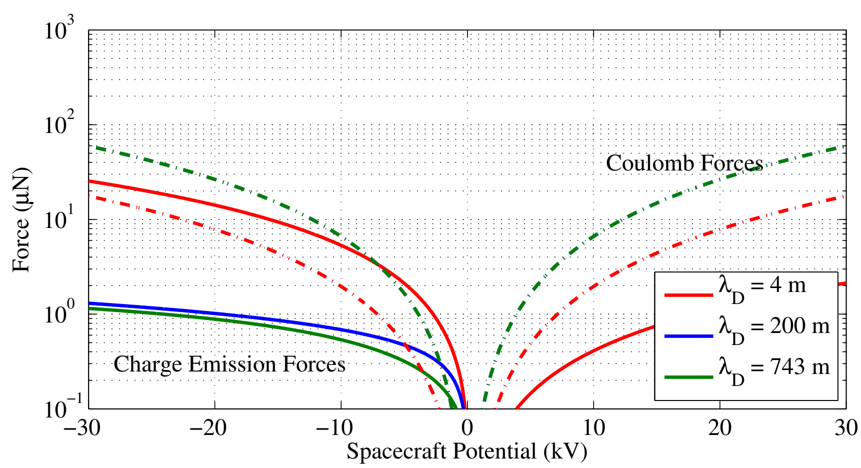

Figure 4.34: *Force magnitude comparison for two craft of 0.25 m radius and 10 m separation in each plasma. Charge control emission forces (solid) and Coulomb forces (dashed).*

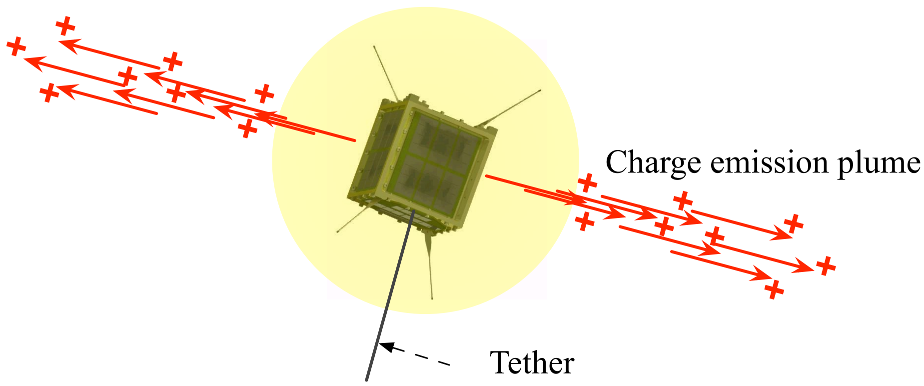

Figure 4.35: *Illustration of bi-directional charge emission*

configuration. The magnitude of the charge emission current is compared to the Coulomb inflation force for an example two node system with separations of 2.5, 5, and 10 meters. It is shown that for all plasma conditions and charging polarities for the close separations (2.5 and 5 m) the Coulomb forces will dominate the charge emission force. However, separations as great as 10 m are approaching the limits of separation that maintain dominant Coulomb forces. This is however only for the rare worst-case plasma operating environments.

This study indicates that consideration for the placement and direction of the charge control device on the nodes should be made. If a single charge control device on a node is used to charge a whole TCS the emission force can be close or even greater than the Coulomb force magnitudes during negative charging and worst-case plasma conditions. With appropriate placement and the use of multiple emitters the emission force can be directed to create zero net force on the node and not interfere with Coulomb inflation forces. An conceptual example of a charged node with zero net force charge emission plumes is shown in Figure 4.35.

Chapter 5

Conclusions and Future Work

5.1 TCS Study Conclusions

This study expands the developments of the TCS concept and highlights the feasibility as a future space structure concept. A TCS uses a unique combination of very thin tethers and electrostatic inflation to maintain a spacecraft formation to a desired size and shape. Electrostatic repulsion is employed to maintain tether tensions and overall structural stiffness. It is demonstrated in this study that this unique spacecraft design combination offers a practical, stable space platform that can overcome perturbations such as GEO differential gravity, solar radiation pressure, and initial rotations. Applications for such TCS systems include interferometry sensing missions, local situational awareness, primary spacecraft inspections, and variable or large baseline sensing missions.

Nonlinear three-dimensional simulations provide insight into how well the TCS is able to reject initial angular rate disturbances and avoid tether/node interaction issues. Here the TCS nodes are modeled through six degrees-of-freedom (translation and rotation), and the tethers are modeled with proportional stiffness components and nonlinear end-point displacements. This nonlinear simulation can simulate hours of TCS dynamic response in a few minutes, and is suitable for doing parametric sweeps. The study is performed for a single-, double- and triple-tether configuration. Additional tethers can increase the rotational stiffness, while reducing the resulting absolute angular node deflection by up to 75%. While the absolute maximum rotation is reduced with multi tethers, the nodes are still susceptible to entanglement as the tether attachment points are initially closer to the maximum rotation angle. With a triple-tether configuration rotational control is achieved about all axis. This assumes potentials in the range of 10-50kV. As a comparison, current GEO spacecraft can naturally charge up at times to levels as high as 20kV. This study indicates that a TCS system can be stiffened under Coulomb forces to resist deployment or external rotational disturbances on the order of 30-60 degrees per minute. While these are small rotational rates, they provide an indication of how smoothly the TCS nodes must be separated and deployed if no force field controls or damping are considered.

To study the motion of the tether itself, a sophisticated nonlinear finite element solver is employed. The TCS nodes are modeled as rigid components, while the fixed length tether is sub-partitioned into a set of finite elements. Such finite element simulations can take many hours for a single test run. However, this increased computation cost provides insight into the conditions where the simpler tether model of the nonlinear TCS dynamics simulation is justified. Several tests are performed to investigate how the tether thickness, mass, and charge can influence the TCS nodal motion. The research shows that the simpler TCS model is sufficient to obtain coarse predictions of the overall TCS motion, and to study the primary effects of tether attachment location choices, TCS node parameters, etc. The more complex finite element TCS dynamics simulation performed a minimum tether strength study to determine what tether thickness is required to be able to withstand initial TCS nodal rotations of 30 degrees per minute. The result was a thin tether with only about 2.6μm diameter. A tether 10 times larger is then used to study the impact of residual strain on the tethered system. Even assuming very conservative worst case strain (i.e. maximum possible thermal difference, strains close to the material yield), the impact on the TCS nodal motion is very small, often only fractions of a degree.

The tether thickness has a strong influence on whether the tether dynamics will impact the TCS nodal dynamics. A sweep is performed with the finite element simulations which show that if the tether cross sectional area is less than 10^{-8}m^2 for the nominal TCS configuration, then the eigen-strains will have negligible influence. Even considering non-uniform eigenstrain distributions, the results indicate that the sufficiently thin tether can avoid impacting the TCS motion in a significant way.

A preliminary TCS tether finite element study is performed to investigate the impact of having the tether itself be charged to the same potential as the TCS nodes. The results indicate that the charged tether can help increase the shape stiffness, and reduce the relative motion of the nodes. The tether charging can also help prevent excessive deformation of the tether as the tether begins to self-repel.

With the development of the TCS concept it is beneficial to understand the effect of TCS node inertia, size, and tether attachment angle (for multiple tethers) on the rotational stiffness. The advantages of a lower inertia are quantified along with the increased moment arm from larger node sizes. Two- to three-fold increases in rotational stiffness can be achieved by moving the node mass towards its center. Further, the impact of the TCS shape on the minimum charge requirements to maintain tether tension in the presence of differential gravity is explored. It was found that adding additional nodes with equal charge polarity does not necessarily increase the tether tensions. In particular, the study fund a case where having charge nodes in a non-fully-interconnected TCS setup can cause some tethers to be in compression. As a result, this study illustrates how care must be taken when designing the TCS nodal spacing and configuration to increase the tether tension.

Larger nodes have to consider space plasma interaction and power requirements which is also investigated in this study. Using representative GEO plasmas it is shown that Coulomb force shielding is minimal in a nominal GEO space plasma environment. In addition, it is demonstrated that the power levels required to maintain a fixed potential using a charge emission device are feasible (Watt levels) with current space proven technology. The required propellant and dry system mass for an example two-node TCS is only kilograms and offers savings over comparable electric propulsion systems.

Of particular interest are the worst-case GEO space weather conditions that must be considered. While nominal plasma Debye lengths are on the order of 200 meters, occasionally the colder plasma-pause region can get pushed into the GEO region. This study adopts worst case GEO Debye lengths on the order of 4 meters. While such low Debye lengths do impact the electrostatic force and associated power computations, the power levels can remain in the 10's of Watt range if ions are emitted and the nodes are charged to negative potentials. Further, numerical simulations of the full Poisson-Vlaslov equations are performed to illustrate that the TCS potentials considered in this study yield effective Debye lengths that are multiple times larger than the regular Debye lengths. As a result, the rotational stiffness of a multi-meter length TCS system only changes by up to 20% during such worst case plasma conditions. Further, advanced numerical particle-in-cell simulations were performed to investigate if having overlapping Debye sheaths will cause our analytical force and power predictions to change. It was found that even with very dense and cold

GEO plasma the overlapping Debye sheaths only caused a very percent change in forces thanks to the relatively large potentials being considered.

5.2 Future Work Considerations

The prospects of the TCS concept are strengthened with these findings and will lead to further developments. Key areas of future investigation could include the feasibility of nodal relative motion damping, controlling initial nodal deployment motions, investigating the TCS deployment challenges, as well as the ability to reconfigure nodal relative positions for TCS shape morphing considerations.

Advanced charge and TCS attitude control laws should be investigated to dampen out both translational and rotational shape deformations. One possibility is consider having a combined Coulomb momentum control law.

The process of how to deploy a TCS system has not been explored in this study, and should be considered in future TCS research. The non-autonomous (time dependent) tether dynamics greatly complicate the associated dynamical systems study. Further, larger TCS systems with more than three nodes are of interest because these system could increase TCS sizes to 100+ m. However, modeling such systems will lead to interesting macro-scale structural stability and stiffness investigations.

To consider the challenges of deployment, the complex electrostatic interactions between close components must be considered in more detail. The induced charge effects can cause repulsive electrostatically force to be reduced significantly when the bodies are almost touching. The current tether finite element simulations assume a fixed charge distribution for a given potential level. A more general multi-physics simulation code would be able to solve the electrostatic field equations simultaneously with the structural continuum mechanics equations to yield higher fidelity TCS simulations. Such complex simulation software would then also be able to simulate the expected response for TCS deployment, reconfigurations, and provide better predictions of any TCS shape damping methods being proposed. Another future research direction is the question on how to do orbit corrections or changes with a TCS system. Due to the small inflationary forces, low thrust options must be considered, and the resulting TCS shape deformation studies. To perform an orbit correction, it is envisioned that the TCS shape will deform considerably during the orbit maneuver, but would then resume its original equilibrium shape after the thrusting. Of interest is how large such deformations would be. Having an effective TCS shape damping mechanism would be critical to assist reduce the final settling times.

Appendix A

TCS Dynamic Model Verification

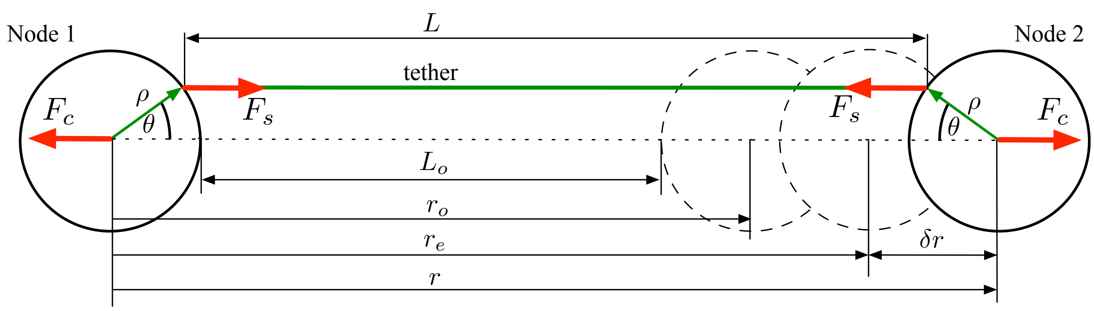

Figure A.1: *Asymmetric two-node system with two degrees of freedom*

A.1 Linearized Equations of Motion

Figure A.1 depicts the prototype benchmark two-node TCS system which is the baseline configuration for many studies. This appendix outlines how the numerical codes were verified. First, analytical equations of motion are obtained for small departure motion cases about the equilibrium configurations. The linearized equations of motion for two-node TCS are[2]

$$\delta\ddot{r} \approx -\frac{1}{m}\left[\frac{2k_cQ}{r_e^3(Q)} + k_s\right]\delta x \tag{A.1}$$

for translation and

$$\ddot{\theta} \approx \frac{-\rho k_s}{I}\left[r_e(Q) - r_o\right]\theta \tag{A.2}$$

for rotation where $r_e(Q)$ is the equilibrium separation distance, r_o is the TCS separation distance with no tension in the tension, Q is the charge product of the two nodes. The tether is modeled as proportional spring with nonlinear displacement model. This setup does not consider any tether inertial or mass properties. The linearized equations of motion yield a translational frequency of

$$\omega_T = \sqrt{\frac{1}{m}\left[\frac{2k_cQ}{r_e^3(Q)} + k_s\right]} \tag{A.3}$$

and a rotational frequency of

$$\omega_R = \sqrt{\frac{\rho k_s}{I}\left[r_e(Q) - r_o\right]} \tag{A.4}$$

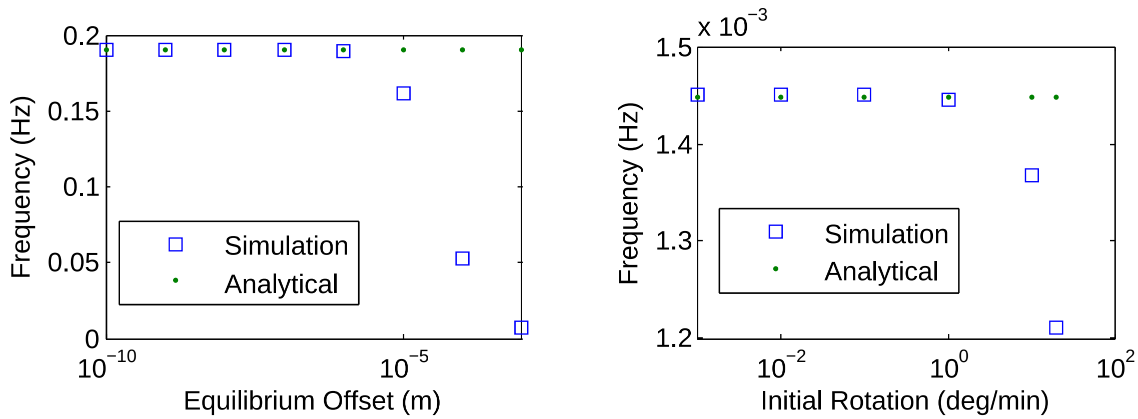

(a) Translational Frequency (b) Rotational Frequency

Figure A.2: *Frequency comparison between simulation and analytics*

Figure A.2 shows a comparison of the 6 degrees of freedom TCS simulation translational and rotational frequencies as compared to the analytical frequencies. For the translational frequencies, the TCS was set with each node offset from equilibrium by an equal distance. For the rotational case, the nodes were set at TCS and then given an initial rotation. Figure A.2 shows that both translational and rotation frequencies agree with the analytically predicted response for small deflections. However, it can be seen that the linearization begins to break down at a translational offset of more than 10^{-4}m and an initial rotation of more that 1 deg/min. Even so, the figure further validates the use of the nonlinear TCS numerical simulation.

A.2 Tether Model Comparison

The numerical simulation (called TCS Sim) for the dynamic modeling of TCS systems models a tether as a proportional spring with non-linear end displacements. This simplified tether model is used to allow for a significantly increased speed in simulation runs. A higher fidelity finite element model (FEM) was used to model TCS tethers as well. Nearly identical simulations for the benchmark system in Figure A.1 were run using both models. The differences are due to the finite element model accounting for small tether inertia and mass terms, as well as abilities to handle compression. The simpler TCS Sim assumes the tethers are massless and cannot handle any compression. The single-element tether model used in these verification runs are only for the purpose of comparing the two code sets. The resulting TCS dynamics should be very similar in both cases. For the detailed structural tether analysis much larger numbers of tether elements are employed, allowing the FEM to simulate tether wrinkling and buckling.

A comparison of the two simulation results for position and rotation states is given in Figure A.3. The simpler TCS Sim models the tether response through a proportional stiffness model, and the FEM case is the result of the finite element code where a single element is used to model the tether. The simulations were conducted with the single-tether two-node rotational TCS configuration in Figure 2.6 with the parameters of Table 2.3. However, the inertia of the craft is modeled as a disk and the initial rotation is 30 deg/min. Additionally, for this comparison a simplified charge model of

$$V_i = \frac{q_i k_c}{\rho}$$

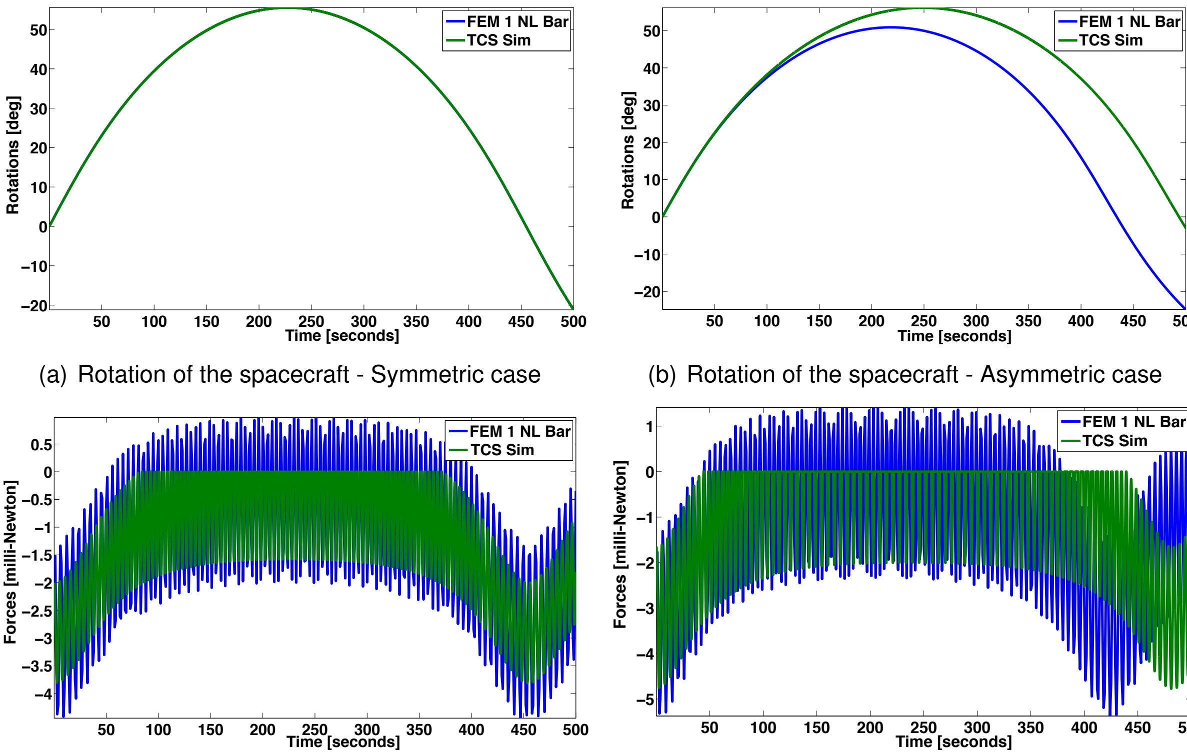

(a) Rotation of the spacecraft - Symmetric case

(b) Rotation of the spacecraft - Asymmetric case

(c) Axial forces on the tether at spacecraft attachment point - Symmetric case

(d) Axial forces on the tether at spacecraft attachment point - Asymmetric case

Figure A.3: *Comparison between nonlinear TCS simulation with proportional tether stiffness model, and the finite element simulation using a single tether element.*

is used because the FEM model is not currently incorporating Equation 2.7.

From the figure it can be seen that both models provide very similar rotational and translational TCS dynamics. The main differences arise with the asymmetric test case where stronger compressive components are encountered, and the differences in handling compression between the two simulations is more noticeable. These plots illustrate that the basic 6-DOF TCS nodal dynamics is being implemented correctly in both sets of numerical simulations. The small oscillation response of the TCS sim was also confirmed with analytical linearized response predictions, providing further confidence in the validity of the numerical simulations.

Appendix B

Charge Control Hardware Options

Charging of spacecraft in a space plasma is a natural process that can be regulated or enhanced for TCS purposes using a charge emission device. Two primary charge control devices that have been proven in space is the use of hollow cathodes to emit noble gas ions and with the field emission technique using metal ions. Documented here is an overview of these technologies used on space missions with the intent that these are similar devices to what is to be used by a TCS system.

Hollow cathode emission uses an electric field to bombard a noble gas with electrons, causing ion generation. The ions are then accelerated away from the spacecraft. Typical gases are Argon, Krypton or Xenon that are typically stored in tanks up to 1000 psi.[96] Table B.1 gives a summary of technologies currently available or in planning or have been used on space missions.

Table B.1: *Hollow Cathode Space Technology Examples*

Mission	Technology Description
SCATHA[97]	Electron gun and Xenon ion beam for positive and negative charging.
ISS[98, 99]	Features a plasma contactor to prevent large structure charging in LEO. It features an electron emitter based on FEEP neutralizer technology. ISS unit mass is 21 kg and uses an idle power of 80 W, peak 180 W. A similar unit with 5 kg mass and 5 W idle, 10 W peak also developed.
ProSEDS[91]	Was intended to be launched in 2003 to test an electrodynamic tether.[1] Stores 245 g of Xenon gas at 8-10 MPa in 0.3 L volume. Emission currents of 0-10 A. At 10 A gas consumed at 0.2 mg/s. The system is 20x30x13 cm in size and weighs 6 kg with a 30 W operating power. A smaller version $<$1 A max output weighs 5.6 kg and operates on 5 W.
POLAR[81]	Emits Xenon plasma to obtain operating potentials as low as 1.8 V relative to plasma.
-	In 2000, a 'state of the art' system is considered a 8W system with Xenon emitted at 100 mA at a rate of 0.1 mg/s.[90]

The alternate charge control device used in space is field emission with metal ions. This technique emits ions from a needle apex that are evaporated from a metal liquid source using field evaporation. Table B.2 gives a summary of field emission technologies used on space missions.

A miniaturized current collection device that operated on a CubeSat project is an alternate

Table B.2: *Field Emission Space Technology Examples*

Mission	Technology Description
ATS - 6[94,100]	Uses Xenon neutralizing current $>$1 mA at energies $<$ 50 eV. Total instrument mass with plasma measurement devices is 19 kg. Total power of 28 W, storing Xenon gas at 800 psi in a 2 L tank. Also featured Cesium attitude thrusters that were shown to neutralize charging. Ions accelerated under the magnetoelectrostatic concept with an emission current of 0.1A at 550 eV.
ATS - 5[101]	Cesium ion engine with filament neutralizers.
CLUSTER[75,36]	Indium ion emitter with feedback control to maintain zero potential relative to the environment. Emission currents of 10-15 μA at energies of 5-8 keV. Liquid indium is kept at 520 K (247 $^\circ$C) with an instrument mass of 1.85 kg and total power $<$ 2.7 W. Only a ion emission source is used as spacecraft is always in sunlight.
Geotail[89,35,102]	Two instruments each containing 4 Indium ion emitters, with a mass of 1.8 kg, measuring 19 x 16 x 17 cm. Ion current of $\approx$ 15 μA at $\approx$ 6 keV with a beam divergence less than 30 degrees. Electrodes operate at $\approx$ 6 kV with a heater power of 0.55 W.
Equator-S[89,35]	Indium ion emitter inherited from Geotail and CLUSTER and designed as test for CLUSTER-II. Instrument mass of 2.7 kg and max power of 2.7 W, with max potential of 8.3 kV. Heaters take 15 mins to heat Indium from 200 mg reservoir to operating liquid temperatures.
Double Star (TC-1)[103,81]	Improved version of CLUSTER Indium ion instrument. A potential of 4-9 kV emits ions between 10-50 μA. Instrument mass is 2.54 kg, max power is 2.9 W and operational life is extended to 16000 hr.

method of performing charge control. The miniaturized electrodynamic experiment was flown on the Calpoly CP-6 spacecraft to measure the collection of electrons from the LEO plasma. At the end of a 1.1 m insulated tape is a tungsten wire that is resistant heated and used to emit electrons. Two collector tapes are then uncoiled and used to collect electrons from the plasma.[104] Ultimately, the hardware required for charge control of the TCS nodes is space-proven technology. In addition, the potential levels anticipated for effective TCS repulsive forces have been demonstrated to date in space with this technology.

Bibliography

[1] Seubert, C. R. and Schaub, H., "Tethered Coulomb Structures: Prospects and Challenges," *Journal of the Astronautical Sciences*, Vol. 57, No. 1-2, Jan.–June 2009, pp. 347–368.

[2] Seubert, C. R. and Schaub, H., "Impact of Nodal Attitude Motion on Two-Element Tethered Coulomb Structures," *AAS/AIAA Spaceflight Mechanics Meeting*, San Diego, CA, Feb. 14–18 2010, Paper AAS 10-268.

[3] Freeland, R. E., Bilyeu, G. D., , Veal, G. R., and Mikulas, M. M., "Inflatable Deployable Space Structures Technology Summary," *49th International Astronautical Congress*, Melbourne, Australia, Sept. 28 – Oct. 2 1998.

[4] Cobb, R. G., Lindemuth, S. N., Slater, J. C., and Maddux, M. R., "Development and Test of a Rigidizable Inflateble Structure Experiment," *45th AIAA/ASME/ASCE/AHS/ASC Structures, Structural Dynamics & Materials Conference*, Palm Springs, CA, April 19–22 2004, Paper No. AIAA 2004–1666.

[5] Tarazaga, P. A., Inman, D. J., and Wilkie, W. K., "Control of a Space Rigidizable Inflatable Boom Using Macro-fiber Composite Actuators," *Journal of Vibration and Control*, Vol. 13, No. 7, 2007, pp. 935–950.

[6] Fang, H., Knarr, K., Quijano, U., Huang, J., and Thomson, M., "In-space Deployable Reflectarray Antenna: Current and Future," *AIAA/ASME/ASCE/AHS/ASC Structures, Structural Dynamics and Materials Conference*, Schaumburg, IL, April 7-10 2008.

[7] Hyde, R., Dixit, S., Weisberg, A., and Rushford, M., "Eyeglass: A Very Large Aperture Diffractive Space Telescope," *Highly Innovative Space Telescope Concepts*, 2002.

[8] Hyde, R., "Eyeglass Large Aperture, Lightweight Space Optics," Tech. Report UCRL-ID-151390, University of California, Lawrence Livermore National Laboratory, Feb. 10 2003.

[9] Carpenter, K. G., Schrijver, C. J., Karovska, M., and Team, S. M. C. D., "The Stellar Imager (SI) Project: A Deep Space UV/Optical Interferometer (UVOI) to Observe the Universe at 0.1 Milli-arcsec Angular Resolution," *Proceedings of the NUVA Conference*, El Escorial, Spain, June 2007.

[10] Blackwood, G., Henry, C., Serabyn, E., Dubovitsky, S., Aung, M., and Gunter, S. M., "Technology and Design of an Infrared Interferometer for the Terrestrial Planet Finder," *AIAA Space 2003*, Long Beach, CA, Sept. 23–25 2003, Paper No. AIAA 2003-6329.

[11] Brown, O. and Eremenko, P., "Fractionated Space Architectures: A Vision for Responsive Space," *4th Responsive Space Conference*, Los Angeles, CA, April 23–26 2006, Paper No. AIAA-RS-2006-1002.

[12] Gill, E., D'Amico, S., and Montenbruck, O., "Autonomous Formation Flying for the PRISMA mission," *AIAA Journal of Spacecraft and Rockets*, Vol. 44, No. 3, May–June 2007, pp. 671–681.

[13] Cover, J. H., Knauer, W., and Maurer, H. A., "Lightweight Reflecting Structures Utilizing Electrostatic Inflation," US Patent 3,546,706, October 1966.

[14] King, L. B., Parker, G. G., Deshmukh, S., and Chong, J.-H., "Spacecraft Formation-Flying using Inter-Vehicle Coulomb Forces," Tech. report, NASA/NIAC, January 2002, `http://www.niac.usra.edu`.

[15] Schaub, H., Parker, G. G., and King, L. B., "Challenges and Prospect of Coulomb Formations," *Journal of the Astronautical Sciences*, Vol. 52, No. 1–2, Jan.–June 2004, pp. 169–193.

[16] Miller, D. W., , Sedwick, R. J., Kong, E. M. C., and Schweighart, S., "Electromagnetic Formation Flight for Sparse Aperture Telescopes," *IEEE Aerospace Conference Proceedings – Volume 2*, Big Sky, Montana, March 9–16 2002.

[17] Peck, M. A., "Prospects and Challenges for Lorentz-Augmented Orbits," *AIAA Guidance, Navigation and Control Conference*, San Francisco, CA, August 15–18 2005, Paper No. AIAA 2005-5995.

[18] Peck, M. A., Streetman, B., Saaj, C. M., and Lappas, V., "Spacecraft Formation Flying using Lorentz Forces," *Journal of British Interplanetary Society*, Vol. 60, July 2007, pp. 263–267.

[19] Streetman, B. and Peck, M. A., "New Synchronous Orbits Using the Geomagentic Lorentz Force," *AIAA Journal of Guidance, Control, and Dynamics*, Vol. 30, No. 6, Nov.–Dec. 2007, pp. 1677–1690.

[20] Yamakawa, H., Bando, M., Yano, K., and Tsujii, S., "Spacecraft Relative Dynamics under the Influence of Geomagnetic Lorentz Force," *AIAA Guidance, Navigation and Control Conference*, Toronto, Canada, Aug. 2–5 2010, Paper No. AIAA 2010-8128.

[21] Jones, L. L. and Peck, M. A., "Stability and Control of a Flux-Pinned Docking Interface for Spacecraft," *AIAA Guidance, Navigation and Control Conference*, Toronto, Canada, Aug. 2–5 2010, Paper No. AIAA 2010-8298.

[22] Gersh, J., "Architecting the Very-Large-Aperture Flux-Pinned Space Telescope: A Scalable, Modular Obtical Array with High Agility and Passively Stable Orbital Dynamics," *AAS/AIAA Astrodynamics Specialist Conference*, Honolulu, Hawaii, Aug. 18–21 2008.

[23] King, L. B., Parker, G. G., Deshmukh, S., and Chong, J.-H., "Study of Interspacecraft Coulomb Forces and Implications for Formation Flying," *AIAA Journal of Propulsion and Power*, Vol. 19, No. 3, May–June 2003, pp. 497–505.

[24] Wang, S. and Schaub, H., "Switched Lyapunov Function Based Coulomb Control of a Triangular 3-Vehicle Cluster," *AAS/AIAA Astrodynamics Specialist Conference*, Pittsburgh, PA, Aug. 9–13 2009, Paper AAS 09–391.

[25] Wang, S. and Schaub, H., "One-Dimensional 3-Craft Coulomb Structure Control," *7th International Conference on Dynamics and Control of Systems and Structures in Space*, Greenwich, London, England, July 16–20 2006, pp. 269–278.

[26] Wang, S. and Schaub, H., "Nonlinear Coulomb Feedback Control of a Spinning Two Spacecraft Virtual Structure," *AAS/AIAA Astrodynamics Specialist Conference*, Pittsburgh, PA, Aug. 9–13 2009, Paper AAS 09–393.

[27] Wang, S. and Schaub, H., "Nonlinear Charge Control for a Collinear Fixed Shape Three-Craft Equilibrium," *AAS/AIAA Astrodynamics Specialist Conference*, Toronto, Canada, Aug. 2–5 2010, AIAA-2010-7955.

[28] Natarajan, A. and Schaub, H., "Linear Dynamics and Stability Analysis of a Coulomb Tether Formation," *AIAA Journal of Guidance, Control, and Dynamics*, Vol. 29, No. 4, July–Aug. 2006, pp. 831–839.

[29] Natarajan, A. and Schaub, H., "Orbit-Nadir Aligned Coulomb Tether Reconfiguration Analysis," *Journal of the Astronautical Sciences*, Vol. 56, No. 4, Oct. – Dec. 2008, pp. 573–592.

[30] Natarajan, A., Schaub, H., and Parker, G. G., "Reconfiguration of a Nadir-Pointing 2-Craft Coulomb Tether," *Journal of British Interplanetary Society*, Vol. 60, No. 6, June 2007, pp. 209–218.

[31] Izzo, D. and Pettazzi, L., "Self-assembly of large structures in space using intersatellite Coulomb forces," *57th International Astronautical Congress*, Valencia, Spain, October 2006, Paper IAC-06-C3.4/D3.4.07.

[32] Mullen, E., Frederickson, A. R., Murphy, G. P., Ray, K. P., Holeman, E. G., Delorey, D., Robson, R., and Farar, M., "An Autonomous Charge Control System at Geosynchronous Altitude: Flight Results for Spacecraft Design Considerations," *IEEE Transactions on Nuclear Science*, Vol. 44, No. 6, December 1997, pp. 2188 – 2914.

[33] Fennell, J. F., Koons, H. C., Roeder, J. L., and Blake, J. B., "Spacecraft Charging: Observations and Relationship to Satellite Anomalies," *Spacecraft Charging Technology*, edited by R. A. Harris, Vol. 476 of *ESA Special Publication*, Nov. 2001, pp. 279–285.

[34] Garrett, H. B. and Whittlesey, A. C., "Spacecraft Charging, An Update," *IEEE Transactions on Plasma Science*, Vol. 28, No. 6, Dec. 2000, pp. 2017–2028.

[35] Torkar, K. and et. al., "Spacecraft Potential Control aboard Equator-S as a Test for Cluster-II," *Annales Geophysicae*, Vol. 17, No. 12, 1999, pp. 1582–1591.

[36] Torkar, K., Riedler, W., and Escoubet, C. P., "Active Spacecraft Potential Control for Cluster – Implementation and First Results," *Annales Geophysicae*, Vol. 19, No. 10/12, 2001, pp. 1289–1302.

[37] Pierrard, V., Goldstein, J., André, N., Jordanova, V., Kotova, G., Lemaire, J., Liemohn, M., and Matsui, H., "Recent Progress in Physics-Based Models of the Plasmasphere," *Space Science Reviews*, Vol. 145, No. 1, 05 2009, pp. 193–229, DOI:10.1007/s11214-008-9480-7.

[38] Gurnett, D. A. and A., B., *Introduction to Plasma Physics - with Space and Laboratory Applications*, Cambridge University Press, New York, NY, 2005, Pages 8–9.

[39] Whipple, E. C., "Potentials on Surfaces in Space," *Rep. Prog. Phys*, Vol. 44, No. 11, 1981, pp. 1197–1250.

[40] Murdoch, N., Izzo, D., Bombardelli, C., Carnelli, I., Hilgers, A., and Rodgers, D., "The Electrostatic Tractor for Asteroid Deflection," *58th International Astronautical Congress*, 2008, Paper IAC-08-A3.I.5.

[41] Smythe, W. R., *Static and Dynamic Electricity*, McGraw–Hill, 3rd ed., 1968.

[42] Sliško, J. and Brito-Orta, R. A., "On approximate formulas for the electrostatic force between two conducting spheres," *American Journal of Physics*, Vol. 66, No. 4, 1998, pp. 352–355.

[43] Soules, J. A., "Precise Calculation of the Electrostatic Force Between Charged Spheres Including Induction Effects," *American Journal of Physics*, Vol. 58, 1990, pp. 1195–1199.

[44] Schaub, H. and Junkins, J. L., *Analytical Mechanics of Space Systems*, AIAA Education Series, Reston, VA, 2nd ed., October 2009.

[45] Hover, F. S., "Simulation of Stiff Massless Tethers," *Ocean Engineering*, 1966.

[46] Valverde, J., Escalona, J., Mayo, J., and Dominguez, J., "Dynamic Analysis of a Light Structure in Outer Space: Short Electrodynamic Tether," *System Dynamics*, 2003.

[47] Yang, H., Hong, J., and Yu, Z., "Dynamics Modelling of a Mlexible Hubbeam System with a Tip Mass," *Journal of Sound and Vibration*, 2003.

[48] Felippa, C. and Haugen, B., "Unified Formulation of Small-Strain Corotational Finite Elements: I. Theory," Tech. report, University of Colorado at Boulder - Center for Aerospace Structures, 2005.

[49] Maxwell, J., editor, *On the Electrical Capacity of a Long Narrow Cylinder and of a Disk of Sensible Thickness*, 1878.

[50] Vainshtein, L., "Static Boundary Problems for a Hollow Cylinder of Finite Length. III Approximate Formulas," *Zh. Tekh. Fiz.*, 1962.

[51] Jackson, J., "Charge Density on Thin Straight Wire, Revisited," *American Journal of Physics*, 2000.

[52] Park, S., "Thermally Induced Attitude Disturbance Control for Spacecraft with a Flexible Boom," *Journal of Spacecraft and Rockets*, 2002.

[53] Bathe, K.-J., *Finite Element Procedures*, Prentice–Hall, London, 1996.

[54] Huebner, K. H., *The Finite Element Method for Engineers*, New York: Wiley, 2001.

[55] Dukkipati, R., Rao, M., and Rama, B., *Computer Aided Analysis and Design of Machine Elements*, New Delhi: New Age International, 2000.

[56] Cunniff, P., Auerbach, M., Vetter, E., and Sikkema, D., "High Performance M5 Fiber for Ballistics / Structural Composites," .

[57] Pearson, J., Levin, E., Oldson, J., and Wykes, H., "Lunar Space Elevators for Cislunar Space Development," Phase i final technical report, Star Technology and Research, Inc., 2005.

[58] "T1000G Data Sheet," Tech. Report CFA-008, Toray Carbon Fiberss America, Inc.

[59] "Zylon Technical Information," Tech. report, Toyobo Co. LTD, 2005.

[60] Gittemeier, K., Hawk, C., Finckenor, M., and Watts, E., "Atomic Oxygen Effects on Coated Tether Materials," AIAA Aerospace Sciences Meeting and Exhibit, 2005.

[61] Polyakov, L. M., "Effect of UV Radiation and Vacuum on the Strength and Failure of Polymer Films," *Mekhanika Polimerov*, Vol. 2, No. 3, 1966, pp. 359–364.

[62] Grossman, E. and Gouzman, I., "Space environment Effects on Polymers in Low Earth Orbit," *Nuclear Instruments and Methods in Physics Research*, 2003.

[63] Gadalla, M., "Prediction of Temperature Variation in a Rotating Spacecraft in Space Environment," *Applied Thermal Engineering*, 2005.

[64] DeForest, S. E., "The Plasma Environment at Geosynchronous Orbit," *1st Spacecraft Charging Technology Conference*, 1977.

[65] Hastings, D. E. and Garrett, H. B., *Spacecraft-Environment Interactions*, Cambridge University Press, 1996.

[66] Pisacane, V. L., *The Space Environment and its Effects on Space Systems*, AIAA Education Series, Reston, VA, 2008, Pages 208–209.

[67] Tribble, A. C., *The Space Environment - Implications for Spacecraft Design*, Princton University Press, revised and expanded ed., 2003.

[68] Purvis, C. K., Garrett, H. B., Whittlesey, A. C., and J., S. N., "Design Guidelines for Assessing and Controlling Spacecraft Charging Effects," Tech. report, NASA, 1984, Paper 2361.

[69] Garrett, H. B. and DeForest, S. E., "An Analytical Simulation of the Geosynchronous Plasma Environment," *Planetary Space Science*, Vol. 27, 1979, pp. 1101–1109.

[70] Lennartsson, W. and Reasoner, D. L., "Low-Energy Plasma Observations at Synchronous Orbit," *Journal of Geophysical Research*, Vol. 83, No. A5, 1978, pp. 2145 – 2156.

[71] Laframboise, J. G., "Theory of spherical and cylindrical Langmuir probes in a collisionless, Maxwellian plasma at rest," Tech. Report 100, Institute for Aerospace Studies, University of Toronto, 1966.

[72] Parrott, M., Storey, L., Parker, L., and Laframboise, J., "Theory of cylindrical and spherical Langmuir probes in the limit of vanishing Debye number," *Physics of Fluids*, Vol. 25, Dec. 1982, pp. 2388–2400.

[73] Katz, I., Jongeward, G. A., Davis, V. A., Mandell, M. J., Kuharski, R. A., Lilley, J. R., J., Raitt, W. J., Cooke, D. L., Torbert, R. B., Larson, G., and Rau, D., "Structure of the Bipolar Plasma Sheath Generated by SPEAR I," *J. Geophys. Res.*, Vol. 94, No. A2, 1989, pp. 1450–1458, DOI:10.1029/JA094iA02p01450.

[74] Lai, S. T. and Tautz, M., "High-Level Spacecraft Charging at Geosynchronous Altitudes: A Statistical Study," *8th Spacecraft Charging Technology Conference*, Oct. 2003.

[75] Riedler and et. al, "Active Spacecraft Potential Control," *Space Science Reviews*, Vol. 79, 1997, pp. 271–302.

[76] Grard, R., "Properties of the Satellite Photoelectron Sheath Derived from Photoemission Laboratroy Measurements," *Journal of Geophysical Research*, Vol. 78, No. 16, 1973, pp. 2885–2906.

[77] Grard, R., Knott, K., and Pedersen, "Spacecraft Charging Effects," *Space Science Reviews*, Vol. 34, 1983, pp. 289–304.

[78] Nakagawa, T., Ishii, T., Tsuruda, K., Hayakawa, H., and Mukai, T., "Net current density of photoelectrons emitted from the surface of the GEOTAIL spacecraft," *Earth Space and Planets*, Vol. 52, 2000, pp. 283–292.

[79] DeForest, S. E., "Spacecraft Charging at Synchronous Orbit," *Journal of Geophysical Research*, Vol. 77, No. 4, Feb. 1972, pp. 651–659.

[80] Samir, U. and Willmore, A. P., "The Equilibrium Potential of a Spacecraft in the Ionosphere," *Planetary and Space Science*, Vol. 14, 1966, pp. 1131–1137.

[81] Torkar, K., Fazakerley, A., and Steiger, W., "Active Spacecraft Potential Control: Results from the Double Star Project," *IEEE Transactions on Plasma Science*, Vol. 34, No. 5, Oct. 2006, pp. 2046–2052.

[82] Whipple, E. C., "Observation of Photoelectrons and Secondary Electrons Reflected from a Potential Barrier in the Vicinity of ATS 6," *Journal of Geophysical Research*, Vol. 81, No. 4, Feb. 1976, pp. 715–719.

[83] Lai, S. T., "The Importance of Surface Conditions for Spacecraft Charging," *AIAA Aerospace Sciences Meeting*, Orlando, FL, Jan. 5 – 8 2009, Paper AIAA 2009-349.

[84] Francis, C., "Electrostatic charging problems of spacecraft," *Journal of Electrostatics*, Vol. 11, No. 3, 1982, pp. 265 – 280, DOI:10.1016/0304-3886(82)90017-1.

[85] Prokopenko, S. M. L. and Laframboise, J. G., "High-Voltage Differential Charging of Geostationary Spacecraft," *Journal of Geophysical Research*, Vol. 85, No. A8, Aug. 1980, pp. 4125–4131.

[86] Garrett, H. B., "The Charging of Spacecraft Surfaces," *Reviews of Geophysics and Space Physics*, Vol. 19, No. 4, Nov. 1981, pp. 577–616.

[87] Lai, S. T., "Spacecraft Charging Thresholds in Single and Double Maxwellian Space Environments," *IEEE Transactions on Nuclear Science*, Vol. 38, No. 6, 1991, pp. 1629–1634.

[88] Lai, S. T., "Theory and Observation of Triple-Root Jump in Spacecraft Charging," *J. Geophys. Res.*, Vol. 96, No. A11, 1991, pp. 19269–19281, DOI:10.1029/91JA01653.

[89] Torkar, K. and et. al, "Spacecraft Potential Control using Indium Ion Source – Experience and Outlook Based on Six Years of Operation in Space," *6th Spacecraft Charging Control Technology Conference*, Hanscom AFB, MA, Sept. 2000, AFRL-VS-TR-20001578.

[90] Marrese, C. M., "A Review of Field Emission Cathode Technologies for Electric Propulsion Systems and Instruments," *IEEE Aerospace Conference Proceedings*, Vol. 4, 2000, pp. 85–98.

[91] Aston, G., B., A. M., and Williams, J. D., "Miniature Plasma Activated Systems for Tether Current Generation," *Space Technology and Applications International Forum*, edited by A. I. of Physics, 2001.

[92] Jahn, R. G. and Choueiri, E. Y., "Electric Propulsion," *Encyclopedia of Physical Science and Technology*, Vol. 5, Academic Press, 2002, pp. 125–141.

[93] Martinez-Sanchez, M. and Pollard, J. E., "Spacecraft Electric Propulsion – An Overview," *Journal of Propulsion and Power*, Vol. 14, No. 5, Sept.–Oct. 1998, pp. 688–699.

[94] Shuman, B. M., Cohn, H. A., Hyman, J., Robson, R. R., Santoru, J., and Willamson, W. S., "Automatic Charge Control System for Geosynchronous Satellites," *Journal of Electrostatics*, Vol. 20, 1987, pp. 141–154.

[95] Goebel, D. M. and Katz, I., *Fundamentals of Electric Propulsion*, JPL Space Science and Technology Series, John Wiley and Sons, Hoboken, NJ, 2008.

[96] Deininger, W. D., Aston, G., and Pless, L. C., "Hollow-cathode plasma source for active spacecraft charge control," *Review of Scientific Instruments*, Vol. 58, No. 6, June 1987, pp. 1053–1062.

[97] Lai, S. T., "An overview of electron and ion beam effects in charging and discharging of spacecraft," *IEEE Transactions on Nuclear Science*, Vol. 36, No. 6, Dec. 1989, pp. 2027–2032.

[98] Matticari, G., Materassi, M., Noci, G. E., Severi, A., and Sabbagh, J., "PLEGPAY: A Plasma Contactor Experiment on the International Space Station," *27th International Electric Propulsion Conference*, Pasadena, CA, Oct. 2001, Paper No. IEPC-01-261.

[99] ThalesAleniaSpace, "Spacecraft Charging Active Control Payload," Information Flyer, Dec. 2006.

[100] Olsen, R. C., "Modification of Spacecraft Potentials by Plasma Emission," *AIAA Journal of Spacecraft and Rockets*, Vol. 18, No. 5, Sept.–Oct. 1981, pp. 462–470.

[101] Olsen, R. C., "Modification of Spacecraft Potentials by Thermal Electron Emission on ATS-5," *AIAA Journal of Spacecraft and Rockets*, Vol. 18, No. 6, Nov. – Dec. 1981, pp. 527 – 532.

[102] Schmidt and et. al, "Results from active spacecraft potential control on the Geotail spacecraft," *Journal of Geophysical Research*, Vol. 100, No. A9, 1995, pp. 253–259.

[103] Torkar, K., Arends, H., W., B., Escoubet, C. P., Fazakerley, A., Fehringer, M., Fremuth, G., Jeszenszky, H., Laky, G., Narheim, B. T., Riedler, W., Rudenauer, F., Steiger, W., Svenes, K., and Zhao, H., "Spacecraft Potential Control for Double Star," *Annales Geophysicae*, Vol. 23, No. 8, Aug. 2005, pp. 2813–2823.

[104] Amatucci, B., Anderson, J., Arnold, S., Bowen, J., Carroll, J., Coffey, S. L., Compton, C., Gatling, G., Huynh, S., Jaffe, P., Kelm, B. E., Koss, S., MCGahagen, J., Tejero, E., and Thurn, A., "CE2: A Cubesat Electron Collector Experiment," *AAS/AIAA Spaceflight Mechanics Meeting*, Savannah, Georgia, Feb. 9–13 2009, Paper AAS 09-239.